Phase Response in Networks of Bursting Neurons:

Modeling Central Pattern Generators

A Dissertation

Presented to the Faculty of the Graduate School

of Cornell University

in Partial Fulfillment of the Requirements for the Degree of

Doctor of Philosophy

by

William Erik Sherwood

January 2008

PHASE RESPONSE IN NETWORKS OF BURSTING NEURONS:

MODELING CENTRAL PATTERN GENERATORS

William Erik Sherwood, Ph.D.

Cornell University 2008

Central pattern generators (CPGs) are localized, autonomous neuronal networks that coordinate the multilayered, rhythmic neuromuscular activity underlying essential behaviors such as respiration, digestion, circulation, and locomotion. A key step in deciphering CPGs' production and modulation of broad repertoires of patterned rhythmic output is understanding how phase relationships are established and maintained in networks of rhythmically active, or 'bursting,' neurons. This thesis presents mathematical and computational investigations of several problems involving phase response, bursting neural models, and phasing in neuronal networks, studied in the context of modeling CPGs.

We first consider the problem of modeling the locomotor central pattern generator responsible for coordinating hindlimb movement in the rodent (RSHL CPG). We propose the first mathematical model for the RSHL CPG, and from the comprehensive, 'full' model we derive several reduced models to test specific hypotheses concerning RSHL CPG architecture. We establish through computational experiments that our models are capable of reproducing the fundamental locomotor rhythm of the RSHL CPG. Our investigations also uncover surprising phase sensitivities and transient behaviors, phenomena unexpected from intuitions based on studies of networks of phase oscillators or tonically spiking neurons.

We pursue the origins of the models' phase sensitivity by studying phase response in single, endogenously bursting neurons. We examine the validity of

several assumptions commonly made by modelers and experimentalists regarding the phase resetting behavior of endogenously bursting neurons in response to single spike perturbations. Our empirical study of burst phase response for a large combination of neuronal models and perturbation types demonstrates that in many circumstances, these assumptions are incorrect. Furthermore, we find that the phase response curves of endogenous bursters differ significantly from those of non-bursting neural oscillators in characteristic ways.

We use fast-slow dissection, phase plane analysis, and isochron portraits to analyze the distinctive shape of burst phase response curves. Our analysis explains the dynamics of burst phase response in regimes of both weak and strong coupling, highlighting the role of fast subsystem structures and bifurcations in determining phase response. We also explain the mechanisms of spike number change due to strong perturbations.

Finally, we apply insights from our study of burst phase response for single neurons to develop a set of discrete maps describing the changes in bursting neurons' phase and spike number in response to single spike perturbations. We also develop a set of map-coupling algorithms that can represent burst activity in arbitrary network architectures, thus reducing the interaction of bursting neurons to the properly sequenced iteration of low-dimensional maps. Our method produces good agreement with the transient and asymptotic phasing behavior of a simple network of biophysically realistic bursters. With further refinement, our algorithmically coupled burst maps may serve as a useful tool for exploring phasing behavior in networks of bursting neurons, especially models of CPGs.

BIOGRAPHICAL SKETCH

William Erik Sherwood was born 150 miles south of Yoknapatawpha on *Walpurgisnacht*, 201 years after Carl Friedrich Gauss accomplished a similar feat in Brunswick, Niedersachsen. A congenital procrastinator, he missed being delivered at the state mental hospital by a few hours (Fortune has striven sedulously to compensate him for being deprived of such an appropriate audience for his entrance, and has succeeded in grand Foucaultean style.); he entered a medical family, and thus was properly welcomed to Triage.

Following a bookish childhood and an adolescence punctuated by overseas trips to learn ripuaren *Kölsch*, but otherwise unremarkable for its boredoms and complaints, Erik enrolled in Cecil Terwilliger's *alma mater*, the premier clown college of Princeton, New Jersey. There he earned trophy degrees in pure and applied mathemagics, information technology, and Teutonic studies, and in his spare time he paddled rowboats, led nature walks, and was a varsity sword fighter.

After four years in the ivy-lined capitalist greenhouse of the Garden State, and in need of a respite from its community of plutocratic ambition, he repaired to the *rote Kaderschmiede* in Bremen at the invitation of the *Deutscher Akademischer Austauschdienst*, where he was spoiled on *Ordnung, Effizienz, und Kohl und Pinkel*. His soul was purified through a year's penance and confinement at the Fortress of Mathematical Sciences and Blenheim Prison in Cambridge, where he rowed the penitentiary galley to victory in the May Bumps.

His odyssey then brought him to Ithaca, which felt like home. Here he flirted with a martial life while dawdling towards his degree. A pleasant time having elapsed, Erik will journey from the limbo of graduate school into postdoctoral purgatory in Beantown. Moving ever upward, he plans thereafter to raise penguins with his soon-to-be wife, perhaps in Finland.

To Melanie

Ick hab' Dir lieb, wah!

ACKNOWLEDGEMENTS

My foremost thanks go to my advisor, John Guckenheimer, who has been a steady source of scientific guidance and support throughout. He has encouraged independence and patiently indulged my tangential interests. It has been a thoroughly edifying apprenticeship.

I am also grateful to Ron Harris-Warrick and John Smillie for serving on my committee, and to Alex Vladimirsky for acting as a proxy during my defense. Ron and the members of his lab group, in particular Bruce Johnson, Manual Díaz-Ríos, Guisheng Zhong, Mark Masino, and Mark Abbinanti, generously shared their time and knowledge of neurobiology with me; they deserve special thanks.

The members of the Guckenheimer group and the PyDSTool coding club, Rob Clewley, Drew Lamar, and Joe Tien, are terrific friends and colleagues whose help — wrestling with mathematics; writing, debugging and occasionally rebugging code; translating delphic pronouncements from Shyriiwook to Earthling and pondering their meanings; and generally maintaining sanity — has been invaluable.

CAMsters have been very fortunate to have been served by student system administrators of uncommon intelligence, technical savvy, and dedication. The computational work that went into this dissertation and the development of PyDSTool benefitted in particular from the support of David Benbennick, Jason Martin, Michael Robinson, and Franco Saliola. Ur-sysadmin Jason Martin is due special recognition for his skill, commitment, and hard work, as well as for being a great pal and lifting partner.

My graduate studies have been supported by a National Defense Science and Engineering Graduate fellowship and grants from the National Institutes of Health and the National Science Foundation. During my first two years of graduate school,

I participated in the NSF-sponsored IGERT program, an experience that sometimes piqued my scientific curiosity, but more rewardingly fostered several friendships.

CAM's fairy godmother, Dolores Pendell, has kept me on track, suffered my whining, boosted my spirits, and reined in my megalomania, all the while ensuring the department ran smoothly. She deserves a heaping helping of praise.

My friends from CAM and the Cornell community have been the best part of my graduate school experience. Because of them, I have felt more like home in Ithaca than anywhere else in a decade. Even at the nadir of the most leaden Ithaca winter, I could always count on Tara Small to brighten my day with her enthusiasm and good humor. My sometime role model and occasional counterweight, fellow Tiger, cynic, and cruciverbalist Mighty Joe Tien was ever a boon companion.[1] I'll keep fond memories of laughter-filled activities (athletic, prandial, bibitory, and otherwise) with Fergmilia Huerta-Sanchez Casey; of caffeination, commiseration, and klatschin' with Robyn Miller; and of jogging, joking, palaver, and pursuit of The Pump with my paisano and protégé Stephen Moseley.

Also among my good friends of these past years are senior CAMsters Marcel Blais, Richard Casey, Sharad Goel, Jason and Carla Martin, Johnny Guzman, and Jesus Rodriguez, exemplars of the amiability, energy, and general lightheartedness that distinguish the sixth floor of Rhodes Hall; and of more recent vintage, Danny Abrams, Lauren Childs, Ryan Gutenkunst, Paul Hurtado, Mike Klotz and the Illiterati, Megan Owen, Mateo Restrepo, Deena Schmidt, Chris Scheper, Laura Sherman, and Evan Variano.

[1] Except for the two times he broke my knee playing basketball, and the time he fired me as his lifting partner.

During a very different, parallel phase of my life, it was my privilege and good fortune to have been befriended by several admirable individuals, among them MAJ Richard Brown, LTC Glenn Reisweber, MSG Ralph DeLosa, 1LT Paul McClelland, 1LT David Napper, 1LT Michael Philpott, 1LT Colleen Reiss, 1LT Caitlin Rizzo, 1LT Chris Shraga, and 1LT Matthew Yalch. I wish them safety, success, and godspeed: $\alpha\iota\varepsilon\nu\ \alpha\varrho\iota\sigma\tau\varepsilon\upsilon\varepsilon\iota\nu\ \kappa\alpha\iota\ \upsilon\pi\varepsilon\iota\varrho\phi\chi\phi\nu\ \varepsilon\mu\mu\varepsilon\nu\alpha\iota\ \alpha\lambda\lambda\omega\nu$.[2]

As comfortable a home as CAM is, this thesis could not have been completed there. *Ich hoffte, nach einem so schlimmen Sommer einen guten Herbst zu genießen.*[3] I am very grateful to Fabio Dercole and Martina, Sergio, and Amalia Rinaldi for their friendship and hospitality in Milan during the homestretch of dissertating.

My relatives in New York — Betty, Eric, and Stephanie Wallace; Sylvie, Brian and Ken Donnelly; Tommy and Lilly Martin; and Frank, Ginette, and Larry Beeftink — provided a welcoming second (or is it third?) home during my grad school years. I am very fortunate to have such warm and wonderful people in my family.

As their devotion and nurturance have been such constants in my life, it would be easy to take my parents, Todd and Julia, for granted, but I know I could not have made it through without them. I could always ask my father to clarify the difference between logarithms and algorithms, and I could turn to Dr. Mom for sage advice on health and well-being — of myself and my apartment's aesthetics. Their bright example inspires me, and their firm support steadies me. I am deeply thankful for their enduring love.

[2] Glaucus, son of Hippolochus, Book VI, line 208 [119].
[3] Karlsbad bis auf den Brenner, 3. September 1786, [84].

Most of all, though, I am grateful to my fiancée, Melanie, who means more to me than I can ever express. Her diligent editorial help greatly improved my writing, and her persistent encouragement was invaluable, seeing me through the bleak stretches of toil when I felt sure I faced insurmountable obstacles. She has brought me unimagined happiness, and I am constantly amazed at the *Lebensglück* we share as *Doppelsterne*. *Forsan et haec olim meminisse iuvabit*[4] — I already do, for her presence leavens every endeavor with joy. This work is dedicated to her, and I look forward to making many more dedications to her in the years to come.

It is fitting that this dissertation is written in the nosistic voice, for I and my work have profited immensely from the personal and intellectual companionship of the individuals mentioned above. They deserve some portion of credit for whatever success this dissertation may represent (its completion being a victory in itself), while any errors of reason or expression herein are my own.

Finishing a thesis seems to be basically an exercise in damage control.[5]

That would certainly be a better name for this planet than Earth, since it would give people who just got here a clearer idea of what they were in for: Triage.

Welcome to Triage.[6]

[4]Book III, line 203, [225].
[5]Robert H. Clewley
[6]"Triage" [226].

TABLE OF CONTENTS

LIST OF FIGURES

LIST OF TABLES

LIST OF ABBREVIATIONS

4-AP	4-aminopyridine
4-CE	two half-center oscillators with cross-excitation
4-IRCE	bi-directional inhibitory ring with cross-excitation
4-IR	bi-directional inhibitory ring
5-HT	serotonin
AB	anterior burster neuron
ACh	acetylcholine
AHP	afterhyperpolarization
BRC	burst resetting curve
BPRC	burst phase response curve
Ca^{2+}	calcium ion
CIN	commissural interneuron
CPG	central pattern generator
DA	dopamine
EP	excitatory pair
HR	Hindmarsh-Rose neuron
ISI	interspike interval
K^{+}	potassium ion
LP	lateral pyloric neuron
Mg^{2+}	magnesium ion
MN	motoneuron
NMA	N-methyl-D,L aspartic acid
Na^{+}	sodium ion

NA	noradrenaline
NMDA	N-methyl-D-aspartate
ODE	ordinary differential equation
PB	pre-Bötzinger neuron
PD	pyloric dilator neuron
PRC	phase response curve
PY	pyloric neuron
R15A	R15 *Aplysia* neuron
RGK	rhythmogenic kernel
RGN	rhythmogenic interneuron
RSHL	rodent spinal hindlimb locomotor
SFA	spike frequency adaptation
SNRC	spike number response curve
STDM	spike time difference map
STG	stomatogastric ganglion
STRC	spike time response curve

LIST OF SYMBOLS

$W^s(M)$	stable manifold of set M
$W^u(M)$	unstable manifold of set M
$\Phi(\mathbf{x}, t)$	flow map of a vector field
Γ	periodic orbit
θ	phase
ϑ	asymptotic phase
ϖ	isochron
φ	phase response curve
$\sigma(\tau), \sigma(\phi)$	spike time shift
$\upsilon(\tau), \upsilon(\phi)$	spike number change
$\omega(\tau), \omega(\phi)$	quiescence length change
$\Sigma(\tau, B)$	spike shift operator
$\Upsilon(\tau, B)$	spike number change operator
$\Omega(\tau, B)$	quiescence operator

PREFACE

Many fundamental motor behaviors, such as heartbeat, breathing, feeding, swimming, and walking, are organized by central pattern generators (CPGs). Independent of sensory input, these spatially compact neuronal networks produce bursts of action potentials in complex patterns; the proper timing and sequencing of these bursts translates into rhythmic neuromuscular activity leading to purposeful movement. Thus, a key challenge in understanding neural control of basic motor patterns is is to answer the question, "How are phase relationships established and maintained in networks of bursting neurons?" This thesis studies several aspects of that problem from a computational and mathematical perspective.

We organize the thesis as follows: Chapter 1 provides a brief introduction to neuronal bursting, multiple time-scale dynamical systems, phase response, and central pattern generators, recurrent topics in the subsequent presentation. In chapter 2, we develop a framework for modeling central pattern generators, construct a model of the rodent spinal hindlimb locomotor CPG, and test it through a variety of computational experiments. Chapter 3 presents an empirical study of the phase response characteristics of several biophysically realistic models of endogenously bursting neurons, testing a large combination of input forms and perturbation strengths. We analyze the mechanisms responsible for the characteristic shape of the model bursters' phase response in chapter 4, and in chapter 5 we develop a method of reducing burst phase response to a set of discrete maps which can be algorithmically coupled to study the phasing behavior of networks of bursting neurons. Chapter 6 concludes with a summary of results and directions for future research. The appendices describe the equations and parameter values for the models used and contain a gallery of burst phase response curves.

CHAPTER 1

BACKGROUND

1.1 Bursting

Electrically excitable cells generically display three modes of behavior: Quiescence, tonic spiking, and bursting. In *quiescence*, a cell maintains a stable resting membrane potential, but if perturbed (via temporary injection of current, for example), the membrane potential makes a large excursion, or action potential, depolarizing far above the resting potential, then hyperpolarizing somewhat below the resting potential, before reestablishing its equilibrium value. *Tonic spiking*, also called *beating*, is marked by continual firing of action potentials, normally at a fixed or slowly declining rate, and it typically occurs in the presence of a steady stimulus, such as an external current. A gradual decrease in the firing rate, normally associated with an increase in the magnitude of slow afterhyperpolarization (AHP) following each spike, is called spike frequency adaptation (SFA); sufficiently strong SFA may cause the cell's membrane potential to remain below its excitability threshold for action potential generation, shifting the cell from tonic spiking to a quiescent state [115].

Bursting[1] is characterized by relatively slow, periodic alternation between periods of spiking (*active state*) and periods of electrical inactivity (*quiescent state*).[2] Bursting can be viewed as an intermediate state between tonic spiking and quies-

[1]Cells exhibiting bursting activity are commonly said to be 'oscillatory' in the neuroscience literature. We will only use the term 'bursting', to avoid confusion with cells that are tonically spiking, which are said to 'oscillate' in the mathematical modeling literature.

[2]The active state is also called the active period, active phase, or the burst, and the quiescent state is also called the quiescent period, quiescent phase, quiet phase, silent phase, etc. To avoid confusion with other key terms, we will refer to the spiking (silent) portion of a bursting cell's oscillatory cycle only as its active (quiescent) *state* or as the active (quiescent) *segment* of the burst.

cence, in which the cell transitions between these two modes.[3] During the active segment of the burst, the action potentials' profiles may change, and their inter-spike intervals may vary, *e.g.* spike frequency adaptation may occur. At the end of the active segment, the membrane potential drops below the cell's spiking threshold and remains there throughout the subsequent quiescent segment. The membrane potential slowly rises over the course of the quiescent segment until it exceeds the spiking threshold, switching the cell into a new active state and initiating a new burst cycle.

Bursting activity is found almost everywhere electrical signals are used for inter-cellular communication. It is ubiquitous in the nervous systems of both vertebrates and invertebrates, occurring in neurons that play a role in controlling respiration [24, 25, 22, 56, 57, 177], motor function [28, 26, 116], digestion [152, 111, 110], cardiac rhythms [31, 51], and cortical function during learning and sensory processing [50, 167]. In some contexts, such as sensory information transmission, bursts may be the fundamental unit of information used by the nervous system, rather than individual spikes [141, 126]. Coordinated bursting activity is essential to the proper functioning of the nervous system, and improper bursting is implicated in diseases of neural and neuromuscular dysfunction, *e.g.* Parkinson's disease, epilepsy, cardiac arrhythmia [194]. Bursting by electrically excitable cells is also critical to hormone secretion by the endocrine system, controlling insulin release by pancreatic β-cells to regulate bloodstream glucose levels [202], the release of gonadotropins by pituitary gonadotrophs to regulate the mammalian reproductive cycle [132], and arginine vasopressin release in the hypothalamus to regulate blood pressure and body temperature [188].

[3]Related to bursting oscillations are plateau oscillations, found in some neurons, in which the membrane voltage rises significantly above its baseline and remains high for some time, during which the membrane voltage makes relatively small oscillations about the elevated baseline potential (but does not make large excursions, as in action potentials), and then the membrane voltage drops back to its original low baseline level.

Cells that burst in isolation due to their intrinsic properties, such as the expression level and activation kinetics of ion channels controlling the passage of current through the cell membrane, are termed *endogenous* bursters. Examples of endogenous neuronal bursters include medullary cells of the pre-Bötzinger complex [22, 56, 57, 177], dopaminergic mammalian midbrain cells [166], thalamic relay cells [189, 203], neocortical pyramidal cells [40, 230], trigeminal motoneurons [55, 54], magnocellular neurosecretory cells [188], spinal interneurons and motoneurons [28, 26, 116, 234, 242, 241, 243]; ganglion neurons of the mollusk *Aplysia* [187]; and neurons in the stomatogastric ganglion of lobsters and crabs [111]. Endogenous neuronal bursters typically have a set of spiking currents with fast kinetics (normally rapid, inactivating sodium channels and voltage-activated potassium channels) which produce action potentials when the baseline membrane voltage rises above their spiking threshold. The baseline membrane voltage is primarily governed by a leak current and a set of currents (*e.g.* calcium, persistent sodium, or calcium-activated potassium) with much slower kinetics than the spiking currents. The course of an endogenous burst cycle typically traces the following pattern [115, 131]: The slow currents raise the base membrane voltage above the action potential threshold, switching the cell into its active state and initiating a period of repeated spiking. As the neuron spikes, the flux of various ions across the membrane changes the intracellular ion concentrations and the membrane voltage, altering the activation levels of the slow currents. Eventually, the slow currents are no longer strong enough to hold the base membrane voltage above the threshold potential, and the neuron stops firing, switching from the active to the quiescent state. During the quiescent segment of the burst, the slow currents recover, perhaps through slow activation or deinactivation, eventually raising the base membrane voltage above the firing threshold, beginning a new active state and a new burst

cycle.

Alternatively, bursting may be a network property, emerging from the interaction of endogenously quiescent or tonically spiking cells that are electrically or synaptically connected [58, 200]. *Network bursting* (also *emergent bursting*) may occur in combinations of quiescent, plateauing, slowly oscillatory, or tonically spiking cells with the appropriate inhibitory or excitatory synaptic connections; myriad configurations that lead to rhythmic bursting are possible even in networks consisting of just a few neurons [191, 35]. Identical, intrinsically spiking cells may burst synchronously when weakly coupled together; small amplitude noise can enhance the strength of the bursting rhythm [52]. Networks of occasionally spiking cells with heterogeneous firing properties show robust bursting activity with strong coupling [53]. Whether bursting activity in a given neuronal network arises endogenously or as a network property has significant implications for the amplitude, frequency range, robustness, and synchronization of bursting oscillations [206, 191, 53, 207].

1.2 Multiple Time-scale Systems

Many dynamical systems models exhibit *multiple time-scales*: For significant portions of a typical trajectory, some phase space variables evolve much more rapidly than others, perhaps on time-scales separated by several orders of magnitude. This phenomenon is found in models for cosmological evolution, chemical reaction systems, electronic circuits, reaction-diffusion systems, and in particular, neuronal dynamics.

The physiology of the nervous system naturally imposes a multiple time-scale structure on biophysically realistic neural models. As pointed out by Guckenheimer *et al.* [101], there are several time-scales relevant to mathematical models

of bursting: action potential durations of a few milliseconds; the active segment duration of 10–500 milliseconds; complete burst cycle periods of 1–5 seconds; and the 10–100 second time-scale for intrinsic cellular adaptations, such as response to neuromodulatory substances and some forms of spike frequency adaptation. The first three of these scales are most relevant to mathematical models of endogenous bursting. In such models, some phase space variables, typically corresponding to the (in)activation of fast currents related to action potential generation, evolve on much more rapid time-scales than other variables corresponding to the (in)activation of slower currents that affect the baseline membrane voltage. One of the most effective tools for analyzing the interplay of fast and slow currents in generating bursting activity is the geometric singular perturbation theory approach, which is sketched in the following subsection, drawing heavily on the exposition in Jones [127], Wiggins [229], Guckenheimer *et al.* [102], and Tien [219].

1.2.1 The Geometric Singular Perturbation Approach

We consider systems of the form

$$\begin{aligned} \mathbf{x}' &= f(\mathbf{x}, \mathbf{y}, \epsilon) \\ \mathbf{y}' &= \epsilon g(\mathbf{x}, \mathbf{y}, \epsilon) \end{aligned} \tag{1.1}$$

where $' = \frac{d}{dt}$, $\mathbf{x} \in \mathbb{R}^m$, $\mathbf{y} \in \mathbb{R}^l$, and ϵ is a small positive parameter. The regime for which $\epsilon \ll 1$ is called the *relaxation regime*, and such a system of equations is called a *singularly perturbed system*. The particular form of (1.1) emphasizes that the variables $\mathbf{y}$ change much more slowly than the variables $\mathbf{x}$. The time scale given by t is said to be fast; $\mathbf{x}$ are said to be the fast variables; and (1.1) may be referred to as the *fast system*.

By rescaling time as $\tau = \epsilon t$ and writing $\dot{} = \frac{d}{d\tau}$ we obtain the formulation

$$\begin{aligned} \epsilon\dot{\mathbf{x}} &= f(\mathbf{x}, \mathbf{y}, \epsilon) \\ \dot{\mathbf{y}} &= g(\mathbf{x}, \mathbf{y}, \epsilon) \end{aligned} \tag{1.2}$$

Here τ is said to be slow time; $\mathbf{y}$ are the slow variables; (1.2) is sometimes called the *slow system*.

Letting $\epsilon \to 0$ in fast system (1.1), we obtain its *singular limit*:

$$\begin{aligned} \mathbf{x}' &= f(\mathbf{x}, \mathbf{y}, 0) \\ \mathbf{y}' &= 0 \end{aligned} \tag{1.3}$$

If we similarly take the limit $\epsilon \to 0$ in system (1.2), the result is sensible only if $f(\mathbf{x}, \mathbf{y}, 0) = 0$. In this case, we obtain the differential algebraic equations

$$\begin{aligned} f(\mathbf{x}, \mathbf{y}, 0) &= 0 \\ \dot{\mathbf{y}} &= g(\mathbf{x}, \mathbf{y}, 0) \end{aligned} \tag{1.4}$$

Formulations (1.1) and (1.2) are equivalent for $\epsilon \neq 0$, and we refer to either formulation as the *full system*. The subsystems defined by the singular limits (1.3) and (1.4) are not equivalent; analyses of their dynamics provide complementary sets of information about the dynamics of the full system.

System (1.3) treats $\mathbf{y}$ as an l-dimensional set of parameters for the equations governing the evolution of the dynamic (fast) variables $\mathbf{x}$. Fixing $\mathbf{y}$, we obtain a particular *fast subsystem*; varying $\mathbf{y}$, it acts as an index into the family of fast subsystems of the full system.

In the singular limit (1.4), on the other hand, $f(\mathbf{x}, \mathbf{y}, 0) = 0$ locally defines an l-dimensional manifold, M_0, which is obtained by applying the implicit function theorem to $f(\mathbf{x}, \mathbf{y}, 0) = 0$ for $\mathbf{x}$. M_0 is called the *critical manifold*, and it consists of the union of equilibria of the fast subsystems of the family (1.3). The remaining equations $\dot{\mathbf{y}} = g(\mathbf{x}, \mathbf{y}, 0)$ define the *slow flow*, a vector field on the critical manifold.

M_0 is normally hyperbolic if each of the equilibria of $\dot{\mathbf{x}} = f(\mathbf{x}, \mathbf{y}, 0)$ is hyperbolic. Assuming a normally hyperbolic critical manifold, the following theorems of Fenichel assure us that the behavior of trajectories in the family of fast subsystems will correspond reasonably closely to the behavior of trajectories in the full system [75, 76, 127].

Theorem 1.2.1. *For sufficiently small $\epsilon > 0$, there exists a manifold M_ϵ within distance $O(\epsilon)$ of and diffeomorphic to M_0, which is locally invariant under the flow of (1.1)–(1.2) and C^r, for any $r < +\infty$.*

Theorem 1.2.2. *For sufficiently small ϵ, there exist stable and unstable manifolds $W^s(M_\epsilon)$ and $W^u(M_\epsilon)$ within a distance $O(\epsilon)$ of and diffeomorphic to the stable and unstable manifolds $W^s(M_0)$ and $W^u(M_0)$, respectively, of M_0. Both $W^s(M_\epsilon)$ and $W^u(M_\epsilon)$ are locally invariant under the flow of (1.1)–(1.2) and C^r, for any $r < +\infty$.*

Further theorems guarantee that the flow on the critical manifold gives an $O(\epsilon)$ approximation to the trajectories of the full system.

1.2.2 Fast-Slow Dissection

The exploitation of separation of time-scales to simplify analysis of neural models dates back to Fitzhugh's reduction of the Hodgkin-Huxley equations to produce a schematic model of action potentials [77, 78]: Trajectories in the Fitzhugh-Nagumo system slowly track a stable branch of the voltage nullcline until they reach a knee or critical point, then they rapidly jump across to the other stable branch of the nullcline and resume their slow movement. Motion near the stable branches corresponds to subthreshold potential changes, while the rapid transits between branches correspond to the sharp rising and falling segments of an action potential.

Rinzel later applied the tools of geometric perturbation theory to analyze bursting via a similar *fast-slow dissection* [187, 185], a technique which has become a standard method for mathematical investigation of bursting. The basic idea is to identify the phase space variable(s) associated with the slowest membrane current and treat it as a quasi-static parameter, thereby obtaining a family of fast subsystems as the parameter varies. Over the course of a bursting cycle in the full system, the slow variable traces out a periodic trajectory, giving a range over which it varies when considered as a quasi-static parameter. The active spiking state of the full system corresponds to the burst trajectory closely tracking a stable limit cycle in the family of fast subsystems, while the quiescent state corresponds to the burst trajectory staying close to a stable fixed point in the fast subsystems. As the slow variable varies, bifurcations in the fast subsystem create, destroy, and change stability of the fixed points and period orbits which the full system trajectory tracks. This causes rapid switching between attractors, and hence rapid changes in the full system's state, in a manner analogous to the transitions between stable nullcline branches for the Fitzhugh-Nagumo model of action potentials.[4]

Since bifurcations in the fast subsystem signal qualitative changes in the dynamical behavior of trajectories in the full system, the pairs of bifurcations marking the initiation and termination of the active state of burst trajectories lead to a classification scheme for bursting models [185, 131]:

- Type I (square-wave) bursters: The active state begins at a saddle-node and ends at a homoclinic bifurcation. For type Ia bursters, the minimum voltage during the active segment is above the baseline voltage of the quiescent segment; in type Ib bursters, it is below. Type I bursters typically show spike

[4]Interestingly, Fitzhugh drew upon the van der Pol equations to develop the Fitzhugh-Nagumo equations [78]; the forced van der Pol equations are also used as a schematic system for mathematical investigation of bursting behavior [102, 9].

frequency adaptation during the active segment of the burst cycle. (One slow variable is required.)

- Type II (parabolic) bursters: The active state begins and ends at homoclinic bifurcations (or saddle-nodes on an invariant circle). The variation in time of the instantaneous period of the spiking limit cycle has the shape of a parabola. (Two slow variables are necessary.)
- Type III (elliptic) bursters: The active state begins at a (subcritical) Hopf bifurcation and ends at a saddle-node bifurcation. (One slow variable is required.)

Extensions to this classification scheme have been put forth, encompassing other experimentally observed bursting behavior [6, 146, 66], including a more complete taxonomy of bursters based on the codimension-1 bifurcations in the fast subsystem at the beginning and end of the active state [124]. Other taxonomies based on bifurcations of symmetric solutions have been proposed for studying bursting in networks of identical cells [90, 89].

Although membrane currents are commonly categorized as being fast or slow, it is not always so easy to classify their corresponding phase space variables as fast or slow in a congruent fashion, since they may describe, for example, fast activation and slow inactivation. An alternative and perhaps more biologically appropriate approach to fast-slow dissection is to collect slow currents into an "effective leak" current of the fast subsystem and to study bifurcations as the effective leak conductance and reversal potential are varied [104]. This allows one to study the combined effects of multiple slow currents, or currents with differing (not necessarily all slow) time-scales, on the bursting activity without singling out one phase space variable. This may be particularly important when there are mixed time scales or multiple variables contributing to the separation of time-scales

during the course of a burst cycle.

1.2.3 Numerical Issues

Numerical integration is an essential tool for studying dynamical systems of any significant complexity. Most systems of interest, and nearly all neuronal models, are described by differential equations that cannot be solved analytically, and hence their solution trajectories must be approximated numerically. No single numerical integration method is best for all problems, and a variety of algorithms exist to solve 'typical' and specialized problems. Runge-Kutta methods are the most popular general-purpose numerical integration schemes, but the relative weight of criteria such as the number of function evaluations, memory overhead, roundoff effects, and the number of steps for which true error exceeds set tolerances ('deception count', a measure of reliability) may make other methods more suitable [121]. Equations possessing a special structure or posing particular difficulties (*e.g.* discontinuities, round-off considerations) may require specialized methods for their solution.

Systems of ordinary differential equations which have multiple time-scales present challenges to standard numerical integration algorithms. They exhibit a quality known as *stiffness*, a frequently used term having no single, accepted definition. Stiffness is typically defined operationally: a differential equation is stiff "if its numerical solution by some methods requires (perhaps in a portion of the solution interval) a significant depression of the step-size to avoid instability" [123]. More succinctly, "[s]tiff equations are problems for which explicit methods don't work" [108].[5]

[5]Note that explicit methods may detect stiffness cheaply by checking whether the product of the dominant eigenvector of the Jacobian and the current step-size is within a tolerance of the boundary of the linear stability domain. *Ibid.*

A more rigorous definition of stiffness may be stated in terms of the linear approximation to an ODE's solution. The equation $\dot{\mathbf{y}} = f(t, \mathbf{y})$, with $\mathbf{y} = \mathbf{y}_0$ at $t = 0$, is approximated near its solution $g(t)$ by

$$\dot{\mathbf{y}} \approx f(t, g(t)) + J(t)(\mathbf{y} - g(t)) \tag{1.5}$$

$$= g'(t) + J(t)(\mathbf{y} - g(t)) \tag{1.6}$$

where $J(t)$ is the Jacobian (also, variational) matrix $J(t) = f_{\mathbf{y}}(t, g(t))$. If the any of eigenvalues $\lambda(t)$ of $J(t)$ are large and positive, then the problem is *unstable*. If the eigenvalues have small magnitude, then the problem is *neutrally stable*, a situation easily handled by most general-purpose numerical integration methods. If the problem is not unstable and $\max_\lambda\{\mathrm{Re}(-\lambda(t))\} \gg \max_\lambda\{\mathrm{Re}(\lambda(t))\}$, then it is said to be *stiff* [176, 196]. Note that a problem may be stiff for some time intervals and not others.

Stiff systems characteristically have short transient periods after which the solution curves to the equation are nearly identical, regardless of the initial value $\mathbf{y}_0$. It is in the region after the initial transient that the systems behave stiffly; a system may alternate between transient periods and regions of stiffness. In the stiff region, step size selection is dominated by stability considerations (minimizing the propagation of error to subsequent steps) instead of accuracy (keeping the local error small at given step).

Stability for explicit methods requires that $|h_n \lambda_{\max}(t)|$ remain small, where h_n is the step-size and $\lambda_{\max}(t)$ is the largest eigenvalue of $J(t)$. In the transient region, the system's movement is dominated by eigendirection associated $\lambda_{\max}(t)$, but step-size is restricted by accuracy considerations, rather than stability constraints. Outside the transient region, however, insufficiently small steps can lead to the accumulation of errors (*e.g.* local truncation errors inherent in IEEE arithmetic)

associated with the non-dominant components. The accumulated errors can lead to the sudden apparent blow-up of otherwise seemingly stable solutions; this problem typically becomes apparent near transition points into and out of regions of stiffness [123].

The simplest way of overcoming stiffness is simply to reduce the maximum integration step size, but this is not effective in all situations, and it is usually highly inefficient, since the integrator then takes small steps even in regions where the system behaves stably. This problem affects all explicit methods, including higher precision techniques, such as Taylor series integration based on automatic differentiation [168, 129]. Numerical continuation packages, such as AUTO, and standard continuous optimization methods may also have difficulty with stiff systems [219].

Implicit methods are generally more effective and efficient for solving stiff systems, allowing larger step sizes to be taken in stiff regions and handling transitions between transient and stiff regions more robustly. Implicit, one-step stiff integration methods may be evaluated with respect to their A-stability, S-stability, stiff accuracy, and stiff order [176]; Lobatto IIIC and Radau IIA (RADAU5) [108] are particularly strong methods. The inherent stiffness of many bursting neural models make such considerations particularly apposite. The multiple time-scale structures associated with bursting phenomena necessitate special care in choosing stable, accurate numerical methods for their computational investigation.

The presence of stiffness is not entirely negative for modeling bursting and other multiple time-scale systems, since it implies that the techniques of geometric singular perturbation theory are especially applicable. Greater stiffness is associated with wider separation of time-scales in multiple time-scale systems, which roughly corresponds to smaller ϵ in the $O(\epsilon)$ approximation of the full system dynamics by the fast and slow subsystem dynamics referred to in theorems (1.2.1) and (1.2.2).

Though it makes computation more difficult, stiffness may increase the accuracy of singular limit approximations as representations of bursting dynamics in the full system.

1.3 Phase Response Curves

A natural topology for the state space of many models of rhythmic biological phenomena, including (bursting) neural oscillations, is that of the circle, rather than Euclidean space. In dynamical systems models of neuronal activity, trajectories that simulate oscillatory membrane voltage activity, such as tonic spiking and bursting in particular, generically correspond to stable periodic orbits. The state of the model neuron as it repeatedly fires an action potential or proceeds through a burst cycle can be described by a single scalar variable, its *phase*, evolving on the circle.

Considering dynamical systems models of neural oscillations in terms of phase brings a number of benefits. First, the dimension reduction involved can simplify mathematical analysis of the systems. Second, explicit acknowledgment of the models' circular phase space brings the rhythmic nature of the underlying processes to the fore, fostering more biologically relevant and illuminating interpretations of the models' behavior. Third, when studying networks of interacting neural oscillators, many of the most biologically pertinent modeling questions, in particular those involving changes in the relative timing of spikes or bursts, *e.g.* synchrony, are posed and addressed most naturally in terms of phasing, *i.e.* the relative positioning of oscillators on their individual periodic orbits. Below we introduce the terminology and notation of phase oscillators and phase response that will be useful for building and analyzing models of bursting neural oscillations and networks of bursting neurons.

Let the evolution of a dynamical system F be governed by the system of ordinary differential equations $\dot{\mathbf{x}} = f(\mathbf{x}), \mathbf{x} \in \mathbb{R}^n$, with associated (smooth) flow $\Phi(\mathbf{x}, t), \Phi : \mathbb{R}^n \times \mathbb{R} \to \mathbb{R}$, and let Γ be a periodic orbit for F with period T. As Γ is a one dimensional manifold, we can describe the state of the dynamical system F restricted to Γ in terms of a single scalar variable $\theta \in [0, 1)$, its natural phase space being diffeomorphic to the circle $\mathbb{S}^1$. Note then that any point $\mathbf{x} \in \Gamma$ is associated with a unique *phase* $\theta(\mathbf{x}) \in [0, 1)$. A natural labeling of phases on Γ is obtained by fixing a reference point $\mathbf{x}_0 \in \Gamma$ and setting $\theta(\mathbf{x}) = t/T \mod 1$ if $\Phi(\mathbf{x}_0, t) = \mathbf{x}$, for $\mathbf{x} \in \Gamma$.

This idea of phase, represented by θ, is strictly meaningful only on Γ, but we can extend the concept to include points in the basin of attraction of Γ, denoted by B, as follows: For $\mathbf{y} \in B$, there exists a unique $\mathbf{x} \in \Gamma$ with phase $\theta(\mathbf{x})$, such that $\|\Phi(x, t) - \Phi(\mathbf{y}, t)\| \to 0$ as $t \to \infty$. When associating the scalar value $\theta(\mathbf{x})$ with $\mathbf{y}$, we call it the *asymptotic* (also *latent*) *phase* of $\mathbf{y}$ and denote it by $\vartheta(\mathbf{y})$. For each $\mathbf{x} \in \Gamma$, we define the *isochron* $\varpi(\mathbf{x})$ of $\mathbf{x}$ as the set of all points in the basin of attraction of Γ having the same asymptotic phase as the actual phase of $\mathbf{x}$, *i.e.* $\varpi(\mathbf{x}) = \{\mathbf{y} \in B : \vartheta(\mathbf{y}) = \theta(\mathbf{x})\}$. For $\mathbf{x} \in \Gamma, \vartheta(x) = \theta(x)$.

Equivalently, isochrons may be considered as cross-sections of Γ (manifolds intersecting Γ transversely at a single point) having a first return time equal to T. If Γ is hyperbolic, their existence follows from a corollary of the Invariant Manifold Theorem stating that for each $\mathbf{x} \in \Gamma, W^s(\mathbf{x})$ is a cross-section of Γ, diffeomorphic to $\mathbb{R}^{n-1}$. Furthermore, $\cup_{\mathbf{x}\in\Gamma} W^s(\mathbf{x})$ is an open neighborhood of Γ and its stable manifold [98]. We can thus define phase rigorously on an open neighborhood $U \subset B$ about Γ by a mapping $\theta : U \to [0, 1)$.

We can also rewrite the dynamical system to emphasize phase evolution, by choosing $\theta(\cdot)$ appropriately, so that F restricted to U has the simple form $\frac{d\theta(\mathbf{x})}{dt} = \omega$,

where $\omega = 1/T$. This is accomplished using the chain rule: $\frac{d\theta(\mathbf{x})}{dt} = \omega = \frac{d\theta}{d\mathbf{x}}(\mathbf{x}) \cdot f(\mathbf{x})$. There is a unique solution, up to translation by a constant, for $\theta(\cdot)$ on U.

If we apply a perturbation P to F at a point $\mathbf{x} \in \Gamma$ with phase $\theta(\mathbf{x})$, after the perturbation the trajectory from x may approach a point $\mathbf{y} \in U$ with (asymptotic) phase $\theta(\mathbf{y})$. If we systematically perturb every point of Γ to obtain a locus of points in $\mathbf{y} \in U$, we obtain a mapping of phases $\varphi : [0, 1) \to [0, 1)$ given by $\varphi(\theta(\mathbf{x})) = \vartheta(\mathbf{y})$ iff $P(\mathbf{x}) = \mathbf{y}$. We call φ the *phase response curve* of Γ for P [236]. The shape of the phase response curve (PRC) depends on the characteristics of P and F.

Whether PRCs are drawn such that the upper half-plane designates phase advance or delay is a matter of convention. Mathematicians usually assign phase advance to the upper-half plane, and biologists do the opposite. We use the latter convention.

There are two classifications of PRC shapes in widespread use. The first is phenomenological [109, 70]: PRCs with no negative part are called Type I; regardless of timing, perturbations can have only one effect on the oscillator's phase (delay or advance, depending on sign). Type II PRCs have both positive and negative portions, so that the oscillator's phase may advance or delay depending on the timing of the perturbation. This classification of PRCs concords with behavioral categories for models of excitable membranes, which are in turn associated with bifurcation structures in the models (*cf.* section 1.2) [186, 70, 125]. Specifically, Type I PRCs are associated with excitable membranes that show arbitrarily low frequency oscillations at the onset of tonic spiking (saddle-node on invariant circle bifurcation). Type II PRCs are associated with excitable membranes for which the onset of tonic spiking occurs only at a fixed minimum (non-zero) frequency (*e.g.* subcritical Hopf bifurcation).

The second classification scheme is topological [236]: Recall $\varphi : \mathbb{S}^1 \to \mathbb{S}^1$ and consider the graph G of φ on the (ϕ, ϕ')-torus $\mathbb{S}^2$. If G has a winding number of 0, *i.e.* it does not pass through the central hole of the torus, then the PRC is also said to have winding number 0 and is called a Type 0 PRC. Otherwise, G must have a winding number greater than zero; the PRC has winding number 1 and is called a Type 1 PRC.[6] Oscillators with Type 1 PRCs may exhibit large changes in their responses even as the phase of perturbation varies only slightly. This feature of the topological classification captures the large excursion and phase-sensitivity characteristics of biological oscillators subjected to strong perturbations. Both classification schemes assume that the oscillator remains in the basin of attraction of the original limit cycle after perturbation; otherwise, the PRC is undefined.

In the context of neural oscillations, a phase response curve describes the effect of an incoming presynaptic spike at a given phase of a postsynaptic neuron's cycle — an advance or delay of the next action potential or burst. Phase response curves for real neurons (and neuron populations) have been measured experimentally [169, 214], and experimental PRCs have been used to study the stability of phasing in neuronal networks and the roles played by identified neurons in setting and maintaining the rhythms of oscillatory neuronal networks [175].

Modeling studies of networks of coupled neural oscillators which employ the phase oscillator methodology describe the effect of presynaptic neurons on the phase of a postsynaptic neuron by adding an interaction term involving the postsynaptic neuron's PRC to its phase evolution equation:

$$\frac{d\theta_k}{dt} = \omega_k + \sum_i \varphi_{k,i}(\theta_k) \cdot I_{\text{syn},k,i}(t) \tag{1.7}$$

Here $\varphi_{k,i}$ is the phase response of the kth postsynaptic neuron to input from its ith presynaptic neighbor, and $I_{\text{syn},k,i}$ is the ith presynaptic current. Assuming that the

[6] Oscillators with type 0 PRCs are occasionally said to show 'strong' or 'even' phase response; those with type 1 PRCs are sometimes referred to as having 'odd' or 'weak' phase response.

interactions between neurons can be reasonably modeled as near infinitesimal, instantaneous pulses, and that the postsynaptic neurons' trajectories remain close to their stable periodic orbits after perturbation, we may be able to rewrite the interaction terms (1.7) in the form $\varphi_{k,i}(\theta_k) \cdot I_{\text{syn},k,i}(\theta_i) = H(\theta_k - \theta_i)$, *i.e.* the interaction between neurons depends only on their phase differences. In this case, predictions of stable phase configurations (*e.g.* synchrony) and firing rates may be calculated by averaging the phase equations over the population of neurons [73, 74, 14]. These averaging methods are also valid for strongly coupled networks comprised of phase oscillators possessing particular kinds of PRC and pulse characteristics [74].

Because of their relative simplicity and analytical tractability, phase oscillator approaches have been widely used to investigate the behavior of neuronal networks, particularly models of cortex and central pattern generators. However, the capacity of phase oscillator modeling approaches to make detailed predictions for specific biological systems may be limited, given the amount of physical detail the models omit.

1.4 Central Pattern Generators

Multilayered rhythmic motor patterns underlie many essential behaviors in both vertebrates and invertebrates, such as respiration, digestion, circulation, and locomotion. The neuronal circuits responsible for coordinating the complex, periodic sequences of muscular contractions and relaxations that comprise such behaviors are called *central pattern generators*, or CPGs. They are spatially localized neuronal networks which function autonomously, producing coherent, behaviorally relevant output in the absence of sensory feedback or input from higher level control centers in the nervous system. In response to neuromodulation, CPGs are capable of producing a wide range of output patterns that are functionally related

to their basic rhythms, demonstrating that relatively compact neuronal circuits potentially encode a very large repertoire of behaviors.[7]

The neuroscientific concept of central pattern generators dates back at least to Brown [18], who introduced the idea to explain observations that rhythmically alternating limb movements resembling walking could be produced in the cat without any external inputs from the central or peripheral nervous system [205, 204, 17]. These experimental results implied that the spinal cord contains an endogenous rhythm generator, and Brown suggested that alternation of flexor and extensor muscle groups in the leg could be produced by central circuits in which the neurons driving each muscle group reciprocally inhibited neurons driving antagonistic muscle groups. Since this early work, neuroscientists have studied CPGs responsible for heartbeat, breathing, chewing, vomiting, swimming, crawling, walking, and flying in organisms as varied as worms, grasshoppers, leeches, fruit flies, lampreys, lobsters, crabs, crayfish, sea slugs, pond snails, frogs, zebrafish, mice, rats, and humans [144].

CPGs are more complex than sensory feedback loops, but simpler than the brain. Their intermediate complexity and experimental characteristics make them an excellent testbed for examining the operation of the nervous system. Their outputs are regular, continuous, and measurable, and their *in vitro* activities are reliable analogues of *in vivo* behaviors.[8]

The CPGs of many different organisms are amenable to electrophysiological,

[7]The following section borrows liberally from [110, 153, 152, 135] in developing its discussion.

[8]This last assertion must be qualified: Fictive motor patterns produced by CPGs *in vitro* may very often look (qualitatively) quite similar to the motor patterns found in the intact organism, but this does not necessarily mean that they faithfully reflect *in vivo* motor activity. It is also not necessarily correct to infer that the rhythmic motor pattern seen *in vitro* is the same as that *in vivo*, even if the same muscles are innervated as those involved in the *in vivo* pattern, particularly if the fictive locomotor pattern is triggered by applying neuromodulators to the experimental preparation. Although some *in vivo* motor patterns may be quite stable in the absence of sensory input, it is likely that the stability of other patterns may require sensory feedback for tuning and modification from cycle to cycle.

anatomical, imaging, and molecular genetic examination, allowing for extensive data collection in a wide range of experimental preparations. Relating network structures and cellular properties to CPG function — establishing and maintaining a (complex) rhythm — is more tractable than deciphering the structure-function relationships for the more complicated behaviors of learning, memory, and sensory processing found in the brain.

Presumably, most neural circuits in the nervous system follow similar assembly, organizational, and functional principles. As building blocks of larger neuromotor control systems, CPGs are natural instances of reduced systems for studying the general organization of neuronal networks, providing a simplified context for understanding how assemblages of neurons act together to produce coherent, purposeful activity. Insights gained from analyzing CPG construction and function should aid in building a comprehensive picture of how neural activity associated with information processing and generating motive behavior is organized in the brain and throughout the central nervous system [135].

1.4.1 Organizational Principles

The structure and operational details of CPGs may vary widely, depending on the organism and the function of the CPG, but two basic organizational principles are assumed to hold for all CPGs: (1) The behavioral output of the complete CPG network depends on the patterned, regulated output of individual constituent neurons, and (2) the output of individual neurons depend in turn on their intrinsic membrane properties, as determined by the ionic currents they express. The rich repertoire of rhythmic patterns produced by the CPG arises from the interplay of cellular behaviors, controlled by the neurons' intrinsic properties, and communication between cells, determined by the network's pattern of connectivity. A

single neuron with a complex set of nonlinear behaviors receives input from an array of other neurons, and its output feeds back into the very cells from which it received input. Furthermore, the intrinsic properties and effective connectivity of the network can be altered rapidly by neuromodulatory substances, such as peptides and neurotransmitters, which may affect cells' ion channels or act on the synapses connecting the neurons.

Experimental and modeling investigations of CPGs involve determining the functional roles played by identified neurons or populations of neurons in generating complex rhythmic patterns. The roles that a cell may play are determined by its intrinsic properties and its location in the network, *i.e.* its connections to other neurons. Research strategies to develop a basis for understanding CPG function include two essential components: cataloguing the electrophysiological properties of individual cells and mapping out the network's 'wiring diagram' — the pattern of synaptic and gap junction connections between cells. Investigations of the network's response to neuromodulators build on this dual foundation by relating changes in membrane properties and synaptic strength to alterations of CPG function, thereby helping delineate the array of output patterns accessible to the CPG. Comprehensive study of intrinsic properties and network circuitry has been accomplished only in a few small, relatively simple rhythmic motor and circulatory systems of invertebrates: leech heart [30], crustacean (crab, lobster) stomatogastric ganglion [208, 85, 86, 212], and the swimming CPGs of the *Xenopus* tadpole [193] and the lamprey [147, 97]. Mammalian CPGs, particularly those for locomotion, are likely to be significantly more complex than those of invertebrates, but the same design principles are expected to apply.

1.4.2 Rhythm Generation and Phase Response

As rhythm generators, CPGs require their components to exhibit some oscillatory behavior, either by tonic firing or rhythmic bursting, and either endogenously or in response to neuromodulation. CPGs may combine some or all of these mechanisms for rhythm generation, and the predominance of particular rhythmogenic mechanisms may be (conceivably) context dependent. There may be a rhythmic core of endogenous bursters, or the network oscillations emerge from the synaptic network connections between active neurons that do not burst endogenously. Rhythm generation may be localized among certain cells in the network, with other parts of the CPG serving to amplify, modulate, and stabilize the basic rhythm. Alternatively, every cell in the CPG assembly could be involved in rhythm generation. In either case, the ultimate output of the CPG is properly phased bursts of action potentials from motoneurons (or interneurons feeding motoneuron pools) to drive coordinated muscular contractions in the correct sequence and with appropriate timing.

CPGs whose rhythm generation is largely produced by individual cells that burst endogenously are sometimes called pacemaker networks. In such networks, the bursts of the endogenous bursters (pacemakers) drive the underlying rhythm and may also provide important timing inputs for ancillary circuits in the CPG [184]. Pacemaker neurons may excite follower interneurons via synapses or gap junctions; the follower cells typically burst in phase with the pacemaker, although the shape of their bursts may vary significantly from those of the pacemaker, depending on their membrane currents. Follower interneurons receiving inhibitory input from the pacemaker typically burst out of phase with it, also with possibly differing burst shapes. Depending on synaptic and intrinsic parameters, follower interneurons in either of the (excitatory/inhibitory) pacemaker-follower configura-

tions can produce bursts in response to the pacemaker whether they are tonically active or quiescent in isolation [191].

Endogenous oscillators are not always present in CPGs, though they are found in the crustacean stomatogastric ganglion, one of the best understood CPGs [111]. Their presence gives pacemaker networks different rhythmogenic properties from those without them: Strongly oscillatory pacemaker neurons can be difficult to entrain to external inputs, they may require strong inputs to reset, and they may express a limited range of burst frequencies.

Another common architecture for rhythm generation in CPGs is the half-center oscillator, found in the leech heart and lamprey swimming CPG: two (groups of) neurons bound together by reciprocal inhibition. Classically, the intrinsically tonic activity of one neuron inhibits the tonic activity of the other until either internal or external forces drive it to a quiescent state, allowing the previously inhibited cell to fire; the reciprocal inhibition leads to alternating bursts from the two neurons. The active cell may become quiescent due to the build up of hyperpolarizing currents from its own activity (*release*), or depolarizing currents building in the quiescent cell may overcome the inhibition it receives from the currently active cell, leading it to begin spiking and silence the other cell (*escape*). Variations on classical escape and release mechanisms in half-center oscillator configurations imply different frequency ranges and entrainment characteristics for the generated rhythm [206, 195]. Although the half-center oscillators known experimentally are comprised of neurons tonically active in isolation, it is also possible to obtain alternating bursts from reciprocal inhibition of endogenous bursters or quiescent cells [191].

For CPGs with either rhythmogenic architecture, the intrinsic properties of interneurons can be strong determinants in shaping the networks' output. Neurons showing spike frequency adaptation slow their firing rates during activity, and this

internally determined change in spike timing can affect the timing of burst onset in their inhibited downstream neighbors, for example. Strong post inhibitory rebound in neurons receiving inhibition can enable extended periods of spike activity at times that lag their inputs by intrinsically set intervals. Interneurons exhibiting plateau potentials can act as switches with memory of their most recent synaptic input, able to produce an action potential response lasting much longer than the duration of their excitatory input. CPGs may exhibit one or both kinds of rhythmogenic mechanisms, and may combine interneurons with a variety of intrinsic properties to form neural circuits of great complexity.

Properly functioning CPGs produce bursts of action potentials in the correct sequence and with the appropriate timing to stimulate a variety of related patterns of muscular contraction that underlie various rhythmic behaviors. Hence the information leading to meaningful movement is encoded in the CPG output by the relative phasing of bursts, interburst frequency, and intraburst spike amplitude and spike frequency.

The modulation and patterning of the basic CPG rhythm is a matter of shaping the timing of individual neurons' activities in relation to one another to alter the sequencing, phasing and shapes of bursts. *In vivo*, such modification occurs continually as the CPG adjusts its program relative to inputs from the rest of the organism and sensory feedback from the environment. The change in CPG output in reaction to perturbation at particular times during its rhythm — the phase response of the system as a whole — is a complex combination of the responses of its components. The phase response characteristics of the neuronal network, considered as a system of interacting nonlinear oscillators, are dynamic properties derived from the phase response of the constituent oscillators as they act upon and

react to one other. In turn, each neuron's individual phase response characteristics are determined through the interplay of its ionic currents operating on multiple time-scales.

Uncovering the relevant neuronal circuitry of a CPG and deciphering how it operates to produce meaningful neuromotor output demands a combination of experimental investigation and mathematical modeling. Studying phase resetting properties at the cellular and network levels is a valuable approach for understanding CPG function, crucially incorporating the concepts of bursting, multiple time-scales, and phase response.

CHAPTER 2

LOCOMOTOR CENTRAL PATTERN GENERATOR MODEL

2.1 Introduction

Although the organization and activity of CPGs may be simpler than those of brain structures responsible for higher level behaviors such as learning and sensory processing, they are nonetheless highly complex. Deciphering the structure and function of CPGs reveals design principles that also apply to other such neural subsystems, and it helps clarify how the nervous system manages to control and coordinate its broad repertoire of behaviors. CPGs comprise many cellular components, each with its own assortment of membrane currents and associated channel properties, together with a matrix of intercellular connections with individual synaptic dynamics. This complexity poses serious obstacles to making comprehensive static descriptions of CPG networks, let alone describing their dynamic behavior.

Mathematical and computational modeling provides a powerful framework for addressing this challenge. Models synthesize experimental data, unify disparate observations, and facilitate analyses of the mechanisms underlying biological phenomena. Providing a quantitative, mechanistic, or even simply schematic foundation for organizing knowledge and ideas about a biological system's functioning, they serve as testbeds to investigate complex phenomena under controlled, simplified conditions *in computo*. Ideally, they also enhance our understanding of biological systems by making testable predictions, inspiring hypotheses, and guiding the design of further experiments. At the least, useful models provide a basis for explaining experimental observations of complex system behavior more rigorously than by intuitive arguments alone.

This chapter describes the design, construction, and testing of models for the central pattern generator responsible for organizing locomotion in the hindlimbs of rodents. The rodent spinal hindlimb locomotor (RSHL) CPG sets the basic walking rhythm, coordinating the contraction of flexor and extensor muscle groups for effective movement. The long term goal of our modeling efforts is to formulate a complete model of spinal coordination of rodent locomotion. At this point, many biological details are unknown, and so we propose models to capture the basic flexor-extensor phasing of the normal walking rhythm, incorporating as much of the current experimental biological understanding of the system as possible. The models we put forth here are amenable to extension and refinement as new experimental results become available.

Below we summarize the experimental data available for the RSHL CPG, organizing the information to facilitate model building. Next we discuss various strategies used to model CPGs mathematically, and we set forth a new approach towards modeling that is better suited to our modeling goals and the current state of our experimental knowledge. Then we describe a family of biologically detailed CPG models developed according to a framework of ansätze consistent with the experimental data. Finally, we report the results of some computational experiments with the CPG models, and discuss their implications for future models and for laboratory experiments.

2.2 Experimental Background

For proper walking movement, the neuromuscular system must repeatedly execute a complex sequence of correctly phased muscular contractions and relaxations in order for the hind legs to move the animal forward. Over a dozen different muscles

in each leg are involved in walking movement, comprising groups of flexors and extensors pulling and pushing at the hips, knees, ankles, feet, and digits [133]. The RSHL CPG is responsible for organizing and coordinating the correct phasing of contraction by the various muscles in the rodent's hindlimbs in order to effectively propel the animal.

During normal walking, the flexor muscles of one side of the animal are active in phase with the extensor muscles of the other side. At the same time, the flexor muscles of one side of the animal are active out of phase with the ipsilateral extensor muscles. We consider this simultaneous ipsilateral flexor-extensor antisynchrony and contralateral flexor-extensor synchrony to be the *fundamental locomotor rhythm* of the CPG,[1] and understanding how the CPG produces its fundamental rhythm is the primary focus of much experimental work, as well as this modeling study.

Experimental characterization of the rodent spinal hindlimb locomotor CPG is an ongoing endeavor of several neurobiology lab groups, with work having been underway for over fifteen years. The data relevant for modeling comes from anatomical, microscopic, electrophysiological, and genetic studies in both rats and mice.[2] The experimental setups included whole cord and slice preparations treated with a variety of neuromodulatory substances, with animals ranging in age from 0–14 days.

In this section, we organize the available biological data in such a way as to facilitate construction of moderately detailed initial models of the RSHL CPG, recognizing that the level of biological realism will be lower for our models than

[1] In actuality, the activation sequences performed by individual muscles in the leg of each side may be quite complicated and violate this heuristic. Some extensor muscles may contract nearly in phase with some of the muscles in the ipsilateral flexor group, and vice versa, during the full motion of the leg through one cycle. It is still grossly accurate to claim ipsilateral flexor-extensor alternation.

[2] A similar situation exists for the stomatogastric ganglion CPG, where studies are made in lobsters and crabs [111].

for biologically detailed models currently used for other systems, such as the leech heart and crustacean stomatogastric ganglion. There is some intentional redundancy in the presentation of the information. As more experimental details emerge, they may be incorporated into refinements of the initial models to add more biological specificity and produce qualitatively and quantitatively more accurate model behavior.

2.2.1 Network Output and Organization

The locomotor CPG of interest is located in the rodent spinal cord of rodents, with relevant activity produced predominantly in the lumbar spinal region, which is composed of six segments, labeled rostrally to caudally L1–L6. The neurons most closely associated with rhythmic locomotor activity are found in the ventral third of the spinal cord, with rhythm generation taking place primarily in L1–L6, though also extending rostrally to some thoracic segments. The strongest rhythmogenesis appears to emanate from the more rostral lumbar segments.

There is a cleft running along the rostral-caudal axis of the spinal cord. This central commissure or commissural fissure divides the whole cord into the left and right hemicords and demarcates the midline boundary between the left and right sides of each spinal segment. Communication between the left and right hemicords is mediated by commissural interneurons whose processes extend across the midline.

The motoneural pathways from the CPG to the flexor and extensor muscle groups in the hindlimbs are collected into nerve fiber bundles that protrude from the underside of the spinal cord. These ventral roots are organized segmentally, such that the L1 and L2 ventral roots primarily innervate flexor muscles, while the L4 and L5 ventral roots primarily innervate extensor muscles. Of these ventral

roots, those from the L2 and L5 segments generally show the most distinct specialization in their muscular targets, and hence they are usually the ones from which extracellular recordings of fictive locomotor activity are made during experiments.

Fictive Locomotion

Patterned activity in the rodent spinal cord takes three basic forms: synchronous, rhythmic left-right alternation, and fictive locomotion. In synchronous activity, neurons in the L2 and L5 segments show regular, periodic bursts of activity, such that neurons in L2 fire in phase with neurons in L5, and neurons on one side of the cord fire in phase with neurons from the other side. Rhythmic left-right alternation is marked by intersegmental synchrony between L2 and L5, and intrasegmental alternation of activity between neurons on either side of the midline. During fictive locomotion, there is both intersegmental and intrasegmental alternation, meaning that L2 neurons on one side of the cord are active in phase with contralateral L5 neurons and out of phase with ipsilateral L5 neurons and contralateral L2 neurons. Spontaneous spinal activity in intact rodents progresses from synchronous to rhythmic left-right alternation to fictive locomotion as the animals proceed normally through the stages of pre- and post-natal development [144].

Several different combinations, or 'cocktails,' of neuromodulatory substances have been found to elicit locomotor like patterns in the lumbar segments of isolated rat and mouse spinal cords: Serotonin (5-HT, 5-hydroxy-tryptamine creatinine sulfate complex) and N-methyl-D-aspartate (NMDA) in combination (rat and mouse) [137]; 5-HT and NMA (N-methyl-D,L-aspartic acid, NMDA excitatory amino acid receptor agonist) in combination (rat) [209]; extracellular K^+(rat) [12]; both 5-HT and dopamine (DA) alone and in combination (rat) [133]; 5-HT, NMDA, and DA in combination (mouse) [242, 234]; 5-HT, NMA, and DA in combination (mouse) [116]; and acetylcholine (ACh) alone (rat) [49].

NMDA alone induces rhythmic bursting in interneurons, but the bursting does not necessarily spontaneously organize into fictive locomotion (rat) [133, 118]. Noradrenaline (NA) alone has little organized effect on the motor pattern, eliciting mostly low-level oscillations and tonic spiking, although occasionally it can also produce slow locomotor-like output (rat) ([136]. Neither application of 4-aminopyridine (4-AP) nor Mg^{2+}free solutions induced fictive locomotion (rat) [5].

The individual neurons of both L2 and L5 tend to fire just a few spikes at a fixed, preferred phase, with the distribution of preferred phases spread around the entire locomotor cycle (rat, mouse) [182, 242, 241]. Single neurons, though active, may skip some cycles, yet retain their phase preference (rat) [221]. The activity of L2 neurons during fictive locomotion is stronger than that of L5 neurons, and L2 neurons' activity tends to cluster more tightly around a fixed set of preferred phases than does neuronal activity in L5 (rat) [220, 221]. The synchronization of motor neurons in their spatially localized motor pools could be partially due to gap junction coupling (fast synchronization) and chemical synapses, while slower synchronization between motoneurons from different motor pools in different areas (segments) was mediated by chemical synapses (rat) [222].

Although each segment was able to produce rhythmogenic activity during fictive locomotion, the greater strength of the L2 activity could indicate that the rhythmogenic drive is produced at the rostral end of the spinal cord and is propagated caudally, with some amplification through each lumbar segment.

Organization and Connectivity

The locomotor rhythm in the CPG appears to be generated by rostral portions of the spinal cord, propagating caudally, but the exact nature of the rhythmogenesis has not been conclusively determined through experiment. Multiple studies have found that neurons in the L2 segment are active during both phases (flexor

and extensor) of the fictive locomotor rhythm (rat) [39, 27]. Serotonin applied to higher regions, including cervical and thoracic spinal segments, elicits rhythmic activity but not fictive locomotion (rat) [49]. Some studies claim that rhythm generation originates in the L1–L2 segments, that lower segments are unable to independently generate the locomotor rhythm, and that the locomotor rhythm feeds directly from L1–L2 to caudal segments without intervening segmental relay (rat) [38, 39]. Other studies indicate that the L4–L5 segments are in fact capable of independent rhythmogenic activity, though it is weaker than the activity from L1–L2 (rat) [220]. Given the lack of consensus, there are three plausible scenarios for the origination of the locomotor rhythm: (1) Rhythmic alternation (bursting) originates in higher regions of the spinal cord and is mediated and patterned by the lumbar spinal network to produce fictive locomotor output (higher level drive). (2) Rhythm generation (endogenous bursting) occurs exclusively in the L1–L2 segments and is propagated to L4–L5 directly, so that the fictive locomotor pattern, including cross-midline coordination, is predominantly determined by the intrasegmental organization of the L1–L2 network. Intrasegmental connections at the L5 level may also contribute to patterning the rhythm for fictive locomotion. (3) Rhythmogenesis emerges from endogenous bursting activity at both the L2 and L5 levels, and intra- and intersegmental synaptic connections coordinate bursting activity to produce fictive locomotor patterns.[3]

There are cross-commissural synaptic connections throughout the lumbar and thoracic regions, involving both excitation and inhibition; there may be considerable redundancy in the organization of reciprocal inhibitory and excitatory connections in the CPG (rat) [49]. Intrasegmental communication between hemicords is mostly inhibitory, implying that left-right alternation is mediated primarily

[3]That is, endogenous bursting occurs continuously from T12–L6, with strong flexor- and extensor-phased activity occurring at the L2 and L5 levels, respectively.

through synaptic inhibition (rat) [142]. However, the inhibitory pathways may be polysynaptic and involve cross-commissural excitatory connections: Within L2, and possibly also within L5, some motoneurons in one hemicord receive (glycineric) inhibition from premotor interneurons that in turn receive (glutamatergic) excitatory input from contralateral interneurons (rat) [138]. Afferent intra- and intersegmental connections may convey inputs to pools of both motoneurons and rhythmogenic neurons, perhaps simultaneously, via similar polysynaptic pathways (rat) [11].

Several descending synaptic connections from L2 to L4–L5 have been reported (rat) [27]: (1) Monosynaptic inhibitory connections from extensor-phased L2 interneurons to contralateral extensor-phased L4 motoneurons; (2) monosynaptic excitatory connections from extensor-phased L2 interneurons to contralateral flexor-phased L4 motoneurons; (3) monosynaptic excitatory connections from flexor-phased L2 interneurons to contralateral extensor-phased L4 motoneurons; (4) monosynaptic inhibitory connections from flexor-phased L2 interneurons to contralateral flexor-phased L4 motoneurons; (5) polysynaptic inhibitory connections, modulated by 5-HT, from flexor-phased L2 interneurons onto contralateral extensor-phased L4 motoneurons.

Molecular genetic studies indicate that excitation plays a primary role in coordinating proper alternation between hemicords during locomotion. Mice that were born with a null mutation in the EphA4 gene, thus lacking the EphA4 (Sek1) receptor, could only hop, not walk [67]. This gross motor abnormality maintained proper flexor-extensor alternation, but improperly synchronized flexor (resp. extensor) activity between the left and right sides. EphA4 is implicated in a signaling mechanism which normally prevents axons of EphA4-expressing interneurons from crossing the midline during development (mice) [238]. Some EphA4 expressive

interneurons that are rhythmically active during fictive locomotion provide excitatory connections onto ipsilateral motor neurons (mice) [29], suggesting that the abnormal hopping occurs due to miswired excitatory connections that cross the midline when they should project only ipsilaterally (from the L2 rhythmogenic pool).

Finally, there is also initial evidence of sensory feedback connections in the propriospinal network. Stimulation of dorsal roots reset the fictive locomotor rhythm, indicating that sensory feedback via pathways along the dorsal roots modifies the basic CPG rhythm during normal locomotion [209].

2.2.2 Neuron Types

Three main classes of neurons involved in the RSHL CPG have been identified or postulated: Motoneurons (MNs), commissural interneurons (CINs), and rhythmogenic interneurons (RGNs). Motoneurons innervate the muscles of the hindlimbs directly, and bunches of their processes constitute the ventral roots from which recordings of fictive locomotor activity are made. Commissural interneurons have axonal processes which cross the midline of the spinal cord; they are responsible for all cross-cord communication, and presumably play a critical role in coordinating the proper phasing of flexor-extensor alternation between the two sides. Rhythmogenic interneurons have not yet been definitively identified, but if the fictive locomotor rhythm is generated from the lumbar region, then that bursting activity should emanate from a distinct subpopulation of neurons that either burst endogenously, or which are tonically active and cooperate to burst at the population level. Ongoing and future anatomical, electrophysiological, molecular genetic, and microscopic studies should further illuminate the subpopulation organization of the neuron types present in the CPG [144, 135, 233].

Below we present the current state of knowledge about the three classes of RSHL CPG neurons. In general, all of the neurons are relatively small and electrically compact, and there are hundreds to thousands of neurons from each class present in the lumbar spinal region. The following information reflects experimental results from many cells of a given class, obtained under a variety of experimental conditions, not data for a single, well-defined, identified cell from that class.

Motoneurons

Motoneurons are distributed throughout the spinal cord, spatially organization to some degree according to the muscle groups they innervate. Significant motoneuron pools that drive extensor muscles are located in L1 and L2, and motoneuron clusters that drive flexor muscles are found in L5 and L6. In addition to the usual spiking currents, the motoneurons possess a hyperpolarization-activated inward cation current, I_{h}, which acts as a tonic leak conductance during locomotion. This current serves to increase motoneuron firing frequency and phase-advance the locomotor drive [134]. MNs in the mouse spinal cord also express a persistent sodium current, $I_{\mathrm{Na(P)}}$, the blockade of which reduces excitability and impedes the ability of MNs to fire tonically in response to extended depolarization (mouse) [243]. 5-HT affects inward rectifiers in rat motoneurons, acting to inhibit $I_{\mathrm{K_{ir}}}$ (fast inward rectification) by reducing instantaneous conductance, and enhancing I_{h} (slow inward rectification) by shifting its activation curve in a depolarized direction [139].

Application of NMDA and 5-HT can evoke stable, locomotor-like rhythmic bursting in pharmacologically isolated motoneurons, without any spike input from pre-motor interneurons (rat) [134]. The local synchronization of motoneurons is primarily due to gap junction coupling, though there is also evidence of synaptic coupling (rat) [134, 222]. Motoneurons also exhibit plateau potentials, and rising activity in phasically active motoneuron pools may be due in large part to de-

polarization from plateau potentials, rather than from recruitment of additional motoneurons.

Commissural Interneurons

Commissural interneurons are ventromedially localized and found throughout the lumbar region, including concentrations in L2–L5 (rat) [178]. There are four types of CINs, distinguished by the direction of their axonal projections. Ascending commissural interneurons (aCINs) cross the midline and project one to seven segments rostrally, while descending commissural interneurons (dCINs) cross the midline and project one to seven segments caudally (rat) [69]. Bifurcating or ascending-descending CINs (adCINs) cross the midline and project both rostrally and caudally, and short range segmental CINs (sCINs) cross the midline and project less than 1.5 segments in either direction, sometimes remaining in the same segment (rat) [211]. CINs make monosynaptic contacts with contralateral motoneuron targets, and there are direct reciprocal synaptic connections between CINs on opposite sides of the midline (rat) [8].

Localized populations of L2 dCINs fire in phase with ipsilateral L2 motoneurons and in phase with contralateral L4–L5 motoneurons. Different subpopulations of L2 dCINs inhibit and excite contralateral L5 motoneurons (rat) [28]. There are monosynaptic inhibitory connections from ipsilateral L2 extensor-phased dCINs to contralateral L4 extensor-phased MNs; monosynaptic excitatory connections from ipsilateral L2 extensor-phased dCINs to contralateral L4 flexor-phased MNs; monosynaptic inhibitory connections from ipsilateral L2 flexor-phased dCINs to contralateral flexor-phased L4 motoneurons; monosynaptic excitatory connections from ipsilateral L2 flexor-phased dCINs to contralateral extensor-phased L4 motoneurons; and polysynaptic, 5-HT-modulated inhibitory connections from ipsilateral L2 flexor-phased dCINs to contralateral L4 extensor-phased MNs (rat) [27].

Both L2 dCINs that are rhythmically active during fictive locomotion and those that are inactive express I_{h} (rat) [28]. The time constant of I_{h} is extremely slow, making it an unlikely candidate for playing a significant role in pacemaker activity, but I_{h} amplitude and spike frequency are highly correlated in dCINs, so that I_{h} may act to tonically depolarize these cells and enhance their firing frequency. L2 aCINs and dCINs have also been found to express a persistent sodium current which may act partly to regulate the interneuron firing frequency (mouse) [243].

L2 aCINs and dCINs in the neonatal mouse are modulated by 5-HT, which depolarizes the average membrane potential, reduces the post-spike afterhyperpolarization amplitude, and decreases action potential threshold. The effect of these changes is to increase CIN excitability (mouse) [242, 241]. 5-HT also modulates the voltage-dependent calcium current I_{Ca} in aCINs and dCINs, lowering the influx of Ca^{2+} (mouse) [63]. This in turn reduces the cells' $I_{\mathrm{K_{Ca}}}$ current, thereby increasing their excitability.

Rhythmogenic Interneurons

Early investigation of intrinsic membrane properties of neurons in the neonatal rat spinal cord found that some interneurons burst rhythmically in the presence of NMDA. Although these oscillations appeared to have been driven mainly by excitatory and inhibitory synaptic inputs, a small number of interneurons continued to burst after synaptic drive had been abolished pharmacologically, indicating that there could be a core of endogenously oscillatory neurons driving the locomotor rhythm [133].

Some members of a population of ventral spinal mouse interneurons that express HB9 homeodomain protein, a genetic marker, burst rhythmically in the presence of 5-HT, NMDA, and DA. Since the bursts are consistent with fictive locomotion, these neurons are candidates for the core of endogenously bursting

rhythmogenic interneurons of the locomotor CPG.

Two subtypes of HB9-positive neurons are distinguished: Type I burst, while Type II are tonically active.[4] Both subtypes show subthreshold oscillations when exposed to a cocktail of 5-HT, NMDA, and DA. Type I neurons show particularly strong postinhibitory rebound, a property which has been shown to be important in rhythm generation in other CPGs, specifically those for respiration [234].

HB9-positive neurons may form excitatory glutamatergic synaptic connections with motoneurons that are rhythmically active during fictive locomotion, and they are themselves rhythmically active during fictive locomotion, indicating that they may be premotor excitatory neurons playing some role in generating the locomotor rhythm [116].

Ongoing work using two-photon microscopy and calcium imaging of labeled fluorescent neurons to monitor calcium activity levels in sliced cord during fictive locomotion may give additional insight into exactly which populations of neurons are involved generating the locomotor rhythm, allowing for more specific measurements of intrinsic properties and mapping of synaptic connections [233].

2.2.3 Synapses and Gap Junctions

Excitatory and inhibitory chemical synaptic connections are known to exist between various populations of CINs and MNs (rat) [28, 27, 8]. The inhibitory synaptic pathways involve GABA-A and glycine (rat) [27], while the excitatory synaptic pathways are glutamatergic (rat)[138]. Localized groups of MNs show

[4]Type II interneurons are not 'real' Hb9 neurons, but rather false positives for Hb9 expression. Though they do not express Hb9, they express green florescent protein (GFP), which is used to label neurons that do express Hb9. Thus they may be misidentified as Hb9-positive cells in microscopic studies due to leaky expression of the GFP transgene, but they can be distinguished by their electrophysiological properties. We use the terminology of the original studies of Hb9 interneurons [234], referring to both types of cells as Hb9 while retaining the Type I/Type II subtype distinction.

gap junction coupling (rat) [134, 222], and there may be gap junctions between CINs and potential RGNs as well (mouse) [242, 241, 234].

Inhibitory and excitatory post-synaptic currents are reciprocally regulated in interneurons active during fictive locomotion, and they are modulated in frequency more than amplitude (rat) [181]. Synaptic inputs have only small effects on the passive membrane properties (input resistance) of post-synaptic interneurons during fictive locomotion, though individual pre-synaptic neurons may have large but short-lived effects on the integration properties of post-synaptic neurons (rat) [179]. Synaptic facilitation and depression have not been shown to play a strong role in information transfer in the RSHL CPG (rat) [181].

Synaptic reversal potentials have been estimated at -53 mV for inhibitory synapses and 0 mV for excitatory synapses in the neonatal rat [179], but the exact strength of synaptic connections (maximal synaptic conductance) has not been measured in the mouse or the rat. However, a relatively small number of post-synaptic currents (corresponding to 1–5 simultaneously active synapses) are needed to alter the cyclic rhythm of post-synaptic neurons in the rat. This indicates that individual cells influence each other strongly, and the activity of a single neuron could have a large effect on the output of the whole locomotor network (rat) [180]. The susceptibility of the locomotor CPG output to synaptic inputs is also supported by studies in which the locomotor rhythm was reset by external stimulation of the isolated spinal cord (rat) [11, 209].

2.2.4 Neuromodulation

There is little evidence that neuromodulators act on muscle fibers directly. Instead, they appear to affect motoneuron pools and rhythmogenic centers, acting differentially on various neuron types. Below we summarize the effects of various

neuromodulators on cells in the RSHL CPG.

- *5-HT* can induce fictive locomotor activity by itself (rat) [133]. 5-HT induced activity tends to be faster and more regular than rhythms produced by DA alone (rat) [133], and slower than those induced by high extracellular K^+ alone (rat) [12]. It enhances excitability in rhythmically active neonatal mouse aCINs and dCINs (but not adCINs) by acting to depolarize the average membrane potential, reduce the post-spike after-hyperpolarization amplitude, broaden the action potential, and decrease action potential threshold (mouse) [242, 241]. It also acts to reduce the influx of Ca^{2+} via the I_{Ca} current, thereby reducing the $I_{\mathrm{K_{Ca}}}$ current and raising the cells' excitability (mouse) [63]. 5-HT does not significantly affect input resistance or sag amplitude of aCINs or dCINs. In rat motoneurons, 5-HT inhibits $I_{\mathrm{K_{ir}}}$ by reducing instantaneous conductance, and it enhances I_{h} by shifting its activation curve in the depolarized direction (rat) [139].
- *NMDA* can excite voltage oscillations in rat spinal neurons, including pacemaker-like conditional bursting (rat) [118]. It facilitates, yet also slows down, the locomotor rhythm induced by K^+ (rat) [12].
- *NA* elicits predominantly unorganized, low level oscillations and some tonic spiking when applied to rat spinal motoneurons. It slows the locomotor rhythm established by 5-HT and/or NMDA, and it may 'rescue' deteriorating rhythms, possibly acting on the same neuromodulatory targets as 5-HT and NMDA (rat) [136].
- *K^+* at high extracellular concentrations produces locomotor rhythms similar to those induced by 5-HT, but having higher frequency (rat) [12].
- *DA* can induce fictive locomotor activity by itself (rat) [133]. DA induced activity tends to be slow and irregular.

- *ACh* can evoke locomotor patterns in lumbar region of the neonatal rat [49].

2.3 Modeling Strategies

Mathematical and computational studies have been undertaken for a variety of central pattern generators, including those controlling lamprey swimming [47, 147], crustacean digestive rhythm (lobster and crab stomatogastric ganglion) [100, 101, 85, 86, 150, 156, 175, 173, 174, 208], cockroach locomotion [81, 80], leech heartbeat [31, 51, 113, 114, 158, 157], rodent respiration [7, 24, 25, 22, 56], and locomotion in horses and other quadrupeds [21, 20]. The ODE models developed for these systems fall into four broad classes: (1) Phase oscillator models, (2) coupled cell network models, (3) detailed conductance-based models, (4) intermediate models. Though all of the classes represent essentially bottom-up approaches to dynamical systems-based neuroscience modeling [183], each is most appropriate for addressing particular kinds of questions and has a circumscribed domain of applicability. Below we summarize the basic characteristics of the four kinds of modeling strategies, and we discuss their advantages and disadvantages as they relate to modeling the RSHL CPG.

2.3.1 Phase Oscillator Models

Phase oscillator CPG models reduce the dynamics of each neuron's state to a one-dimensional ODE describing the motion of the cell on a limit cycle that represents its natural oscillatory cycle (tonic spiking or bursting). The neurons are assumed to evolve identically in isolation and thus have identical governing equations. Model neurons interact by advancing or delaying each other's phase; the amount of phase change induced by one cell on another depends only on the phase difference between

the two cells.

The equations for an N-oscillator model have the following basic form:

$$\dot{\phi}_i = f(\phi_i) + \sum_{j \neq i} g_{ij}(\phi_i - \phi_j) \tag{2.1}$$

Here f describes the phase evolution of an isolated oscillator, and g_{ij} is the phase response of the ith neuron due to input from the jth oscillator.

A fixed reference phase θ is taken to represent the peak of neuronal activity, *e.g.* the peak of an action potential or middle of the active segment of a burst; $-\theta$ corresponds to minimum activity. The spatiotemporal arrangement of these peaks in the model CPG maps to patterns of neural activation levels, muscular contraction, and movement; the aptness of a given phase oscillator CPG model may be judged by the biological plausibility of these patterns. Features of particular interest in these CPG models are the existence and stability of functionally significant phase configurations, *e.g.* synchrony or phase lags, and their dependence on network architecture, network size, and parameters such as coupling strength and intrinsic oscillator frequency. General predictions about such features for broad classes of CPG architectures may be made without referring to specific cellular models or biological examples, though only qualitative correspondence can be expected.

Phase oscillator models for the swimming CPG of the lamprey [46] have had notable success. The neuromuscular patterns of interest in this case are rostral to caudal waves of alternating segmental contractions which bend the lampreys body to produce an undulatory motion that propels the animal through the water. The basic phase oscillator CPG model is a chain of longitudinally coupled segments, each of which comprises a half-center oscillator pair with intrasegmental cross-cord coupling. Variations on this model have been used to study the dependence of

phasing stability on the ratio of oscillation frequency to coupling strength [47], the necessity of intrinsic frequency differences for traveling waves of phase oscillation, and the importance of the functional form of coupling in determining the stability of CPG oscillations [140].

2.3.2 Coupled Cell Network Models

The basic units of a coupled cell network CPGs are arbitrary ODE vector fields, called *cells*. Cells may have different governing equations, phase space dimensions, and parameter values. Generalizing the phase oscillator framework further, coupling between cells may depend on arbitrary combinations of the internal phase variables of the coupled cells. The equations governing the ith cell's state take the form

$$\dot{\mathbf{x}}_i = F_i(\mathbf{x}_i) + \sum_{j \to i} H_{ij}(\mathbf{x}_j, \mathbf{x}_i) \tag{2.2}$$

Here $\mathbf{x}_i \in \mathbb{R}^{k_i}$ are the internal state variables for cell i, $F_i : \mathbb{R}^{k_i} \to \mathbb{R}^{k_i}$ is the internal dynamics for cell i, and $H_{ij} : \mathbb{R}^{k_j} \times \mathbb{R}^{k_i} \to \mathbb{R}^{k_i}$ is the coupling from cell j to cell i; *cf.* equation (2.1). The sum is taken over the set of cells j which have upstream connections to cell i; this set is called the *input set* for cell i and denoted $I(i)$.

The collection of cells and connections is represented as a directed graph, with cells as colored nodes and connections as colored arrows. Cells i and j have the same internal dynamics if $k_i = k_j$ and F_i and F_j are identical for corresponding labeling of the components of $\mathbf{x}_i$ and $\mathbf{x}_j$, and the cells are assigned the same color. Arrows (a, b) and (c, d) have the same color if cells a and c, b and d have the same internal dynamics, respectively, and if the coupling functions H_{ab} and H_{cd} are identical under corresponding labeling of the components of $\mathbf{x}_a, \mathbf{x}_b, \mathbf{x}_c, \mathbf{x}_d$.

The input sets determine an important equivalence relation on a coupled cell network: Two cells i and j are equivalent if (1) i and j have the same internal dynamics, and (2) $I(i)$ and $I(j)$ have the same size and consist of arrows with the same distribution of connection types, *i.e.* there exists a bijection $h : I(i) \to I(j)$ such that $h(a) = h(b)$ iff a and b are arrows of the same connection type. Quotient networks are derived from the original coupled cell network by replacing nodes and arrows by representatives from equivalence classes based on input sets.

Although the coupled cell network formalism allows internal neuronal dynamics and synaptic coupling to be modeled with complete biophysical detail, this modeling approach concentrates on the role of network architecture in determining CPG output by ignoring the details of the cells' internal dynamics and the coupling functions [210, 91]. Independent of the details of the vector fields, certain time-periodic solutions of the network's ODEs must be equivariant under permutations of the cells that respect the cells' input sets. Such solutions correspond to synchronies among the cells in the network, both full synchrony, in which each cell is in phase with every other cell, and more general forms of synchronous solutions where subsets of cells are phase-locked with respect to other subsets of cells in the network.

Coupled cell network analysis concentrates on determining the existence and stability of equivariant solutions which arise through bifurcations of the steady-state, fully synchronous solution [92]. It proceeds by deriving reductions of the full network to quotient networks and considering the spatio-temporal symmetries which constrain the equivariant solutions for the quotient networks. The symmetries of the equations determines the conditions for bifurcations and sequences in which the bifurcations unfold [145]; the coupled cell approach reveals synchrony patterns that are not obvious from conventional symmetry considerations [88].

The coupled cell network formalism has been used to construct minimal models of quadruped locomotor CPGs composed of identical cells with identical coupling and to show that at least eight cells are required to express all of the primary and secondary gaits found in real quadrupeds [21, 20]. Related coupled cell models have been used to study gaits corresponding to arm-leg coordination in bipedal locomotion [171]. Attempts to categorize bursting behavior in small networks of cells with internal fast-slow dynamics have employed coupled cell network analysis and unfolding theory for symmetric dynamical systems [89, 90], and the mathematical theory has been used to study the emergence of (nearly) synchronized clusters of phase oscillators in large networks resembling cortices [87].

2.3.3 Conductance-based Models

Conductance-based models attempt to represent the CPG with a high degree of biophysical realism at the intracellular, synaptic, and network levels. The membrane voltage dynamics of individual neurons are modeled with equations that typically take the form

$$
\begin{aligned}
C\dot{V} &= -(\sum I_{\text{ionic}} + \sum I_{\text{syn}} + I_{\text{app}}) && (2.3)\\
I_{\text{ionic}} &= \bar{g} m^p h^q (V - V_{\text{rev}}) && (2.4)\\
\dot{x} &= \alpha_x(V)(1-x) - \beta_x(V)x,\ x \in \{m, h\} && (2.5)\\
&= (x_\infty(V) - x)/\tau_x(V) && (2.6)
\end{aligned}
$$

The $\dot{V}$ equation (2.3) governs the membrane voltage, which is determined by the activity of intrinsic ionic currents, I_{ionic}, and synaptic currents, I_{syn}, which are triggered by the activity of presynaptic neurons. Terms are included for each of the ionic currents found in a particular neuron type; the equational forms for the

ionic currents and their gating (activation and inactivation) variables reflect the underlying biophysics of the ion channels [115]. Experimental data from voltage clamp and current clamp studies are used to fit parameter values for maximal conductances, $\bar{g}$, and ionic reversal potentials, V_{rev}. The terms of the gating variable equations typically have exponential or multi-exponential forms, and their parameters are also fit to clamp study data.[5] Multi-compartment conductance-based models reflect neuronal morphology by modeling the cell as a set of electrically coupled compartments, *e.g.* soma and axons, each with its own set of membrane voltage and ionic current ODEs.

Constructing conductance-based CPG models is standard practice when there is a relatively large body of experimental data available about the intrinsic properties of identified neurons and the architecture of synaptic and electrotonic connections between them. Two invertebrate preparations, the crustacean stomatogastric ganglion (STG) and the leech heart, have been the subject of extensive conductance-based modeling. Each of these CPGs comprises a small number (10–20) of large constituent cells whose intrinsic membrane properties are well-characterized and whose connections have been extensively mapped. The physical characteristics of the networks facilitate repeated measurements of the biophysical properties of identified cells, and the wealth of available experimental data make these CPGs particularly suitable for the parameter estimation needed to build accurate conductance-based models. Furthermore, the CPGs are amenable to experimentation on functionally significant subnetworks to test model predictions.

Much of the modeling work on the crustacean STG has focused on building detailed single and multi-compartment models of a few cells that play important roles in the CPG, such as the anterior burster (AB), pyloric dilator (PD), lateral

[5]See Sections 2 and 3 of [231] for an excellent review of Hodgkin-Huxley style, conductance-based models and standard methods of matching their parameters to experimental data.

pyloric (LP), and pyloric cells (PY) [100, 101, 173, 174, 208]. Modeling studies have helped clarify the roles of particular currents in controlling excitability and endogenous bursting [239, 100, 208] and in determining the phase response properties for isolated cells [175, 162]. Several generations of models for subnetworks of the STG, particularly the AB/PD-PY-LP complex responsible for the pyloric rhythm, have been used to study the role of various parameters in controlling rhythmic properties [85, 86, 150, 156, 174].

The leech heart CPG is composed of several connected rhythmically active segments, and conductance-based models have been constructed to investigate the properties of the elemental half-center oscillators in individual segments, as well as the activity of multiple connected segmental oscillators. Studies of elemental oscillator models have distinguished multiple mechanisms for intrasegmental bursting, elucidating the effects of intrinsic and synaptic currents and quantifying the dependence of the oscillatory period on various parameters [158, 157]. Multiple segmental oscillator models have demonstrated that coordinating interneurons contribute to the oscillations within a single ganglion, in addition to their role of intersegmental coordination [114]. Other multiple segmental model studies have found that the half-center configuration for intersegmental oscillation is more tunable and more robust to perturbation than purely endogenous bursting [51].

2.3.4 Intermediate Models

Phase oscillators and detailed, conductance-based models mark opposite ends of the dual spectra of mathematical tractability and biological realism in CPG models. Situated between them are two kinds of intermediate models: phase-reduced models and systems-level models.

Phase-reduced or 'minimal' models for CPGs are built from component generic,

single compartment neurons possessing the 'minimal' equation structure necessary to reproduce the presumed activity patterns of neurons in the real animal. The membrane voltage equations have forms similar to (2.3), but their right hand sides are sums of pseudo-currents that do not correspond to specific ions. Currents are classified according to their roles in creating and setting the stability of fixed points and periodic orbits in the full and fast-subsystems. Their equational forms and parameter values are chosen to produce the appropriate configurations of fixed points, time-scales, and sequences of fast subsystem bifurcations such that the model produces phenomenologically correct spiking or bursting behavior, as measured by characteristics such as burst frequency, duty cycle, interspike interval, and spike number [81].

Once the constituent neurons have been modeled in this fashion, they are connected according to a known or posited network architecture to form a prospective CPG, and the network parameters may be tuned to match the model's output to experimental data [80]. This approach has been used to construct an 18 neuron locomotor CPG model for the cockroach which roughly reproduces experimentally observed stepping frequency, duty cycle, and motoneuron outputs. The neuronal models were also reduced to phase oscillators, and the resulting phase oscillator network model was used to prove the existence and stability of particular gaits using PRCs and averaging theory.

The systems-level modeling approach posits a connected oscillators architecture for the CPG based on the morphology and functional constraints of the animal, but does not model the oscillators as dynamic variables, *i.e.* with ODEs. Instead, curve fits of input-output data from biological experiments are used to construct 'black box' nonlinear response functions that serve as oscillator units. This approach has been used to construct an oscillator chain model for the leech swimming CPG [240].

Numerical simulations reproduce experimental measurements of phase, amplitude, and period, and the model gives experimentally testable estimates of synaptic coupling strengths and intrinsic period gradients along the nerve cord.

2.3.5 Modeling Framework Selection

Good mathematical and computational models of biological systems help scientists perform several kinds of conceptual tasks that are essential to scientific inquiry:

- *Synthesis*: A model should integrate the available experimental data and current theoretical understanding of a system in a single coherent, self-consistent framework. It should rest on explicit assumptions and ansätze that are biologically plausible and congruent with current experimental knowledge.
- *Analysis*: A model should allow specific features or structures of a system to be isolated for intensive investigation. It should support the reductive approach that is fundamental to the scientific process: decomposing a complex system into its constituent parts, comprehending the operation of the components, and assembling a theory for the whole system by understanding its parts.
- *Hypothesis*: A model should suggest potential causes for observed phenomena, stimulate ideas for possible experiments to check the validity of candidate explanations, and foster the formulation of questions of biological, mathematical, and computational interest.
- *Validation*: A model should act as a testing ground for evaluating tentative concepts, intuitive arguments and contingent hypotheses derived from experiments. Furthermore, a model must itself be susceptible to invalidation through quantitative comparison with experimental measurements. If a

model prediction is disconfirmed experimentally, the failure should point out specific gaps in biological knowledge or incorrect modeling hypotheses.

- *Explanation*: A model should illuminate the mechanisms and principles underlying particular phenomena of interest, uncovering the parameters and dynamics fundamentally responsible for various properties, *e.g.* phasing, period, spike amplitude, etc. It should provide a cogent narrative tying together disparate experimental results and theoretical ideas, and it should promise the integration of seemingly unrelated facts and concepts in the future. If multiple alternative explanations for a phenomenon are allowed due to complexity or redundancy in the model, then it should be possible to encode the competing alternatives in reduced models and test them against one another according to experimentally measurable criteria.

Given the appropriate context, each of the four standard CPG modeling frameworks can successfully fulfill these functions. Each class is best suited for addressing certain kinds of questions about CPG organization, and the most useful modeling approach may change as investigation progresses. One approach may be supplanted by another as the state of experimental knowledge evolves; employing multiple modeling strategies simultaneously may offer complementary perspectives on a given set of questions. We briefly summarize some of the pros and cons of the four standard modeling strategies before outlining our modeling approach for the RSHL CPG:

- *Phase oscillators*: Phase oscillator models have a number of attractive properties: First, they are simple to simulate and are often amenable to mathematical analysis. Second, model output is usually easy to interpret biologically. Third, given the models' relative simplicity, they may generate

hypotheses about CPG structure and phasing behavior which may be experimentally testable. Phase oscillator models may serve well for determining the appropriate network architecture for producing the phasing patterns observed in CPGs, and they may also serve as good substrates on which to build more detailed models.

The simplicity of phase oscillator models is also a limitation. The lack of detailed biophysics hampers investigation of the role of intrinsic membrane properties and neuromodulation in shaping network output. Differences between spiking and bursting in CPG activity is obscured by the use of phase oscillators as component neurons. In general, there is no direct correspondence between the parameters and outputs of the schematic model and the structures, parameters, and outputs of the biological system. It is normally possible to match model predictions to experimental measurements only in qualitative terms.

- *Coupled cell networks*: The main attractions of the coupled cell network approach are its mathematical elegance and its explicit separation of network architecture from cellular dynamics. Without relying on computer simulation or requiring any particular form for the internal neuronal dynamics or synaptic coupling, it is possible to determine the set of synchrony configurations compatible with a given network architecture, allowing hypothetical CPG designs to be ruled in or ruled out.

  The high level of abstraction is a drawback, however, for making experimentally testable predictions for specific biological systems. Coupled cell network theory analysis may establish the existence of certain stable synchrony configurations, but it gives no information about the parameter regimes in which they are realized. The lack of numerical continuation software for tracking

bifurcations of coupled cell systems reduces the applicability of this technique to realistic models. Ensuring that stable solutions exist and bifurcate in biologically realistic parameter regimes is essential for the modeling results to have biological relevance. These limitations restrict the usefulness of the coupled cell network approach to ruling in or out potential CPG architectures when there is little experimental data to constrain the possibilities.

- *Conductance-based models*: Conductance-based models have the advantage of incorporating the maximum available biological information, matching equational forms to the underlying biophysics and fitting parameter values to experimental measurements. Every new experimental result presents a direct opportunity for model validation, and new experimental data can be incorporated into the model as it is acquired, *e.g.* by adding ionic current terms or modifying parameters, without having to start from scratch. The immediate correspondence between the components of the model and the underlying biology makes interpretation of parameter variation easy, as well as facilitating *in computo* experiments that mirror those performed *in vitro* or *in vivo* , and vice versa.

  The disadvantages of conductance-based CPG models largely stem from their inherent complexity. The equations are typically intractable for closed form mathematical analysis, and large numbers of currents and parameters make comprehensive computational exploration of model output infeasible. Discerning the role of particular currents in shaping model output may be difficult, as may distinguishing cell-autonomous and network-based mechanisms for oscillations, bursts, and phase regulation. Incomplete knowledge may hinder model building (for instance, a highly detailed, biophysically accurate representation of one set of currents may lead to a model which does not

produce action potentials without the addition of other currents *ad hoc.*), and parameter values may have to be guessed at. Some model features may arise from overfitting parameters, and models may be particularly sensitive to parameter variations. Complex conductance-based models may be vulnerable to criticisms that they present 'just-so' stories, replicating available data without shedding light on the mechanisms underlying behaviors of interest.

- *Intermediate models*: Intermediate models encompass a variety of approaches that provide insight into the minimal conditions that suffice for a neuronal system to produce certain kinds of behaviors. For instance, they can provide examples of basic network architectures that produce appropriate phasing patterns in CPGs, such as gaits, or examples of simple cellular models that reproduce certain experimentally measurable properties, such as interspike interval or duty cycle. The models may be constructed in a manner that facilitates reduction to more abstract formalisms, such as phase oscillator or coupled cell network models, for tractable mathematical analysis. They may also suggest general principles or algorithms for designing biologically plausible models that functionally mimic natural systems, which may in turn inspire experimentally testable biological hypothesis.

  The constructive, minimalist strategy adopted in building intermediate CPG models is problematic, however. The approach of "judicious selection, rather than inclusion of biological data" [81] begs the question of how one decides the important data to include and what features should be built into the model, particularly when the modeling requires estimation of many unknown parameters. Engineering a model to reproduce certain experimental data and then invoking features of the model to explain those data raises the specter of logical circularity. Furthermore, it may be unclear whether the CPG model

"captures the neuronal dynamics essential for generation of the observed oscillation profile" [240], since the minimal mechanisms built into the model may not resemble the mechanisms responsible for the same outputs in the biological system. The genericity of the models may prevent them from providing a strong enough bridge to the biology, as they may obscure specific biophysical aspects that may be important in understanding the interplay of cellular properties and network architecture in determining CPG output. Finally, certain kinds of intermediate models, such as systems-level models, are not amenable to standard dynamical systems techniques, such as continuation.

2.3.6 Modeling Startup

Our long term goal is to formulate a complete model for the rodent spinal locomotor central pattern generator, including both forelimb and hindlimb movements. The model we envision should capture the CPG at the intracellular, synaptic, and network levels with sufficient biological detail to reproduce a wide range of experimental results, including those of anatomical, electrophysiological, pharmacological, and microscopy studies. We would eventually like to be able to determine the role played by the intrinsic properties of various cell types versus network architecture in specifying CPG behavior (*cf.* [193]).

Unfortunately, the available experimental knowledge is insufficient to constrain the set of possible models so as exclude all but one plausible scenario. We do not have enough electrophysiological data to model individual neurons of the CPG in detail, nor do we have sufficient anatomical data to specify the network architecture with certainty. It will likely prove necessary to use several different kinds of models with varying degrees of abstraction in the course of studying the RSHL

CPG. We would like a starting point that (1) supports extension and refinement in the direction of increasing biological realism, and (2) facilitates reduction and abstraction to focus on specific subproblems. The question is, where to begin?

Our initial focus is understanding how the fundamental locomotor rhythm is established and maintained. The kinds of architectural questions amenable to phase oscillator or coupled cell network modeling, *e.g.* existence and stability of gaits, are simple enough to answer with symmetry arguments for networks comprised of simple oscillators. More interesting and more relevant for comparison to available experimental data are modeling studies involving biophysically realistic neural components. But we do not have the right sort of phenomenological data to engineer experimentally testable intermediate 'minimal' models that functionally reproduce CPG output, nor are there enough experimental measurements of intrinsic properties to build detailed conductance-based models specific to the neurons in the RSHL CPG.

Design

We propose a model which maximally incorporates the available experimental results, built from biophysically realistic component neurons that are coupled according to connection patterns suggested by anatomical studies. Since we do not have sufficient data to formulate cellular models specific to this CPG, we use conductance-based neuronal models from other systems that have the right sorts of membrane currents as 'off the shelf' components. The original studies explore the models' properties extensively, obviating the need to characterize them ourselves. They also provide roadmaps to guide us in adjusting a few parameters to better match the models' output to the experimental data for the RSHL CPG. As additional experimental data emerge, the neuronal models can be modified to change

their components or to adjust their parameters to better fit measured properties. Or the models could be replaced entirely. Similarly, the synaptic connections of the CPG model can be reconfigured to reflect updated anatomical knowledge.

By including as much detail as possible from the beginning, we create a full model from which to derive reduced models to facilitate computational investigation and mathematical analysis. These smaller models are constructed through explicit simplifications and omission of details, isolating the features relevant to the phenomena of interest. By subtracting detail to obtain derivative models (*cf.* the intermediate, 'minimal' approach), we are assured that the core features of our derived models are consistent with the biology, and we can keep track of exactly which aspects of the models are in conflict with our experimental picture.

The full model, on the other hand, serves to synthesize experimental results and to provide a computational testbed for validating the reduced models' predictions in a context that more closely matches the realities of the biological system. Computational experiments with the full model can refute the hypothetical explanations implicit in the reduced models, and the biophysical realism of the full model facilitates the suggestion of biological experiments to test the hypotheses it generates (and vice versa).

Testing

An important functional characteristic of locomotor CPGs is the ability to respond to fast changes in stimulation without extended transients, *i.e.* rapid recovery from perturbation. This is important for escape behavior in the lamprey [97], for example, and this functional criterion has been used to rule out single component modulation as a mechanism for controlling burst frequency [147].

In the context of locomotor CPGs, rapid resumption of the fundamental loco-

motor rhythm after perturbation is essential for successful walking movement. An animal must be able to compensate for sudden changes in posture or terrain within a few periods of the locomotor cycle [122]. This leads to three criteria for evaluating models of the RSHL CPG: (1) Is the phase configuration corresponding to the fundamental locomotor rhythm producible and stable? How stable? (2) How quickly can the system establish the fundamental rhythm starting from a different, unorganized state? (3) What are the phase resetting properties of the CPG model when the locomotor rhythm is interrupted and restarted?

The next section describes the full model constructed according to the design principles discussed above. We list our modeling assumptions and ansätze explicitly, and we note areas where we anticipate modifications to the model. In the subsequent section, we report on the output of reductions of the full model in experiments that address the testing criteria listed above.

2.4 Model Description

We construct our initial models with the biological description of section 2.2 and the testing criteria of section 2.3.6 in mind. In order to clarify the reasoning behind our modeling study and to make its scope and boundaries explicit, we enumerate its main assumptions below. We refer to these starting points as ansätze: hypotheses about the biological system whose validity is checked by working through their implications via modeling and simulation, rather than direct experimental measurement.

2.4.1 Ansätze

1. The CPG comprises three species of neurons (MNs, RGNs, CINs).
2. The model neurons (and hence the neuronal clusters being represented) are strictly segregated according to whether they are associated with flexor or extensor activity, corresponding to the spatial distribution of phasically active cells in the L2/L5 spinal segments.
3. MN activity corresponds to ventral root activity recorded experimentally in the biological system; model output designated as flexor/extensor represents activity measurable at the L2/L5 ventral roots. Phasing of MN bursts is an output feature of particular importance in evaluating the model.
4. Each neuron group can be modeled by a single compartment, conductance-based model neuron with representative parameter values that produce average functional output.
5. Intergroup/interspecies communication is via non-adaptive chemical synapse, not gap junction.
6. Excitatory and inhibitory synaptic connections are symmetric across the midline and between flexor and extensor groups.
7. Rhythmogenesis occurs in both the L2 and L5 segments, rather than being driven from higher spinal regions or exclusively in segment L2 (*cf.* scenarios 1–3 in section 2.2.1 above).
8. Endogenous bursting by Hb9 interneurons is the source of rhythmic oscillations within each segment.
9. $I_{\mathrm{Na(P)}}$ is the critical slow current that controls endogenous bursting.
10. Ipsilateral flexor-extensor burst alternation is promoted by a half-center oscillator configuration of endogenous bursters on each side of the CPG.

2.4.2 Full Model

The full model comprises twelve neurons, four each of MNs, RGNs, and CINs. One neuron of each type represents the activity of corresponding clusters of like neurons in the (left or right) L2 (flexor) and L5 (extensor) segments of the spinal cord. The neurons are connected by sixty synapses (32 inhibitory, 28 excitatory); the network architecture of the model is best described by the wiring diagram in figure 2.1.

The following subsections describe in greater detail how cellular properties, synaptic transmission, and network architecture are represented.

Neuron types

The equations for all three neuron types were adapted from model I from [24], which was originally developed for neurons from the pre-Bötzinger complex of neonatal rats.[6] The pre-Bötzinger complex is involved in the basic breathing rhythm; the original model I neurons include a fast activating, slowly inactivating persistent sodium current, $I_{\mathrm{Na(P)}}$, which helps set the baseline excitability of the cells and is the slow current responsible for bursting. The bursts are square-wave, or Type I, with spike frequency adaptation. The burst frequency and duty cycle can be controlled by adjusting the maximal persistent sodium conductance and the leak reversal potential simultaneously. Initial studies showed that hyperpolarization could reset burst phase, but no systematic study of the phase resetting properties was made [24]. Studies of excitatorily coupled populations of model I neurons with a distribution of parameter values found that parameter heterogeneity and increased coupling broadened the range of depolarizing inputs for which the networks could be induced to burst synchronously, though stronger excitatory coupling de-

[6] A closely related four dimensional model model with similar properties is explored in [192].

creased the frequency of synchronous bursting in pairs of model neurons [25]. These modeling predictions generally accorded with experimental results [56].

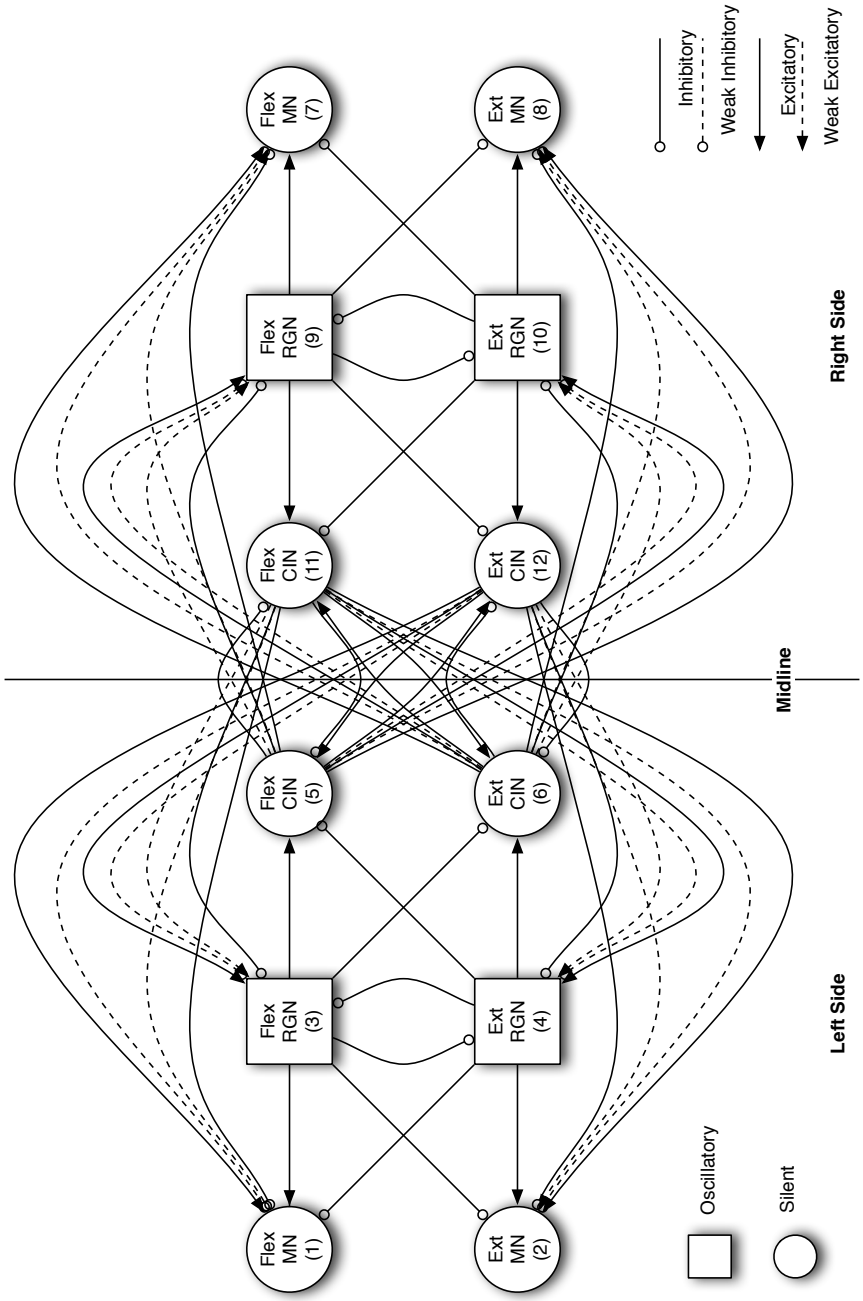

Figure 2.1: Diagram of the full CPG model.

The RGN neurons of our model followed the pre-Bötzinger model I structure, but with some parameter changes to more closely match measurements for Hb9 interneurons [234]. Exact burst frequency, duty cycle, and related measurements for Hb9 cells were not available, though published voltage traces indicate a period of 2-5 seconds and a 'duty cycle' slightly greater than 50 percent. This agrees with ventral root measurements that give similar periods and duty cycles greater than 50 percent for the motoneurons for L2 and L5 during fictive locomotion.The activation kinetics of $I_{\mathrm{Na(P)}}$ were thus adjusted to better match these estimates. The resulting parameter set produced a period of 2309 ms, a duty cycle of 0.5289, and a spike number of 28. This spike number is in some accord with the aggregate population output recorded at the ventral roots, though measurements from individual Hb9 or MNs do not report as high a spike number.

The current balance equations are identical for MNs and CINs. They omit the $I_{\mathrm{Na(P)}}$ terms from the pre-Bötzinger model I formulation and are capable of tonic spiking, but not bursting. The parameter regime chosen for the MNs and CINs leaves them passive but capable of being excited to spike repeatedly in response to small depolarizations. They act as conduits for the burst depolarizations from the RGNs, with their responses being modified by an array of synaptic inputs. The omission of $I_{\mathrm{Na(P)}}$ from the equations also speeds computer simulations.

Equations and parameter values for RGNs, MNs, and CINs are given in Appendix A. The thrust of our current modeling studies is to examine possible mechanisms underlying the rhythmic alternation of bursts in the RSHL CPG. An initial hypothesis supported by our modeling ansätze is that appropriately phased endogenous bursting is primarily responsible, and hence our neuronal modeling concentrates on the properties of the RGNs. We also lack the experimental data necessary to significantly constrain the cellular models used for MNs and CINs,

and so we use a conventional model of excitable neurons that is compatible with our ansätze and does not introduce any extra properties.

The RGNs could be modeled alternatively as tonic spiking, with flexor-extensor alternation in each hemicord being established and controlled via the standard half-center configuration. MNs and CINs in the biological system are known to express $I_{\mathrm{Na(P)}}$, and although they do not burst endogenously, they may respond to depolarizing inputs by firing multiple spikes. An alternate parameter regime could put them in a passive mode at the edge of bursting (rather than tonic firing), so that weak or extended synaptic excitation could trigger bursting output. Finally, each model neuron could be replaced by a heterogeneous population of neurons, coupled by excitatory chemical synapses and gap junctions within the group.

Synapses

A synapse model with graded neurotransmitter release [61, 62] is used for both excitatory and inhibitory synapses. The model equations have the form:

$$I_{\mathrm{syn}} = g_{\mathrm{syn}} s (V - V_{\mathrm{syn}}) \tag{2.7}$$

$$\dot{s} = \alpha_{\mathrm{syn}} T_{\infty}(V_{\mathrm{pre}})(1 - s) - \beta_{\mathrm{syn}} s \tag{2.8}$$

$$T_{\infty}(V_{\mathrm{pre}}) = (1 + \exp(-(V_{\mathrm{pre}} - V_p)/K_p))^{-1} \tag{2.9}$$

Here s represents the level of neurotransmitter released into the synaptic cleft and thus actively affecting the post-synaptic cell. The neurotransmitter release rate is determined by Equation 2.8, and depends on the presynaptic membrane voltage, V_{pre}, and the amount of neurotransmitter already released. The value of the synaptic reversal potential, V_{syn}, determines whether the synapse is excitatory or inhibitory; in all other respects (activation time constants, etc.) inhibitory and excitatory synapses are identical. The parameter values used for CPG model

synapses match those listed for the pre-Bötzinger (PB) model in Tables B.6, B.7, and B.8 in appendix B. In the original formulation of this synapse model, parameters were chosen to match fast AMPA receptor kinetics [62, 4]; the synaptic activity profile is similar for the parameter set chosen for the CPG model.

Alternatives to this synaptic form include alpha functions [30, 15] and adaptive synapses [156, 10]. Although widely used, particularly by experimentalists fitting electrophysiological data, alpha functions have the distinct disadvantage of rendering the dynamical system non-autonomous, which complicates analysis and some computations.

Although there is likely to be considerable adaption in the biological system, there is currently no specific information about facilitation or depression in the RSHL CPG. The synapse equations can be modified for adaptation by adding a dynamic (in)activation variable of a form analogous to standard equations for membrane channel gating variables [156, 10].

The activation variable s could also be replaced by an appropriately shaped instantaneous function of voltage [156, 151]. This third alternative form could speed numerical simulations, though dynamic variables would need to be reintroduced in order to make it adaptive.

Architecture

Due to the symmetries inherent in the full model, its synaptic connections naturally form groups of four. These groups correspond to the anatomy of the biological system and plausible functional arrangements:

1. Ipsilateral RGN-MN flexor-extensor inhibition: $\{(3,2),(4,1),(9,8),(10,7)\}$
2. Ipsilateral RGN-RGN flexor-extensor inhibition: $\{(3,4),(4,3),(9,10),(10,9)\}$
3. Ipsilateral RGN-MN excitation: $\{(3,1),(4,2),(9,7),(10,8)\}$

4. Ipsilateral RGN-CIN excitation: $\{(3,5),(4,6),(9,11),(10,12)\}$
5. Ipsilateral RGN-CIN flexor-extensor inhibition: $\{(3,6),(4,5),(9,12),(10,11)\}$
6. Contralateral CIN-CIN inhibition: $\{(5,11),(11,5),(6,12),(12,6)\}$
7. Contralateral CIN-CIN flexor-extensor excitation: $\{(5,12),(12,5),(6,11),(11,6)\}$
8. Contralateral CIN-MN inhibition: $\{(5,7),(11,1),(6,8),(12,2)\}$
9. Contralateral CIN-RGN flexor-extensor excitation: $\{(5,10),(11,4),(6,9),(12,3)\}$
10. Contralateral CIN-RGN inhibition: $\{(5,9),(11,3),(6,10),(12,4)\}$
11. Contralateral CIN-MN flexor-extensor excitation: $\{(5,8),(11,2),(6,7),(12,1)\}$
12. Contralateral CIN-RGN weak excitation: $\{(5,9),(11,3),(6,10),(12,4)\}$
13. Contralateral CIN-RGN flexor-extensor weak inhibition: $\{(5,10),(11,4),(6,9),(12,3)\}$
14. Contralateral CIN-MN flexor-extensor weak inhibition: $\{(5,8),(11,2),(6,7),(12,1)\}$
15. Contralateral CIN-MN weak excitation: $\{(5,7),(11,1),(6,8),(12,2)\}$

Note that commissural interneurons mediate all cross-cord communication.

There is considerable functional redundancy apparent among the synaptic groups listed above, and the activity of some synaptic groups may be counterproductive *vis-à-vis* creating the fundamental locomotor rhythm. Contralateral CIN-MN inhibition and excitation obviously work to counteract one another, for example. Opposing synaptic groups (especially those marked as 'weak') could have strengths that vary over time or in a phasic manner, such that they serve to modify the rhythm during maneuvers like turning or reversal. For initial model exploration, the synaptic strengths of many groups may be set to zero.

2.4.3 Derived Models

The full model is a dynamical system with 88 phase space variables and a parameter space of order 1000. Even considering the symmetries of the model, the wiring diagram is complicated. Tracing the downstream phasing effects of some connections is not easy, and the size of the model makes numerical simulation quite computationally intensive. Brute-force exploration of the space of synaptic weightings for the full model at this stage is neither computationally feasible nor likely to be particularly comprehensible or enlightening. To facilitate analysis and speed computations, we concentrate on two sets of subnetworks that have obvious functional importance for the operation of the full model.

The first set consists of two-cell models, a pair of reciprocally inhibitory RGNs and a pair of mutually excitatory RGNs, both shown in figure 2.2 (a). The inhibitory pair is the two-cell rhythmogenic kernel (RGK) present on each side of the full model. It is a variation on the usual half-center oscillator configuration, comprising two reciprocally inhibitory endogenous bursters rather than coupled tonically spiking neurons. In accordance with ansatz 10, it is presumed that this subnetwork drives the rhythm of flexor-extensor alternation in each hemicord.

The excitatory pair (EP), on the other hand, is not present in the full model. It is a reduction of the excitatory cross-cord communication route that is mediated by CINs in the full model. We use the EP model to determine the range of excitation strengths that produce rapid synchronization of contralateral flexor-extensor pairs.

The second set of derived models consists of three four-cell networks: (1) a bi-directional inhibitory ring, (2) two half-center oscillators with cross-excitation, and (3) a bi-directional inhibitory ring with cross-excitation. We refer to these models as 4-IR, 4-CE, and 4-IRCE, respectively; their diagrams are shown in figure 2.2 (b), (c), and (d). These networks are three plausible arrangements for

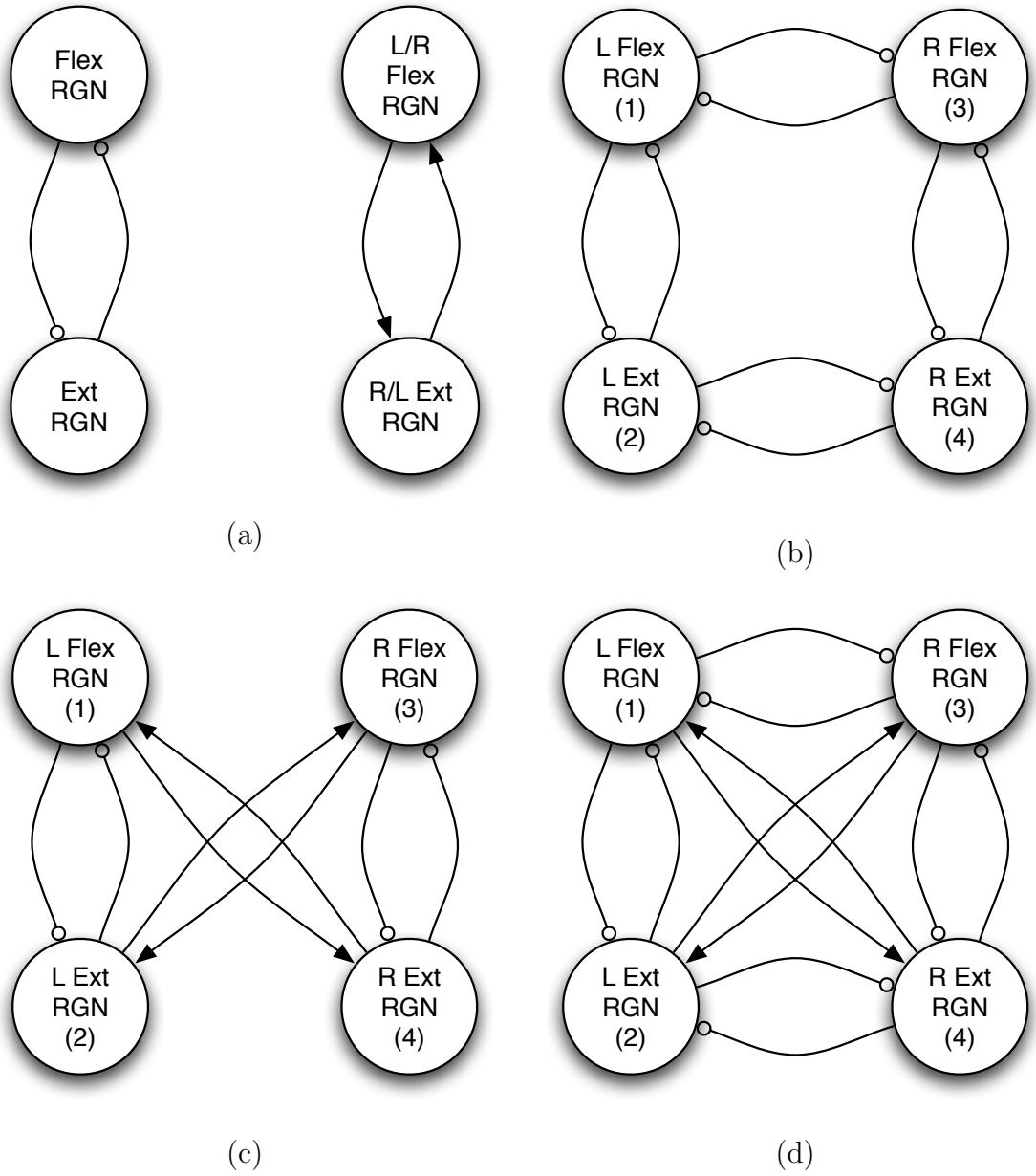

Figure 2.2: Diagrams of reduced CPG models. (a) Left: rhythmogenic kernel (RGK), right: mutually excitatory pair (EP). (b) Bi-directional inhibitory ring (4-IR). (c) Two half-center oscillators with cross-excitation (4-CE). (d) Bi-directional inhibitory ring with cross-excitation (4-IRCE).

coordinating flexor-extensor burst alternation across the midline in order to set up the fundamental locomotor rhythm. They may be considered reductions of the full model in which most of the excitatory connections have been removed and the

MNs and CINs have been collapsed together with the RGNs.

In the next section, we study the phasing characteristics of the derived models to gain insight into the potential output repertoire and properties of the full model.

2.5 Model Output

As stated at the end of section 2.3.6, we have three basic criteria for evaluating models of the RSHL CPG: (1) stability of the phase configuration corresponding to the fundamental locomotor rhythm; (2) duration of transients in establishing the fundamental rhythm from an unorganized state; (3) phase resetting properties when the locomotor rhythm is interrupted. In the experiments described below, we directly investigate (1) and (2) for our reduced models in order to gain insight into the behavior of the full model with respect to all three criteria. We focus particularly on the role of synaptic connection strength in determining phasing stability and transient behavior.

2.5.1 Two-cell Models

In the full model, reciprocally inhibitory pairs of RGN cells are responsible for setting up the basic flexor-extensor alternation for each side. We may thus consider antiphasic alternation of bursts (phase difference of 0.5) to be the target configuration of the RGK subnetwork. As an indicator of the stability of the fundamental locomotor rhythm, we ask: From any initial phase configuration and for a given coupling strength, how rapidly does the RGK network approach its target phasing?

Similarly, cross-cord excitation plays a role in synchronizing contralateral pairs of flexors and extensors. The analogous question for the EP model is: From any initial phase configuration and for a given coupling strength, how rapidly does the

EP achieve burst synchrony?

For each two-cell network, we begin by considering its two neurons in an uncoupled state, *i.e.* $g_{\text{syn}} = 0$. Since the neurons have identical parameters, they would each settle onto the same bursting periodic orbit if allowed to evolve without interacting with the other. We consider this uncoupled bursting orbit for a single neuron to be the *individual reference orbit* or *individual reference burst*. Choosing the start of the active segment of the individual reference burst as the reference phase 0, we fix the initial conditions of one neuron, designated the 'leader,' at that point. The initial conditions of the other neuron, designated the 'follower,' are set to correspond to a phase $\theta \in [0, 1]$. The synaptic strength is then set to its chosen value (coupling is symmetric), the synaptic activation variables are initialized to 0, and the evolution of the two-cell model from this initial phase offset is simulated by numerically integrating for at least 15 burst cycles.[7] The phase offset between the leader and follower neurons is calculated for the ith burst cycle as $(t_F^i - t_L^i)/T$ mod 1, where $t_{\{L,F\}}^i$ is the starting time of the ith burst of the leader or follower, respectively, and T is the period of the burst cycle.[8]

RGK Model

Coupling strengths ranging from 0.0001 to 40 were tested; for each coupling strength, 50 evenly spaced initial follower phases $\theta \in [0, 1]$ were used as initial conditions. Figure 2.3 shows the results for six representative coupling strengths. In the plots, the θ_0-axis represents the initial follower phases, and the θ_n-axis corresponds to the follower phases (relative to the leader) after n burst cycles. Different line styles

[7] We determine the start and end of the active segment of each neuron's burst cycle according to the methods described in section 3.2.3 of chapter 3.

[8] The period T here can be taken as the period of the individual reference burst or as the period of the ith (coupled) burst without any qualitative difference in the results, and only a very slight quantitative difference in the measured phase offsets. The results in this chapter use the individual reference burst period.

indicate the various values of n. Instantaneous convergence to antiphase would produce a horizontal line at $\theta_n = 0.5$, while the uncoupled system would produce a straight line through (0.5, 0.5) with a 45-degree slope.

Convergence and Coupling Strength

For coupling strengths below 1, the RGK model did not achieve the antiphase configuration from any initial conditions in less than 20 burst cycles; for coupling strengths greater than 20, every initial condition led to the antiphase configuration within three cycles, and usually within two. None of the higher coupling strengths tested achieved the antiphase configuration within one cycle from every initial condition.

The results shown in figure 2.3 indicate that $g_{\text{syn}} = 20$ is approximately the lowest coupling strength for which the transient period is short enough to consider the model's behavior to be biologically plausible. For lower coupling strengths, the convergence to the antiphase configuration from many initial conditions is so slow that the model could be considered as not having a functionally stable antiphase configuration at all. The transient behavior of the RGK subnetwork is discussed in more detail in the next subsection.

There is no clearly articulated standard by which to classify the value $g_{\text{syn}} = 20$ as strong or weak coupling. One measure of relative synaptic strength is the size of the maximal synaptic current to the strongest intrinsic current. For most models, the spiking Na^+ current is typically the strongest factor in depolarizing the membrane, and hence it is the current against which synaptic inhibition must work the hardest. Other studies involving conductance-based neural models subjected to synaptic input (both excitatory and inhibitory) have used maximal synaptic currents whose ratio to the maximal spiking Na^+ current magnitudes range from on the order of 0.0001 [4] to 0.1 [158] to $0.5 - 1$ [25, 175].

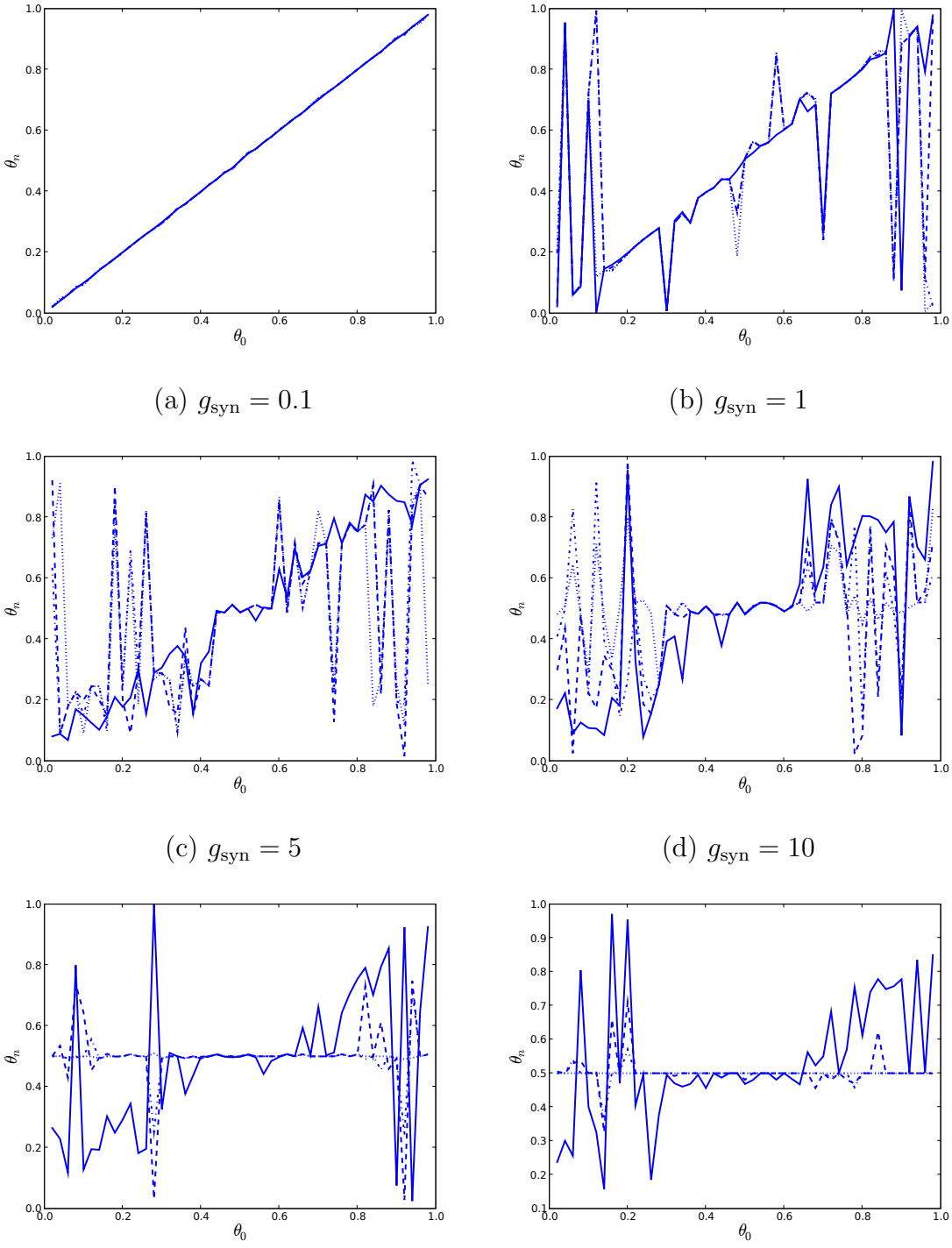

(a) $g_{\text{syn}} = 0.1$

(b) $g_{\text{syn}} = 1$

(c) $g_{\text{syn}} = 5$

(d) $g_{\text{syn}} = 10$

(e) $g_{\text{syn}} = 15$

(f) $g_{\text{syn}} = 20$

Figure 2.3: Relative phasing of bursts in RGK model (half-center configuration). Blue lines indicate relative phase of follower after n burst cycles. Solid: $n = 1$. Dashed: $n = 3$. Dash-dotted: $n = 5$. Dotted: $n = 10$.

In one study, a ratio of 0.0001 was considered weak, while a ratio of 0.001 was considered strong [4]. The other studies did not explicitly classify the synaptic input strength [158, 25, 175]. Given that the magnitude of inhibitory synaptic currents required to effect significant phase changes in our models were equal or greater than the maximum inward spiking current, we categorize this coupling as (very) 'strong.'

Transient Behavior and Leader-Follower Switching

One feature of the coupled neurons' transient behavior is the change in their spike numbers as they approach the phase target configuration, a change consistently seen at higher coupling strengths. The duty cycle of the uncoupled neurons is approximately 0.5289, with 28 spikes per burst. In the antiphase configuration, coupled neurons typically have 26 spikes per burst and a duty cycle of about 0.505; their active segments normally overlap by one spike. In a sense, the neurons in the half-center configuration settle onto coupled periodic orbits that lie near their uncoupled starting orbits, but which minimize the amount of overlap between them, thus shrinking their duty cycles.

The most surprising observation is the RGK model's high degree of sensitivity to initial phasing conditions, which can be seen in figure 2.3. At the lowest coupling strength, $g_{\text{syn}} = 0.1$, this sensitivity is not readily apparent; the neurons' relative phase after even 10 burst cycles are essentially the same as the initial phase offset. For all of the stronger couplings, though, the relative phases of the neurons may change significantly from cycle to cycle in a fashion that does not converge monotonically to a phase difference of 0.5. As the number of cycles n increases, the 45-degree line in figure 2.3 (b)-(f) does not transform smoothly to a horizontal line; the pictures are instead quite jagged.[9] An initial phase difference of 0.2 may

[9]Recall that phase is measured on a circle, so that the seemingly large deviations from the

become 0.22, while an initial phase difference of 0.24 may become 0.14 (see figure 2.3 (c)). This sensitivity to initial conditions is most evident at lower to intermediate coupling strengths. As the coupling strength increases, a flatter interval of the relative phasing curve emerges about $\phi_0 = 0.5$, indicating that the neurons move rapidly to the antiphase configuration from nearby initial conditions. This flatter interval broadens as the coupling strength increases, but phase sensitivity remains at initial phases closer to 0 or 1, although the phase differences still converge to 0.5 in a few burst cycles for these initial conditions as well.

A related observation about transient behavior of the RGK model is that the position of leader and follower may reverse in the course of converging on the antiphase configuration. An example of this phenomenon is shown in figure 2.4. (To make this figure and figure 2.5 clearer, neuronal parameters were changed to reduce the spike number for the individual reference burst, but the same effect occurs in the model for the standard RGN parameter values. The value of g_{syn} is 1 for both figures.) The follower initially lags the leader neuron by a phase difference of 0.03, but subsequently precedes it in beginning to burst, a switch which is permanent. What happens is that the active segment of the follower's initial burst is prolonged, with many spikes added, while the leader completes two full burst cycles (see figure 2.4 (b)). When the follower resumes normal bursting, its active segment begins before that of the leader cell, so that the positions are reversed.

Whether roles are reversed in this fashion is also highly sensitive to initial phasing conditions, as demonstrated by figure 2.5. Here the same version of the RGK model is initialized to have a phase difference of 0.05, and although both the

45-degree line seen, for example, at the left and right edges of 2.3 (b), (c), and (d) are in fact smaller than they appear. Large 'peaks' that lie on the opposite side of the horizontal line at $\phi_n = 0.5$ from the 45-degree line indicate that the follower neuron now bursts *before* the leader neuron.

leader and follower at first have elongated bursts, the leader neuron permanently precedes the follower. (Note that the follower undergoes two elongated bursts, but does not precede the leader once it resumes normal bursting. See figure 2.5 (b) in particular.)

The biological significance of leader-follower switching is not entirely clear. Starting from small phase differences, the near simultaneity of the two neurons' initial spiking would cause flexors and extensors to contract simultaneously, resulting in stiffening of the limbs and little or no locomotor-like movement. In this case, the exchange of leader and follower roles *per se* would not have much effect, but the prolongation of one neuron's spiking segment while the other goes through a regular cycle of spiking and quiescence would result in ineffective partial motion. Burst prolongation, particularly if leader and follower roles also reverse, has a greater effect on movement if it occurs for initial phase differences closer to 0.5. In that case, it changes near alternation of flexors and extensors to synchronous contraction for a cycle, interrupting relatively effective movement. The phenomenon does occur at higher coupling strengths for phase differences between 0.25 and 0.35. Overall, the leader-follower switching phenomenon appears to have mostly negative implications for the CPG's ability to produce effective walking rhythms rapidly after perturbation.

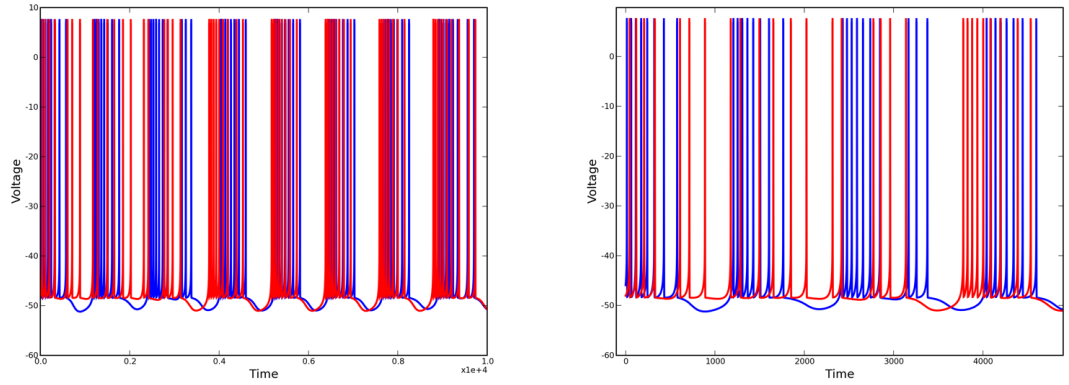

(a) (b)

Figure 2.4: Leader-follower switching example, $\theta_0 = 0.03$. The leader's voltage trace is drawn in blue, the follower's in red. (a) Full voltage trace. Leader and follower exchange order. (b) Close-up of initial transient period. Note that the follower's first burst is elongated and the leader undergoes two burst cycles while the follower undergoes one.

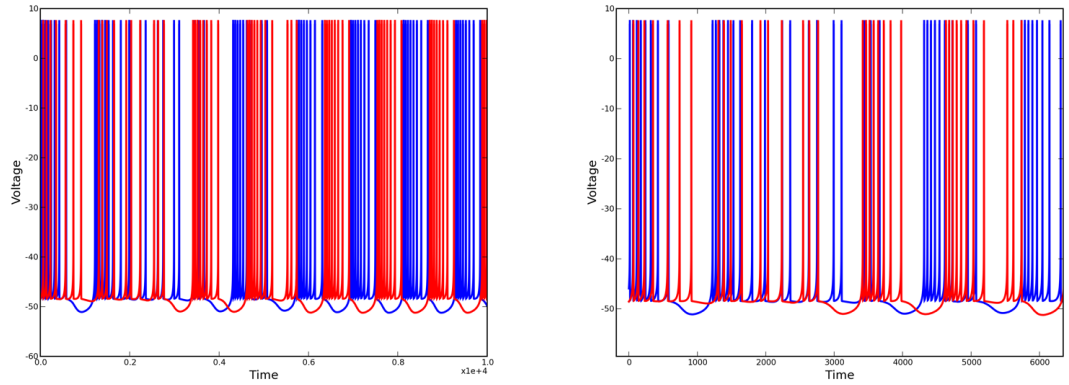

(a) (b)

Figure 2.5: Leader-follower switching example, $\theta_0 = 0.05$. The leader's voltage trace is drawn in blue, the follower's in red. (a) Full voltage trace. Leader and follower maintain their order. (b) Close-up of initial transient period. Both leader's and follower's first bursts are elongated, and the leader and follower undergo the same number of burst cycles.

EP Model

As for the RGK model, 50 evenly spaced initial follower phases $\theta \in [0, 1]$ were used as initial conditions; coupling strengths for the EP model ranged from 0.00001 to 20. Figure 2.6 shows the results for six representative coupling strengths; the line styles and axes have the same meaning as in figure 2.6 for the RGK model. The θ_n-axis is centered about 0, however, so that instantaneous convergence to synchrony would produce a horizontal line at $\theta_n = 0.0$, the middle of the plots. The centering about 0 means that phase θ_n is displayed between -0.5 and 0.5, and so apparent discontinuities (*e.g.* figure 2.6 (a) near $\theta_0 = 0.5$) are visualization artifacts and do not reflect actual phase discontinuities.

For coupling strengths below $g_{\text{syn}} = 1$, the EP model neurons did not synchronize their bursts for at least 15 cycles (figure 2.6 (a)–(c)), while for strengths equal to or greater than $g_{\text{syn}} = 1$, bursts synchronized within 8 cycles (figure 2.6 (d)–(f)). Biologically reasonable synchronization rates (within 2-3 cycles) were achieved only for strengths 5 and higher. If we compare the magnitude of the synaptic currents to the magnitude of I_{Na}, as for the RGK model, relatively strong coupling is required to achieve rapid burst synchrony in the EP model.

Unlike the RGK model, the EP model does not exhibit significant sensitivity to initial phasing conditions, nor leader-follower switching behavior. All initial conditions eventually lead to synchrony, and nearby initial conditions synchronize by moving the bursts in the same direction. As can be seen in figure 2.6 (e) and (f), the rate of synchronization is slower for initial conditions near antiphase (solid line peaks near $\theta_0 = 0.5$). These initial conditions correspond to the alignment of one neuron's active segment with the other's quiescent segment, and the slower convergence reflects the weaker phase response of the quiescent bursting neuron (see chapters 3 and 4).

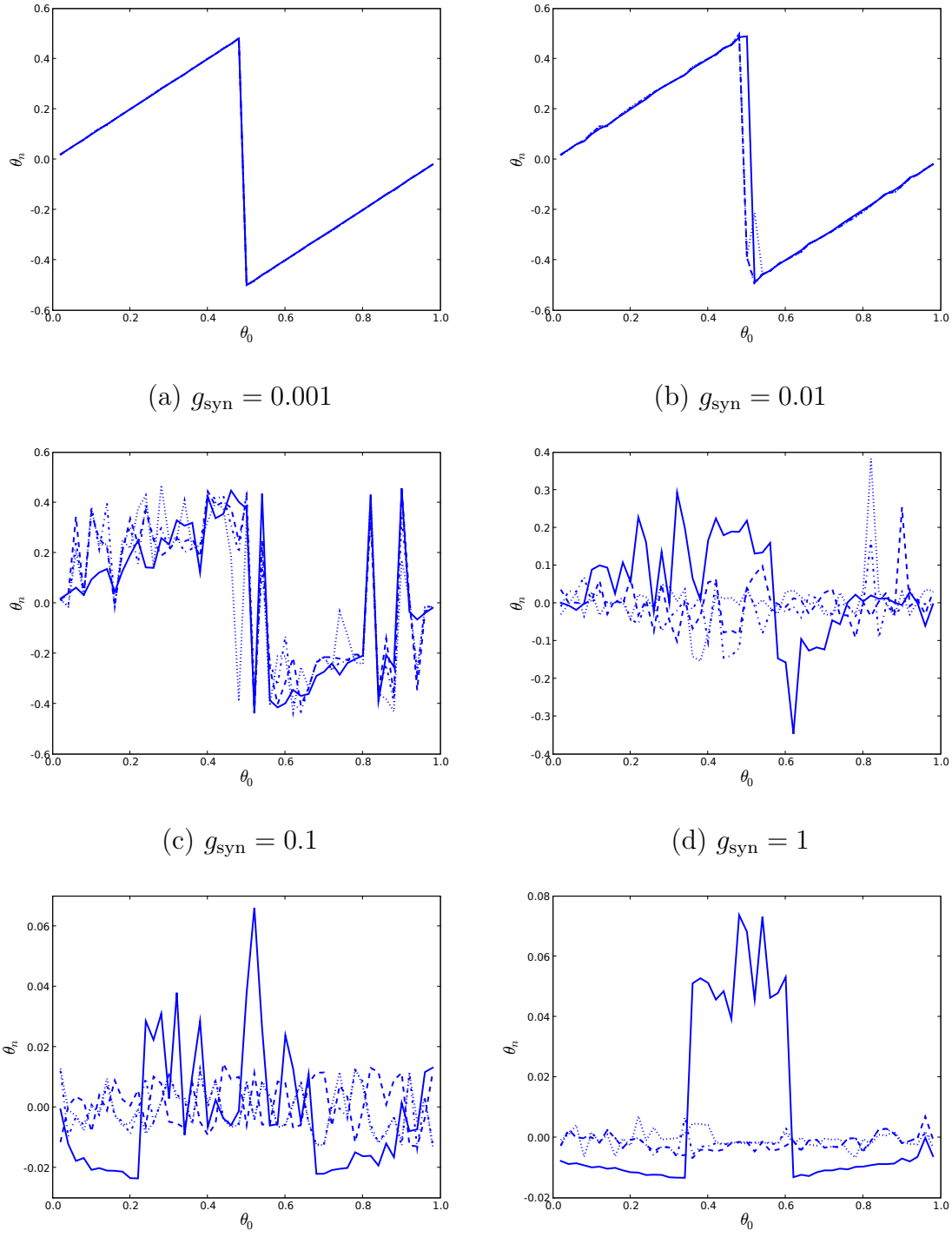

(a) $g_{\text{syn}} = 0.001$

(b) $g_{\text{syn}} = 0.01$

(c) $g_{\text{syn}} = 0.1$

(d) $g_{\text{syn}} = 1$

(e) $g_{\text{syn}} = 5$

(f) $g_{\text{syn}} = 10$

Figure 2.6: Relative phasing of bursts in EP model (reciprocal excitation). Blue lines indicate relative phase of follower after n burst cycles. Solid: $n = 1$. Dashed: $n = 3$. Dash-dotted: $n = 5$. Dotted: $n = 10$.

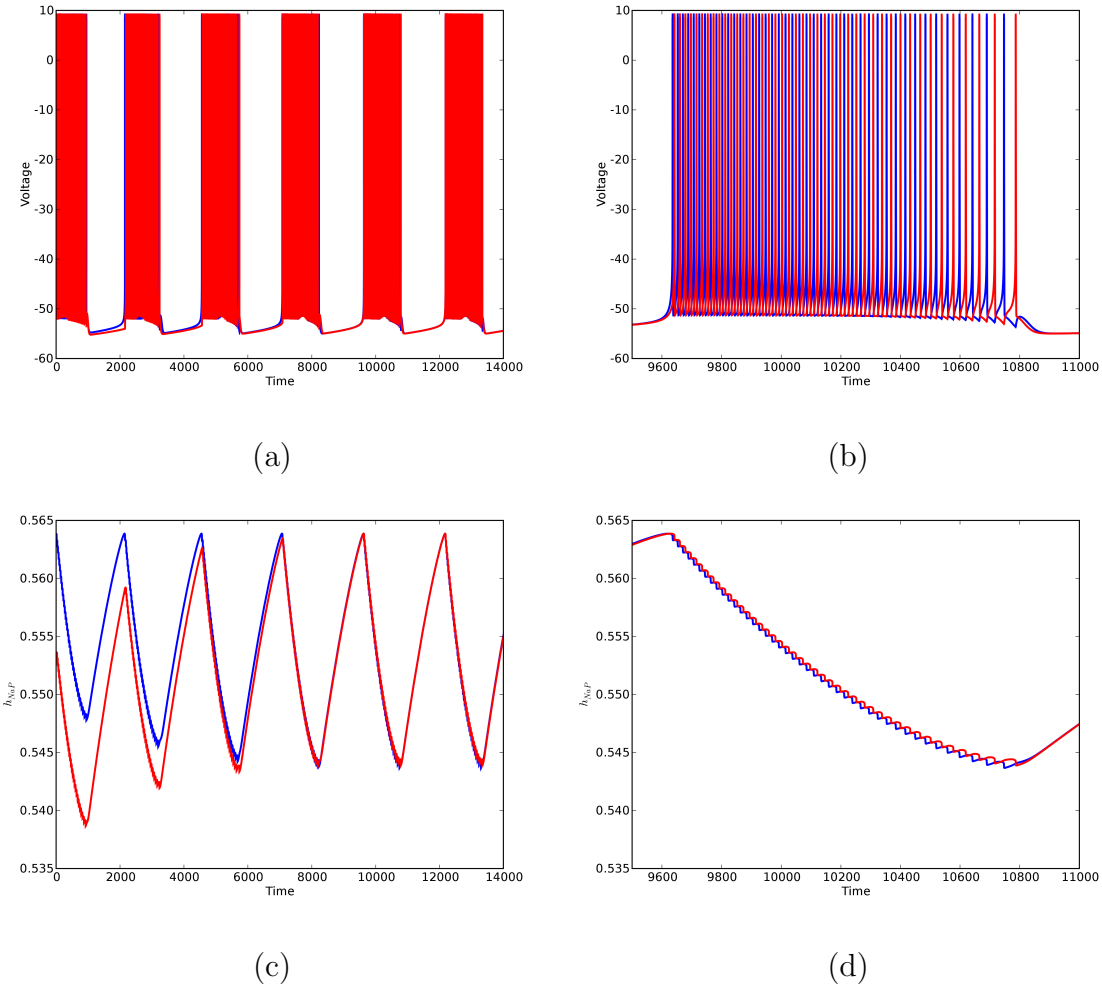

Figure 2.7: Burst synchronization and spike anti-synchronization in EP model. The leader's traces are drawn in blue, the follower's in red. $g_{\text{syn}} = 10, \theta_0 = 0.3$. (a) Full voltage trace. (b) Voltage trace, close-up of fourth burst. (c) $I_{\text{Na(P)}}$ activation level (h_{NaP}), full trace. (d) $I_{\text{Na(P)}}$ activation level (h_{NaP}), close-up of fourth burst.

Finally, we note that the neurons of the EP model typically settle into configurations of burst synchrony with intraburst spike anti-synchrony, a phenomenon reported in models of bursting in pancreatic β-cells [201] and in pre-Bötzinger model I, for somewhat different coupling [7]. Figure 2.7 shows an example: The spikes of the two neurons alternate (figure 2.7 (a) and (b)), but their burst envelopes (defined by the activity of $I_{\text{Na(P)}}$) are almost completely synchronous (figure 2.7 (c) and (d)). The alternation of spikes within synchronized bursts probably

has little biological significance in terms of synchronization of flexor and extensor contraction.

2.5.2 Four-cell Models

We assess the four-cell models' sensitivities to initial phasing conditions and stable phase configurations by a procedure similar to the one used for the two-cell models. For each model, we designate neuron 1 (corresponding to the left flexor) as the reference neuron against which all relative phases are measured. We fix the initial conditions of neuron 1 at reference phase 0, the start of the active segment of the individual reference burst. The initial conditions of the other neurons are set to correspond to random phases $\theta_i, i = 2, 3, 4$, chosen uniformly in $[0, 1]$. The coupling strengths and synaptic variables are then initialized (all excitatory synapses having the same strength, and similarly for the inhibitory synapses), and the model is simulated for at least 8 burst cycles. The phase offset $\Delta\theta_i^n$ of the ith neuron's nth burst is measured with respect to the nth burst of neuron 1, *i.e.* $\Delta\theta_i^n = (t_i^n - t_1^n)/T \mod 1$, where t_i^n is the starting time of the nth burst of cell i and T is measured as for the two-cell case.

Each model was simulated starting from 100 random initial phase configurations for each set of excitation/inhibition strengths. Inhibitory g_{syn} values were 0.001, 0.01, 0.1, 1, 5, 10, 15, 20; excitatory g_{syn} values were 0.0001, 0.001, 0.01, 0.1, 1, 5. The results of the simulations are presented as three-dimensional scatter plots in figures 2.8–2.12. Each axis corresponds to a phase offset $\Delta\theta_i^n$; the plot symbols indicate the value of n: blue circles, $n = 1$ (one cycle after initial phase settings); red triangles, $n = 3$; green squares, $n = 5$; black diamonds, $n = 8$. The four plots in each of the figures correspond to representative sets of excitation/inhibition strengths.

4-IR Model

The 4-IR model possesses at least four potentially stable phase configurations of biological interest: (1) complete synchrony ($\Delta\theta_i = 0, \forall i$); (2) 'hopping' ($\Delta\theta_2 = \Delta\theta_4 = 0.5, \Delta\theta_3 = 0$); (3) 'walking' ($\Delta\theta_2 = \Delta\theta_3 = 0.5, \Delta\theta_4 = 0$); (4) 'overlapped walking' ($\Delta\theta_2 = 0.25, \Delta\theta_3 = 0.5, \Delta\theta_4 = 0.75$).[10] The proportion of simulations that evolve to phasing arrangements near a given configuration is indicative of the size of the terminal configuration's basin of attraction; the rate of accumulation reflects both the stability of the terminal configuration and the influence of the chosen synaptic strength.

Figure 2.8 shows the behavior of the 4-IR model for inhibition levels 0.1, 5, 10, 20. The weakest coupling strength shows evenly distributed phase configurations, with the blue, red, green, and black markers very close to one another (figure 2.8 (a)). This indicates that the neurons' relative phases change very little over the course of the simulation. Inhibition less than $g_{\text{syn}} = 1$ produced practically no change in cell phasing from most initial conditions, even after eight burst cycles.

There is much more movement at strong-intermediate levels of inhibition ($g_{\text{syn}} = 5, 10$, figure 2.8 (b) and (c)), and some clustering emerges after 5 or more cycles. Some green and many black markers clump together near $\Delta\theta_2 = 0.5, \Delta\theta_4 = 0.5, \Delta\theta_3 = 0$, the 'hopping' configuration. (Since phase is a circular variable, $\Delta\theta_3 = 0$ is equivalent to $\Delta\theta_3 = 1$, so there is only one cluster, though it appears as two clusters on opposite faces of the $\Delta\theta_2 \times \Delta\theta_3 \times \Delta\theta_4$ cube.) This clustering is most prominent at $g_{\text{syn}} = 20$; the emergence of the hopping configuration is evident after three cycles in figure 2.8 (d). A smaller cluster corresponding to synchrony is also visible in the upper near corner of the same figure; it appears after 5 cycles.

[10] If the output of each cell in the 4-IR model corresponded to a limb movement, then 'overlapped walking' would simply be the standard walking gait [21]. However, the cells represent flexor or extensor activation, and this configuration does not have a standard interpretation in terms of bipedal gaits [171].

These results indicate that inhibition alone moves the network towards its stable configurations rather slowly, and at a biologically reasonable rate only for strong coupling strengths. Furthermore, it appears that hopping, rather than walking, is the most attractive stable configuration available to the inhibitory ring network.

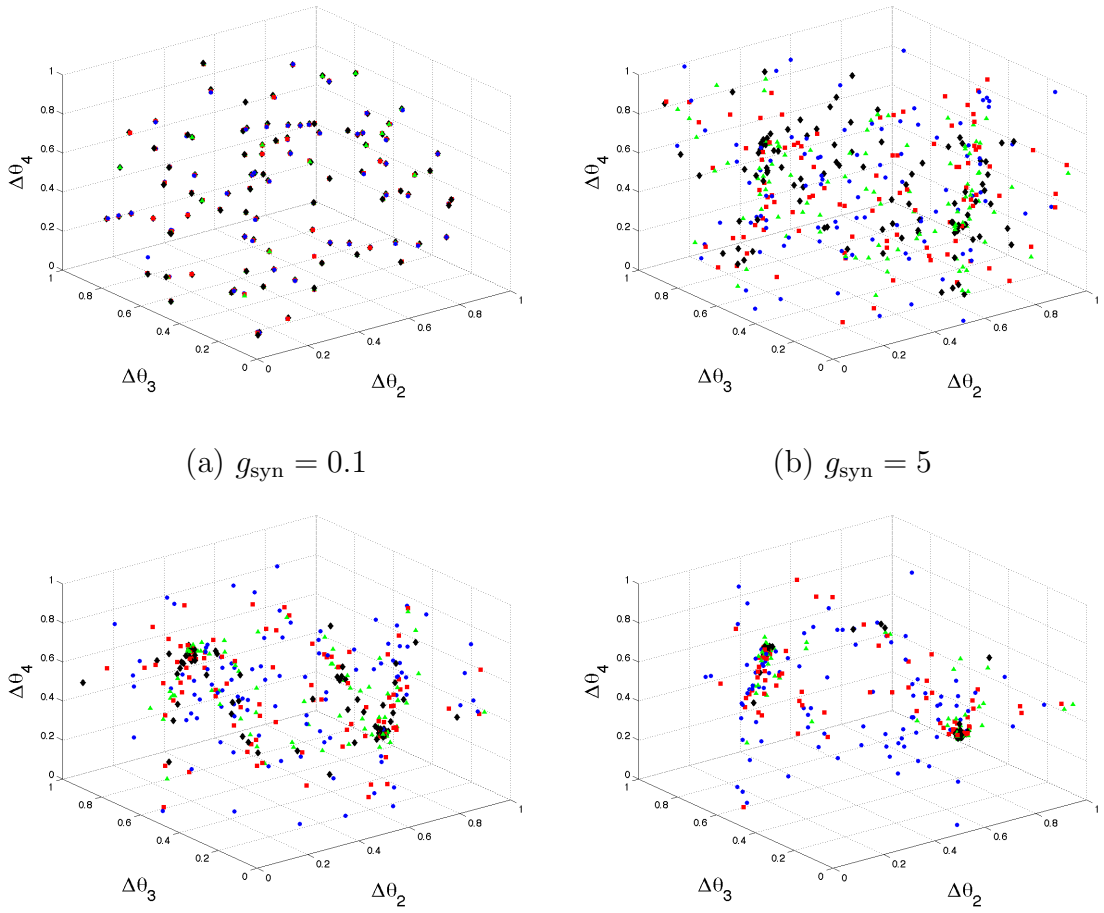

(a) $g_{\text{syn}} = 0.1$ (b) $g_{\text{syn}} = 5$

(c) $g_{\text{syn}} = 10$ (d) $g_{\text{syn}} = 20$

Figure 2.8: Relative phasing of bursts in 4-IR model.

4-CE and 4-IRCE Models

The 4-CE and 4-IRCE models are very similar, differing only by four synapses that provide reciprocal flexor-flexor and extensor-extensor inhibition in the 4-IRCE model. It is evident by inspection that the models have two biologically meaningful potentially stable phase configurations: synchrony and walking. We check the existence and strength of attraction of the models' potentially stable phase configurations according to the same protocol as for the 4-IR model.

'Weak' coupling

For given g^i_{syn} (inhibition) and g^e_{syn} (excitation) values, the 4-CE and the 4-IRCE model had convergence behaviors similar to those of the RGK and EP models at the same levels of inhibition and excitation. That is, the rate of convergence to synchrony in excitatorily coupled pairs in the four-cell networks were similar to that of the EP model for a given g^e_{syn} value; the analogous statement for the convergence of inhibitorily coupled pairs was also true. Excitation below $g^e_{\text{syn}} = 1$ and inhibition below $g^e_{\text{syn}} = 10$ were effectively weak.[11]

Figure 2.9 shows the behavior of the 4-CE model at representative combinations of weak excitation and inhibition; figure 2.10 shows the behavior of the 4-IRCE model for the same values of g^e_{syn} and g^i_{syn}. The figures are virtually indistinguishable; the models' convergence behavior at any given combination of weak coupling strengths is essentially identical. The extra inhibition present in the 4-IRCE model has no noticeable effect.

[11] Weak in terms of achieving biologically reasonable convergence rates. This is a different use of the terminology 'weak' and 'strong' than the earlier comparison to the magnitude of the I_{Na} spiking current.

For the weakest levels of g^i_{syn} and g^e_{syn}, the models' relative phases change little over the course of the simulations (figures 2.9 (a), 2.10 (a)), behavior also seen in the RGK, EP, and 4-IR models (*cf.* figures 2.3 (a), (b), (c); 2.6 (a), (b), (c); and 2.8 (a)). As either of g^i_{syn} or g^e_{syn} is increased, there is noticeable movement of the models' relative phases from earlier to later burst cycles, but the models do not settle into stable configurations (figures 2.9 (b), (c), (d) and 2.10 (b), (c), (d)).

At relatively weak levels of inhibition but stronger excitation, *i.e.* $g^i_{\text{syn}} = 1, 5; g^e_{\text{syn}} = 1, 5$, the models converge fairly rapidly to contralateral flexor-extensor synchrony. This is seen in subplots (e) and (f) of figures 2.9 and 2.10. The models' neurons' phases align along the line $\Delta\theta_4 \approx 0 \mod 1, \Delta\theta_2 + \Delta\theta_3 \approx 0 \mod 1$. Since the phase differences are measured with respect to neuron 1, these relations imply that the phase difference between neuron 2 and neuron 3 is approximately 0. Thus neurons 1 and 4 are synchronized, and 2 and 3 are synchronized, but the relative phasing is uniformly distributed between 0 and 1. The lack of clustering along the $\Delta\theta_2 + \Delta\theta_3 \approx 0 \mod 1$ line indicates that the synchronization due to excitation does not help the ipsilateral neuron pairs antisynchronize. That is, the effects of excitation and inhibition are more or less independent of one another at these lower coupling strengths.

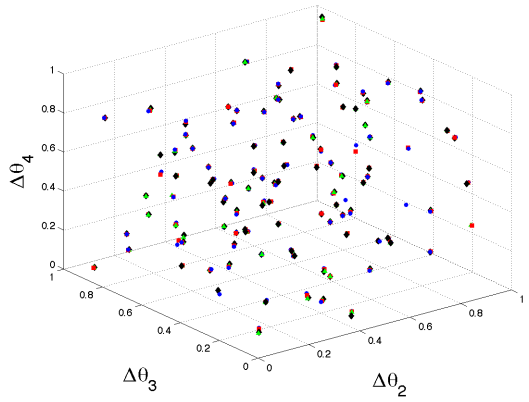

(a) $g^i_{\text{syn}} = 0.1, g^e_{\text{syn}} = 0.01$

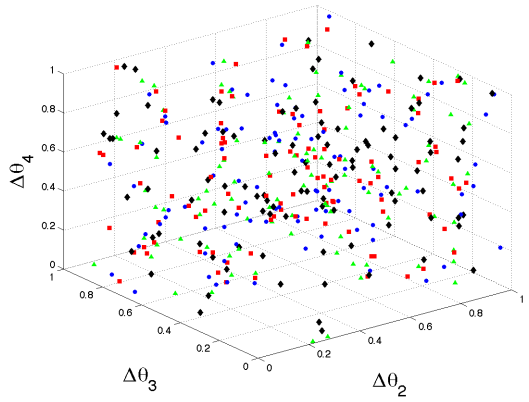

(b) $g^i_{\text{syn}} = 0.1, g^e_{\text{syn}} = 0.1$

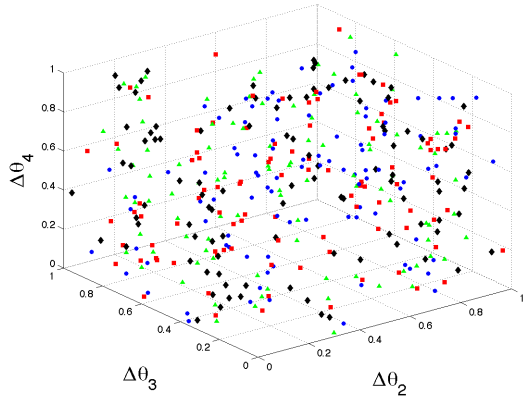

(c) $g^i_{\text{syn}} = 1, g^e_{\text{syn}} = 0.01$

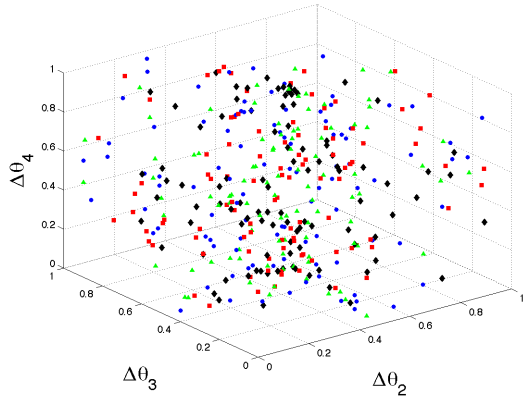

(d) $g^i_{\text{syn}} = 5, g^e_{\text{syn}} = 0.1$

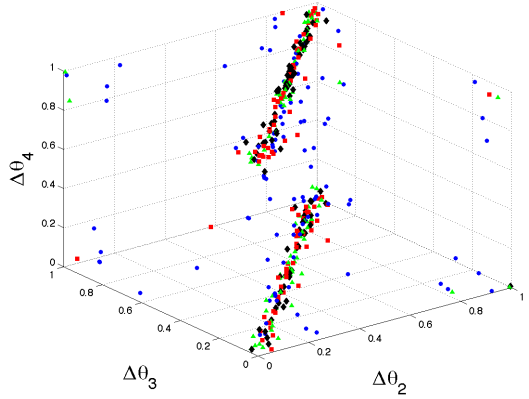

(e) $g^i_{\text{syn}} = 1, g^e_{\text{syn}} = 1$

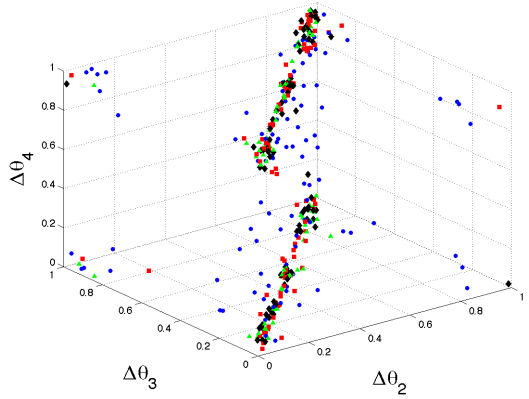

(f) $g^i_{\text{syn}} = 5, g^e_{\text{syn}} = 1$

Figure 2.9: Relative phasing of bursts in 4-CE model for weak coupling strengths.

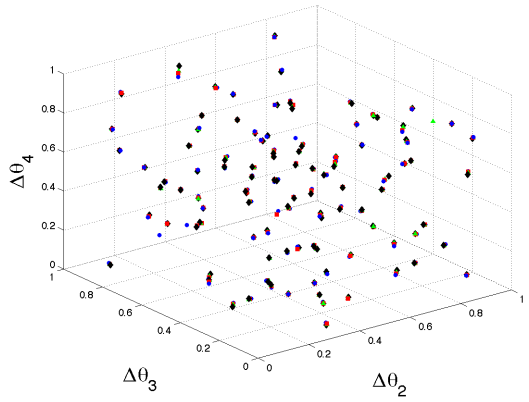

(a) $g^i_{\text{syn}} = 0.1, g^e_{\text{syn}} = 0.01$

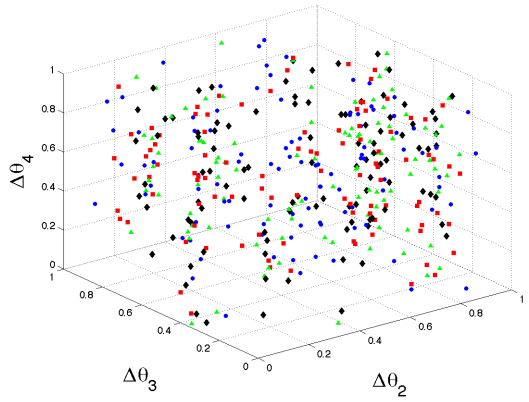

(b) $g^i_{\text{syn}} = 0.1, g^e_{\text{syn}} = 0.1$

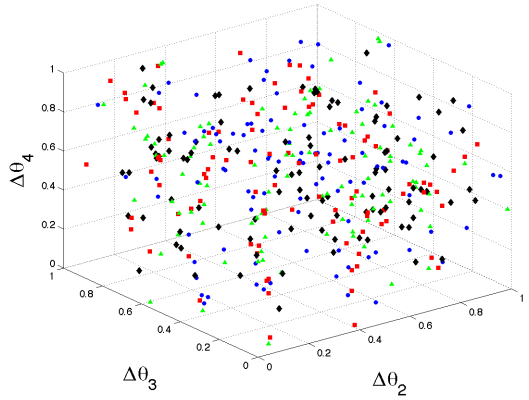

(c) $g^i_{\text{syn}} = 1, g^e_{\text{syn}} = 0.01$

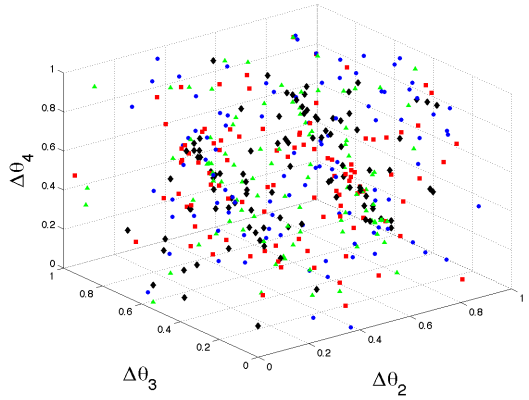

(d) $g^i_{\text{syn}} = 5, g^e_{\text{syn}} = 0.1$

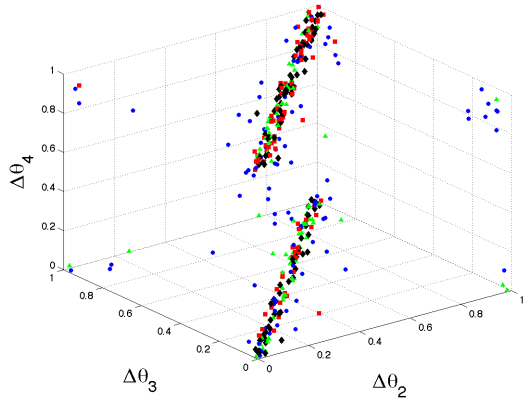

(e) $g^i_{\text{syn}} = 1, g^e_{\text{syn}} = 1$

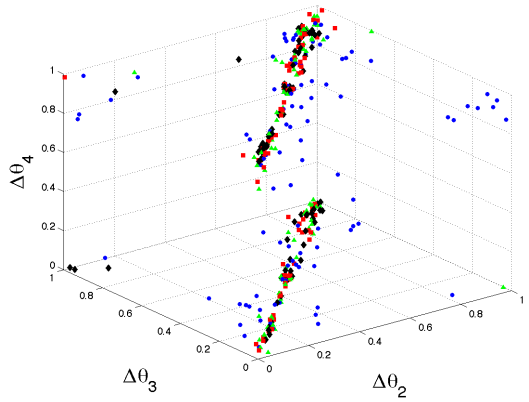

(f) $g^i_{\text{syn}} = 5, g^e_{\text{syn}} = 1$

Figure 2.10: Relative phasing of bursts in 4-IRCE model for weak coupling strengths.

'Strong' coupling

At higher levels of g^i_{syn} and g^e_{syn}, just as for lower levels, the convergence behaviors of the 4-CE and 4-IRCE models were very similar; the evolution of relative phases in the models for representative combinations of inhibition and excitation are shown in figures 2.11 and 2.12.

For moderate inhibition and very strong excitation ($g^i_{\text{syn}} = 5, g^e_{\text{syn}} = 5$, figures 2.11 (a) and 2.12 (a)), the relative phases immediately align along $\Delta\theta_4 \approx 0 \mod 1, \Delta\theta_2 + \Delta\theta_3 \approx 0 \mod 1$. Once on this line, however, the relative phases do not move far from their positions after the first or second burst cycles. With stronger inhibition and weaker, but still strong excitation ($g^i_{\text{syn}} = 10, g^e_{\text{syn}} = 1$, figures 2.11 (c) and 2.12 (c)), the relative phases also align along the contralateral flexor-extensor synchrony axis, but at a slower rate. Once on the line, the relative phases continue to move, so that by the eighth burst cycle some clustering is evident near the walking phase configuration.

For stronger inhibition and moderate excitation ($g^i_{\text{syn}} = 10$ and $20, g^e_{\text{syn}} = 0.1$, figures 2.11 (b), (d) and 2.12 (b), (d)), the models' relative phases do not move as rapidly towards contralateral flexor-extensor synchrony. Instead, the relatively stronger inhibition first draws the phases towards the line of ipsilateral flexor-extensor alternation: $\Delta\theta_2 \approx 0.5, \Delta\theta_3 - \Delta\theta_4 \approx 0.5 \mod 1$. Once on this line, the phases begin to converge towards the walking configuration, doing so more rapidly for stronger excitation. (Note that the effect of the additional inhibitory synapses in the 4-IRCE model is weak, but noticeable at these coupling strengths, *cf.* 2.11 (d), 2.12 (d), 2.9 (c) and 2.10 (c).)

The walking configuration is reached fairly rapidly from every initial condition for $g^i_{\text{syn}} = 20, g^e_{\text{syn}} = 1$ (figures 2.11 (e) and 2.12 (e)). Within 3–5 cycles, both

models' phases cluster quite close to $\Delta\theta_2 = \Delta\theta_3 = 0.5, \Delta\theta_4 = 0$. When excitation is increased, however, the convergence slows considerably. The phases first align along the contralateral flexor-extensor synchrony axis, then move towards the walking configuration, which is reached only after 7 or 8 cycles, rather than 3–5 (figures 2.11 (f) and 2.12 (f)).

The differences in convergence seen in the models at various combinations of strong coupling can be understood in terms of the relative 'phasing speeds' of inhibition and excitation and competition between the two types of coupling. Inhibition acts more slowly than excitation: even at the highest levels of inhibition, the antiphase configuration is reached only after 2-3 cycles, whereas strong excitation can cause neurons to synchronize within 1-2 cycles. Once excitation has synchronized two neurons, inhibition must move both of them towards antiphase (relative to a third neuron) simultaneously. The synchronized pair may effectively act like a single, 'heavier' neuron that is more intransigent and less responsive to the 'pushes' that inhibition imparts to it than individual, unsynchronized neurons would be at the same coupling strengths. If, for example, the contralateral flexor-extensor pairs are synchronized but the ipsilateral flexor-extensor pairs are not anti-synchronized, then inhibition on either side may actually work against inhibition on the other, depending on the relative phasing of the contralateral pairs. Conversely, if the ipsilateral neurons are already set in the antiphase configuration by inhibition, this impedes the contralateral synchronization activity of excitation, which may have to disrupt the antiphase configurations on each side in order to synchronize flexors and extensor on opposite sides. Just as excitation opposes the disruption of synchrony by inhibition in the other situation, inhibition opposes the disruption of antisynchrony by excitation in this case. Thus too much excitation relative to inhibition, and vice versa, may slow the models' approach to the walk-

ing configuration. There is an optimal balance of inhibition and excitation around $g^i_{\text{syn}} = 20, g^e_{\text{syn}} = 1$.

Before turning to a review and discussion of the modeling efforts and computational results presented in this chapter, we note that output and phase sensitivity seen in the reduced models is also reproducible in the full model for a wide range of comparable synaptic weightings. The behavior of the 4-IR model is easily reproduced by setting all synaptic strengths to zero except for ipsilateral RGN-RGN flexor-extensor inhibition, ipsilateral RGN-MN excitation, ipsilateral RGN-CIN excitation, and contralateral CIN-RGN inhibition. Substituting the contralateral CIN-RGN weak excitation for contralateral CIN-RGN inhibition reproduces 4-CE model behavior; the 4-IRCE model can be reproduced by including both of these sets of synapses. This is to be expected, since the MNs and CINs in their current formulations are equipped with limited intrinsic properties. They essentially act as passive conduits (possibly amplifiers), propagating the endogenously generated bursts of the RGNs that serve as the rhythmic drivers at the heart of both the full and reduced models.

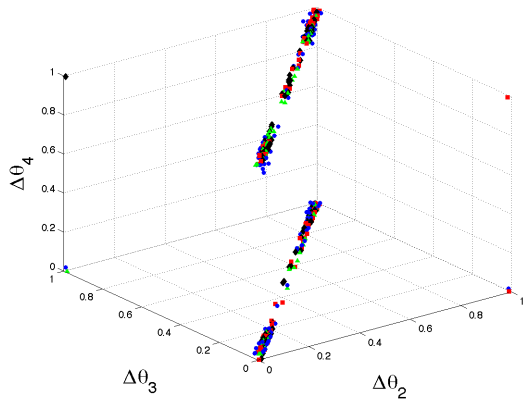

(a) $g^i_{\text{syn}} = 5, g^e_{\text{syn}} = 5$

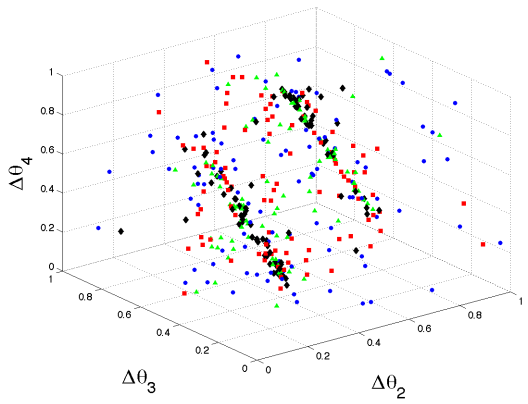

(b) $g^i_{\text{syn}} = 10, g^e_{\text{syn}} = 0.1$

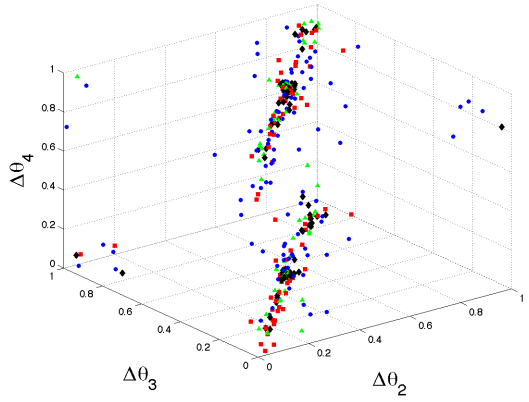

(c) $g^i_{\text{syn}} = 10, g^e_{\text{syn}} = 1$

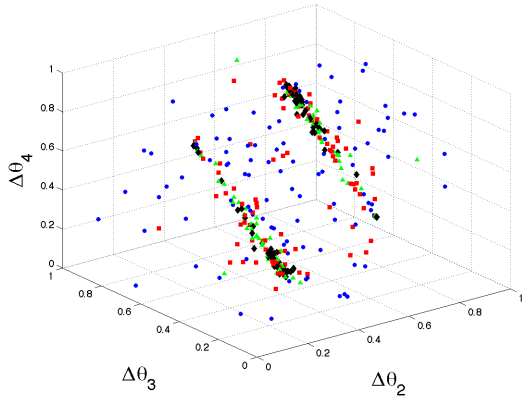

(d) $g^i_{\text{syn}} = 20, g^e_{\text{syn}} = 0.1$

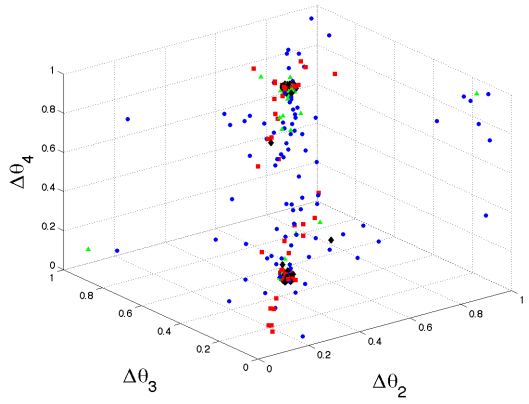

(e) $g^i_{\text{syn}} = 20, g^e_{\text{syn}} = 1$

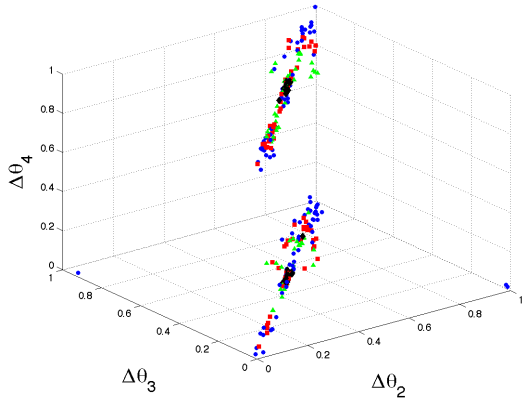

(f) $g^i_{\text{syn}} = 20, g^e_{\text{syn}} = 5$

Figure 2.11: Relative phasing of bursts in 4-CE model for strong coupling strengths.

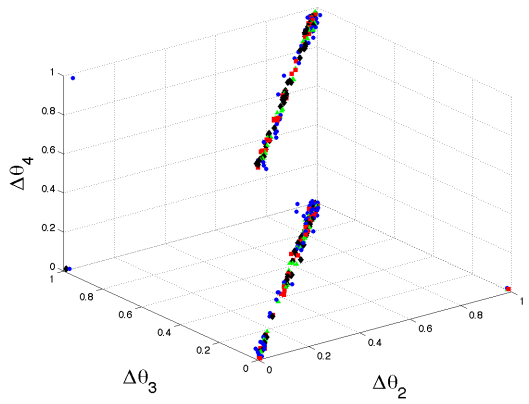

(a) $g^i_{\text{syn}} = 5, g^e_{\text{syn}} = 5$

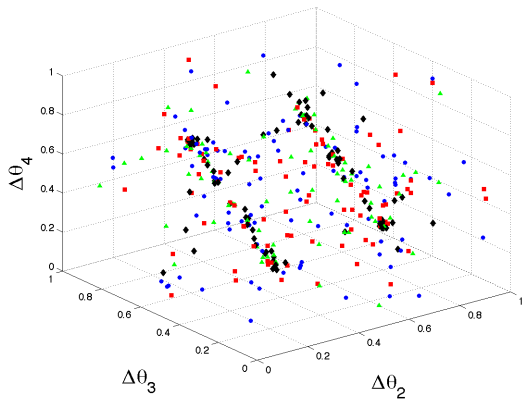

(b) $g^i_{\text{syn}} = 10, g^e_{\text{syn}} = 0.1$

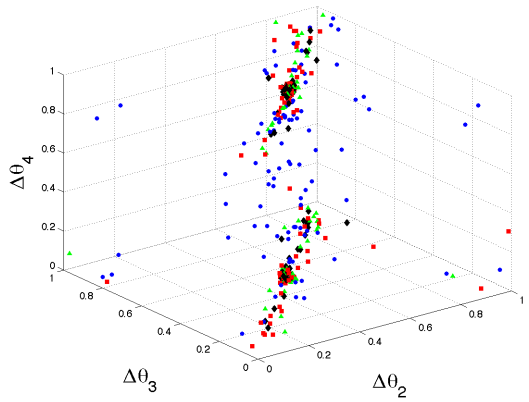

(c) $g^i_{\text{syn}} = 10, g^e_{\text{syn}} = 1$

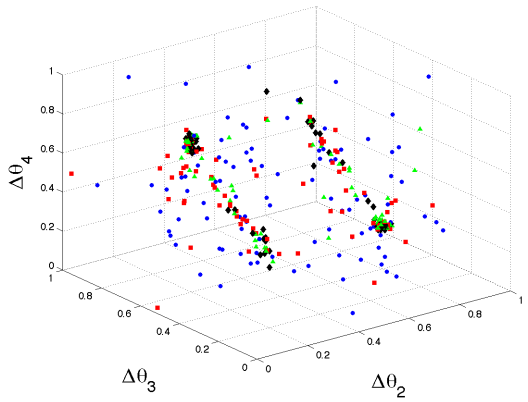

(d) $g^i_{\text{syn}} = 20, g^e_{\text{syn}} = 0.1$

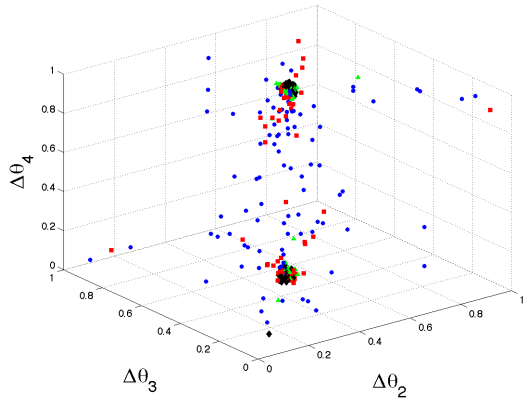

(e) $g^i_{\text{syn}} = 20, g^e_{\text{syn}} = 1$

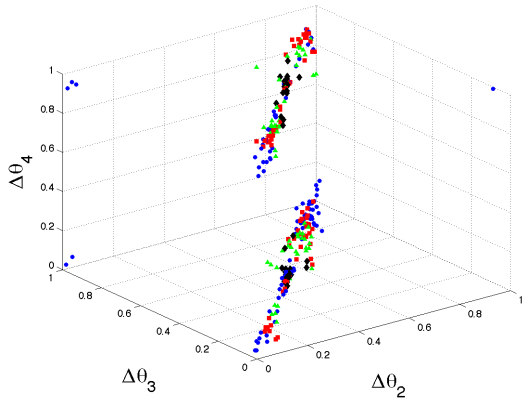

(f) $g^i_{\text{syn}} = 20, g^e_{\text{syn}} = 5$

Figure 2.12: Relative phasing of bursts in 4-IRCE model for strong coupling strengths.

2.6 Discussion

This chapter described the design and testing of the first mathematical model of the rodent spinal hindlimb locomotor CPG. Its development involved three stages: a thorough survey of the relevant biological and modeling literature; careful articulation of the goals, underlying assumptions, and testing criteria for the model; and the assembly of well-studied, biophysically realistic, 'off-the-shelf' neuronal and synaptic components into a network architecture such that the resulting model conformed to explicit ansätze.

The basic goal of the initial model was to reproduce the fundamental locomotor rhythm, *viz.* ipsilateral alternation between flexor and extensor bursts simultaneous with contralateral synchronization of flexor and extensor bursts. The evaluation criteria for the model reflected the biological requirement of rapid recovery to the fundamental locomotor rhythm after perturbation. The CPG model's performance was tested through computational experiments using smaller models derived from the full CPG model; the derived models isolated particular features of the network architecture for examination and comparison across a range of coupling strengths.

Our computational studies reveal that the CPG model is surprisingly sensitive to initial phasing conditions. Viewed from a biological perspective, some of the sequences of intermediate, transient states that the model moves through as in reaching its final stable configuration may be detrimental. Relatively strong excitation and inhibition are required to bring the model to a walking configuration with biologically acceptable rapidity. Inhibition alone induces a hopping configuration, while too strong excitation impedes the model's convergence to the walking configuration. There appears to be an optimal combination of strong inhibition and moderately strong excitation that leads reliably to the walking configuration, but the rate of convergence of the model is not as fast as one would like.

Thus, though we have shown that the model is capable of producing the fundamental locomotor rhythm, issues of stability, transient behavior, and phase resetting in response to perturbation remain to be addressed. The model needs further refinement and expansion; below we enumerate some of the questions posed by the model that invite further biological experimentation and additional modeling work.

Experimental questions

The model's biological realism will improve as more experimental data are collected and incorporated into it. The current model suggests a number of issues of particular relevance for designing future laboratory experiments.

First, the different roles of excitation and inhibition require further exploration. The model requires strong inhibition and strong excitation; any experimental indication of the effective strength of synaptic coupling in the RSHL CPG would be of great interest. Similarly, the effects of inhibition and excitation were seen to have different relative 'speeds' in terms of establishing certain phase configurations; one set of experiments that might be illuminating in this regard would be to selectively block and/or slowly degrade inhibition or excitation (in the whole cord or isolated segments) during fictive locomotion and observe the changes in the rhythm. Determining the appropriateness of ansatz 5, *viz.* the role of gap junctions and synaptic adaptation, is also important.

Second, the half-center endogenous burster configuration is central to the architecture of the initial model (ansatz 10, as the presumption of symmetry in flexor-extensor connectivity (ansatz 6). Although these ansätze are not ruled out by the available biological data, neither are they directly supported by specific experiments. Additional anatomical and imaging studies could shed light on the

suitability of these ansätze, and their contradiction would lead to model revisions likely to produce substantially different behaviors.

Third, the focus on Hb9 interneurons and the $I_{\mathrm{Na(P)}}$ current strongly affects the construction of the CPG model. Further biological investigation of the function of Hb9 interneurons in the RSHL CPG and the role of $I_{\mathrm{Na(P)}}$ in bursting is needed. The parameters and structure of the RGN model may require significant revision as evidence for the rhythmogenic importance of other cell types and other currents becomes available. Furthermore, the present MN and CIN models are sorely lacking in detail and contribute little to the behavior of the current CPG model. More information about these cells' electrophysiological properties are needed to improve the model so that their roles can be studied.

Modeling questions

In addition to reproducing essential features of the biological RSHL CPG, the CPG model is intended to illuminate aspects of bursting and phasing in neuronal networks that are interesting from a mathematical and computational standpoint. The behavior of the present model suggests several topics of interest from a modeling perspective, independent of their relation to the specific biology of the RSHL CPG.

First, and still related to biological issues, is the difference made by using an endogenously bursting versus tonically spiking neuron model in the half-center oscillator subnetwork that forms the rhythmogenic kernel. Changing this setup may produce very different convergence and frequency control properties [206, 191, 195]. Alternative models might replace the endogenously bursting RGNs of the RGK with tonically spiking neurons to produce alternating bursts via standard mechanisms (intrinsic or synaptic escape and release); neuronal models that are

quiescent but easily excited to transient bursting could also replace passive CINs and MNs.

Second, the sensitivity and transient behavior of the model does not conform to intuitions from phase oscillator models, a particularly intriguing discrepancy. The non-smooth phase responses of interacting bursting neurons, leader-follower switching, and changes in spike number, are some of the unexpected phenomena encountered in this CPG model. Additional modeling and analysis must be done to resolve whether such features as are specific to this particular choice of neuronal model, or are instead more generic properties of models for endogenously bursting neurons.

A third, somewhat overlapping question is what role the nature of the slow current plays in determining the phase response behavior of the bursting neuron when coupled. In particular, $I_{\mathrm{Na(P)}}$ may be modeled as an additional membrane current, as in pre-Bötzinger model I [24, 192], or as an alternative activation state of the spiking Na^+ current [213, 43]. If either form produces bursting behavior, qualitative differences in the phase response characteristics associated with the different $I_{\mathrm{Na(P)}}$ forms may make one form preferable to the other; it may also have more general implications for the importance of membrane current models in shaping cellular models' phase response characteristics.

Fourth, the need for strong coupling and the competition between excitation and inhibition seen in the 4-CE and 4-IRCE models may be worthy of further exploration. Few modeling studies have investigated the behavior of individual neurons receiving both excitatory and inhibitory inputs; most studies incorporating excitation and inhibition consider large populations of (sparsely) connected neurons [232, 223, 19, 228]. Revisions of the CPG model that replace single neuron representatives with heterogeneous populations of neurons may not exhibit such

behavior. Previous studies have reported the greater robustness of population models [25, 112, 227] and the problems associated with building single-neuron, conductance-based models to reproduce average population properties [86], but the issues associated with ansatz 4 have not been explored in depth. Further investigation of CPG models based on populations of neurons is needed to determine the appropriateness of network models that represent collections of many cells by a single neuron.

Fifth, and finally, the computational requirements for investigating the CPG models proposed in this chapter, even the reduced models with two or four cells, are quite steep. The amount of processing time needed for simulation and data processing make detailed, comprehensive sweeps through the space of coupling strengths and intrinsic parameter values infeasible. There is clearly a need to develop more efficient and effective methods for studying the phasing behavior of intermediate-sized, biophysically detailed CPG models.

The work presented in this chapter contributes to effective modeling of the RSHL CPG in two ways: by establishing a framework for creating and evaluating models, and by offering an initial model as a point of departure. The careful evaluation of available modeling approaches, explicit listing of assumptions, and proposal of biologically relevant testing criteria lay the conceptual basis for a strategy to produce several generations of useful CPG models. While the performance of the initial RSHL CPG model may be viewed as somewhat negative *vis-à-vis* our modeling ansätze, the results are suggestive. The model's surprising features raise questions that prompt further investigation through modeling and biological experimentation. Several of these issues are explored in the subsequent chapters of this thesis.

CHAPTER 3

BURST PHASE RESPONSE: EMPIRICAL STUDIES

3.1 Introduction

The bursting neurons in the model locomotor CPG of the previous chapter behaved surprisingly when coupled together in various network configurations. In particular, their high degree of sensitivity to initial phasing conditions — as seen, for example, in their transient behavior as they approached antiphase when coupled in a half-center oscillator configuration — was unexpected. As the neurons interacted via spikes, the relative phasing of their bursts shifted unpredictably, not following a monotonic path to their final configurations.

Mathematical investigation of burst phasing has primarily used the standard tools of phase response curves [34]. These PRC analyses assume that the internal structure of the burst, that is, the intraburst interspike timing, is not important in determining the shift of burst timing as bursters interact, and that the lengths of the active segments of bursts are either unaltered or altered instantaneously as the neurons interact [162, 165]. The phase response of a bursting neuron is treated by considering the active segment of the burst as a single, opaque unit, and the mechanism of interaction of the bursts is not considered in detail. Current applications of PRCs to predict burst phasing ignore multiple time-scale effects in bursting and do not treat the issue of transient burst phase configurations. The prediction of final, stable phase configurations for various network architectures is the main goal of these analyses.

PRC theory has developed primarily in the context of phase oscillator models and weakly coupled networks, modeling frameworks that eschew biophysical realism for mathematical tractability. Applications have focused on spiking oscillators,

and mathematical results can typically be proven to hold only for small perturbations. There has been little exploration of the mathematical issues involved in extending PRC theory to multiple time-scale systems and large perturbation regimes. Furthermore, claims of the theory's broad applicability and biological relevance depend implicitly on four sets of assumptions: (1) Theoretical results for phase oscillators and other schematic models transfer directly to biophysically detailed models. (2) The shapes of perturbations make little difference in determining the shapes of the PRCs. (3) PRCs scale linearly with perturbation strength; excitation and inhibition are equivalent modulo a sign change; and the weak regime is the biologically relevant range of perturbation strengths. (4) Conclusions drawn for spiking neural oscillators apply to bursting neural models.

These assumptions may be plausible, but their validity must be checked. In light of the previous chapter's modeling results for coupled bursting neurons, the lack of rigorous confirmation is a worrisome methodological lacuna that makes applying standard PRC analyses to interacting bursting neurons somewhat dubious.

In this chapter, we make a first step in addressing these issues by investigating the basic question of how bursting neurons respond to synaptic inputs corresponding to single pre-synaptic spikes. We consider several models of endogenously bursting neurons, both schematic and biophysically accurate, and we subject them to different kinds of synaptic inputs having biologically realistic forms. We describe the resulting phase response curves and compare them with the mathematical idealizations commonly used in modeling and mathematical studies of neuronal networks. We then evaluate the assumptions enumerated above based on our empirical results.

3.2 Methods

3.2.1 Models

We examined five models of bursting neurons: Hindmarsh-Rose (HR) [117], pre-Bötzinger (PB) [24], R15 *Aplysia* ganglion interneuron (R15A) [187], and isolated pyloric dilator (PD) [208] and anterior burster (AB) [100] neurons of the lobster stomatogastric ganglion. Each model except for HR is a biophysically realistic conductance-based (Hodgkin-Huxley style) model of an experimentally identified neuron, with currents and parameter values that correspond to those found experimentally. Each model has a single compartment, with the exception of the two-compartment PD model, which has separate compartments for axon and soma. The models' phase spaces range in size from 3 to 15 dimensions. Complete descriptions of the models, including their parameter values and characteristics of their stereotypical bursts and spikes, are given in Appendix B.

3.2.2 Numerical Methods

Except for locating some periodic orbits, all calculations were performed with PyDSTool, a software package written in C and Python for the simulation and analysis of dynamical systems [44]. The integrators used were a variable time-step fifth-order Runge-Kutta solver (Dormand-Prince-853, [107]) with eighth-order dense output for the non-stiff systems (HR, AB) and a fifth-order variable-time step implicit solver with eighth-order dense output (Radau5, [108]) for stiff systems (R15, PB, PD). The relative and absolute error tolerances were 10^{-12} for both solvers.[1]

[1]The maximum accuracy for the Dormand-Prince-853 and Radau5 solvers is 10^{-13} using double precision IEEE floating point arithmetic [107, 108].

Phenomena of interest, such as spike peaks or the onset of the active segment of the burst cycle (described below), were defined by zeros of 'event' functions, and corresponded mathematically to local extrema or particular target values for given phase space variables. Events were detected during integration by testing for zero crossings of the event functions at each time step. The location of any zero crossing found during a particular time step was then refined within that time step via bisection, using the dense output of the integrator, so that events were located within an accuracy of 10^{-9}.

Periodic orbits corresponding to a complete burst oscillation were either found using multiple shooting with automatic differentiation [103], as implemented in the ADMC++ automatic differentiation package for MATLAB [168], or with a single-shooting algorithm implemented in PyDSTool. The latter method uses Newton's method to locate the zero of $P(\mathbf{x})-\mathbf{x}$, where $P(x)$ is the return map to a hyperplane H transverse to the periodic orbit. H was defined by a value of the membrane voltage that was chosen to lie in the quiescent segment of the periodic orbit. Both methods produced initial conditions close to the true periodic orbit, with error less than 10^{-9}.

3.2.3 Spike and Burst Definitions

For each neuron model, we start from initial conditions at time $t = 0$ that lie on a periodic orbit Γ representing a burst cycle having period T. We call the unperturbed periodic orbit Γ the *reference burst* or *reference orbit*. A gallery showing reference orbits for each of the models is found in figure C.1 of appendix B.

We identify *spike peaks* as local maxima of the membrane voltage variable V ($\dot{V} = 0$, $\ddot{V} < 0$) with $V \geq V_{\text{thresh}}$, a threshold value. (We refer to local maxima of

V with $V < V_{\text{thresh}}$ as peaks of *pseudospikes*.) The *spike position* or *spike time* t_i is defined as the time at which the ith spike of the burst achieves its peak. Note that each spike peak in the burst is preceded and followed by local minima of V. For each spike other than the first and last of the burst, we refer to these minima as the starting and ending *troughs* of the spike, and we refer to their respective times as the start and end times of the spike (t_i^{start} and t_i^{end}, respectively). For the first spike, we take the trough following its peak to be its ending trough, and we take the first point preceding its peak that has the same voltage value as the ending trough to be its starting trough; the corresponding times are the start and end times of that spike. The start and end troughs and times for the last spike are defined similarly. We define the base voltage of the spike to be the lower of the voltage values of its starting and ending troughs. The spike *height* is the difference between the voltage at the spike peak and the base voltage. The spike *base-width* is the difference between the end and start times of the spike. The spike *half-height* is the base voltage plus one half the spike height; the spike *half-width* is the difference in the two times at which the spike achieves its half-height.

We chose the third spike of the reference burst of each model as the *stereotypical spike* for that model. The numerically calculated voltage profile between the spike start and spike end for each model's stereotypical spike was saved for later use in calculating the spike injection PRC, and is referred to as $V_{\text{spike}}(t)$ defined over any interval of length $t_3^{end} - t_3^{start}$. Our results were not sensitive to the use of other spikes from the bursts as stereotypical spikes, although the first and last spikes of a burst are the least likely to be good candidates as they are associated with strong transient changes in the neuron.

We identify two special phase space variables in each neuron model: V, representing the membrane voltage (in the multicompartment PD model, $V = V_a$,

the axonal membrane voltage), and ζ, a 'recovery' variable. Bursting phenomena commonly depend on the oscillation of the recovery variable on a time-scale much slower than the time-scales of the variables responsible for spiking currents [125]. For example, when ζ is high enough, the basal membrane voltage is high enough for the neuron to spike, but spiking activity lowers the value of ζ until the basal membrane voltage drops below the threshold for spiking to occur, and spiking ceases. During the subsequent quiescent period, the level of ζ increases until the threshold for spiking activity is reached again, and the bursting cycle repeats.

For each neuron model, we choose one slow phase space variable to play the role of ζ, and we use its value over one periodic orbit to separate the orbit into two segments, an *active* segment, during which spiking occurs, and a *quiescent* segment, during which there are no spikes. The correspondence between ζ and the activation variables in specific models is shown in Table B.1 in Appendix B.

For simplicity of explanation, let us first assume that over the course of Γ, $\dot{\zeta} = 0$ exactly twice, at points ζ_A and ζ_B, corresponding to minimum and maximum values of ζ on Γ (not necessarily respectively). Suppose these occur at times t_A and t_B, respectively, and furthermore, $t_A < t_B$. Also suppose that all spikes in the cycle occur at times $t_i : t_A \leq t_i \leq t_B$. We term models for which we can choose ζ so that this is the case *simple* bursters (HR, AB). Then we label the segment of Γ corresponding to $[t_A, t_B]$ as the *active* segment, and the remainder of Γ as the *quiescent* segment. Given this arrangement, we choose ζ_A as our initial conditions, and set $t_A = 0$, redefining t_B accordingly.

We refer to t_B/T as the *duty cycle* of the neuron model. If ζ_A is a local minimum, we call the model an *ascending* burster, otherwise we call it a *descending* burster.

For some models (PB, PD, R15A), $\dot{\zeta} = 0$ several times over the course of Γ, so that there are multiple local maxima and minima of ζ in one cycle (*non-simple*

bursters). In this case, we select $\zeta_{\min}$ to be the smallest local minimum of ζ, and $\zeta_{\max}$ to be the greatest local maximum of ζ, and set $t_{\zeta_{\min}}$, $t_{\zeta_{\max}}$ accordingly. If $t_{\zeta_{\min}} < t_{\zeta_{\max}}$, we set $\zeta_A = \zeta_{\min}$, $\zeta_B = \zeta_{\max}$, $t_A = t_{\zeta_{\min}}$, $t_B = t_{\zeta_{\max}}$, as for the *ascending* case above. The *descending* case ($t_{\zeta_{\max}} < t_{\zeta_{\min}}$), is handled analogously. For each of the non-simple bursters, the times of all local extrema of ζ lie between t_A and t_B.

Table B.1 of appendix B lists the slow variable chosen as ζ and the burster type for each model.

3.2.4 Burst Phase Response Curves

Burst phase response curves record the shift in the timing of the onset of the active segment of a neuron's next burst cycle due to perturbation at a particular phase of the its current burst cycle. This approximates the change in burst timing caused by a single incoming spike from a pre-synaptic neuron. We calculated burst phase response curves for our five models using two different methods.

Linear Method

For any stable periodic orbit Γ, having period T, of a dynamical system, such as a burst cycle in one of our neural models, we can define the phase response of Γ to an infinitesimal, instantaneous perturbation. Following [95], we note that if an input pulse I is applied to the system at the point $x(t) \in \Gamma$, then there exists exactly one point $x(t') \in \Gamma$, with $t' \in [0, T]$, such that $x(t)+I$ and $x(t')$ lie on the same isochron. We can therefore define the phase response at t as $G(t, I) = (t' - t)/T$. The phase response curve for Γ for a given perturbation strength I is then $\{G(t, I) : t \in [0, T]\}$. The perturbation I could be in any direction in the phase space of the dynamical system, but we consider only perturbations in the V component, which correspond

to membrane voltage perturbations and are biologically most relevant.[2]

The PRC method sketched above, known as the adjoint method [74], predicts the phase response of the orbit in the full dynamical system from the system's linearization about Γ. Inferences about the response of the full system to non-infinitesimal perturbations using PRCs calculated with the adjoint method implicitly assume that the phase response scales linearly with perturbation strength. For these reasons, we refer to PRCs calculated with these methods as *linear* PRCs.

We used the PyCont component of PyDSTool, which provides an interface to routines in AUTO [65], to calculate linear PRCs for each model, following the numerical implementation of the adjoint method in [95]. The linear PRCs calculated this way correspond to infinitesimal excitatory perturbations; inhibitory linear PRCs are obtained by reflecting across the ϕ-axis.

The algorithmic parameters for AUTO were the same for each model: collocation points, 4; number of intervals, 500; maximum step size, 10^{-4}, initial step size, 10^{-6}; maximum number of steps, 15. The resolution of the PRCs was 2500 points. The exact location of each point on a PRC was determined automatically by continuation routines in AUTO, and the resulting curves were quite smooth. Note that the use of a continuation routine to find the adjoint PRC means that the calculated curve is for a slightly different parameter value of the continuation parameter (always the applied current) than for the model parameters used to generate the reference burst trajectory. However, the resulting PRC was always for a parameter value within 10^{-5} of the reference parameters, so the correspondence with the true PRC for the reference parameter model should be very close.

The linear PRCs for each model give the phase response in the limit of small

[2]For a more complete and very readable description of the mathematical method and numerical implementation of the adjoint PRC calculation, we refer the reader to Section 5 of [95]. The original method and its mathematical justification are found in Appendix 1 of [74] and Section 2 of [73].

perturbation, as contrasted with the direct PRC methods described in the next section.

Direct Methods

Two forms of 'direct' method were used to calculate phase response curves: in one case the input is a conductance pulse and in the other it is a synapse-mediated spike injection. In both cases, perturbations were applied at different times $t \in [0, T]$ to the model neuron on its periodic orbit Γ. The PRCs were calculated by perturbing at 300–500 time points, depending on the model, with 60% of the time points evenly spaced in the active segment of Γ and the remainder evenly spaced in the quiescent segment.

For a perturbation at time $t \in [0, T]$ (equivalently, at phase $\phi = t/T, \phi \in [0, 1]$) we define the *perturbation phase* as t/T. Let T' be the time of the onset of the subsequent burst cycle after the perturbation. We define the *phase difference* $\Delta\phi$ as $(T' - T)/T$. Negative $\Delta\phi$ means that the subsequent burst cycle started earlier than it would have in the absence of the perturbation (phase advance); positive $\Delta\phi$ means that the subsequent burst started later than normal (phase delay). We define the n-th order phase shift, $\Delta\phi_n$, to be the phase shift of the nth burst cycle following the burst cycle to which the perturbation was applied. We call the PRC formed by considering the set of n-th order phase shifts the n-th *asymptotic* phase response curve. The shapes of the n-th order asymptotic PRCs, in comparison to the shape of the (0-th order) PRC, provide a measure of the long term persistence of phase shifts.[3]

After perturbation, the trajectory of the model neuron reapproaches its original limit cycle, eventually getting close enough to be considered as having returned to

[3]Our definitions of phase difference and asymptotic phase difference are essentially identical to the corresponding definitions in [175].

the unperturbed limit cycle. In every case, regardless of model, perturbation type, or perturbation strength, the perturbed trajectory returned to the original limit cycle within three burst cycles.

In addition to computing the phase response, we computed the *spike number response curve* (SNRC) for each perturbation, which tallies the number of spikes in the perturbed burst for each phase ϕ at which it is perturbed. The n-th order SNRC counts the number of spikes in the n-th burst, so that the 0-th SNRC measures the change in spike number for the burst being perturbed, not the succeeding burst (*cf.* the 0-th order PRC). Differences in SNRC values from the spike number of the reference burst mean that the perturbation added or deleted spikes from burst, thus indicating large deviations from the original periodic orbit due to the perturbation.

In both direct methods, a synaptic current term I_{syn} was added to the equation for $\dot{V}$, so that the models' voltage equations had the form $C\dot{V} = -(\sum I_{\text{ionic}} + I_{\text{syn}})$. The I_{syn} term modeled the action of synaptic input to the bursting cell and took one of the two forms described below:

Spike injection

This form of the I_{syn} term modeled the activity of a synapse with graded release of neurotransmitter [61, 62], in the absence of any activity-modulated facilitation or depression.

$$I_{\text{syn}} = g_{\text{syn}} s (V - V_{\text{syn}}) \tag{3.1}$$

$$\dot{s} = \alpha_{\text{syn}} T_\infty(V_{\text{pre}})(1 - s) - \beta_{\text{syn}} s \tag{3.2}$$

$$T_\infty(V_{\text{pre}}) = (1 + \exp(-(V_{\text{pre}} - V_p)/K_p))^{-1} \tag{3.3}$$

Here s represents the level of neurotransmitter released into the synaptic cleft

and actively affecting the post-synaptic cell. The rate of neurotransmitter release is given by Equation 3.2, and depends on the concentration of neurotransmitter already released as well as the voltage of the presynaptic cell, *i.e.* the instantaneous strength of the incoming spike that constitutes the perturbation.

For each neuron model, the incoming spike was taken to be the voltage profile of the model's stereotypical spike $V_{\text{spike}}(t)$, aligned in time with the start of the perturbation. Prior to the time of perturbation, $g_{syn} = 0$ and $s = 0$. During the perturbation, the vector field defining the neuron model, including the synaptic input equations, was integrated with $V_{\text{pre}} = V_{\text{spike}}(t)$. If the numerical integration required voltage values for the stereotypical spike profile at times not given in the spike profile, these values were determined using linear interpolation.

The synaptic reversal potential V_{syn} determined whether the action of the synaptic input was excitatory or inhibitory. The excitatory and inhibitory values of V_{syn} for each model are given in Table B.6. The parameter values for the PB model synapse were taken from neurophysiological data for neonatal rat synapses [179] and corresponded to voltages at 0 and 88.32 percent of the total spike height for the PB model's stereotypical spike. In lieu of experimentally determined values for the other models, their V_{syn} values were chosen to lie at the same positions relative to their respective stereotypical spikes.

The half-activation point for the voltage-dependent neurotransmitter release, V_p, was taken from neurophysiological data for the PB model synapse and corresponded to a voltage at 55 percent of the total spike height for the stereotypical spike of that model. In lieu of experimentally determined values for the other models, their V_p values were chosen to lie at the same positions relative to their respective stereotypical spikes.

The response of the simulated synapse to the injected pre-synaptic action po-

tential spike was also sensitive to K_p, the steepness of the voltage response curve for neurotransmitter release, and the forward and backward rate constants for neurotransmitter release, α_{syn} and β_{syn}. These parameters were chosen to ensure that the response to an injected spike was relatively fast and decayed before the typical interspike interval elapsed. For each model, α_{syn} was set to 110/ISI, where ISI is the shortest interspike interval of the model's reference burst. β_{syn} was set to $0.1 \cdot \alpha_{\text{syn}}$. The parameter K_p was fixed at 4 for the PB model (as in [62]); its value for other models was chosen such that the ratio of the models' K_p values to the K_p value of the PB model equaled the ratio of the models' stereotypical spike heights to the stereotypical spike height of the PB model. These parameter choices ensured that the activation curves for the models over the voltage ranges of their reference bursts were essentially identical when appropriately normalized. Model-specific values V_p, K_p, α_{syn}, and β_{syn} are given in Tables B.7 and B.8.

Conductance pulse

This version of I_{syn} modeled synaptic input as a square pulse of synaptic conductance, or equivalently, as a synapse with instantaneous activation, saturation, and then reuptake of neurotransmitter. The synaptic current equation had the form

$$I_{\text{syn}} = g_{\text{syn}}(V - V_{\text{syn}}) \tag{3.4}$$

Perturbation by a square conductance pulse was simulated by setting the maximal synaptic conductance $g_{\text{syn}} = 0$ at all times before and after the perturbation. Two pulse durations were tried, one equal to the stereotypical spike base width, and the other equal to the stereotypical spike half-width. The values of V_{syn} used for excitation and inhibition were the same as those for the synapse mediated spike injection case.

For the conductance pulse, effective strength of the perturbation was determined by g_{syn} during the pulse and the pulse duration; these two parameters largely determined the total charge injected into the post-synaptic neuron during the perturbation. In the case of synapse-mediated spike injection, the total amount of charge injected into the post-synaptic neuron was also determined by the level of released neurotransmitter, *i.e.* it was proportional to the integral of s over the time course of a perturbation.

In order to facilitate comparison of the effects of different forms of I_{syn} on phase response, the perturbations were adjusted to roughly equalize the amount of charge injected by each synaptic form at a given perturbation level. For each choice of g_{syn} for the synapse mediated spike injection form of I_{syn}, the maximal conductances g'_{syn} for the conductance pulse synapses were scaled such that $g'_{\text{syn}} \cdot \Delta t = g_{\text{syn}} \cdot \int s$, where Δt is the duration of the conductance pulse and the integral on the right hand side is taken over the entire perturbation. The amount of injected charge depends on g_{syn} and $V_{\text{eff}} = V - V_{\text{syn}}$ over the duration of the perturbation, but given the rapid rise and decay of the synaptic activation variable for the spike injection synaptic form, differences in the instantaneous V_{eff} between synaptic forms could be neglected. The chosen scaling ensured that the magnitude of the perturbation, in terms of total charge injected, was approximately equal for each synapse model and pulse duration, for a given choice of g_{syn}. The scaling factors are given in Tables B.9 and B.10. The base-width conductance pulses had amplitudes roughly comparable to the maximum synaptic activation levels for spike-injection, while the half-width conductance pulses were typically much taller and shorter in duration.

PRCs were calculated for each model with each form of I_{syn} for g_{syn} values ranging over six orders of magnitude.[4] A large range of g_{syn} values was chosen

[4]The sizes of g_{syn} mentioned in this and subsequent paragraphs refer to the numerical value of g_{syn} for spike injection perturbations. The corresponding numerical values of g_{syn} for conductance pulse perturbations were scaled as explained in the previous paragraph.

because there is little experimental data on the appropriate maximal synaptic conductance strengths for the neural systems from which our neuron models were taken. Modeling studies typically take g_{syn} to be small, relative to the maximal conductances of the intrinsic membrane currents, but it is not clear whether this assumption is valid. Furthermore, network models which represent large clusters of neurons by a single representative also have to account for the fact that the synaptic input to the single neuron represents simultaneous input from many cells in the cluster, which may warrant using higher g_{syn} values.

The exact ranges for g_{syn} varied by model, as the maximum perturbation strength for which the perturbed differential equations remained stable enough to integrate depended on each model's equations and the scale chosen for its parameters and variables. The range of g_{syn} for which excitatory PRCs could be calculated was typically lower than the range for inhibition, primarily because of two issues. First, large excitatory inputs could destabilize the integrators, causing the numerical calculations to fail even when using the Radau5 stiff integrator. Second, excitation could send the system into a state of extended tonic spiking, effectively destroying bursting behavior and making the notion of burst phase response undefined. The g_{syn} ranges for excitation were chosen to avoid these problems.

We also calculated direct BPRCs for g_{syn} values as low as 10^{-12}, for comparison with the predictions of PRC theory for small perturbations. The resulting PRC curves are not shown, as they very closely resemble the curves for the lowest perturbation levels that are shown in Appendix C.

Table 3.1: Ranges of perturbation strengths

Model	**Excitatory** g_{syn}	**Inhibitory** g_{syn}
HR	10^{-4}–10	10^{-4}–10
PB	10^{-6}–10^{-1}	10^{-4}–10
R15A	10^{-10}–10^{-5}	10^{-5}–1
AB	10^{-6}–10^{-2}	10^{-5}–1
PD	10^{-6}–10^{-1}	10^{-5}–1

3.3 Results: Linear Burst PRCs

Linear PRCs calculated for the HR, AB, and R15A models are shown in figures 3.1–3.3, along with a close-up of the linear PRC in the phase segment corresponding to the active segment of the reference burst. Numerical issues, particularly stiffness, prevented calculation of linear PRCs for the PB and PD models. For those two models, AUTO could not locate or track the periodic orbit reliably.

As expected for a method which numerically simulates an infinitesimal, instantaneous perturbation, the magnitude of the maximum (absolute) phase response is generally quite small for each model, ranging from approximately 10^{-3} for the AB model to 10^{-1} for the HR model. The biologically realistic models had lower amplitude phase responses than did the schematic HR model.

The linear PRCs have several features in common and can be visually decomposed into three segments: (1) A spiky portion at the beginning of the perturbed burst which shows the greatest change in phase and the greatest variation in phase response; (2) a largely flat segment, beginning near the end of the active segment of the perturbed burst cycle and extending to a phase close to 1.0, during which there is little or no response to perturbation; (3) a brief segment, or hump, of increased phase response near phase 1.0, immediately before the start of the next burst cycle.

In PRC segment (1), there is a strong correlation between the timing of spikes

in the reference trajectory, as demarcated by their voltage maxima, and location of the greatest phase response. As can be seen from close-ups of the models' linear PRCs (figures 3.1–3.3 (b)), the amplitude of phase response increases over the course of each interspike interval, reaching a maximum just before or just after the impending spike. Immediately after the spike, the phase response decreases significantly, crossing the $\Delta\phi$-axis to change sign. After the zero crossing, the phase response amplitude increases again as the next spike peak approaches. (For the HR model, the greatest phase response amplitude is coincident with the zero crossings.)

The amplitude of the phase responses associated with the spikes increases as the end of the active segment approaches. Except near the ultimate (or penultimate, for the R15A model) spike, the phase responses at the spikes have essentially identical shapes; only their amplitudes change significantly.

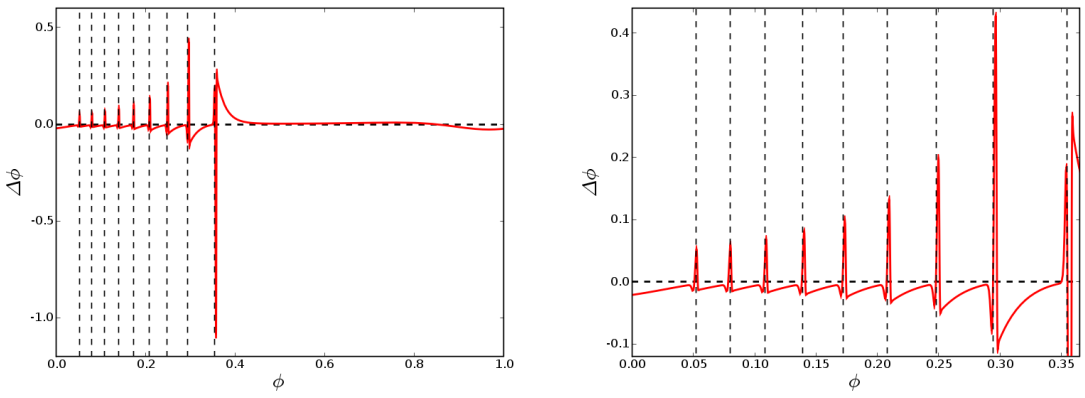

(a) (b)

Figure 3.1: HR Model Linear PRCs. Dashed black lines indicate spike phases in reference trajectory. (a) Complete PRC. (b) Close-up of active segment of burst, with $\phi \in [0, 0.365]$.

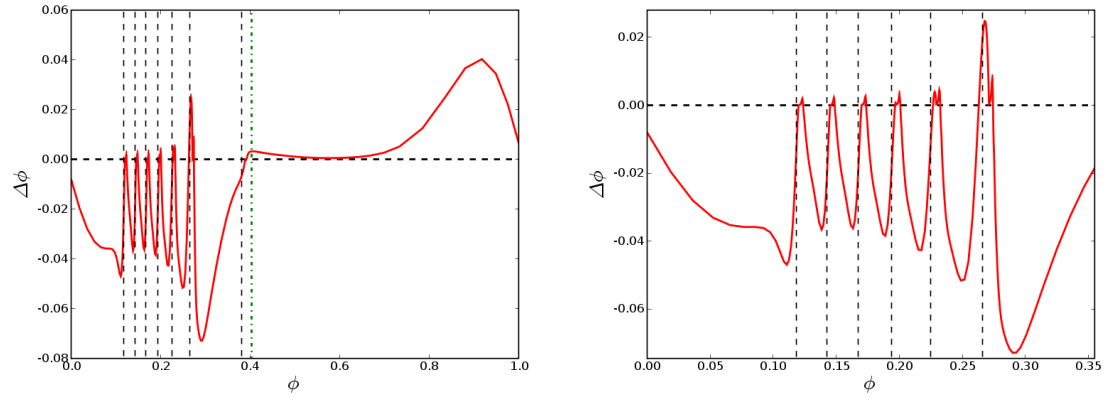

(a) (b)

Figure 3.2: R15A Model Linear PRCs. Dashed black lines indicate spike phases in reference trajectory, green dash-dotted lines indicate pseudospike phases in reference trajectory. (a) Complete PRC. (b) Close-up of active segment of burst, with $\phi \in [0, 0.355]$.

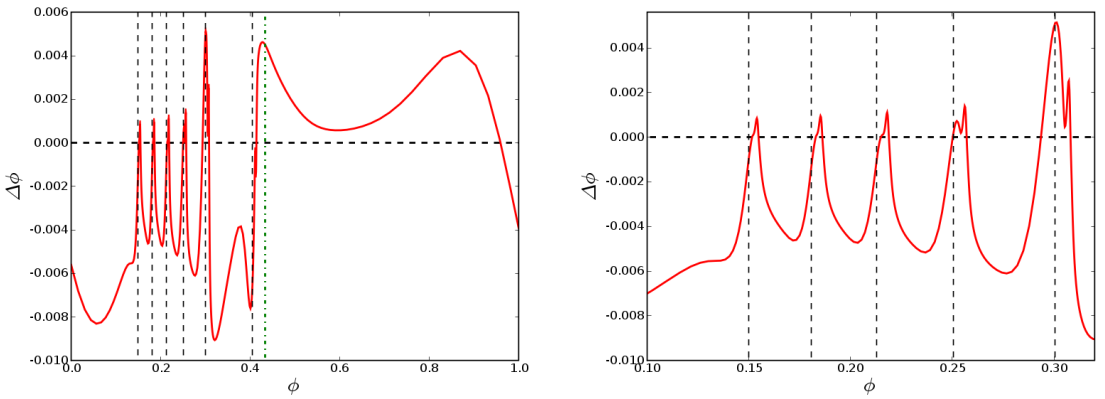

(a) (b)

Figure 3.3: AB Model Linear PRCs. Dashed black lines indicate spike phases in reference trajectory, green dash-dotted lines indicate pseudospike phases in reference trajectory. (a) Complete PRC. (b) Close-up of active segment of burst, with $\phi \in [0.1, 0.32]$.

The phase response near the final spike of the burst has a different character than the phase response associated with the preceding spikes. For HR and AB, the bulk of the PRC associated with the final spike is of sign or orientation opposite that of the phase response near the other spikes. The phase response for R15A does not change sign at this point, but it does elongate. Its phase response shows a steep decline followed by a more gradual rise between the penultimate and ultimate spikes, in contrast to the gentler decline followed by sharp ascent of the phase response near earlier spikes. Note also that the phase response for the penultimate-ultimate spike of R15A occurs over a substantially longer phase segment than for the other spikes, *i.e.* the final interspike interval is very long relative to the others.

PRC segment (2) shows diminished response to perturbation, with little phase advance or delay. For HR and R15A, this segment of the PRC is essentially flat and near zero, indicating no phase response whatsoever. The response is never zero for AB, but in this model there is a marked drop in phase response amplitude over this segment.

Phase response amplitude resurges in PRC segment (3), with the direction of amplitude increase depending on the model. HR showed slightly increased phase advancement, R15A showed relatively large phase delay, and AB showed large phase delay followed by phase advancement near phase 1.0.

3.4 Results: Direct Burst PRCs

The direct BPRCs calculated for each combination of neuron model, synapse form (spike injection, base-width conductance pulse, half-width conductance pulse), perturbation direction (excitation/inhibition), and perturbation strength are presented in Appendix C. For each model, there are two sets of BPRC figures, one

for excitation and one for inhibition. Each figure set comprises six subfigures, one for each g_{syn} value, *i.e.* each perturbation strength. Three BPRCs are depicted in each subfigure, one for each synapse form: spike injection (solid line), base-width conductance pulse (dotted line), and half-width conductance pulse (dashed line). Each g_{syn} value is denoted by the specific color given in Table C.2. All of the BPRCs shown have order 0, though order 1 and order 2 BPRCs were also calculated. Below we summarize the results for each model, then point out features of the direct BPRCs common across the models. As in the discussion of linear PRC results, we refer to three segments of the PRCs: segment (1), during the active segment of the burst cycle; segment (2), during the majority of the quiescent segment of the burst cycle; and segment (3), near the end of the quiescent segment and just prior to the start of the next burst cycle.

3.4.1 Model-specific PRCs

HR Model

Even at the lowest perturbation strengths, the HR model exhibited large phase response to excitation. For $g_{\text{syn}} = 10^{-4}$ and 10^{-3}, excitation induced phase shifts on the order of 10^{-3} and 10^{-2}, respectively, while at higher levels the phase shifts were of order 0.1. Within PRC segment (1), weaker excitation caused phase delay; strong excitation could cause phase advancement as well. In PRC segment (2), excitation induced less phase response at the lower four perturbation strengths, causing more phase advancement than delay for conductance pulse perturbations. Spike injection advanced the burst phase at lower perturbation strengths. At higher perturbation strengths, PRC segment (2) showed increasing delay, rather than advancement. Across all perturbation strengths, both spike injection and conductance pulse PRCs showed phase advancement in PRC segment (3).

At every perturbation strength, the excitatory conductance pulse synapse forms induced PRCs that more closely resembled the shape of the linear PRC than did the PRCs for excitatory spike injection. The conductance pulse PRCs were generally spikier than the spike injection PRCs, while the spike injection PRCs were smoother curves. At the highest perturbation strengths, the spike injection PRCs flattened to become effectively piecewise linear, while the conductance pulse PRCs remained spiky. The magnitude of the phase response to perturbation by excitatory spike injection was also significantly greater than the size of the responses to excitatory conductance pulses.

At the lower levels of inhibition, the HR model PRCs for each synapse form resembled (ϕ-reflected) linear PRCs. As the strength of perturbation increased, this resemblance became less exact, and at the two highest perturbation strengths, the PRCs had shapes distinctly different from the linear PRC. At $g_{\text{syn}} = 1$ and 10, PRC segment (1) predominantly showed phase advancement, with some small variations in phase response at spike times. Segment (2) was largely flat at larger perturbation strengths, showing either relatively small phase advance or larger phase delay, and segment (3) was typically phase delaying.

As in the linear PRC, phase response in PRC segment (1) of the inhibitory and excitatory BPRCs was closely associated with spike times, generally increasing in magnitude towards the ultimate spike of the active segment. This was the case across all perturbation strengths for all three synapse forms.

PB Model

The magnitude and shape of phase response to excitatory perturbations in the PB model was very similar for all three synapse forms.[5] For all but the high-

[5]The BPRCs for the two lowest levels of g_{syn} show much more numerical jitter than BPRCs calculated at other strengths and for other models, but the overall shape of the phase response is still discernible for each figure. However, the scale for figure C.4 (a) is 10^{-6} and $g_{\text{syn}} = 10^{-7}$,

est perturbation strength, excitation predominantly caused phase advancement in PRC segment (1) for the PB model, except near the final spike, where there was relatively large phase delay. PRC segment (2) showed a nearly constant level of phase delay for each synapse type, and PRC segment (3) showed relatively strong phase advancement. For the strongest excitation, each BPRC showed a substantial amount of phase delay at the end of the PRC segment (1), with the spike injection BPRC having the bulk of this phase delay before the penultimate spike of the burst, and the conductance pulse BPRCs having the greatest amount of phase delay after the final spike.

As for excitation, the shapes of the inhibitory BPRCs for the PB model were quite similar for all three synapse forms. However, the magnitude of phase response was much smaller for spike injection than for the conductance pulses except at the highest level of perturbation, where the magnitudes were roughly the same. At low levels of inhibition, the BPRCs resembled ϕ-reflected excitatory BPRCs, with closely spike-associated phase delays in PRC segment (1), slight phase advancement in the mostly flat PRC segment (2), and some phase delay in PRC segment (3). At higher levels of inhibition, later portions of PRC segment (1) showed significant phase advancement, with an abrupt discontinuity between phase delay and phase advancement occurring near the fourth spike of the burst. This discontinuity was not an artifact of displaying phase, a circular variable, rectilinearly.

R15A Model

At all strengths of excitation, the R15A model showed much greater phase response to spike injection than to conductance pulses. Also at every perturbation strength, the conductance pulse BPRCs had shapes very similar to the linear BPRC.

In PRC segment (1), the spike injection BPRC showed relatively strong phase

raising the issue of numerical noise versus accuracy and making this particular plot dubious.

advancement prior to the first spike of the active segment, strong phase delay between the penultimate and final spikes, and an abrupt drop in phase response (to nearly zero) immediately after the final spike. This pattern held for each g_{syn} value except the highest one, for which the region of phase advancement during the active segment included all but the final spike. PRC segment (2) was phase advancing for spike injection, and PRC segment (3) was either essentially zero or slightly phase advancing.

At the two lowest inhibitory perturbation strengths, the direct PRCs for the R15A model closely resembled the linear PRC, reflected across the ϕ-axis. The amplitude of the conductance pulse PRCs was about two to three times larger than that of the spike injection PRC. In the mid-range of perturbation strengths, all three synapse forms gave sharper spikes of phase response in PRC segment (1) than at the lower perturbation strengths, but the decomposition into three PRC segments remained clear. The amplitude of the phase response for the three synapse forms was also roughly the same in the mid-range.

In the lower four inhibition strengths, the R15A model responded to perturbations with relatively strong phase delay in PRC segment (1), flat delay in PRC segment (2), and a slight increase in phase delay in segment (3) which grew more prominent with perturbation strength. The two highest perturbation strengths showed a distinct smoothing of the phase response in segment (1), and a strong change to phase advance for $g_{\text{syn}} = 10^{-1}$ and strong phase delay for $g_{\text{syn}} = 1$. At these perturbation strengths, the resemblance to the linear PRCs was largely absent. The amplitudes of phase response at the highest perturbation strengths was comparable for all of the synapse forms.

AB Model

The excitatory PRCs for the AB model scale linearly with perturbation strength from $g_{\text{syn}} = 10^{-7}$ to $g_{\text{syn}} = 10^{-4}$, but have markedly different shapes for the two highest perturbation strengths. The shapes of both conductance pulse PRCs closely resembled the shape of the linear PRC for the four lowest perturbation strengths, and both types of conductance pulse PRCs had roughly the same magnitude of phase response across this range.

Also for this lower range of perturbation strength, PRC segment (1) was predominantly phase advancing for the conductance pulses, and the regions of greatest phase response PRCs closely tracked the location of spikes. Segment (2) was essentially flat and phase delaying for weakly excitatory conductance pulses, which also produced phase delay in segment (3).

Phase response for the spike injection PRC was significantly greater in magnitude in the lower range of perturbation strength. Segment (1) was phase advancing prior to the first spike and thereafter completely phase delaying, with the greatest delay occurring immediately before the ultimate spike time. Segment (2) was phase delaying, with a steady decrease in the magnitude of phase response, changing to phase advance in segment (3).

At the two highest perturbation strengths, the resemblance of the conductance pulse PRCs to the linear PRC shape was still discernible, but both forms showed more phase delay during segment (2). The shape of the spike injection PRC at $g_{\text{syn}} = 10^{-3}$ changed markedly, being predominantly phase delaying, with a peak of phase delay just before the first spike time. At $g_{\text{syn}} = 10^{-2}$, the spike injection PRC takes on a very different, effectively piecewise linear shape, with large phase advance at the start of the burst cycle becoming large phase delay by the end of the burst cycle, with the transition point just after the final spike.

For the four lowest perturbation strengths, the shapes of all three synaptic forms of inhibitory PRC appeared to be reflected and scaled versions of the linear PRC. The magnitudes of the phase responses of the conductance pulse PRCs were approximately twice those of spike injection PRCs. In segment (1), the base-width conductance pulse BPRCs had the sharpest phase response at spike times, compared to the phase responses for the other synapse forms near spike times. At $g_{\text{syn}} = 10^{-1}$, the phase advance near the termination of the active segment of the burst becomes larger and more pronounced for each of the synapse forms (though the spike injection PRC shows a 'rebound' of phase delay just after the end of the active segment). At $g_{\text{syn}} = 1$, all of the PRCs show phase delay prior to the first spike of the active segment, strong phase advancement just after the first spike, declining (but still strong) phase advancement during the active segment, and milder phase delay afterwards, in PRC segments (2) and (3).

PD Model

At lower levels of perturbation, for all three synapse forms, the PD model responded to excitation with phase advancement for nearly the entirety of the burst cycle. The response was nearly constant for conductance pulses, while the response to spike injection showed a growing peak of phase advancement near phase 0.8. In PRC segment (1), there was some increased phase response associated with spike times, but this was overwhelmed by the magnitude of the phase response near the end of the burst cycle.

At higher levels of excitation, the conductance pulse BPRCs maintained shapes similar to those at lower levels. The spike injection PRC showed relatively large phase delay over nearly the entire cycle at the second highest g_{syn} value, and phase advancement followed by phase delay for the strongest perturbation.

The response of the PD model to inhibitory perturbations was strikingly dif-

ferent to the BPRCs for other models. The PRCs for all three synapse forms were roughly identical at all levels of perturbation, though the amplitude of the response for the conductance pulses was somewhat higher than that for spike injection.

As for other models, inhibitory BPRCs for PD decomposed into three segments, but the phase response amplitudes in the segments were unusual. The greatest phase response was found in segment (3) and consisted of a broad, high peak of phase delay, preceded by a smaller dip indicating phase advance. PRC segment (1) displayed a strong relationship between spike times and the peaks of phase response, but the amplitude of phase response in this segment was so small relative to that of segment (3) that the curves appeared almost flat in this region. (Close-ups of the active segment revealed small peaks of phase response aligned with spike times.) PRC segment (2) was almost completely flat.

The shape of the BPRC remained essentially constant across the entire perturbation range. The only noticeable changes, visible at the highest perturbation level, were a sharpening of the segment (3) peaks for the conductance pulse PRCs and a slight increase in phase response close to phase 0.

3.4.2 Common Features

Although there was significant phase response variation from model to model to different combinations of synapse form, perturbation direction, and perturbation strength, there were nonetheless some notable features of the direct PRCs that were widely shared. Some of these features could be anticipated intuitively or from the results of the linear BPRC calculations, while others were unexpected.

The magnitude of phase response scaled with the strength of perturbation. For most of the models and perturbation types, the size of the phase response was roughly proportional to the magnitude of g_{syn}. However, the amplitude of phase

response at any given perturbation strength was often quite different for different synapse forms. The shapes of the phase response curves for higher values g_{syn} also differed markedly from those for lower values, with inhibition in the PD model being an exception.

The phase response curves at all perturbation strengths, synapse types, perturbation directions, and models decomposed into three segments, just as for the linear BPRCs. However, the excitatory and inhibitory direct BPRCs were not simply scalings of the linear BPRCs. As was most evident at higher perturbation strengths, direct BPRCs could have strikingly different shapes from their linear counterparts.

At low levels of perturbation, the shape of the linear BPRCs was easily discernible in the direct BPRCs, though usually the shapes were not exact matches. The similarity between the linear and direct BPRCs grew as the perturbation strength decreased, so that the linear and direct BPRCs for some models were nearly identical, as can be seen at the lowest perturbation strengths for the AB, HR, and R15A models. This increase in similarity is expected from the mathematical theory of PRCs, and was confirmed by direct BPRC calculations at perturbation strengths as low as 10^{-12} (not shown).

Both excitatory and inhibitory BPRCs clearly showed a qualitative transition in shapes at the second or third highest values of g_{syn}. At the highest levels of perturbation, there were normally strong changes in the phase response in segments (1) and (2), so that a given model's BPRC could look completely different from its BPRCs for the lowest perturbation strengths.

Furthermore, inhibitory and excitatory BPRCs calculated with direct methods were definitely not simply scaled versions of each other, reflected across the ϕ-axis.

Instead, phase response to inhibition and excitation were quite asymmetric in each model.

3.4.3 Spike Number Response

For lower levels of excitation and inhibition, and for all synapse forms, the zeroth and first order spike number response curves of the models were flat, indicating that perturbation did not change the number of spikes in either the current or the subsequent burst cycle.[6] For the highest perturbation levels, the zeroth order SNRCs were often quite different; figures 3.4 and 3.5 show two representative examples. Each plot shows the SNRCs at each perturbation strength for a single model, single perturbation type, and single perturbation direction. The colors of the lines correspond to the g_{syn} values and match the colors used for BPRCs at the same perturbation strength. Note how the spike numbers shown in the plots match closely with the regions of greatest phase response in the corresponding BPRCs.

Though the figures show the spike number responses of only two models and a single perturbation type (both excitation and inhibition), similar results, namely changes in spike number associated with strong changes in phase, were found for the other models and synapse forms as well.

As seen in figure 3.4, high levels of excitation could either add or delete spikes from the active segment of the perturbed burst, depending on the phase of the perturbation. In the PB model, strong perturbations close to the end of the active segment, near the penultimate spike, had the effect of adding an extra spike and thereby delaying the onset of the next burst cycle, thus causing phase delay.

[6]For every combination of neuron model, synapse form, perturbation direction, and perturbation strength, the second and higher order SNRCs were flat and showed the same number of spikes per burst as the models' reference bursts. This indicated that burst orbits of the models recovered to a point very close to their original, unperturbed trajectories within a few cycles. For the levels of perturbation discussed in this chapter, there was no permanent change in the models' bursting behavior.

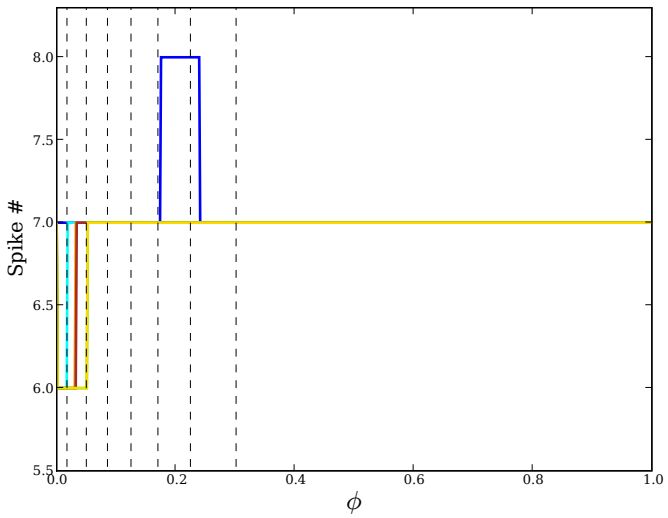

Figure 3.4: Spike number response curve for excitation by spike injection, PB model.

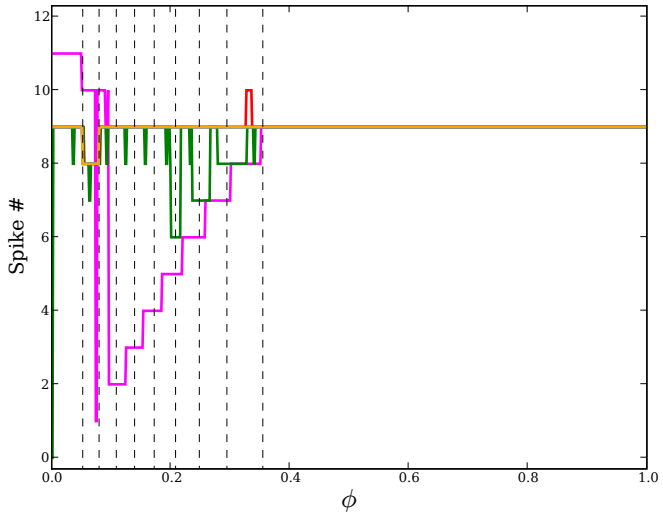

Figure 3.5: Spike number response curve for inhibition by spike injection, HR model.

In other models, excitation could substantially increase the length of the active segment by sending the perturbed neuron into a state of rapid spiking with interspike intervals much shorter than normal (HR), or it could delete spikes (AB).

The typical effect of strong inhibition is clearly visible in figure 3.5: The spike number in the HR model is reduced the most by strong perturbations applied early in the active segment. These effectively terminate the active segment early and switch the perturbed neuron into the quiescent state, which lasts approximately the normal amount of time. Thus the amount of phase advance that occurs is essentially the fraction of the burst cycle normally occupied by the missing spikes.

Though spike number changes typically happened only for perturbations applied during the active segment of the burst cycle, strong enough excitatory perturbations in the quiescent segment could add spikes, and both excitation and inhibition applied near phase 1.0 could alter the spike number of the subsequent burst.

3.5 Discussion

The work presented in this chapter is the first extensive investigation of the phase response properties of model of endogenously bursting neurons. We studied many combinations of models, synaptic forms, perturbation directions, and perturbation strengths through careful computational experiments. In this way, we could examine the validity of common assumptions about phase response for bursting neurons that are often made by modelers and experimentalists, but which have seldom been subjected to much scrutiny. Our results reveal that some of the approximations made by modelers and intuitions of experimentalists may not be entirely valid. Below we summarize the main results of our study.

First, directly calculated or 'realistic' burst phase response curves are not sim-

ply linear scalings of BPRCs calculated via adjoint methods or other linearized techniques. They have different shapes, though realistic BPRCs and linear BPRCs do resemble each other, and their similarity increases as perturbation strength decreases.

Second, realistic excitatory and inhibitory BPRCs differ significantly from each other, both qualitatively and quantitatively. Unlike linear BPRCs, excitation and inhibition produce realistic BPRCs that are not simply reflections of one another across the ϕ-axis.

Third, burst phase response curves (both linear and direct) typically comprise three visually distinct segments, each of which shows distinctive phase response characteristics. In particular, phase response in the active segment of the burst cycle is strongly associated with intraburst spike times.

Fourth, the shape and magnitude of burst phase response can depend heavily on the choice of synapse model. Different synapse models can produce very different BPRCs for the same neuron model for the same perturbation level, and conversely the same synapse model may produce results that differ in a consistent fashion for different neuron models.

Fifth, burst phase response changes dramatically as perturbation strength increases, and discontinuities in the phase response curve may arise at high levels of perturbation. For the strongest perturbations, spike addition and deletion play a dominant role in determining the timing and magnitude of burst phase response.

Our results show that phase response for bursting neural models is a complex phenomenon, and that the assumed forms of burst phase response used in standard PRC analyses may not approximate the behavior of coupled model (or biological) neurons well. For realistic modeling, BPRCs calculated with direct methods may be superior to those relying on linear approximations like the adjoint PRC method.

The biophysical details of the neuron model and the synapse model may be crucial in determining the shape of the BPRC. The characteristics of individual spikes and the multiple time-scale structures inherent in the models also play critical roles in shaping the BPRC.

The importance of these factors reinforce that modelers and biologists should take care to identify assumptions and their domains of validity when making inferences about individual neurons' phase responses and their relations to phasing in neuronal networks. The biological relevance of the modeling results presented here may be tested by comparing them to experimental burst phase response curves obtained from real neurons (*e.g.* using dynamic clamp techniques) where the synaptic inputs are realistically modeled (*cf.* [59, 175, 162]).

CHAPTER 4

BURST PHASE RESPONSE: ANALYSIS

4.1 Introduction

The burst phase response curves calculated in the previous chapter had a striking appearance that corresponded closely to the current activity (spiking *vs.* quiescence) of the perturbed trajectory. The BPRCs visually decomposed into three segments: (1) An initial 'spiky' segment, coincident with the active segment of the burst cycle, in which the greatest magnitude and variation in phase response were seen; (2) a middle segment of minimal phase response which lasted for most of the quiescent segment of the burst cycle; (3) a final segment, usually exhibiting some phase advancement or delay, respectively, for excitation or inhibition, at the end of the burst cycle.

Roughly the same decomposition of the PRCs held for both low and high perturbation strengths. However, the phase response magnitude did not scale linearly with the strength of perturbation at the upper ranges, and the shapes of the phase response curves for strong perturbations differed substantially from those for weaker perturbations. Sufficiently strong perturbations at particular phases disturbed the model neurons enough to shift them far enough away from their original periodic orbits to change the spike number of the burst.

In this chapter, we investigate phase response phenomena in the Hindmarsh-Rose (HR) model from the perspective of geometric singular perturbation theory. We employ fast-slow dissection, phase plane analysis, and isochron portraits to explain some notable features of linear and direct phase response curves for both weak and strong perturbations. Our analysis illustrates how the multiple time-scales inherent in the bursting model critically shape its phase response characteristics.

4.2 Fast-slow dissection

In calculating the direct BPRCs for the full Hindmarsh-Rose model, extrema of the slowest variable, the recovery variable h, marked the transitions between the active and quiescent segments of the burst cycle. Treating h as a quasi-static parameter (and fixing all other parameters at the values listed in Table B.11), we obtain a family of fast subsystems:

$$\begin{aligned} \dot{V} &= n - aV^3 + bV^2 - h + I \\ \dot{n} &= c - dV^2 - n \end{aligned} \tag{4.1}$$

The fast subsystems (4.1) are planar vector fields, which greatly simplifies analysis. Bifurcations in the fast subsystem, marking qualitative changes in the geometry of the planar vector fields as h changes, correspond to transitions between spiking and quiescence in the full system. The sequence of bifurcations in the fast subsystems of the HR model is well known; here we summarize the bifurcations and their relationships to bursting behavior.

Figure (4.1) shows the bifurcation diagram for (4.1), treating h as the continuation parameter. For large negative h values, there exists a lone stable fixed point, and at $h \approx -9.5931404587$ there is a supercritical Hopf bifurcation (denoted H2 in figure 4.1 (a)) where the fixed point loses stability and a stable periodic orbit is created. At large positive h values, there again exists a lone fixed point, though at lower (negative) V values than the fixed point that exists for large, negative h. At $h = 3.0$ a pair of fixed points (one stable, the other unstable) is born at the saddle-node bifurcation denoted LP2 in figure 4.1. These fixed points have higher V values than the other stable fixed point; the lower, unstable member of the pair is a saddle. As h decreases to 2.92647388572, the supercritical Hopf bifurcation point denoted H1, the upper stable fixed point loses stability (becoming the upper

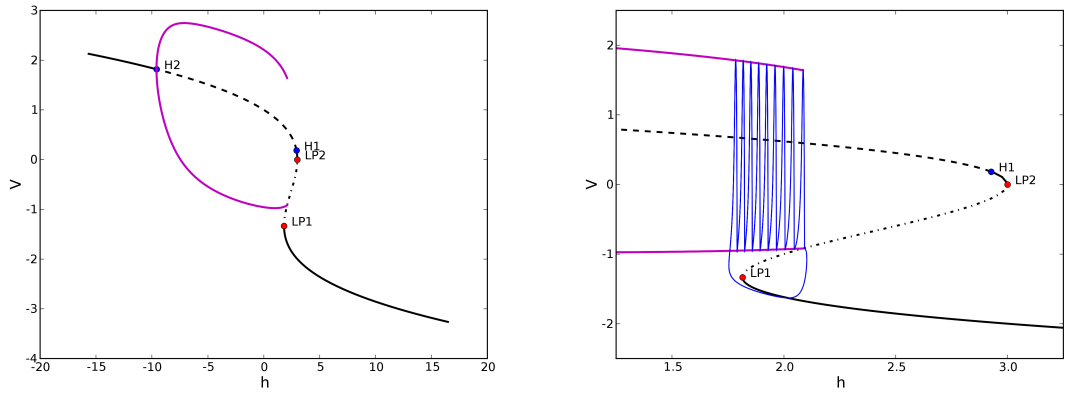

Figure 4.1: Bifurcation diagram for the HR fast subsystem. Solid black lines indicate stable fixed points, dashed black lines show unstable fixed points. Solid magenta lines show the maximum and minimum V values of stable periodic orbits. Saddle-node bifurcation points: LP1, LP2. Hopf bifurcation points: H1, H2. (a) Full bifurcation diagram. (b) Close-up of h range for bursts in the full subsystem. A (h, V)-plane projection of a full system trajectory is superimposed in blue.

unstable fixed point that emanated from H2) and a small stable periodic orbit emerges. This small periodic orbit is quickly destroyed in a homoclinic bifurcation with the lower saddle point. At $h \approx 1.81481481481$, denoted LP1, the lower stable fixed point merges with the saddle, and the two lower fixed points disappear, leaving only the upper, unstable fixed point and the stable periodic orbit (from H2) around it. The stable periodic orbit from H2 is destroyed in a homoclinic bifurcation, merging with the saddle point at $h \approx 2.08560088198$.

The upper unstable fixed point, saddle point, lower stable fixed point, and stable periodic orbit from H2 are the only fast subsystem structures which play a role in full system bursting. As shown in figure 4.2 (b), h varies between 1.75415439813 and 2.10256601768 in the full HR system over the course of a burst cycle. Figure 4.1 (b) shows a close-up of this region of the bifurcation diagram along with a burst trajectory in the full subsystem projected onto the (h, V)-plane. The line of fixed points at lower V corresponds to the resting membrane voltage during quiescence,

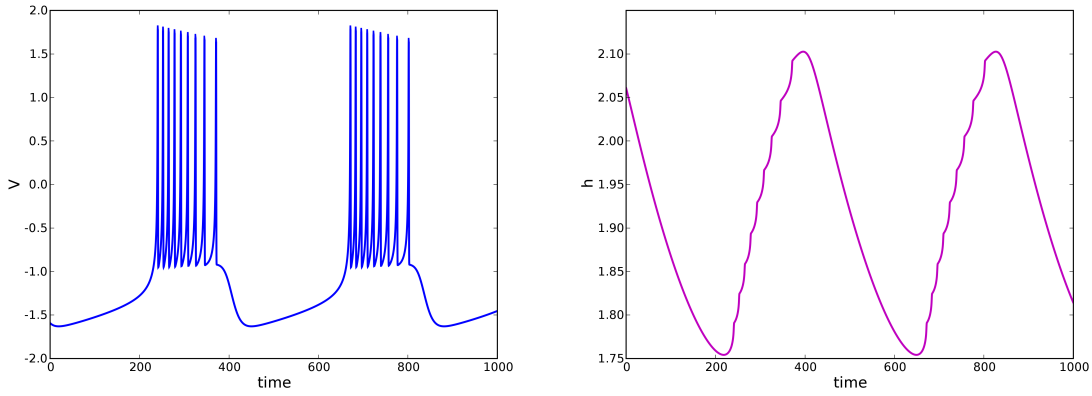

(a) (b)

Figure 4.2: Full system burst trajectories for HR model. (a) V vs. time. (b) h vs. time.

when h decreases from the maximum value it achieved during the previous bout of spiking. The disappearance of these fixed points at the saddle-node bifurcation LP1 corresponds to the start of the next active segment and the onset of spiking, when the full system ceases tracking the line of low voltage stable fixed points and begins following the family of stable periodic orbits as h begins to increase. The homoclinic bifurcation near the maximum value of h marks the end of the active segment, when the full system trajectory leaves the vicinity of the family of (now extinguished) periodic orbits and follows the line of low voltage stable fixed points.

One feature of note is that h has a single maximum and a single minimum over the course of one burst cycle in the full system, as seen in figure 4.2 (b). This 'piecewise' monotonicity — decomposition into one period of increasing h and one period of decreasing h — serves to simplify extrapolation from reasoning about activity in the fast subsystem in the singular case to behavior in the full system when h varies as a slow dynamic variable.

4.3 Weak Perturbations

As described in the introductory section (4.1) and chapter (3), the linear PRCs and direct BPRCs at low g_{syn} visually decomposed into three distinct segments, corresponding temporally to the active segment, early to middle quiescence, and late quiescence in the full system. Figure (4.3) shows the linear PRC for the HR model.

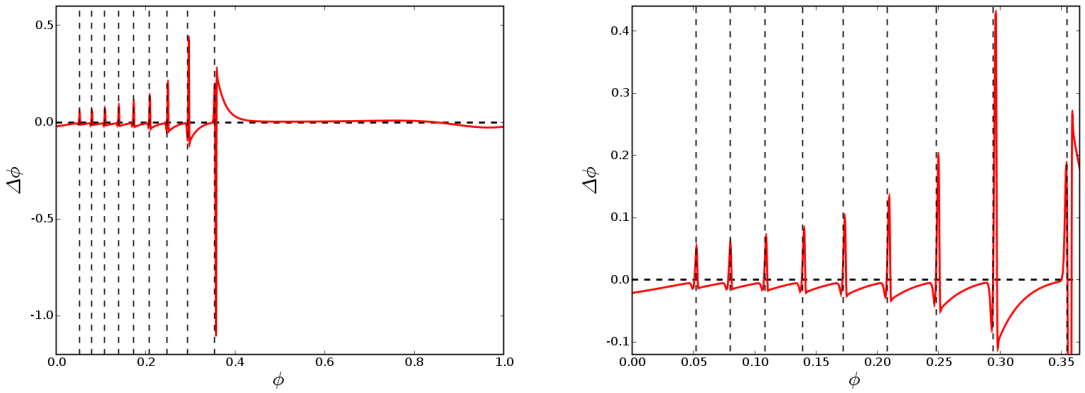

(a) (b)

Figure 4.3: HR Model Linear PRCs. Dashed black lines indicate spike phases in reference trajectory. (a) Complete PRC. (b) Close-up of active segment of burst, with $\phi \in [0, 0.365]$.

In this section, we analyze the phase response of the HR model to weak perturbation using the phase portraits and isochrons of the fast subsystems, treating the quiescent and active segments separately. Our analysis helps explain the origin and noteworthy characteristics of the three distinct regimes of phase response in the full system.

4.3.1 Quiescent Segment

PRC segment (2) corresponds to the quiescent portion of the burst cycle, when h recovers from 2.10256601768 to 1.75415439813. Following the destruction of

the family of stable periodic orbits in the fast subsystem at a homoclinic bifurcation, the burst trajectory in the full system tracks the line of low voltage stable fixed points. These fixed points are the only remaining stable structures in the fast subsystem, having a large domain of attraction and relatively large, negative eigenvalues so that the rate of approach of a trajectory in the full system is quite rapid. Furthermore, the vector field for the full system is largely parallel to the h direction in the fast subsystem. Thus small perturbations in the V direction during this segment have little effect, since the trajectory is drawn immediately back to the stable fixed point, with only a small change in h and therefore only a small change in phase. Hence the phase response in PRC segment (2), as recorded in the linear and low amplitude direct BPRCs, is negligible.

In PRC segment (3), the perturbed neuron approaches the end of the quiescent segment of its current burst cycle and the onset of the subsequent round of spiking. In the fast subsystem, this corresponds to nearing the saddle-node bifurcation at which the low voltage fixed point being tracked by full system trajectory disappears. At that bifurcation point, the trajectory immediately switches to following the coexistent stable periodic orbit. As the saddle-node bifurcation point gets closer, the eigenvalues of the stable fixed point diminish, reducing its rate and domain of attraction so that small perturbations may knock the full system trajectory into the basin of attraction for the stable periodic orbit. Such an event marks the early advent of the next burst cycle, and hence PRC segment (3) shows a slight phase advancement.

4.3.2 Active Segment

Phase response in the active segment of the burst has a more complicated structure and appearance than the shape of the phase response during the quiescence. The

main features we wish to explain are (1) the close association of peaks of phase response to the spike maxima in the full system trajectory, (2) the increase in amplitude of these phase response peaks closer to the end of the active segment, and (3) the large magnitude and sign reversal of the phase response at the end of the active segment. Phase portraits of the fast subsystem and isochron calculations are the main tools we employ in our analysis.

Phase Portraits

We investigate the phase portrait of the fast subsystem at three cross-sectional h values, 1.8, 1.95, and 2.085, shown in figures 4.4 (a), (b), and (c), respectively. At $h = 1.8$, the fast subsystem is at the beginning of the active segment, and there exists no stable fixed point, only the stable periodic orbit (corresponding to spikes in the full system) surrounding an unstable fixed point. The value $h = 1.95$ lies in the middle of the active segment, after the stable fixed point and a saddle have emerged via the saddle-node bifurcation. The stable eigendirections for the saddle and stable fixed point are drawn as dashed green lines, and the unstable eigendirection of the saddle is drawn as a dashed red line. For $h = 2.085$, the fast subsystem is very close to the homoclinic bifurcation, and the saddle and the periodic orbit nearly touch. Phase breaks down in the limit cycle at the homoclinic point; the period of the orbit goes to infinity. Past the homoclinic point, the fast subsystem has no periodic orbit, though the full solution may still emit one spike. Phase is undefined in the fast subsystem, though the excitability of the full system means that perturbations from the stable fixed point may follow trajectories which track "ghosts" of the stable structures which existed in the fast subsystem at lower h values.

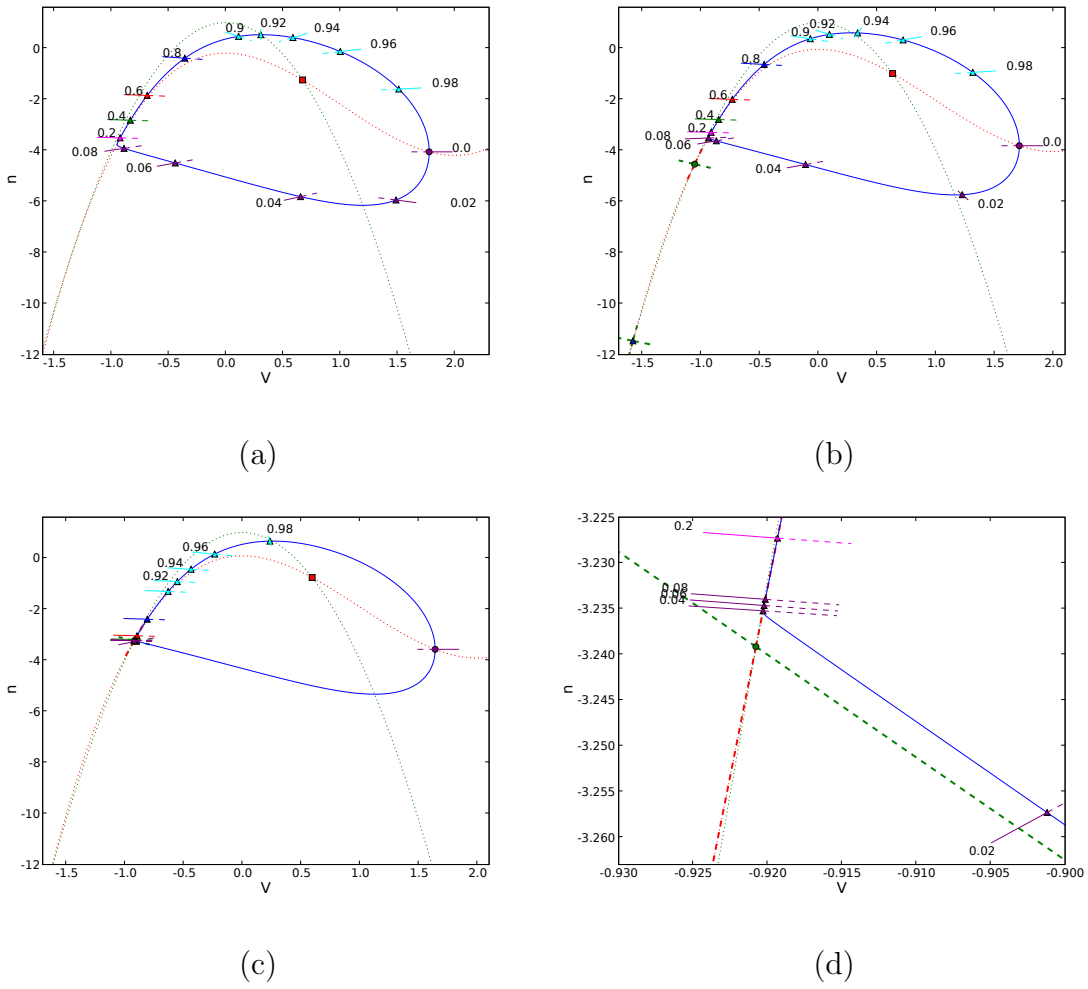

Figure 4.4: Phase portraits for the HR fast subsystem. Dashed red line: V nullcline. Dashed green line: n nullcline. Blue triangle: stable fixed point. Red square: unstable fixed point. Green circle: saddle point. Stable and unstable eigendirections of fixed points are indicated by green and red dash-dotted lines, respectively. (a) $h = 1.8$. (b) $h = 1.95$. (c) $h = 2.085$. (d) $h = 2.085$, close up near saddle point.

In each of the phase portraits, the cubic V nullcline is drawn with a dotted red line, and the parabolic n nullcline is drawn with a dotted green line. This parabolic-cubic nullcline configuration is different from the standard slow-fast system picture in which the slow variable has a linear nullcline and periodic trajectories alternate via fast jumps between slowly following one branch of the fast nullcline to the other. The left branches of the two nullclines in the HR fast subsystem lie very close together, so that trajectories proceed very slowly in their vicinity. Near the right branch of the n nullcline, away from the fast nullcline, V evolves very rapidly; this is the depolarizing region of the spike.

Normalizing by the period, we plot several phases around the periodic orbit, assigning phase 0 to the point of maximum voltage. At each labeled phase, we also draw a line normal to the vector field at that point on the periodic orbit. Trajectories near the periodic orbit proceed clockwise around or inside of it.

The nonuniform spatial distribution of points on the periodic orbit that are equally spaced in phase shows how the speed of spiking trajectories varies in different regions of phase space. The movement is most rapid where phase points are spread farthest apart, namely during hyperpolarization after the spike maximum, between phases 0 and 0.1. It is almost as fast during depolarization before the spike maximum, from phase 0.9 to phase 0, and it is slowest at low V values, between phases 0.1 and 0.8. The speed of the hyperpolarized portion of the orbit relative to the spike slows dramatically as the homoclinic point approaches, as can be seen by noting the compression of phases 0.1 to 0.8 along the left arc of the periodic orbit for $h = 2.085$ in figures 4.4 (c) and (d). The proximity of the saddle point to the periodic orbit, shown in figure 4.4 (d), has a stark retarding effect on the trajectory. In early and middle parts of the active segment, figures 4.4 (a) and (b), the spike occurs in the phase interval 0.9 to 0.1, but at the end of the

active segment, this has shrunk to the interval between 0.96 and 0.04. Hence the hyperpolarized interspike intervals increase in length as the active segment of the burst progresses.

4.3.3 Isochrons

Recall that the *asymptotic phase* $\vartheta(\mathbf{y})$ of a point $\mathbf{y}$ in the basin of attraction B of a stable periodic orbit Γ is the phase $\theta(\mathbf{x})$ of the unique point $\mathbf{x} \in \Gamma$ such that $\|\Phi(x,t) - \Phi(\mathbf{y},t)\| \to 0$ as $t \to \infty$, where Φ is the flow of the dynamical system under consideration. We define the the *isochron* $\varpi(\mathbf{x})$ of $\mathbf{x}$ as the set of all points in the basin of attraction of Γ having the same asymptotic phase as the actual phase of $\mathbf{x}$, *i.e.* $\varpi(\mathbf{x}) = \{\mathbf{y} \in B : \vartheta(\mathbf{y}) = \theta(\mathbf{x})\}$.[1] Equivalently, isochrons are cross-sections of Γ (manifolds intersecting Γ transversely at a single point) having a first return time equal to T, the period of Γ [98].

At the end of a perturbation of the burst cycle of the full HR model that does not permanently silence the neuron, the perturbed trajectory has been moved to a point $\mathbf{y}$ in the basin of attraction of the (full system) burst periodic orbit Γ. Then $\mathbf{y}$ lies on an isochron $\varpi(\mathbf{x})$ for $\mathbf{x} \in \Gamma$, and this isochron determines the phase shift due to the perturbation. During the active segment of the burst cycle, the unperturbed trajectory tracks the stable periodic orbits Γ_h in the fast subsystems associated with a narrow range of h values (those that the unperturbed trajectory traverses), and the isochrons of Γ_h lie near related isochrons of Γ. The repositioning of the perturbed trajectory relative to the isochrons of Γ is reflected in its shift relative to the isochrons of Γ_h, and so examination of the geometry of the isochrons of the fast subsystem for several representative h values may present an informative picture with respect to phase response in the full HR model. We calculate isochrons in

[1] For $\mathbf{x} \in \Gamma, \vartheta(x) = \theta(x)$ [236, 235]. We also use the notation θ_x for the scalar value $\theta(\mathbf{x})$.

the fast subsystems for cross-sections of the active segment at $h = 1.8$, 1.95, and 2.085.

We emphasize that the notion of phase for the full and fast subsystems are not identical, and that the isochrons for the full and fast subsystems are different mathematical objects with different meanings for the behavior of the model. Isochrons in the full system are two-dimensional manifolds with asymptotic phases relative to the full burst cycle, whereas isochrons in the fast subsystem are one-dimensional curves with asymptotic phases associated with a periodic orbit approximating a single spike of the full burst cycle. That is, a phase θ_h (and its associated isochron) in the fast subsystem is not the same as θ in the full system, even if they have the same scalar value, since the former refers to phase in a smaller subset (a single spike) of the periodic orbit associated with the latter. However, phase shifts $\Delta\theta_h$ and $\Delta\theta$ are directly related, since advancement or delay along a single spike implies a similar shift along the full burst cycle. Hence knowledge of the configuration of isochrons in the fast subsystem is useful for analyzing phase response in the full system.

Isochron calculation

Analytical solutions for isochrons can be calculated only for some simple systems [236, 215, 161], though closed form approximations to isochrons locally (very close to the periodic orbit) may be obtained for systems near bifurcation (near homoclinic points, in particular) by considering the specific normal forms of the bifurcation [14, 16]. In general, isochrons must be numerically approximated.

Backwards integration is typically used to find points lying near a particular isochron [130]. Let $\theta_x = \theta(\mathbf{x}), \mathbf{x} \in \Gamma$ be the phase for which we wish to calculate the isochron. If we choose a point $\mathbf{x}_0$ such that $\|\mathbf{x} - \mathbf{x}_0\| < \epsilon, \epsilon > 0$, and ϵ sufficiently small, then integrating backwards for time τ, we obtain $\Phi_{-\tau}(\mathbf{x}_0)$, which lies on

approximately the same isochron as $\Phi_{-\tau}(\mathbf{x})$. Hence if we choose relative phase $\theta' \in [0,1]$, $\mathbf{y} \in \Gamma$ such that $\theta(\mathbf{y}) = \theta_x + \theta'$, and $\mathbf{y}_0$ such that $\|\mathbf{y} - \mathbf{y}_0\| < \epsilon$, then integrating backwards for time $\tau' = \theta'/T$, we obtain $\Phi_{-\tau'}(\mathbf{y}_0)$, which lies near the isochron for $\Phi_{-\tau'}(\mathbf{y}) = \mathbf{x}$.

Thus calculating the isochron curve for a given phase θ_x is a matter of choosing a set of relative phases and integrating backwards from the associated test points. Considerable care must be taken with the backwards integration and the test points must be chosen judiciously in order to obtain visually comprehensible curves with reasonable efficiency.

Although the fast subsystem may not be particularly stiff in comparison to the full system, backwards integration in the fast subsystem is quite susceptible to failure due to numerical instabilities. This necessitates a good choice of integration routine and careful control of step sizes and integration tolerances. We use the RADAU5 stiff integrator [108] with an initial step size of $10^{-5} - 10^{-11}$, maximum step size of 10^{-4}, and relative and absolute tolerances of 10^{-12}.

For a given relative phase θ' and $\mathbf{y}$ such that $\theta(\mathbf{y}) = \theta_x + \theta'$, we let $\mathbf{y}_0 = \mathbf{y} + \gamma\mathbf{w}$, where $\gamma = \pm\epsilon$ and $\mathbf{w}$ is the unit vector normal to the vector field at $\mathbf{y}$ pointing outward from Γ. We refer to the segment of the isochron calculated for γ positive (negative) and thus lying outside (inside) Γ as the *outer* (*inner*) isochron for phase θ_x.

The hyperbolicity of the stable periodic orbit implies that trajectories are attracted to it exponentially in forwards time and disperse from it exponentially in backwards time. Therefore we choose a set S of K logarithmically spaced relative phases in an interval $[\theta_{\text{low}}, \theta_{\text{high}}]$, with θ_{low} close to θ_x. Since the calculations may not be stable for every relative phase in $[\theta_{\text{low}}, \theta_{\text{high}}]$ (this is particularly problematic for larger θ_{high}), we find the largest relative phase $\theta_{\max} \in S$ for which backwards

integration succeeds. We then set $\theta_{\text{high}} = \theta_{\max}$, and recalculate S to have K relative phases in the new interval, if necessary. For each relative phase in S, we integrate backwards to find its associated point on the isochron for θ_x; we repeat the process until we obtain N points on the isochron. We summarize our isochron calculation method in Algorithm 1.

Algorithm 1 GROWISOCHRON$(\theta_x, \theta_{\text{low}}, \theta_{\text{high}}, N, K)$

Require: $\theta_x, \theta_{\text{low}}, \theta_{\text{high}} \in [0, 1]$, $\theta_{\text{low}} < \theta_{\text{high}}$, integers $N, K \geq 1$.
Ensure: Isochron curve C, $|C| = N$.

```
Initialize C = {}
while |C| < N do
    Initialize S := {θ_1, ..., θ_K} logarithmically spaced phases in [θ_low, θ_high]
    Use bisection to find largest θ_max ∈ S such that backwards integration succeeds.
    if θ_max < θ_high then
        θ_high ← θ_max
        Reinitialize S
    end if
    for 1 ≤ i ≤ K do
        τ ← θ_i · T
        Initialize test point y_θ for phase θ_x + θ_i
        Compute p = Φ_{-τ}(y_θ)
        if computation of p fails then
            break
        else
            Append p to C
        end if
    end for
    if computation of p failed for θ_i ∈ S then
        θ_high ← θ_i
        θ_low ← θ_{i-1}
    else
        θ_high ← θ_high + |θ_high − θ_low|
        θ_low ← θ_high
    end if
end while
return C
```

Early Active Segment

Figure 4.5 shows the fast subsystem phase portrait with isochrons at $h = 1.8$, near the beginning of the active segment of the full burst cycle. For comparison, figure 4.6 shows the linear burst phase response in the full system in the interval corresponding to $h \in [1.78464559529, 1.85251757552]$. Figure 4.6 is centered about the second spike of the burst. The dashed-dotted lines left of the center spike mark ten equally spaced phases between the phases of the first and second spikes of the burst; the dashed-dotted lines to the right are similarly spaced between the second and third spikes. These lines provide a visual reference for comparison with fast subsystem phases and their corresponding isochrons in 4.5 and subsequent phase portraits.

The outer isochrons for phases in the hyperpolarized portion of the spike, 0.1 to 0.7, extend linearly from the left edge of the periodic orbit and are nearly parallel to one another.[2] The inner isochrons at the same phases also have extended parallel linear segments, but past the right branch of the n nullcline, they begin to curve and spiral into the unstable fixed point, coming close to the inside depolarized edge of the orbit. The phases of the upswing of the spike, 0.8 to 0.0, have outer isochrons that bend to the right and curve around the depolarized side of the orbit; to the left of the right branch of the n nullcline, they straighten and extend parallel to the 0.1 to 0.7 isochrons. The inner isochrons of the spike upswing also spiral into the unstable fixed point, but they remain away from the depolarized edge of the periodic orbit. The inner 0.0 isochron, corresponding to the spike peak, lies very close to the depolarized edge of the periodic orbit above the V nullcline, and the outer isochron hugs the outer edge of the periodic orbit tightly. The isochrons

[2]In each of the fast subsystems we consider, the outer isochrons for each extend out nearly linearly to V values below -200, but we focus on the area of the phase plane close to the periodic orbit.

for phases 0.9 to 0.08 are nearly tangent to the periodic orbit where they intersect it.

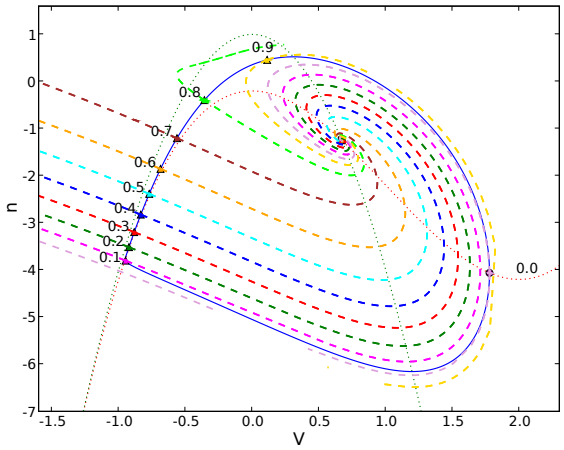

Figure 4.5: Phase portrait and isochrons in the HR fast subsystem near the beginning of the active segment of the full system, $h = 1.8$.

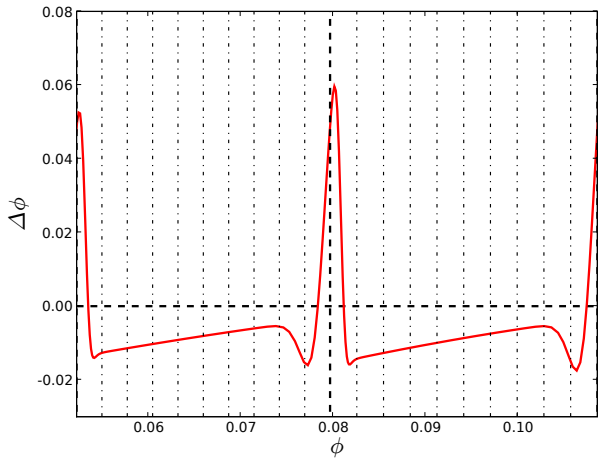

Figure 4.6: Close-up of linear burst phase response curve in the full HR model near the beginning of the active segment. The heavy dashed line marks the spike peak for spike closest to $h = 1.8$ slow variable value. Light dash-dotted lines denote equally spaced interspike phases in the full system.

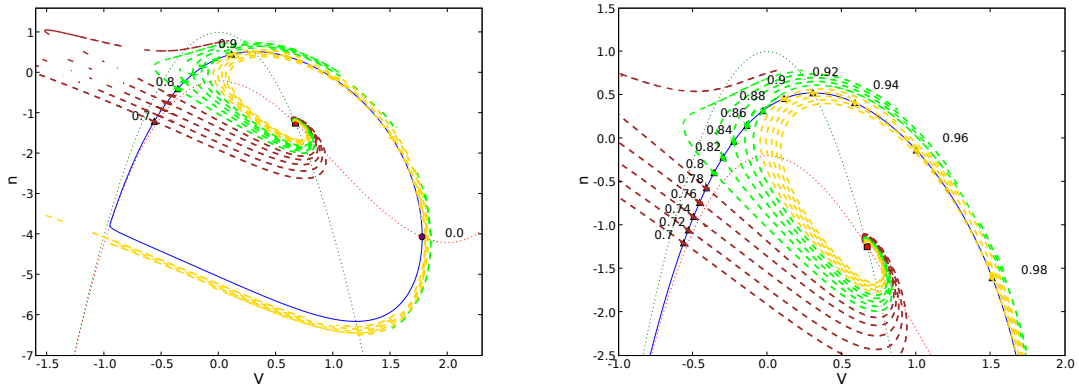

(a) (b)

Figure 4.7: Phase portrait of the HR fast subsystem and isochrons for phases in $[0.7, 0.0)$, $h = 1.8$. Isochrons with phases in $[0.7, 0.8)$ are colored brown; $[0.8, 0.9)$, green; $[0.9, 0.0)$, yellow. (a) Full orbit. (b) Close-up of late phase region.

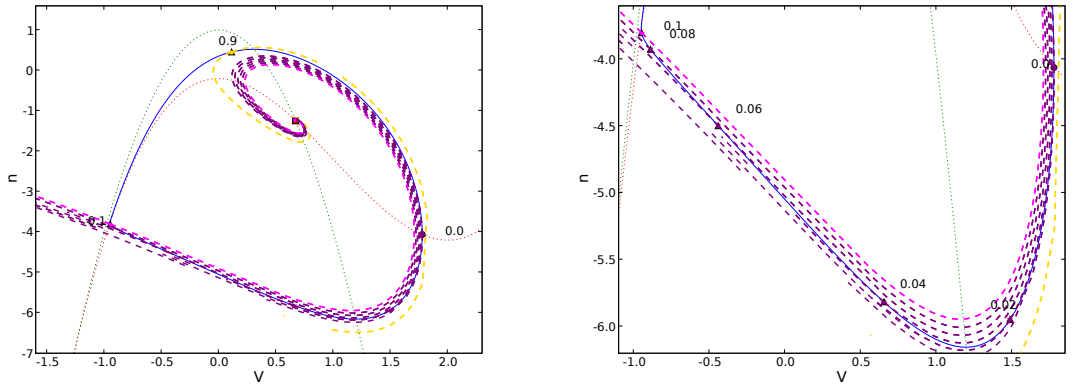

(a) (b)

Figure 4.8: Phase portrait of the HR fast subsystem and isochrons for phases in $[0.9, 0.1]$, $h = 1.8$. Isochrons with phases in $[0.0, 0.1)$ are colored purple; the 0.9 isochron, yellow; the 0.1 isochron, pink. (a) Full orbit. (b) Close-up of early phase region.

The effect of a small excitatory perturbation, such as that approximated in the linear BPRC method or direct BPRC calculations at low g_{syn}, is to move the trajectory away from the limit cycle in the positive V direction. Imagine the action of such a perturbation as a short horizontal line segment in the phase plane with its left end point on the limit cycle. The right end point ('perturbation point') marks the position of the trajectory after perturbation. As the left end point moves around the limit cycle, the intersection of the perturbation point with the isochrons forms a curve in the phase plane. Following this curve, we can trace the phase response over the course of a spike; it is a fast subsystem approximation to the burst phase response curve in the full system at corresponding h values.

When the left end point phase is between 0.1 and 0.82, the perturbation point intersects the straight portions of inner isochrons for larger phases, and so the phase is advanced (negative $\Delta\phi$ according to the convention in figure 4.6). The inner isochrons are spaced further apart at larger phases in this range, so the magnitude of phase response for the same size perturbation decreases as the phase increases. Thus the linear PRC segment of figure 4.6 between $\phi \approx 0.055$ and $\phi \approx 0.075$ is negative and increasing.

As shown in figure 4.7, between 0.82 and 0.92, the perturbation point intersects curved portions of isochrons as they spiral into the unstable fixed point. In this region of phase space, the isochrons bunch together, so the magnitude of the phase advancement increases, hence we see the dip near $\phi \approx 0.075$ in figure 4.6.

After the maximum n value of the periodic orbit, starting just past phase 0.92, the perturbation point lies outside the orbit and intersects isochrons of lower phases as they wrap around the periodic orbit's depolarized edge. This configuration persists through the majority of the depolarized portion of the spike, until approximately phase 0.03 (see figures 4.7 (b) and 4.8 (b)). Around phase 0.0,

the isochrons lie nearly tangent to the periodic orbit where they intersect it, and significant portions of their inner and outer segments (away from the point of intersection) remain very close to the periodic orbit. Hence this is a region of phase delay, and there is a sharp peak in the magnitude of phase delay very close to phase 0.0, the spike maximum (*cf.* figure 4.6 near $\phi \approx 0.08$).

Past phase 0.03, the perturbation point lies inside the periodic orbit again, so that perturbation advances the phase. Since the inner (and outer) isochrons between phase 0.0 and 0.1 lie very close the periodic orbit, the magnitude of the phase change in this region is relatively large, and the change from phase 0.0 is steep. The cycle of phase response repeats beyond phase 0.1.

Late Active Segment

The configuration of the isochrons in the middle and later portions of the active segment largely resembles that of the early portion, and the corresponding regions of the linear burst PRC also have similar shapes. Figure 4.9, the phase portrait for $h = 1.95$, shows the same basic spiral pattern of inner isochrons as figure portrait 4.5. The section of the linear BPRC corresponding to $h \in [1.92341235175, 1.99914946946]$ (including the sixth spike of the full system), shown in figure 4.10, also has a shape very similar to the one seen in figure 4.6 for $h = 1.8$. The isochrons at phases in the upswing and downswing of the spike depolarization (see figures 4.11 and 4.12) are arranged quite similarly to their counterparts in the fast subsystem at $h = 1.8$.

The most significant change in the isochron geometry between $h = 1.8$ and $h = 1.95$ is that the isochrons lie closer together, particularly near the depolarized edge of the periodic orbit. This compression is visible in figure 4.9 for the isochrons at phases 0.1 to 0.6. The closeness does not simply stem from the tighter arrangement of these phase points along the hyperpolarized edge of the periodic orbit, as can

be seen by comparing it with figure 4.5.

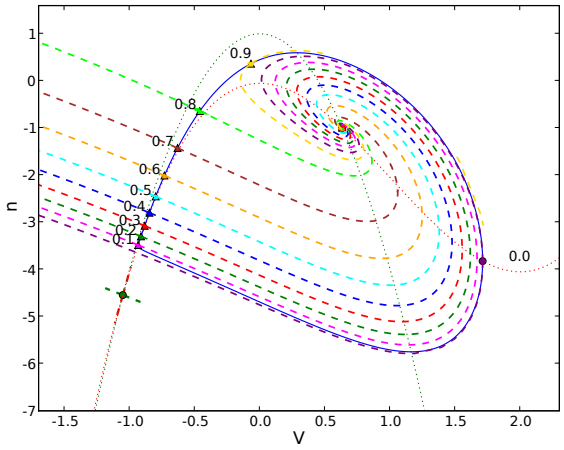

Figure 4.9: Phase portrait and isochrons in the HR fast subsystem latter half of the active segment of the full system, $h = 1.95$.

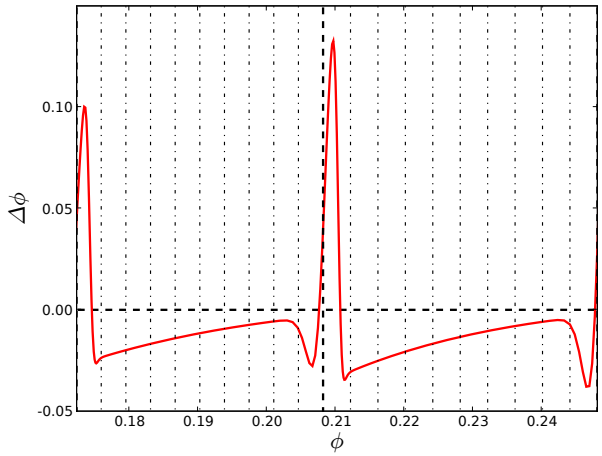

Figure 4.10: Close-up of linear burst phase response curve in the full HR model in the latter half of the active segment. The heavy dashed line marks the spike peak for spike closest to $h = 1.95$ slow variable value. Light dash-dotted lines denote equally spaced interspike phases in the full system.

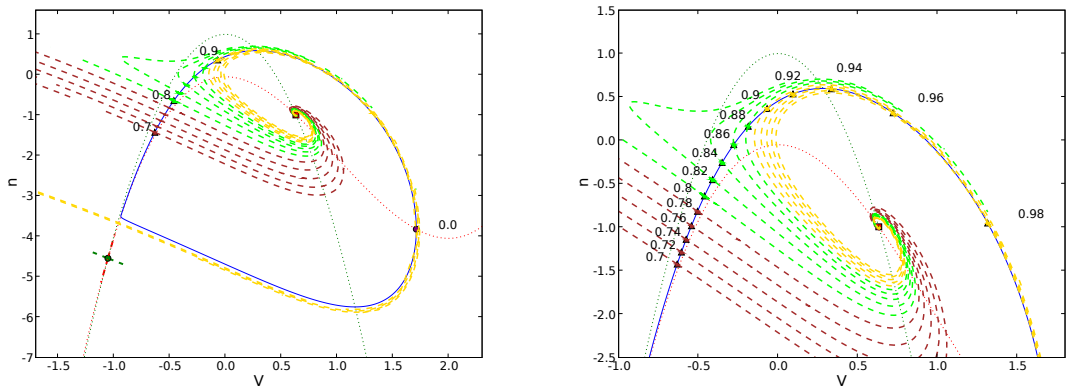

(a) (b)

Figure 4.11: Phase portrait of the HR fast subsystem and isochrons for phases in $[0.7, 0.0)$, $h = 1.95$. Isochrons with phases in $[0.7, 0.8)$ are colored brown; $[0.8, 0.9)$, green; $[0.9, 0.0)$, yellow. (a) Full orbit. (b) Close-up of late phase region.

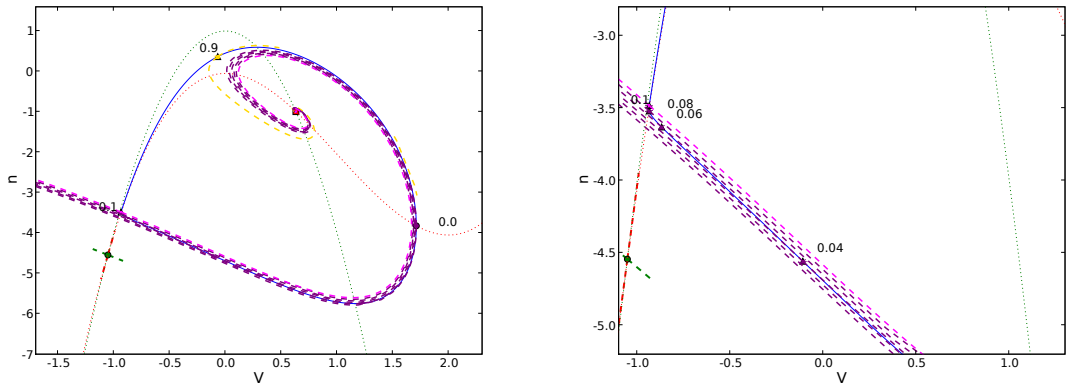

(a) (b)

Figure 4.12: Phase portrait of the HR fast subsystem and isochrons for phases in $[0.9, 0.1]$, $h = 1.95$. Isochrons with phases in $[0.0, 0.1)$ are colored purple; the 0.9 isochron, yellow; the 0.1 isochron, pink. (a) Full orbit. (b) Close-up of early phase region.

A similar pattern of compression can be seen for the isochrons at phases between 0.8 and 0.1 in figures 4.11 and 4.12. To the right of the n nullcline, the inner isochrons hug the inside of the periodic orbit. The outer isochrons remain close to the outer rim of the periodic orbit, passing between the saddle point and the periodic orbit and extending linearly beyond the left branches of the nullclines. The

saddle point moves closer to the periodic orbit as h increases and the homoclinic bifurcation approaches. This forces the isochrons closer together in order to pass through the narrowing of the gap between the saddle and the orbit.

Since the arrangement of the isochrons is roughly the same for fast subsystem at $h = 1.95$ and $h = 1.8$, the full system phase response curves have very similar forms, but with two notable differences. First, the magnitude of the phase response is larger for $h = 1.95$. This follows from the closer proximity of isochrons of a given phase to the periodic orbit. If we consider the horizontal line segment representing a voltage perturbation, as above, then for a fixed line length (perturbation strength), the perturbation point for a perturbation at a given phase will lie at nearby locations in phase space for $h = 1.8$ and $h = 1.95$. However, since the isochrons for $h = 1.95$ lie closer to the periodic orbit, the perturbation point for $h = 1.95$ lies on an isochron with a greater phase difference (further away in phase) than does the perturbation point for $h = 1.8$. This difference is reflected in the greater magnitude of phase response in the full subsystem, as seen in figure 4.10. This pattern of isochron compression progresses as h increases, so that the isochrons lie increasingly close together over the course of the active segment, and the magnitude of phase response in the full system grows accordingly.

The second difference between the linear PRCs is that the peak of phase response is shifted further past the position spike peak. The maximum n value of the periodic orbit now lies near 0.94, rather than 0.92 for $h = 1.8$, so that the zero crossing of phase response in the full system is shifted closer to the spike maximum. The point of maximum proximity of the outer isochrons to the periodic orbit is shifted further past phase 0.0 as well. In addition, the h value of the spike peak pictured in figure 4.10 is 1.96048585711, so that the exactly corresponding fast subsystem has even greater isochron compression than the one drawn for

$h = 1.95$. These differences in the isochron configuration and h value produce a phase response peak that lies further to the right of the spike peak.

Active Segment Termination

The active segment of the HR burst cycle ends in a homoclinic bifurcation in which the saddle point and the periodic orbit merge. This seals the gap through which the outer isochrons for phases near 0.0 must pass, and it increases the period of the orbit towards infinity. As the homoclinic point approaches, the inner isochrons press closer to the inner rim of the periodic orbit, and outer isochrons along the depolarized portion of the periodic orbit are forced closer to the orbit's outer edge. Outer isochrons in the hyperpolarized part of the orbit straighten, extending further and more linearly in the $-V$ direction. These changes can be seen in figures 4.13, 4.15, and 4.16, which show the isochrons and phase portraits for the fast subsystem at $h = 2.085$, very close to the bifurcation point at $h \approx 2.08560088198$.

The periodic orbit is destroyed in the homoclinic bifurcation; afterwards, isochrons do not exist and phase has no meaning in the fast subsystem. Thus we expect a significant change in the phase response of the full system near the end of the active segment. Figure 4.14 shows the linear phase response curve for the full system at the end of the active segment. The left (penultimate) spike peak of the figure occurs at $h \approx 2.04023469758$, and the final spike, marked in the center of the figure, occurs at $h \approx 2.08623316653$. The phase response near the final spike is indeed quite different from the phase response near preceding spikes.

It is possible to derive analytic approximations to the PRC for spiking neural models near a homoclinic bifurcation [14], but it is perhaps more informative to consider the phase portraits and isochron geometry of the fast subsystem in order to understand the shape of the PRC in the full system.

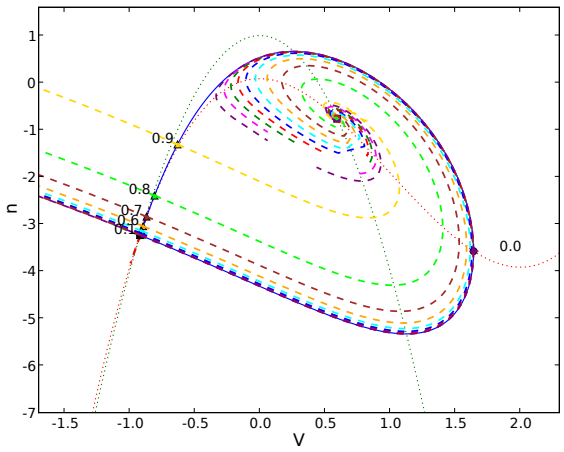

Figure 4.13: Phase portrait and isochrons in the HR fast subsystem near the end of the active segment of the full system, $h = 2.085$.

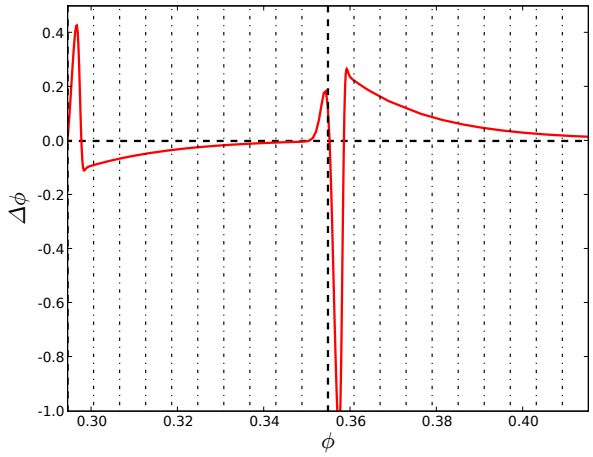

Figure 4.14: Close-up of linear burst phase response curve in the full HR model at the end of the active segment. The heavy dashed line marks the spike peak for spike closest to $h = 2.085$ slow variable value. Light dash-dotted lines denote equally spaced phases in the full system.

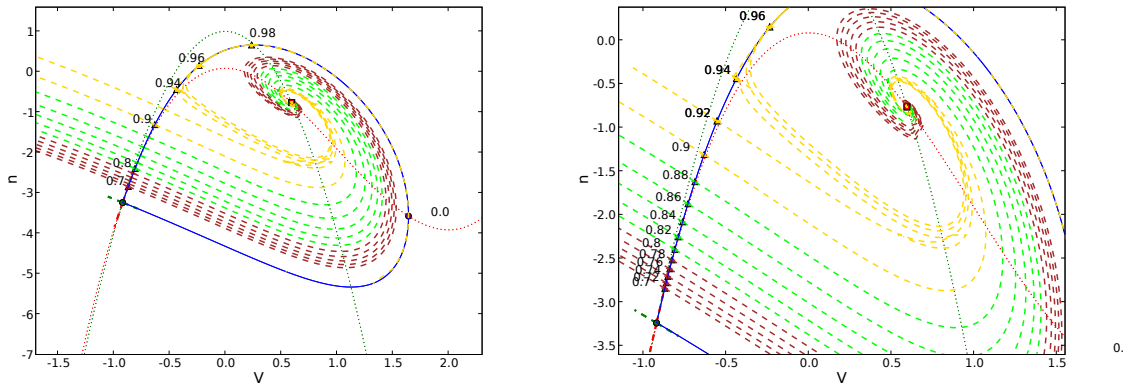

(a) (b)

Figure 4.15: Phase portrait of the HR fast subsystem and isochrons for phases in $[0.7, 0.0)$, $h = 2.085$. Isochrons with phases in $[0.7, 0.8)$ are colored brown; $[0.8, 0.9)$, green; $[0.9, 0.0)$, yellow. (a) Full orbit. (b) Close-up of late phase region.

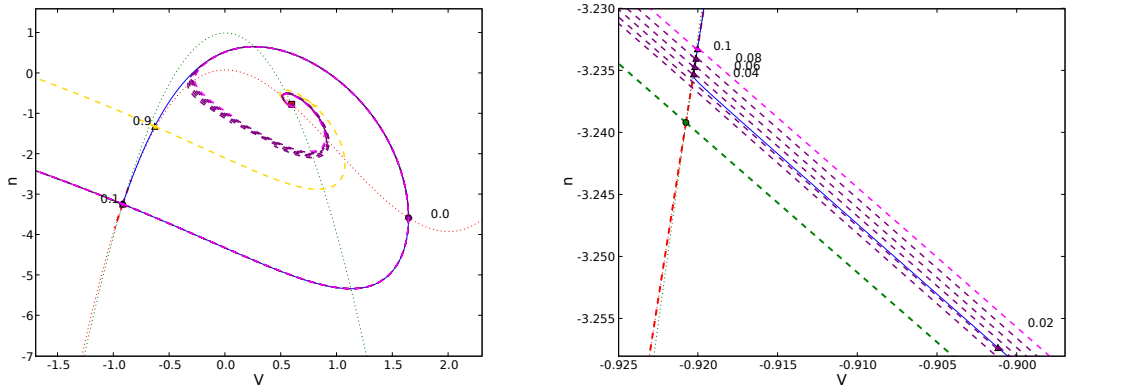

(a) (b)

Figure 4.16: Phase portrait of the HR fast subsystem and isochrons for phases in $[0.9, 0.1]$, $h = 2.085$. Isochrons with phases in $[0.0, 0.1)$ are colored purple; the 0.9 isochron, yellow; the 0.1 isochron, pink. (a) Full orbit. (b) Close-up of early phase region near saddle point.

Before the final spike peak, the full HR system responds to perturbation with relatively large phase delay, which reaches a maximum just before the spike peak. This phase delay occurs for the same reasons as the spike upswing phase delays at earlier spikes in the active segment.

Immediately after the spike peak, however, there is an extremely large, abrupt

switch to phase advancement, after which there is an abrupt return to phase delay. This phase delay gradually declines; the peak of this last phase delay marks the transition between PRC segments (1) and (2).

The sharp phase advancement is due to the qualitative change in the fast subsystem at the homoclinic point, which occurs at a (V, n, h) phase space point in the full system that projects to a point (V, n) lying on the periodic orbit at a phase just before 0.0 in the fast subsystem. At the homoclinic point and beyond, the isochrons no longer exist, but one can think of their 'ghosts' as merging with the periodic orbit during the homoclinic bifurcation. The outer isochrons along the depolarized portions of the periodic orbit merge with the right edge of the orbit, and their linear parts, which passed between the saddle and the periodic orbit, merge with the lower half of the periodic orbit and the stable manifold of the saddle.

Loosely speaking, each of the isochrons become tangent everywhere to the periodic orbit, and this tangency occurs first near the spike peak at phase 0.0. This means that the slight perturbation used to construct the PRC no longer records phase delay around 0.0; its perturbation point no longer touches any isochrons after the homoclinic bifurcation. Instead, any small perturbation in the V direction crosses the stable manifold of the saddle and leaves the perturbation point in the basin of attraction of the stable fixed point. This stable fixed point is the one that the full system tracks during quiescence; the attraction of the perturbed trajectory to the stable fixed point corresponds to advancing the onset of quiescence and therefore substantially advancing the phase of the full burst cycle.

The large magnitude of the phase advancement recorded in figure 4.14 is in some sense a numerical artifact. As the homoclinic point nears, the resolvable phases on the fast subsystem periodic orbit are compressed along the hyperpolarized edge of the orbit, except for 0.0, by definition. The corresponding compression of the

isochrons against the periodic orbit and the unbounded increase of the period cause a large, rapid increase in the size of the numerical estimates of phase delay given by the adjoint method. The discontinuity in phase response after the homoclinic point is resolved numerically as a huge phase advancement; the magnitude of this peak grows dramatically as the resolution of the numerical calculations is increased.

The final region of phase delay recorded after the homoclinic point can also be understood in terms of 'ghosts' of the structures in the phase plane before the bifurcation. Perturbations after the spike peak occur at (V, n, h) phase space points in the full system that project to points (V, n) on the periodic orbit at phases just after 0.0 in the fast subsystem. Prior to the homoclinic bifurcation, the perturbation points corresponding to these phases would have lain inside the periodic orbit and above the stable manifold for the saddle. The trajectories followed by the system from the perturbation points remain inside the stable manifold, tracking it to the vicinity of the saddle, and then follow the unstable manifold of the saddle until it joins the stable fixed point. This extended excursion, mimicking the addition of a spike, is recorded as a large phase delay in the linear PRC.

Before considering the case of strong perturbations, we note that the isochron portraits above appear to represent the first calculations of isochrons for fast subsystem cross-sections of a bursting neural model. Since the fast subsystems we consider are derived via direct fast-slow dissection, taking the singular limit of the full system for fixed slow variable values, they likely present the most accurate fast subsystem approximation to the phase response dynamics of the full system.

Our portraits of the fast subsystem phase plane and isochrons differ substantially from those presented in [16, 15, 130] for a planar reduction of the Rose-Hindmarsh model.[3] For those calculations, performed for only for 10 phases, the

[3]This model is different from the HR Hindmarsh-Rose model, but related in form. It is the planar reduction of a three-dimensional thalamic cell model [190], which is itself a reduction of a model that modifies the original Hodgkin-Huxley equations to include an A-current [48].

isochrons radiate nearly linearly from the central fixed point, crossing the periodic orbit almost normal to it. In contrast, the isochrons for the fast subsystem given by (4.1) have a complicated geometry, bending around the periodic orbit in a very different fashion; their geometry changes significantly as the homoclinic point approaches. These differences, and the ability of our isochron calculations to explain the salient features of the burst phase response curve[4] for the full system, indicate that the assumptions and reductions used in studying the phase response dynamics of neural oscillators presented in [14, 16, 15] may not be valid for more realistic neuron models, especially those which endogenously burst. In particular, our results directly contradict a central assumption used in [14, 16] to derive analytic approximations of phase response near bifurcations, namely that phase response is approximately 0 at the peak of a spike.

4.4 Strong Perturbations

Strong perturbations to the HR model, *i.e.* $g_{\text{syn}} \geq 1$, may affect the spike structure of the perturbed burst in three ways that are closely related to the model's phase response: alteration of the intraburst interspike interval, deletion of spikes from the active segment, or addition of spikes to the active segment. Perturbations that change the spike number typically also induce a large change in phase, while changes in spike timing that leave the spike number unchanged have a weaker effect on phase response.

Figures 4.17, 4.19 and 4.20 illustrate the three cases, showing representative trajectories of the full system in three dimensions. In each figure, the unperturbed (reference) trajectory is drawn as a solid black line, and the perturbed trajectory is drawn with three colors: blue for the portion of the trajectory prior to perturba-

[4]Calculated using the adjoint method advocated and used in [14, 16]

tion, red for the portion during the perturbation, and yellow for the portion after perturbation. The two-dimensional time series representation in figure 4.18 follows the same color key as the three dimensional figures. The perturbations used in each figure are inhibitory synapse-mediated spike injections, but the pictures for excitation and for other synaptic forms and their interpretations are very similar, and their interpretations are essentially identical.

Along with the full system trajectories, the figures show lines of fixed points from the fast subsystems for the relevant h values. The line of stable fixed points is drawn as a solid green line, and a solid light blue line represents the line of saddle points; these join at a saddle-node bifurcation near the left front edge of each figure. The stable eigendirections of the saddle points are drawn in green, and the unstable eigendirections are drawn in red. Note that the values of the voltage variable, V, for the fixed points and saddles are always lower than the minimum voltage values of the fast-subsystem periodic orbits and of the full system trajectory during its active segment.

4.4.1 Spike Shift

At most phases, strong perturbations do not change the spike number of the burst, and the explanation for the shape of the PRC curve in PRC segments (2) and (3) is analogous to the explanation for weak perturbations. For most of the quiescent segment, the full system trajectory tracks the stable fixed point of the fast subsystem, returning rapidly to the fixed point and thus incurring little phase change after voltage perturbations. Perturbations near the end of the quiescent segment, where the stability of the fixed point is waning, may move the trajectory into the domain of attraction for the stable periodic orbit and so accelerate the onset of the active segment of the next burst cycle, thereby inducing phase advancement.

In neither of these two cases does the spike number change in the current burst, nor is the intraburst interspike timing affected, since the active segment of the current burst cycle is already complete. Perturbations during the active segment of the burst that do not affect the spike number typically alter the interspike intervals for the spikes following the perturbation, as illustrated in figure 4.17. Note that the inhibitory perturbation depicted occurs near the base of a spike, when the voltage value of the full system trajectory brings it closest to the line of fast subsystem saddle points. Although it depresses the voltage variable in the full system, the perturbation does not bring the trajectory close enough the saddles for there to be any interaction.

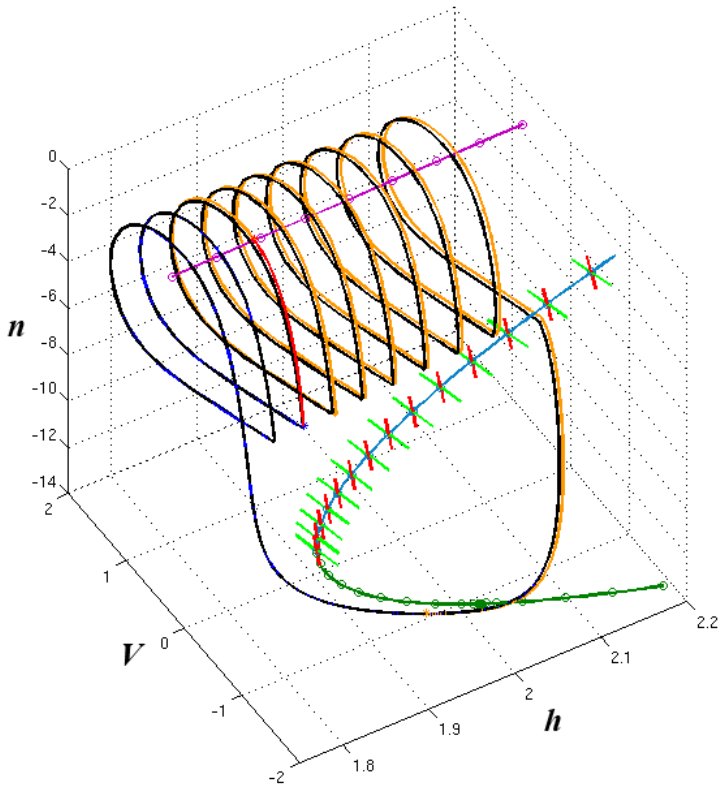

Figure 4.17: Shift in intraburst interspike timing (spike shift).

The effect of the inhibitory perturbation is to decrease V, thus slowing the change in h, relative to its value in the reference trajectory. This delays the next spike peak, a timing change which propagates to the subsequent spike times approximately linearly (see figure 4.18). An excitatory perturbation increases V and accelerates the change in h, triggering an early spike peak and shifting the immediately following spikes to earlier times.

Even without changing spike number, the effect of excitation can be phase delay, although it typically accelerates the advent of the subsequent spike (see figure C.2 (c) and (d)). As explained below in subsection 4.4.3, this paradoxical effect is due to changes in the interspike intervals near the end of the active segment, where the fast subsystem is approaching the homoclinic bifurcation point.

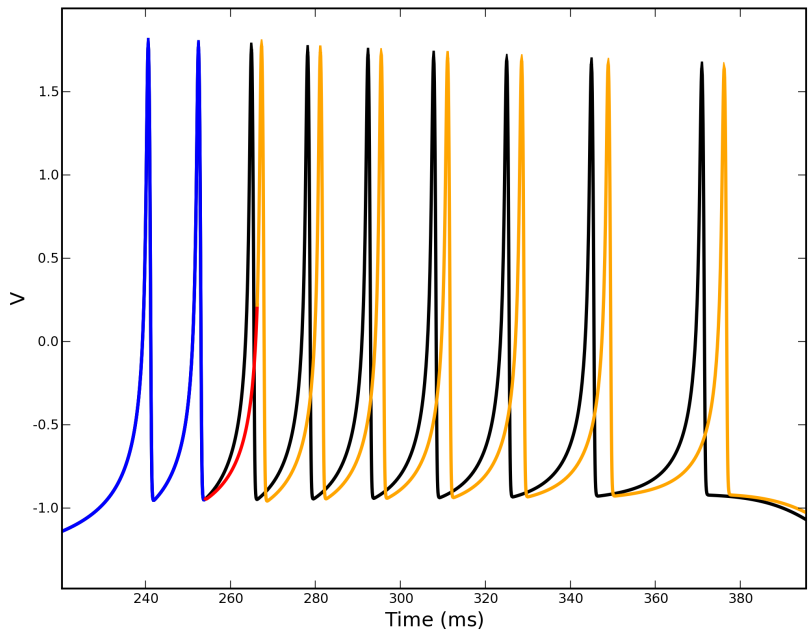

Figure 4.18: Time series trace of spike shift perturbation.

4.4.2 Spike Deletion

Spike deletion occurs when the full system trajectory is knocked away prematurely from the basin of attraction around the stable periodic orbit and enters the basin of attraction of the stable fixed point. In this case, the burst cycle ends early as one or more spikes are dropped from the end of the active segment. Inhibitory perturbation drives the voltage value to a hyperpolarized level that is more negative than the line of saddle points in the fast subsystem. The perturbed trajectory rapidly approaches the saddles along the stable eigendirection and then quickly leaves along the unstable eigendirection once it has crossed the line of saddle points, as shown in figure 4.19.

Once past the saddles, the trajectory is strongly and immediately attracted to the stable fixed point corresponding to quiescence. The full system trajectory then tracks the stable fixed points as h recovers. The duration of this quiescent segment is shorter than normal in proportion to the difference in h values at the end of active segments of the perturbed and reference trajectories. This change in duration is typically negligible. By the onset of the next burst cycle, the perturbed trajectory recovers to follow a path nearly identical to the reference trajectory, as seen in figure 4.19. The effect of strong perturbations that delete spikes is to shut off the active segment of the burst early, thus resetting the trajectory for a new burst cycle and causing a large phase advancement.

Though not shown in figure 4.19, the magnitudes of both eigenvalues for the saddle point grow by about one and a half orders of magnitude as h increases and the homoclinic point approaches, though the stable eigenvalue is always about three orders of magnitude larger than the unstable eigenvalue. Similarly, the eigenvalues for the stable fixed point also increase in magnitude towards the homoclinic point, with the larger eigenvalue typically one or two orders of magnitude larger than

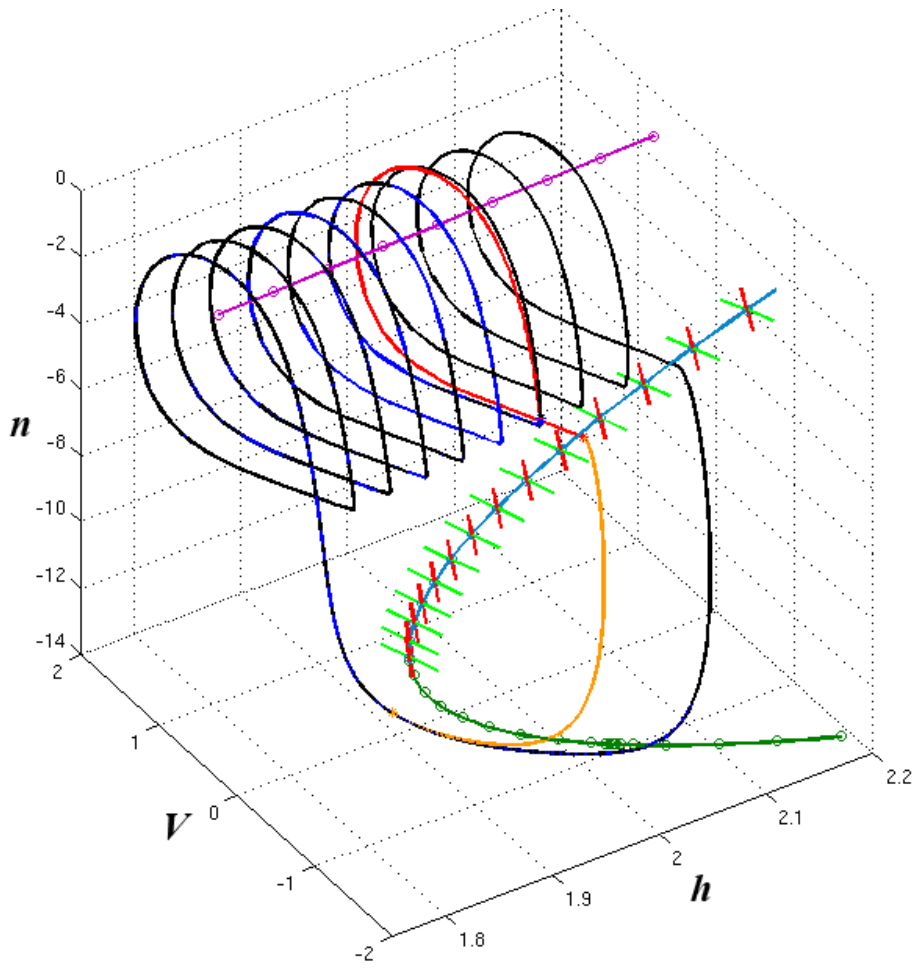

Figure 4.19: Spike deletion.

the stable eigenvalue of the saddle at the same h value. At the same time, the stable manifolds of the saddle points lie very close to the periodic orbits near the homoclinic point. This increase in the strength of attraction to and repulsion from the fixed points, along with the greater proximity of periodic orbits to the saddle points and their stable manifolds means that perturbations can more easily push the full system trajectory past the line of saddles, across the saddle points' stable manifolds, and towards the stable fixed point at h values closer to the homoclinic bifurcation that terminates the active segment. Said differently, perturbations of a given strength that occur near the end of the active segment are more likely to

drive the system into quiescence and delete spikes than those near the start of the active segment. Inhibitory perturbations at the very start of the burst, *i.e.* at h values below the saddle-node bifurcation, cannot change the spike number, and so they have a phase delaying effect by retarding the first spike.

4.4.3 Spike Addition

Spike addition in the HR model is critically related to the behavior of the system near the homoclinic bifurcation at the end of the active segment. In the homoclinic bifurcation, the periodic orbit merges with the stable and unstable manifolds of the coexistent saddle point. The period of the orbit increases as the bifurcation approaches, becoming infinite at the homoclinic point. The periodic orbit no longer exists after the homoclinic bifurcation, and the branch of the unstable manifold of the saddle which formerly wrapped around the periodic orbit now terminates at the stable fixed point. For the full system trajectory tracking these fast subsystem objects, this means that the interspike interval grows as the end of the active segment nears.

The final spike of the full system begins at an h value where the periodic orbit still exists in the family of fast subsystems, and it finishes at an h value past the homoclinic point, so that it is drawn to the stable fixed point representing quiescence. The closer the end of the full system spike is to the homoclinic point, the longer the final spike lasts because it tracks periodic orbits with periods diverging to infinity. The final interspike interval depends on this position relative to the homoclinic point.

Perturbations add spikes by altering the full system trajectory such that it tracks the fast subsystem periodic orbits long enough to make extra revolutions prior to the homoclinic point. In effect, they add an extra spike at the beginning of

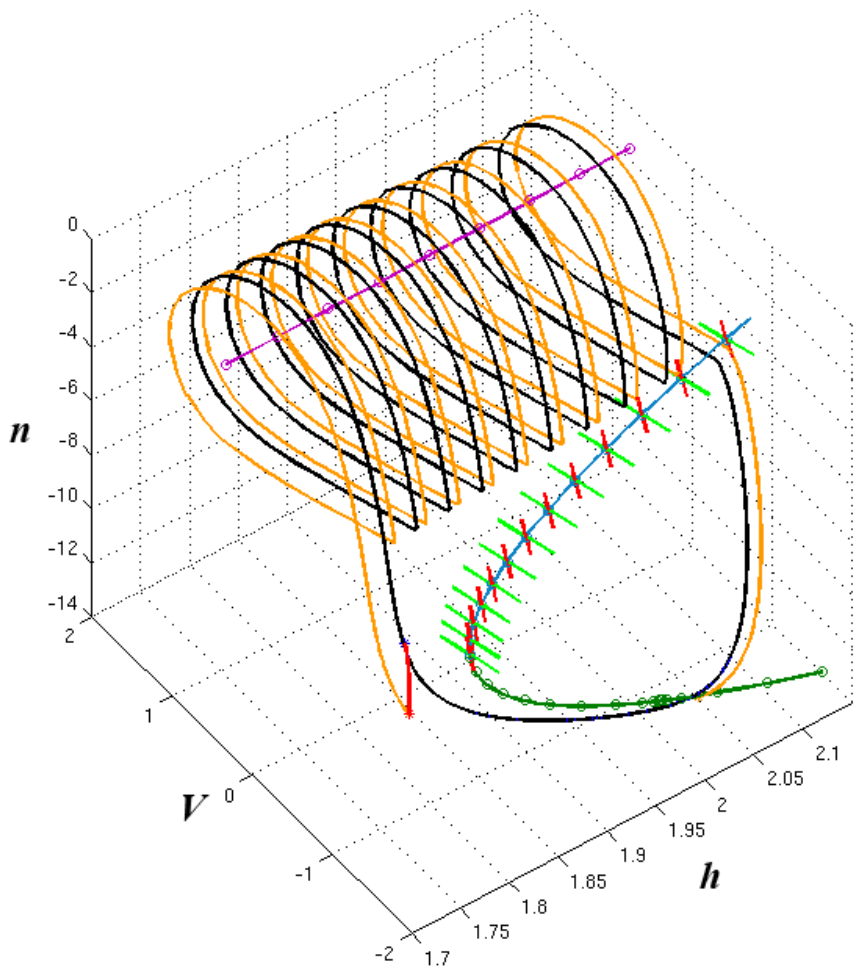

Figure 4.20: Spike addition.

the active segment. As seen in figure 4.20, early inhibition shifts the burst trajectory in the positive h direction, so that the trajectory makes an extra revolution before terminating past the homoclinic point. Note that the perturbation does not necessarily have to occur at the start of the active segment to add a spike, but later perturbations are more likely to have the spike deletion effects described above in section 4.4.2. Increasing the spike number adds to the burst cycle period an amount equal to the duration of the extra spike(s), and it may also increase the time taken for the final spike by shifting the onset of the last spike with respect to the homoclinic point so that the final interspike interval changes.

The behavior of the trajectory near the homoclinic point explain how excitation at the start of the active segment may cause phase delay without changing spike number. Excitation causes the next spike to occur prematurely and also shifts the position of the subsequent spikes to earlier times. This means that the spikes occur at lower h values, and so a greater portion of the orbit may occur prior to the homoclinic point where the period of the fast subsystem periodic orbits it tracks are longest. The effect is to extend the final interspike interval. The elongation of the final spike may counteract any phase advancing effects from the acceleration of earlier spikes, thus resulting in overall phase delay.

4.5 Discussion

The analysis presented here explains the outstanding features of the phase response curves calculated for the HR model in chapter 3. Fast-slow dissection, phase plane analysis, and isochron calculations illuminate the mechanisms underlying the phase response of the model to both small and large perturbations. Our results demonstrate the importance of multiple time-scale dynamics in shaping the phase response features of bursting neural models, characteristics that are important to understand in order to develop a comprehensive theory of how coherent patterns of activity emerge in networks of bursting neurons.

The phase response of the HR model to different forms of direct perturbation closely resembles its linear PRC over a broad range of perturbation strengths, and as do the PRCs of biophysically realistic, conductance-based neuron models. The models' PRCs share a number of striking features, including visual decomposition to three distinct segments and a strong association between spike times and peaks of phase response in the active segments of their bursts. Our analysis for the HR model shows that the changing geometry of isochrons in the fast subsystem

explains the salient features of phase response in the regime of weak perturbations.

Spike shift, spike deletion, and spike addition account for the most significant phase response dynamics at the upper ranges of perturbation strength. The arrangement and stabilities of the fixed points of the fast subsystem at different phases determine the susceptibility of the full system to each type of perturbation event. Our phase plane analysis of the strong perturbation regime explains the mechanisms that account for the three possible effects.

Our analysis appears to be exhaustive for the HR model, except in the transition regime between weak and strong perturbations where spike number does not necessarily change, but the shape of direct BPRCs begins to deviate significantly from the shape of the linear BPRC. Investigating this case requires first locating the critical g_{syn} values demarcating the transition region, a time- and computation-intensive endeavor.

Given the striking visual similarity of other models' BPRCs to those of the HR model, it seems likely that similar factors shape their phase responses and that analogous explanations obtain in their cases. The planarity of the HR fast subsystem is essential to our analysis, and so we cannot directly apply the same approach to most of the other models examined in chapter 3. Reductions of those models that produce planar fast subsystems may be amenable to a similar analysis.

Our analysis also depended implicitly on the 'piecewise' monotonicity of the evolution of the slow variable h in the full system. The three-dimensional pre-Bötzinger model has a planar fast subsystem, but its slow variable evolves 'non-monotonically'. This significantly complicates attempts to analyze its phase response with the approach used in this chapter. The back and forth motion of the slow variable causes the full system trajectory to weave in and out of the stable and unstable manifolds in the fast subsystem near the homoclinic point, which adds

greatly to the complexity of the spike addition and deletion mechanisms near the end of the active segment of the burst. In addition, the extreme stiffness of the pre-Bötzinger model seriously hampers numerical investigation of both the full and fast subsystem, particularly hindering the necessary manifold and isochron calculations.

The study presented in this chapter relies on intuitive arguments and careful numerical calculations, rather than mathematical proofs, to explain interesting features of phase response and their underlying mechanisms. The geometric reasoning and fast-slow analysis we use are very similar to the analysis in Terman's studies of mechanisms of spike number change and transitions between tonic spiking and bursting [216, 217], and it seems likely that the arguments presented here could be translated into rigorous proofs in an analogous manner.

CHAPTER 5

BURST PHASE RESPONSE IN NETWORKS: REDUCTION TO ALGORITHMICALLY COUPLED DISCRETE MAPS

5.1 Introduction

Understanding how phase relationships are established and maintained in networks of bursting neurons is an essential step towards developing a theory of central pattern generators. Of particular biological interest are the stable phasing arrangements for a given CPG architecture and the transient behavior (sequences of intermediate phase configurations and rates of convergence) of the network as it approaches a stable state. Beneath the patterning of CPG output lie the combined complexities of neuronal bursting and synaptic interaction; deciphering the interplay of their influences requires mathematical and computational modeling approaches in addition to biological experimentation.

Previous chapters report our studies of various aspects of phasing in CPGs, *viz.* the development and testing of a biologically detailed locomotor CPG model (chapter 2), empirical investigation of the phase response characteristics of biophysically realistic models of bursting neurons (chapter 3), and mathematical analysis of the mechanisms that shape typical burst phase response (chapter 4). These investigations point out a number of issues regarding the larger enterprise of studying phasing patterns of networks of bursting neurons.

First, exploring biophysically realistic CPG models, even substantially reduced models, is quite challenging computationally and conceptually. Large numbers of computationally expensive simulations are needed to study the stable phase configurations and transient behavior of the model. High dimensionality and broad parameter regimes make comprehensive exploration of the space of synaptic weight-

ings and initial phase configurations difficult to plan and execute; visualizing and interpreting the results is also challenging.

Second, multiple time-scale dynamics and strong perturbations play a prominent role in determining the phase response of bursting neurons connected in networks that accurately portray biological systems. Neurons interact via individual spikes which operate on a relatively fast time-scale, but whose functionally relevant effects are measured at the level of bursts, on a slower time-scale. Achieving biologically reasonable phasing behavior in CPG network models may require relatively strong coupling strengths, and the interacting neurons may be perturbed far from their uncoupled states. Mathematical studies of phasing in networks of coupled neurons has traditionally focused on models based on assumptions counter to these observations (phase oscillator models, weak coupling); their broad applicability to questions of phasing in networks is somewhat dubious.

Third, although the phase response characteristics of bursting neurons are much more complicated than those of tonically spiking neurons, they are nonetheless comprehensible and display significant regularities. In both weak and strong coupling regimes, perturbations have stereotyped effects on burst phase and spike number, suggesting that the dynamics that shape phase response are intrinsically low-dimensional or constrained in some fashion. The simpler structure of these dynamics may be exploited to facilitate modeling and analysis of phasing in networks of bursting neurons.

In this chapter, we present a method for reducing the response of a bursting neuron to perturbation to a collection of discrete maps. When coupled together appropriately, these maps can efficiently approximate the phasing behavior of bursting neurons in a network. We first review prior related work, contrasting its limitations with results presented in previous chapters. Next, we describe a set of

discrete map reductions of single neuron phase response dynamics that depend on assumptions supported by our prior results. We then present algorithms to couple these maps and to keep track of their interactions so as to simulate phasing activity for a given network architecture. Finally, we apply this technique to an example network comprising biophysically realistic bursting model neurons, and we compare the maps' predictions to simulations of the full network model. With further refinement, our method of using algorithmically coupled discrete maps promises to provide a useful approach for efficiently obtaining close approximations to stable configurations and transient behavior.

5.2 Discrete Map Reduction

The idea of reducing ODE models to discrete maps in order to capture the essentials of specific phenomena is commonly used in the field of dynamical systems, and it has been particularly fruitful in mathematical neuroscience. The conceptual variant developed here uses multiple maps to model the effect of an individual spike on a post-synaptic neuron's burst cycle, interspike timing, and spike number. This information is then applied iteratively to predict changes in the relative phasing of bursts in networks of coupled neurons. Below we review related prior work and then present the details of our approach and its implementation.

5.2.1 Background

Coupled Phase Response Curves

Using phase response curves to predict the effect of synaptic inputs on a neuron's oscillatory behavior is a standard approach for addressing phasing in neuronal networks [120, 73, 72, 140]. Maps based on PRCs predict a post-synaptic neuron's

shift along its limit cycle due to perturbations from pre-synaptic neurons. The PRC maps are coupled to reflect the network structure; chains, rings, and all-to-all coupling are the most commonly modeled architectures, since they are most amenable to mathematical analysis [33, 83]. Synaptic interactions are considered to be instantaneous, the effects of multiple perturbations are presumed to be additive, and phase response is assumed to scale linearly with perturbation strength. Linearizations about fixed points of the coupled maps are used to determine the stability of particular phase configurations.

The mathematical theory has largely been worked out in the context of phase oscillator models, and supporting numerical examples are almost always based on relatively simple, low-dimensional models of tonically spiking neurons. Synchronous solutions produced by excitation [71, 159, 70] or inhibition [224, 148] have been objects of particular interest. Investigations going beyond phase oscillator models have focused on differences between Type I and Type II oscillators in terms of their synchronization properties [70] and the reconstruction of their phase response curves from real data [79]. Nearly every phasing study based on the PRC approach is restricted to the single spike, tonic oscillator setting.

Spike Time Response Curves

Similar to PRCs are *spike time response curves* (STRCs), which measure the change in a post-synaptic neuron's spike timing due to a single spike perturbation [4]. STRCs use time, rather than phase, as their metric, so that they remain well-defined even if strong inputs significantly alter the period of the post-synaptic cell (large changes in cycle period make phase ill-defined). STRCs may be coupled together to produce *spike time difference maps* (STDMs), which are analogous to coupled PRCs. Linear analysis of STDMs predicts the existence and stability of

relative 'spike timing' (equivalent to phasing) configurations [128, 4].

The chief advantage of STRCs and STDMs over coupled PRC techniques is their robustness in strong perturbation regimes and transient periods, where cycle lengths may vary substantially. This has enabled the analysis of phenomena such as 'cycle skipping' in pairs of strongly excitatorily coupled neurons [4] and state transitions in small networks with mixed excitation and inhibition [172]. Experimental studies have recreated STRCs from electrophysiological recordings and have incorporated them in hybrid circuits (one model and one biological neuron) to validate model predictions of synchrony [160]. However, all STRC formulations concern the effect of a single spike input on the immediately subsequent spike time of a tonically spiking neural oscillator.

Coupled Burst Maps

Although the results of coupled PRC analyses are sometimes claimed to apply to coupled bursting neurons, few studies have considered this situation specifically. A handful of papers treat the bursting case by considering bursts as single spikes of extended duration and then applying standard PRC techniques to them, with a few modifications [32, 68, 165, 34, 151]. A 'burst' is defined as a single continuous period of repetitive spiking; the intervals between spiking periods are not considered part of the burst (*cf.* our active and quiescent segment terminology). Associated with a burst is its 'phase response curve' (bPRC), which determines the change in timing of the beginning of the burst in response to perturbation, and its 'burst resetting curve' (BRC), which specifies the change in burst duration due to perturbation. The internal structure of bursts, *i.e.* intraburst interspike timing, is ignored. Linear analysis of compositions of bPRCs and BRCs is used to predict stable phasing configurations for simple network architectures (chains and rings)

[165, 34, 151]. Most of this analysis relies on the assumption that perturbations have only short term effects on burst duration and bPRC shape, though some work considers effects that persist through two burst cycles [165, 34]. Some attempts have also been made to combine coupled burst map analysis with biological experiments [163, 162].

We note that although studies using coupled burst maps claim that their analytical predictions apply to a broad class of network architectures and models for bursting, these analyses are supported by computer simulations of non-bursting neural models, *e.g.* Type II Morris-Lecar neurons [165, 34]. The oscillations of the non-bursting model are divided into segments labeled 'burst' and 'interburst' according to an arbitrary threshold; the 'burst' portion of the model's waveform is presumed to adequately approximate the voltage envelope of the active segment for a hypothetical bursting neuron. Validations of the coupled burst map approach using schematic or biophysically realistic neuronal models that truly burst have not been published; spike-level interactions are not considered in the analysis or simulations.

The results of previous chapters emphasize the tenuousness of several of the assumptions upon which the aforementioned methods rest. To briefly recapitulate: Burst PRC shape changes significantly with perturbation strength; phase response is quite different during the active and quiescent portions of a burst; and phase response in the active segment is closely related to a burst's internal spike structure. A single pre-synaptic spike can alter the timing of multiple spikes in the post-synaptic neuron, or it may perturb the post-synaptic neuron far from its original limit cycle, changing its spike number. The greatest changes in burst phasing are due to spike addition and deletion, and changes in spike number are highly

sensitive to the phase at which the perturbation is applied.

In particular, the multiple time-scale structure of bursting neuronal dynamics makes individual spikes much more important than the aforementioned approaches presume. Events at fast time-scales (spikes) may have large consequences at slower time-scales (burst cycles). Furthermore, coupling feeds each spike's effects back from post-synaptic neurons to pre-synaptic neurons, potentially amplifying its downstream influence.

5.2.2 Assumptions

The analysis presented in previous chapters for the phase response dynamics of bursting neurons indicates that single spikes have a few stereotypical effects on the structure of the burst cycle: shifting spike timing[1], spike addition, and spike deletion. Changes in burst phase are a consequence of these effects. A small number of key parameters and variables appear to shape the phase response, *viz.* perturbation phase, slow variable value, and synaptic strength. This implies that the burst phase response has effectively low-dimensional dynamics, and by taking into account interactions across multiple time-scales, we may exploit this low-dimensionality to compute with discrete maps, rather than ODEs.

Our discrete map reductions rely on a number of assumptions about the perturbations and the model neurons' phase response:

1. Perturbations are shorter in duration than the interspike interval.
2. The trajectories of coupled neurons lie close to their unperturbed, uncoupled orbits.
3. After perturbation, the system's trajectory rapidly relaxes back to the original periodic orbit.

[1] In the current or subsequent burst cycle.

4. Phase response in the active and quiescent segments of the burst may be treated separately.

5. The dynamics of the active segment are fully characterized by spike times and slow variable.

6. Perturbation resets the burst phase via a linear shift of spike times, possibly concomitant with spike deletion or addition.

For synapse models having forms like equation 2.7, assumption 1 requires the synaptic gating variable to decay to nearly zero within one interspike interval. Greater system stiffness helps fulfill assumption 3; weaker perturbations also help fulfill assumptions 2 and 3, but weak coupling is not required to apply the discrete map reductions.

The first three assumptions support treating each pre-synaptic spike's effects as being independent of other spikes, and using the uncoupled neuron's phase response characteristics to estimate its responses when coupled. The last three assumptions relate to our particular form of reduction and discretization of a burst and its phase response. The results of previous chapters agree with these premises. We use the information acquired in computing a single BPRC to construct a mapping of burst spike trains, as explained in the next section.

5.2.3 Discrete Map Formulation

We consider the trajectory of an individual neuron as a skeleton of spike times and interburst intervals; we omit any information about its membrane voltage, other phase space variables, etc. We decompose a neuron's burst cycle B into an *active segment* A and a *quiescent segment* Q. A is an ordered set of *spike times*; the ith spike time t_i represents the time at which the ith spike of the burst achieves its

peak: $A = \{t_1, \ldots, t_n\}$. The burst cycle is not assumed to begin with the first spike time of A, *i.e.* t_1 is not necessarily 0, though the active segment is presumed to precede the quiescent segment. $Q = \{q\}$ is simply the time between the final spike of A and the start of the next burst cycle; we use q to denote this time, and Q when referring to the quiescent segment. If B has n spikes, the period of B is $T = t_n + q$.

An uncoupled, unperturbed neuron is assumed to have an active segment with K spikes at known interspike intervals, $A_{\text{ref}} = \{t_1, \ldots, t_K\}_{\text{ref}}$, a quiescent segment of length q_{ref}, and period T_{ref}. We refer to the representation $B_{\text{ref}} = (A_{\text{ref}}; Q_{\text{ref}}) = (\{t_1, \ldots, t_K\}_{\text{ref}}; q_{\text{ref}})$ of the uncoupled, unperturbed neuron as the *reference burst* or *reference burst skeleton*.

When coupled, the internal structure of B may be altered by pre-synaptic spikes, which may cause a shift in the spike times, add or delete spikes to A, change the length of Q, or a combination of these. Any of these effects may also change the period of the neuron, and hence alter the notion of phase. Suppose $B = (A; Q) = (\{t_1, \ldots, t_n\}; q)$ at time t. Then we define $\alpha(\tau, B) = \tau/(t_n + q) \mod 1$ to be the *current burst phase* corresponding to the time τ.

Now consider the burst cycle of an uncoupled, previously unperturbed neuron, $B = B_{\text{ref}}$, which receives a perturbation of fixed strength at time τ. Let $B'_\tau = (A'_\tau; Q'_\tau) = (\{t'_1, \ldots, t'_L\}_\tau; q'_\tau)$ be the representation of the burst cycle after the perturbation. Let $s_\tau = \min\{t_i \in A : t \geq \tau\}$ and $s'_\tau = \min\{t_i \in A'_\tau : t \geq \tau\}$. By perturbing the neuron at every time $\tau \in [0, T]$ we obtain three burst response functions:

$$\sigma(\tau) = s'_\tau - s_\tau \tag{5.1}$$

$$\upsilon(\tau) = |A'| - |A| \tag{5.2}$$

$$\omega(\tau) = q' \tag{5.3}$$

Normalizing by the period, we may treat σ, υ, and ω as functions of phase $\phi = \tau/T$.

We now describe the effects of a single spike perturbation of fixed strength on an arbitrary burst $B = (A; Q) = (\{t_1, \ldots, t_n\}; q)$ in terms of maps based on the burst response functions. In the following, $\phi = \alpha(\tau, B)$.

Spike shift

Let index $j = \min_i\{1 \leq i \leq n : t_i \in A, t_i \leq \tau\}$. The spike shift operator Σ produces a burst with a new set of spike times according to

$$\Sigma(\tau, B) = (\{t_1, \ldots, t_j, t_{j+1} + \sigma(\phi), \ldots, t_n + \sigma(\phi)\}; q) \tag{5.4}$$

The spike shift operator converts the perturbation time τ to phase ϕ (with respect to the period T of burst B), then calculates the amount by which the next spike in the reference burst would be shifted due a perturbation at phase ϕ. It then shifts each subsequent spike time in B by this amount.

The empirical studies of burst phase response presented in chapter 3 generally support the assumption that spike shifts are linear. When there is no change in spike number, particularly for weaker perturbation strengths, most of the biophysically realistic models tested exhibit nearly linear shifts in the interspike timing of spikes after the time of the perturbation.

Quiescence

$$\Omega(\tau, B) = (\{t_1, \ldots, t_n\}; \omega(\phi)) \tag{5.5}$$

The quiescence operator converts the perturbation time τ to phase ϕ, then replaces the previous quiescent period with the length of the quiescent segment produced by perturbing the reference burst at phase ϕ.

Both empirical investigations and mathematical analysis of burst phase response indicate that single spike perturbations do not change the duration of the quiescent segment very much. The bulk of phase response in bursting neural models is concentrated in the active segment. During its quiescent segment, a neuron's trajectory closely tracks the hyperpolarized stable equilibrium of its fast subsystem, and voltage perturbations do little to accelerate its movement. The length of time it takes for the neuron to traverse its quiescent segment does not vary significantly, regardless of whether its initial conditions at the beginning of the quiescent segment reflect the normal end of the active segment or premature termination of spiking. Thus the exact form of quiescent segment adjustment that Ω takes (constant, multiplicative, additive, replacement) does not significantly affect the performance of the discrete map reduction when coupled according to the algorithms described in the next section.

Spike number change

The spike number change operator comprises two additional maps, one for spike addition and one for spike deletion:

$$\Upsilon(\tau, B) = \begin{cases} v(\phi) = 0 & : \quad (A, Q) \\ v(\phi) < 0 & : \quad \Upsilon^{+}(\tau, B) \\ v(\phi) > 0 & : \quad \Upsilon^{-}(\tau, B) \end{cases} \tag{5.6}$$

Let $l = v(\phi)$. Write the spike times of A_{ref} as $\{t_1^r, \ldots, t_K^r\}$, and let $\Delta_i^r = t_i^r - t_{i-1}^r, 2 \leq i \leq K$. Then the spike addition map is given by

$$\Upsilon^+(\tau, B) = \begin{cases} n \geq K \quad : & (\{t_1, \ldots, t_n, t_n + \Delta^r_K, t_n + 2\Delta^r_K, \ldots, \\ & \qquad t_n + l\Delta^r_K\}; q) \\ n < K, \quad : & (\{t_1, \ldots, t_n, t_n + \Delta^r_{n+1}, t_n + \sum_{i=1}^{2} \Delta^r_{n+i}, \ldots, \\ n + l \leq K & \qquad t_n + \sum_{i=1}^{l} \Delta^r_{n+i}\}; q) \\ n < K, \quad : & (\{t_1, \ldots, t_n, t_n + \Delta^r_{n+1}, t_n + \sum_{i=1}^{2} \Delta^r_{n+i}, \ldots, \\ n + l > K & \quad t_n + \sum_{i=1}^{K-n} \Delta^r_{n+i}, t_n + \sum_{i=1}^{K-n} \Delta^r_{n+i} + \Delta^r_K, \ldots, \\ & \qquad t_n + \sum_{i=1}^{K-n} \Delta^r_{n+i} + (n + l - K)\Delta^r_K\}; q) \end{cases} \tag{5.7}$$

In the event that A has as many or more spikes than A_{ref}, Υ^+ appends l spikes having interspike intervals equal to the time between the ultimate and penultimate spikes of the reference burst. If A has fewer spikes than A_{ref}, and the magnitude of l implies that A' will also have fewer spikes than A_{ref}, then Υ^+ appends l spikes to A at interspike intervals identical to those of spikes n to $n + l$ of the reference burst. If A has fewer spikes than A_{ref}, and the magnitude of l implies that A' will have more spikes than A_{ref}, Υ^+ appends $K - n$ spikes to A at interspike intervals identical to those of the last $n+l-K$ spikes of the reference burst. It then appends $n+l-K$ spikes having interspike intervals equal to the time between the ultimate and penultimate spikes of the reference burst.

The spike addition phenomena observed in biophysically realistic models of bursting typically involves extra revolutions about the fast subsystem periodic orbit, or its 'ghost,' just before or just after the homoclinic point. The final interspike interval of the unperturbed burst is close to the duration of spikes added in this fashion, and so the approximation of adding spikes with that interspike interval to the end of the active segment serves as a reasonable caricature of the actual mechanism of spike addition.

Let $m_\tau = \min(|\{t_i \in A : t \geq \tau\}|, |l|)$. Then the spike deletion map is given by

$$\Upsilon^-(\tau, B) = (\{t_1, \ldots, t_{n-m_\tau}\}; q) \tag{5.8}$$

The action of Υ^- is to remove spikes from the end of the active segment. In case there are not enough spikes available for removal (later than the current time τ), Υ^- removes all of the remaining spikes. As shown in previous chapters, spike deletion normally implies that the perturbation has prematurely ended the active segment of the burst cycle.

Roughly speaking, the spike number change maps act on (possibly shifted) schematic representations of the reference burst, chopping spikes off of the end in case of spike deletion, and gluing them back on in case of spike addition. When spikes are added beyond the size of the active segment of the reference burst, the last spike of the reference burst is repeated to fill in the additional spikes.

The maps Σ, Ω, and Υ are all specific to a given form of perturbation. Different sets of maps must be constructed whenever the perturbation strength (g_{syn}), synapse type (inhibitory, excitatory), pre-synaptic spike profile, or other parameters vary. Furthermore, if a neuron receives synaptic input from a number of other neurons, then a set of maps $\{\Sigma, \Omega, \Upsilon\}$ must be calculated for each combination of synaptic inputs that the neuron might receive simultaneously. For example, if a neuron has one excitatory (e_1) and two identical inhibitory (i_1, i_2) afferent synaptic inputs, then 5 map sets must be constructed: $\{e_1\}, \{i_{1,2}\}, \{e_1, i_{1,2}\}, \{i_1, i_2\}, \{e_1, i_1, i_2\}$.

Although none of the maps Σ, Ω, or Υ are burst phase response curves (BPRCs) or directly derivable from BPRCs, the information needed for their construction (*viz.* the shift of the subsequent spike time, the spike number, and the length of the quiescent phase) can be obtained concurrently with direct BPRC calculation (section 3.2.4 of chapter 3), requiring almost no extra computation.

5.3 Algorithmic Coupling

We consider a network $\mathcal{N}$ of M bursting neurons, $X^1, \ldots, X^M$; we will define the neurons' representations later. The neurons need not be identical; in the following we assume that each neuron is an endogenous burster, but this need not be the case, as we clarify below.

We call the set of pre-synaptic neurons coupled to a neuron X^i its *input set*, written $\mathcal{I}(i)$, and we define the set of *input indices* $I(i) = \{j : X^j \in \mathcal{I}(i)\}$ accordingly. We call the set of neurons onto which X^i synapses its *output set*, denoted $\mathcal{O}(i)$, and define the set of *output indices* $O(i) = \{j : X^j \in \mathcal{O}(i)\}$ similarly.[2]

Let $\mathcal{P}^i$ be the set of all perturbations, *i.e.* unique combinations of synaptic inputs, that neuron X^i can receive. Denote by $G^i_p = \{\Sigma^i_p, \Omega^i_p, \Upsilon^i_p\}$ the map set corresponding to a perturbation $p \in \mathcal{P}^i$. We define the collection of all map sets for X^i by $\mathcal{G}^i = \{G^i_p : p \in \mathcal{P}^i\}$.

Let $B^i_{\text{ref}} = (A^i_{\text{ref}}, Q^i_{\text{ref}})$ be the reference burst for X^i. Let $\mathcal{B}^i = \{B^i_1, B^i_2, \ldots : B^i_j = B^i_{\text{ref}}, \forall j\}$ be the *burst queue* of neuron X^i. We think of the neuron's behavior as being represented by a sequence of spike times and interburst intervals; uncoupled and unperturbed, the neuron would repeat its reference burst indefinitely. As X^i interacts with other neurons, its spike pattern and interburst interval change. We trace the evolution of X^i through the alteration of copies of its reference burst.

We may start X^i from initial conditions B^i_0 corresponding to any time $t^i_0 \in [0, T_{\text{ref}})$ (equivalently, phase $\theta^i_0 \in [0, 1), \theta^i_0 = t^i_0/T_{\text{ref}}$). If $t^i_0 > t_K$, then we set $B^i_0 = (\emptyset; T_{\text{ref}} - t^i_0)$. Otherwise, we let $l = \min_j\{t_j \in A_{\text{ref}} : t_j \geq t^i_0\}$ and set $B^i_0 = (\{t_l - t^i_0, \ldots, t_K - t^i_0\}; q_{\text{ref}})$.

We now define the ith neuron by $X^i = \{I(i), O(i), \mathcal{P}^i, \mathcal{G}^i, \mathcal{B}^i, B^i_0, t^i_0\}$.

[2]We do not exclude autosynaptic connections, *i.e.* $X^i \in \mathcal{I}(i), X^i \in \mathcal{O}(i)$ is allowed.

We simulate the behavior of the neurons in $\mathcal{N}$ by iteratively applying the appropriate map sets in an event-driven fashion. We set a global time $t = 0$ and which neuron has the soonest upcoming spike time, say neuron X^i at time τ (simultaneous spikes from multiple neurons are allowed). We set $t = \tau$ and apply the appropriate burst maps to each neuron $X^j \in \mathcal{O}(i)$. We repeat until certain termination criteria are met, such as reaching a maximum elapsed time or maximum number of burst cycles. This process is detailed in Algorithms 2 and 3 below. In practice, we implement each neuron X^i as having a queue of potential spike times and interburst intervals, initially corresponding to $B_0^i \cup B_1^i$. As time approaches the last spike time in the queue, another copy of B_{ref}^i is added to the queue.

A single pre-synaptic spike from neuron X^i affects the spike times and possibly spike numbers of the neurons in $\mathcal{O}(i)$, and these neurons in turn fire their spikes at altered times, propagating the influence of X^i's spike downstream. Eventually the changes caused by the initial spike may lead a neuron in $\mathcal{I}(i)$ to fire at a time different from its unperturbed firing schedule, and thus alter the structure X^i's burst. The accumulation of changes in spike patterns and interburst intervals results in changes in the relative phasing of the bursts in the network. With algorithmically coupled maps, the role of individual spikes in determining burst phasing can be traced through many rounds of synaptic interactions.

In the case of two reciprocally coupled neurons, a spike from the first neuron advances or delays the spikes of the second, and vice versa, with the neurons' spike times potentially shifting back and forth like a ping-pong ball. With this image in mind, we bestow the moniker 'spike-time ping-pong' on our coupled map algorithm.

Algorithm 2 SpikeTimePingPong($\mathcal{N}$)

Require: Network of bursting neurons $\mathcal{N} = \{X^1, \ldots, X^M\}$, termination criteria.
Ensure: $\mathcal{N}$.

Set global time $t = 0$
while termination criteria not met **do**
    Poll each neuron to determine the soonest spike time $t_{\text{next}} \geq t$
    Assign $\mathcal{F}$ to be the set of the neurons whose next spike times equal t_{next}, and F to be the set of their indices.
    $t \leftarrow t_{\text{next}}$
    for j in F **do**
        for k in $O(j)$ **do**
            $P \leftarrow \mathcal{F} \cap \mathcal{I}(k)$
            UpdateNeuron(X^k, P, t)
        end for
    end for
end while
return $\mathcal{N}$

Algorithm 3 UpdateNeuron(X^i, P, τ)

Require: Post-synaptic neuron X^i, list of active pre-synaptic neurons $P = \{Y^1, \ldots, Y^l\} \subset \mathcal{I}(i)$, perturbation time τ.
Ensure: X^i.

Select current $B \in \mathcal{B}^i$.
Select $G^i_p = \{\Sigma^i_p, \Omega^i_p, \Upsilon^i_p\}$ for $p \in \mathcal{P}^i$ corresponding to P
$B \leftarrow \Upsilon(\tau, B)$
$B \leftarrow \Sigma(\tau, B)$
$B \leftarrow \Omega(\tau, B)$
return X^i

Before proceeding to an example of the spike-time ping-pong algorithm in action, we note that a tonically spiking neuron may be represented as a burster with a single spike in its active segment and a quiescent segment equal to its normal interspike interval, ρ, so that $B_{\text{ref}} = (A_{\text{ref}}; Q_{\text{ref}}) = (\{t_1\}; \rho)$. The spike shift, quiescence, and spike number change maps then capture changes in spike timing in a manner analogous to spike time response curves [4]. Temporary suppression of spikes or increases in the firing rate are handled by appropriately constructed qui-

escence and spike number change maps. Since neurons interact only at the level of individual spikes, networks may comprise a mix of endogenously bursting and tonically spiking neurons. Thus our spike-time ping-pong approach, at least as a formal framework, subsumes methods of coupled spike time response curves and coupled spike time difference maps (and hence phase response curves) as a special case, and it also provides an immediate means of extending those approaches to arbitrary networks of interacting neurons.

5.4 An Example

The spike-time ping-pong approach was originally developed to understand and predict the phase sensitivity and transient behavior first noticed in simulations of the rhythmogenic kernel (RGK) subnetwork of the rodent spinal hindlimb locomotor central pattern generator (RSHL CPG) model described in chapter 2. The RGK model comprises a pair endogenously bursting rhythmogenic interneurons (RGN) with reciprocally inhibitory coupling. (The RGN neuron model, synaptic coupling, and the RGK subnetwork are described in detail in subsection 2.4.2 of chapter 2 and Appendix A; subsection 3.2.4 of chapter 3 and appendix B; and subsection 2.5.1 of chapter 2, respectively.) We assess the performance of the spike-time ping-pong algorithm by comparing its predictions of burst phasing to the actual behavior of the RGK model.

We repeat the computational experiment described in section 2.5.1 of chapter 2 for the RGK model: We begin with its two neurons in the uncoupled state, *i.e.* $g_{\text{syn}} = 0$. Designating the uncoupled bursting orbit followed by a single neuron as the *individual reference orbit* or *individual reference burst*, we label the start of the active segment of the individual reference burst as the reference phase 0. We choose one neuron as the 'leader' and fix its initial conditions to correspond to

phase 0. We choose a phase offset $\theta \in [0, 1]$ and set the initial conditions of the 'follower' neuron to correspond to θ. We then set the the synaptic strength g_{syn} to its chosen value, initialize the synaptic activation variables to 0, and simulate the evolution of the two-cell model by numerical integration. We calculate the phase offset between the leader and follower at the ith burst cycle as $(t_F^i - t_L^i)/T \mod 1$, where $t_{\{L,F\}}^i$ is the starting time of the ith burst of the leader or follower, respectively, and T is the period of the reference burst cycle.

We follow a similar protocol with the spike-time ping-pong algorithm, using reference burst skeletons derived from the individual reference orbit and maps constructed from information collected during the computation of direct burst phase response curves for synapse-mediated spike injection perturbations, described in section 3.2.4 of chapter 3. For both the RGK model and the spike-time ping-pong algorithm, we use 500 evenly spaced follower phases $\theta \in [0, 1]$ as initial conditions, and we test coupling strengths g_{syn} between 0.0001 and 20.

Figures 5.1–5.4 show the results from the RGK simulations and the spike-time ping-pong algorithm for various coupling strengths. In each of the figures, θ (plotted on the horizontal axis) is the phase offset at which the follower neuron was started with respect to the leader. The vertical axis, labeled $\Delta\theta$, measures the change in phase difference (mod 1); that is, the difference between the neurons' initial phasing and their relative phase offset after one burst cycle. In the terminology of 2.5.1 of chapter 2, $\Delta\theta = \Delta\theta_1 - \Delta\theta_0 \mod 1$. The blue curve represents the change in phase $\Delta\theta$ for the RGK model simulation (the 'true' phase change), and the red curve represents the change in phase predicted by spike-time ping-pong.

Weak coupling

For weak coupling, *i.e.* $g_{\text{syn}} \leq 0.1$, the predictions of the spike-time ping-pong

algorithm match the actual behavior of the RGK network quite closely. Figures 5.1 and 5.2 show the predictions of the spike-time ping-pong algorithm for the change in relative phasing of the RGK neurons after one burst cycle versus the actual change in their phase differences, for $g_{\text{syn}} = 0.01$. Although the correspondence between the spike-time ping-pong predictions and the RGK phasing is not perfect, it is very close for both initial phase offsets $\theta \leq 0.8$ (figures 5.1 and 5.2 (a)) and $\theta \geq 0.9$ (figure 5.2 (a)). For most initial phasing conditions, the spike-time ping-pong algorithm captures the transient behavior of the RGK system well at weaker coupling strengths.

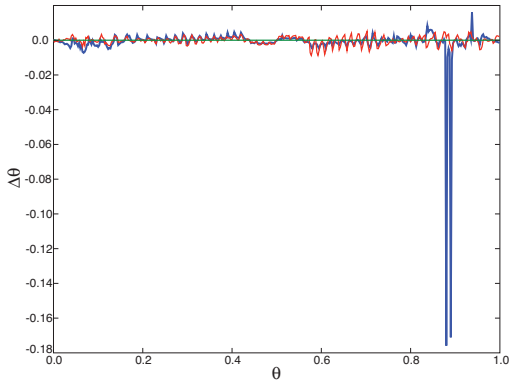

Figure 5.1: Phase differences predicted by RGK model and spike-time ping-pong algorithm for weak coupling, $g_{\text{syn}} = 0.01$. Results from RGK model simulations are drawn in blue, spike-time ping-pong predictions in red.

The most dramatic failure of the spike-time ping-pong algorithm occurs for the two initial phase differences 0.88 and 0.89, as is prominently visible in figure 5.1. The actual change in relative phasing is quite large, but the algorithm predicts almost zero change in the neurons' relative phases. This discrepancy is due to the addition of two extra spikes with long interspike intervals in the leader's active segment, a spike number change not predicted by the algorithm. The algorithm misjudged the neurons' spike numbers, anticipating no changes, and thus

misestimated the neurons' resultant phase difference.

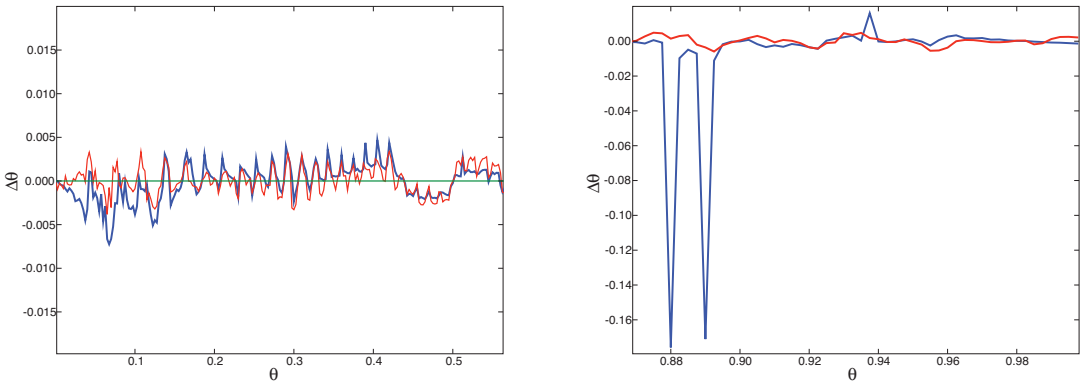

(a) (b)

Figure 5.2: Close-ups of phase differences predicted by RGK model and spike-time ping-pong algorithm for weak coupling, $g_{\text{syn}} = 0.01$. Results from RGK model simulations are drawn in blue, spike-time ping-pong predictions in red. (a) Close-up of early phases. (b) Close-up of late phases.

In the weak coupling regime, the assumptions on which the spike-time ping-pong method rests are particularly well supported, which accounts for the close agreement between the discrete map approximation and the behavior of the full RGK system. However, the inherent phase and spike number sensitivities associated with perturbations near the fast-subsystem homoclinic bifurcation at the end of the active segment make the algorithm's reproduction of the phasing behavior of the full system imperfect. Given the amount of information lost in reducing the ODE model to a set of coupled maps, the overall performance of the spike-time ping-pong approach in the weak coupling regime is nonetheless quite good.

Strong coupling

At higher coupling strengths ($g_{\text{syn}} > 10$), the RGK model tends asymptotically to the antiphase configuration from every initial phasing condition except synchrony. This change in relative phasing takes two to three burst cycles, and the sequence

intermediate phases followed by the neurons depends sensitively on initial conditions.

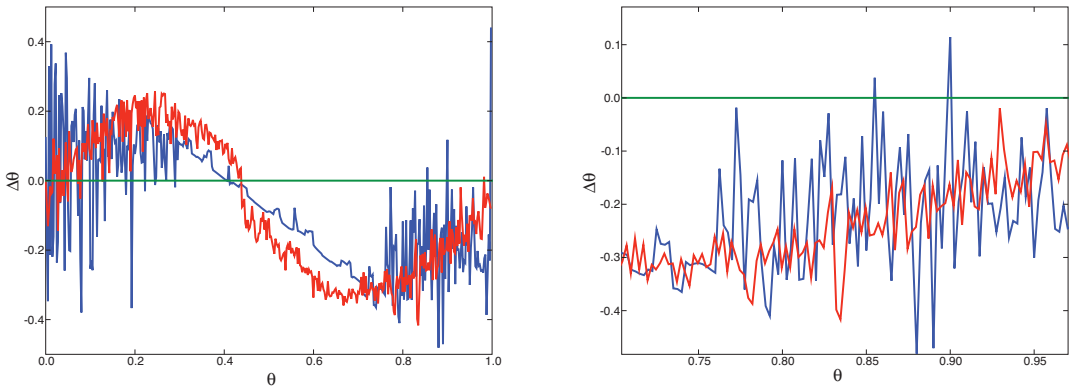

(a) (b)

Figure 5.3: Phase differences predicted by RGK model and spike-time ping-pong algorithm for strong coupling, $g_{\text{syn}} = 20$. Results from RGK model simulations are drawn in blue, spike-time ping-pong predictions in red. (a) All phases. (b) Close-up of later phases.

As can be seen in figure 5.3 (a), the spike-time ping-pong algorithm captures the long-term phasing dynamics of the RGK network in the strong coupling regime. The predicted phase change is positive for phase offsets $\theta < 0.5$ and negative for phase offsets $\theta > 0.5$. This implies that a phase difference of 0.5, *i.e.* the antiphase configuration, is the sole stable state for the RGK network, as it in fact is. The magnitude of the predicted phase change curve implies that convergence to antiphase is rapid, but the actual convergence of the RGK network is somewhat slow.

The true phase change curve for the RGK network is comparatively jagged, with dramatic differences in phase response for nearby initial conditions. Overall, the phase movement over one cycle is towards the antiphase configuration; the progression is smoothest from phases close to 0.5. As can be seen in figure 5.3 (b), the spike-time ping-pong algorithm underestimates the change in phasing for

many initial conditions, but its predictions are generally in the right direction, even where they differ in magnitude.

The algorithm tends to overestimate the number of spikes added to bursts at high coupling strengths, often predicting two to four more spikes than are actually added. These errors appear to be due to 'doubled' spike addition when two spikes impinge near a single phase that is particularly prone to spike addition. The ODE model incurs extra spikes for only one of the pre-synaptic inputs, but the spike-time ping-pong algorithm counts the effects of both inputs towards the tally of spikes to be added. This shortcoming impairs the method's prediction of the RGK model's transient behavior, but its forecasts of asymptotic behavior are very accurate.

Intermediate coupling

As the strength of coupling increases from $g_{\text{syn}} = 0.1$, the quality of the spike-time ping-pong algorithm's predictions of transient behavior degrade. At $g_{\text{syn}} = 1$ and above, the algorithm predicts fairly smooth, rapid convergence to the antiphase configuration (figure 5.4). In contrast, for some initial phases, the RGK model may at first move away from antiphase, and phase movements over the course of one cycle may be quite large. But close inspection of the blue curve of figure 5.4 reveals that the overall trend of the one-cycle phase movements of the RGK model is towards antiphase. The large magnitude of many of the phase movements counter to this trend obscures the numerous, but less dramatic intervals of initial phases which tend towards antiphase. The number of initial conditions from which the RGK model moves in the direction of the antiphase configuration is roughly equal to the number of phases from which the model moves in the opposite direction.

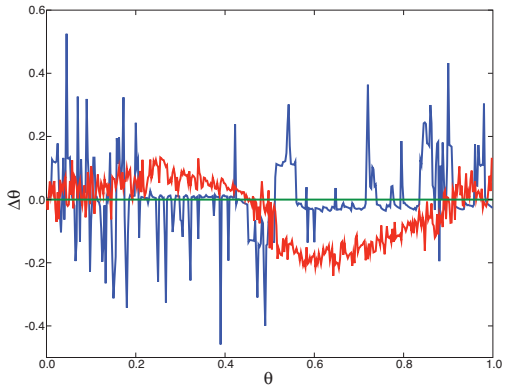

Figure 5.4: Phase differences predicted by RGK model and spike-time ping-pong algorithm for intermediate coupling, $g_{\text{syn}} = 1$. Results from RGK model simulations are drawn in blue, spike-time ping-pong predictions in red.

Again, overestimation of the number of added spikes undermines the algorithm's predictions for transient behavior, but it correctly predicts the system's eventual phase configuration.

The example discussed in this section demonstrates that the spike-time ping-pong approach can identify the stable phase configurations of a network of interacting bursting neurons, and may also provide useful information about the transient states the network traverses in approaching its final phase configuration. The results of similar experiments with a different bursting model (Hindmarsh-Rose, not shown) were rather poor. For that system, the spike-time ping-pong made poor predictions of changes in relative phasing, largely because of misestimates of spike number changes. However, we note that the method's invention was prompted by the behavior observed in the RGK network, and its development was largely guided by tests using the RGN model. Refinements of the map reductions and coupling algorithm based on experiences with other systems should improve its performance for a wide range of models.

5.5 Discussion

Coupled phase response curves, spike time difference maps, and burst response curves aim to capture and compactly represent those aspects of synaptic transmission essential to phasing behavior, thus simplifying the analysis of neuronal interactions. When applied to interacting bursting neurons, however, these methods do not take the multiple time-scale character of the phase response dynamics into account. They either overlook the division of the burst cycle into alternating periods of spiking and quiescence, treating them identically to tonically spiking neurons, or they ignore the internal spike structure of the bursts' active segments.

The spike-time ping-pong approach also reduces the dynamics of neuronal interactions to low-dimensional maps, but it also preserves the biological reality that both tonically spiking and endogenously bursting neurons interact on a spike-by-spike basis. A single pre-synaptic spike may affect the relative phasing of many post-synaptic neurons, and as these changes propagate they may eventually feedback to the neuron that originated the spike. The spike-time ping-pong algorithm provides an 'audit trail' of these interactions, tracing the downstream effects of individual spikes. By accounting for interactive processes across multiple time-scales, it predicts the basic features of interacting bursts, such as the length of active and quiescent phases, spike number, and the existence and stability of synchronous network states and other phase configurations.

The discrete map reductions produced by the method are fast, efficient low-dimensional representations of the full system dynamics which can be constructed concurrently with phase response curves, without any increase in computational cost. The resulting maps serve as estimators for phasing robustness and predictors of transient activity that may partially obviate the need to conduct exhaustive parameter sweeps and expensive numerical simulations in order to study neuronal

network behavior.

For weak coupling regimes, the spike-time ping-pong algorithm accurately predicts both the transient and asymptotic phasing behavior of simple networks of biophysically realistic models of bursting neurons. The quality of its predictions of transient activity declines as coupling strength increases, primarily due to misestimation of spike number changes, but its forecasts of long-term behavior remain accurate.

The method's discrete map formalism automatically covers tonically spiking neurons as special case of bursting neurons, and it naturally extends to heterogeneous collections of neurons and arbitrary network architectures. However, incorporating a variety of neuronal species and coupling types involves a factorial increase in number of discrete maps that must be computed, and there is no clear way to handle adaptive synapses. And although the algorithm is simple to comprehend, it is not as amenable to mathematical analysis as other coupled map approaches.

The spike-time ping-pong method is only at the proof of concept stage, but its initial results are promising. There are many possible directions for further development; incorporating additional slow variable information appears especially likely to improve performance significantly. With some refinement, the spike-time ping-pong algorithm should prove to be a useful tool for studying the evolution of phase relationships in neuronal networks.

CHAPTER 6

CONCLUSION

6.1 Summary

The work presented in this thesis addressed the question, "How are phase relationships established and maintained in networks of rhythmically active neurons?" Our pursuit of answers involved repeated treks into domains where the biology of neuronal bursting, the theory of multiple time-scale dynamical systems, and the study of phase response overlap. Guiding our investigations was the larger aim of furthering the development of a mathematical and computational theory of central pattern generators.

In chapter 1, we surveyed four areas from which our work drew heavily: bursting oscillations, multiple time-scale dynamical systems, phase response, and central pattern generators. We summarized their main techniques and results, defined the relevant terms in their argots, and highlighted their interrelationships. In addition to introducing background knowledge and key ideas to be developed in later chapters, this presentation was intended to provide a concise survey of topics and concepts useful in the study of other problems.

The subject of chapter 2 was the development of the first mathematical model for the rodent spinal hindlimb locomotor central pattern generator (RSHL CPG). We began by organizing the results of numerous experimental studies of the RSHL CPG, synthesizing information about the network's architecture and the properties of its neuronal constituents from anatomical, microscopic, electrophysiological, and neuromodulatory studies. We then reviewed four CPG modeling methodologies,

viz. phase oscillators, coupled cell networks, detailed conductance-based models, and intermediate approaches, weighing the advantages and drawbacks of each. Based on these two surveys, we articulated a set of explicit modeling ansätze, consistent with current experimental knowledge, and a set of biologically relevant testing criteria. The intent of this preparatory work was to provide an intellectually sound foundation upon which to establish a modeling framework that would support the development of several generations of useful, biologically realistic models.

Using this framework, we assembled a comprehensive, biophysically detailed model from components taken from well-studied, off-the-shelf models for other neural systems, adjusting parameters to fit the biology of the RSHL CPG. The chief goal for this model was that it stably reproduced the fundamental locomotor rhythm: ipsilateral flexor-extensor alternation concurrent with contralateral flexor-extensor synchronization. The model's suitability was judged according to the stability of the rhythm under phase perturbations and the transient behavior of the network in (re)establishing the rhythm.

From the full CPG model we derived several reduced models, comprising functionally important two- and four-cell network configurations, which were used to isolate and study various phasing-related mechanisms across a range of coupling strengths. Computational experiments demonstrated that the CPG model could produce the fundamental locomotor rhythm, but they also revealed surprising sensitivity to initial phasing conditions and synaptic coupling levels. The two- and four-cell models displayed unexpected transient behavior, and the four-cell networks required a narrow balance of strong inhibition and moderately strong excitation to achieve biologically reasonable rates of convergence to the walking rhythm. Based on these results, we suggested an array of revisions to our ansätze,

adjustments to the model, and directions for future biological experiments.

Chapter 3 explored the origin of the surprising phase response behavior seen in the CPG models. We identified four sets of common, largely untested modeling and experimental assumptions regarding the phase response properties of endogenous bursters. To check these assumptions, we performed an empirical study of burst phase response to single spike perturbations. We investigated five models of endogenous bursters (one schematic model and four biophysically realistic, conductance-based models), for a wide variety of perturbation types and a broad range of perturbation strengths. Our study produced a number of interesting results, largely contradicting the body of assumptions underlying many modelers' and experimentalists' use of phase response curve (PRC) techniques: First, the direct methods for calculating burst phase response curves produce PRCs shaped differently from those obtained via linear methods. Second, phase response to excitation differs from response to inhibition both qualitatively and quantitatively. Third, burst phase response curves for bursting neural models share a characteristic visual pattern, and phase response is closely correlated with intraburst spike times. Fourth, the shape and magnitude of burst phase response may be heavily dependent on the shape of the perturbing input (*i.e.* synapse model). Fifth, burst phase response is dramatically different in the weak and strong perturbation regimes; at higher perturbation strengths, changes in spike number predominantly determine the shape of the PRC.

In chapter 4, we used the techniques of geometric singular perturbation theory to investigate the distinctive shape of the phase response curves for models of bursting neurons, focusing specifically on the Hindmarsh-Rose model. We used

fast-slow dissection, numerical continuation, and phase portraits to study the arrangement of organizing structures (equilibria, periodic orbits) for the dynamics of both the fast subsystem and the full bursting model. We also developed a simple, but effective algorithm to compute one-dimensional isochrons, which we used for the first calculation of isochrons for a bursting neural model.

We incorporated the isochron calculations into phase portraits of the fast subsystem at the beginning, middle, and end of the active spiking segment of the burst cycle. These isochron portraits presented snapshots of the development of the model's phase resetting characteristics over the course of a burst cycle. Using them, we showed that strong correlation between peaks of phase response and spike times in the full system derive from the peculiar geometry of the isochrons, which have a curved shape distinctly different from those of isochrons for planar spiking models. In particular, the tight curving of the isochrons around the fast subsystem's periodic orbit near the spike maximum causes a peak of phase response in the full system near its spikes. The magnitude of the spike-associated phase response grows over the course of the active segment due to isochron compression caused by the increasing proximity of the saddle point to the periodic orbit. The interaction of isochron 'ghosts' and the stable and unstable manifolds of the saddle point near the homoclinic bifurcation explain the phase response reversal near the termination of the active segment.

Further fast-slow dissection and phase plane analysis revealed the mechanisms underlying spike-time shifts, spike deletion, and spike addition at higher perturbation strengths. Spike deletion involves the perturbation of the full system trajectory away from the fast subsystem periodic orbit, past the line of saddle points, and into the basin of attraction for the hyperpolarized fixed point; spikes are dropped because the active segment of the burst is shut off prematurely. Spike addition

occurs when a perturbation shifts the full system trajectory with respect to the location of the homoclinic point such that it is able to track the fast subsystem periodic orbit for extra revolutions. The propensity of a bursting neural model to change spike number was shown to depend critically on the proximity of the full system trajectory to the saddle points and the homoclinic point of the fast subsystem at the time of perturbation.

We returned to the problem of phasing in networks of bursting neurons in Chapter 5, developing a method for deriving a collection of reduced discrete maps to describe the response of a bursting neuron to a single-spike perturbation. These maps were based on insights garnered from our empirical studies and mathematical analysis of burst phase response, which indicated that bursting neurons respond to incoming spikes in characteristic, somewhat stereotyped ways. The maps we proposed captured the basic features of spike shifting, spike number alteration, and cycle period changes, overcoming the limitations of other methods that ignore intraburst spike structure in describing burst dynamics. We also developed a set of 'spike-time ping-pong' algorithms that couple our maps so as to approximate the spike-by-spike interaction of neurons in a network. The framework we proposed naturally handles arbitrary network architectures, multiple synaptic models, and heterogeneous collections of neurons; it also subsumes PRC and spike time difference maps as a special case.

Tests of the algorithm on a small network of interacting bursting neurons found that it accurately predicted the transient and long-term phasing behavior of the neurons at weaker coupling strengths. As coupling strength increased, the quality of its estimates of transient behavior diminished, but its prediction of asymptotic phase configurations remained good. Most of the error in the algorithm's predic-

tions was due to overestimation of the number of spikes added by repeated perturbations near sensitive phases. Even at the proof of concept stage, the method we introduced effectively captured the multiple time-scale dynamics inherent in interactions of bursting neurons, and with continued improvement should serve as an efficient, robust estimator of phasing behavior in neuronal network models, in particular those for central pattern generators.

6.2 Future Directions

6.2.1 Central Pattern Generator Models

The modeling framework we established in chapter 2 should support many iterations of RSHL CPG model building. Taking our full model as a point of departure, there are several directions that further model development might fruitfully explore.

There is a clear need for greater biological specificity in the current model, which relies on conductance-based models originally constructed for other neural systems. In order to study the roles played by different cell types, *e.g.* commissural interneurons and motoneurons, in shaping particular features CPG output, we need more information about the intrinsic properties that determine their behavior and differentiate them from one another. The conductance-based models for each cell type should incorporate more specific details about the cells' membrane currents; this requires additional experimental measurements of their electrophysiological parameters and neuromodulatory properties.

In particular, $I_{\mathrm{Na(P)}}$ was presumed to play a critical role in driving the endogenous bursting of the model Hb9 cells hypothesized to form the rhythmogenic nucleus of the CPG. Further biological study of this current and interneuron species

is needed, but the activities of other currents, such as the h-current and T-type Ca^{2+} currents, should also be investigated, and alternative hypotheses for burst production should be explored.

While awaiting the results of electrophysiological and neuromodulatory studies of the biological system, neuron models with a generic Hodgkin-Huxley-style structure could be adapted to match the available data on the firing properties of identified cell groups, such as ascending and descending commissural interneurons. These cell models could be inserted into the existing network architecture and the output of the new CPG version could be studied via computational experiments similar to those of chapter 2. With this approach, which has been used successfully for the *Xenopus* swimming CPG [193], work on modeling the cellular and network level response of the CPG to neuromodulation might proceed concurrently with identification of important currents.

The strength of synaptic coupling is a key parameter of both the biological CPG and any mathematical model of it. The present model requires relatively strong excitation and inhibition to function properly, predictions that require experimental verification. Even without experimental confirmation, by replacing the current synapse model with alternative formulations and repeating the simulations of chapter 2, we might easily study the effects of different synapse models on network behavior, a subject little explored but potentially quite important. In particular, introducing adaptation is likely to have a substantial effect on the model CPG's behavior [156, 155, 10, 218].

We can conceive of many modifications to network architecture that might be of potential interest as means for testing various of our ansätze about the CPG organization. Perhaps the most intriguing architectural change would replace the current configuration of the rhythmogenic kernel as a half-center of endogenous

bursters by a two-cell arrangement that produces alternating flexor-extensor bursting via synaptic or intrinsic escape and release mechanisms [206]. This would be a major alteration that is likely to have substantial consequences, not easily foretold intuitively, for the phasing behavior of the network. Half-center gastric mill configurations in the lobster stomatogastric ganglion have been studied with dynamic clamp techniques [199], so that the results of computer simulations could be easily compared with the behavior of a (similar, but not identical) biological system. Other changes to the network architecture, such as removing the symmetry in the synaptic coupling between flexor and extensor groups, might enable studies of alternative hypothesis for the origin of rhythmogenesis, *e.g.* endogenous bursting confined to flexor segments, or tonic drive from higher spinal segments modulated by the CPG at the lumbar level.

Keeping the architectures of the present CPG models intact, several questions remain from our initial computational experiments. We investigated the stability of the fundamental locomotor rhythm in three four-cell models derived from the full CPG model, but we did not study in depth their transient behavior in reaching the walking configuration. More thorough, systematic sweeps of the space of initial phasing conditions and synaptic coupling strengths are needed to determine the relative stabilities of other phasing modes. Such studies would be computationally expensive undertakings, but they are necessary to build up an understanding of how the CPG switches between biologically relevant phase configurations, *e.g.* walking, hopping, turning, and reversal. Eight-cell models may be useful for studying the roles of commissural interneurons and additional synaptic groups in promoting and modulating the fundamental locomotor rhythm.

A central tenet of our modeling approach was that the collected behavior of groups of neurons could be reasonably modeled by a detailed, conductance-based

model of a single neuron having appropriate parameter values. The validity of this ansatz should be tested with models that replace the representative cells of the current CPG model with heterogenous populations of cells having distribution of parameter values. Questions about the robustness of phasing behaviors in single-cell versus population models have not been addressed before; the CPG models and testing criteria we have established would serve as a good framework in which to study this subject.

The operational requirements and behavioral repertoire of the biological RSHL CPG are much broader and more complex than simply producing the fundamental locomotor rhythm. Once that more satisfactory and more biologically specific models to support the basic walking pattern have been developed and their phasing properties understood, work should begin to expand the models to encompass the detailed activation sequences of the dozens of individual muscles currently subsumed into either flexor or extensor groups.

6.2.2 Phase Response

The unusual burst phase response patterns we found in our empirical studies are likely to have considerable biological significance and deserve further study. The higher-dimensional, biophysically realistic bursting models had burst phase response curves whose shapes resembled that of the schematic Hindmarsh-Rose and the three dimensional pre-Bötzinger model overall, yet differed in significant ways. Their additional currents must be responsible for the differences; exactly how is an intriguing topic to explore. One approach to the question is to investigate various lower dimensional reductions of these models using the same techniques we employed to analyze the burst phase response of the Hindmarsh-Rose model. By keeping careful track of the assumptions of the reduced models and comparing

their burst phase responses, we may gain insight into the roles of specific intrinsic properties in shaping the phase response.

The association between strong phase response and spike times was much weaker in the pyloric dilator model, the only multicompartmental model we examined, than in any other model. It also had a much larger range of coupling strengths over which its phase response curves scaled linearly. These biologically consequential properties are also likely to be due to the activity of its (many) intrinsic currents, but its multicompartmental structure may also be an important determinant [66, 208, 37, 170]. An empirical study of the burst phase response of multi-compartmental endogenously bursting models, similar to the work in chapter 3, would clarify this issue. If it is the case that multicompartmental models have significantly different phase response characteristics than single-compartment model, it would imply that more complex models are needed to properly capture the phasing behavior of bursting neurons in CPG networks like the crustacean stomatogastric ganglion. Whether or not the phase response characteristics of multicompartmental models differ systematically from those of single-compartmental models, the biological purpose of the pyloric dilator's atypical phase response remains to be explained.

The biological presence or relevance of the results of chapter 3 also requires experimental confirmation. Most studies of voltage and current clamp studies of phase response in real neurons use square pulse current injections as perturbatory inputs [59, 175, 162]; dynamic clamp studies of synaptic effects synapses largely simulate synaptic activity as background noise [82, 237]. Dynamic clamp experiments using realistic synapse models to simulate single-spike perturbations to isolated cells offer a means to verify whether the computational results of chapter 3 hold true for real neurons [82, 197, 198].

Both our empirical investigation and mathematical analysis of burst phase response focused mainly on models whose endogenous bursting mechanisms were associated with a Hopf-homoclinic bifurcation structure in their fast subsystems. There are many slow current bursting mechanisms that correspond to other fast subsystem bifurcations [146, 124]; systematically investigating the burst phase responses of the canonical models for different bursting mechanisms catalogued in [124], including empirical study and isochron portrait analyses similar to chapters 3 and 4, would constitute an interesting study. In connecting its results to biology, however, there is the 'inverse' problem of finding or constructing biophysically realistic, conductance-based models that possess the same bifurcation structure [81].

A natural next step for our analysis of burst phase response is to apply the techniques we used for the Hindmarsh-Rose model to the pre-Bötzinger model. Of particular interest are the consequences of having a 'non-monotonic' slow variable on spike addition and deletion; the interplay between local oscillations of the slow variable and the stable and unstable manifolds of the saddle point near the fast subsystem homoclinic bifurcation is likely to have complicated, possibly chaotic effects [216, 217]. Our analysis of bursters' response to strong perturbations could also be improved by carefully calculating the stable and unstable manifolds and basins of attraction for the organizing structures of the fast subsystem (*e.g.* periodic orbit and hyperpolarized fixed point). This information could be used to better predict regions of the active segment of the burst at which the system is most prone to spike number changes when perturbed. In combination with improved isochron portraits, such calculations would help us tighten the intuitive arguments of our analysis into rigorous mathematical proofs.

Computing isochrons is theoretically easy, but difficult in practice due to nu-

merical and algorithmic challenges; thus only a handful of studies have calculated isochrons for non-trivial systems. Our simple isochron calculation scheme is effective, but it requires intensive computations to produce curves of acceptable resolution. There is much room for improvement of the algorithm's efficiency and numerical accuracy; formulation of isochron computation as a continuation problem may be the most effective way to calculate the curves.

We speculate that the ideas developed in this thesis for studying burst phase response in neural systems may also be useful in other contexts. Domains where issues of synchronization and phasing in networks of multiple time-scale oscillators are of interest might benefit from our extensions of standard PRC techniques; problems in ecology (forest fires, coupled predator-prey systems) and physics (nonlinear circuits) are possible examples.

6.2.3 Discrete Maps

Our spike-time ping-pong method is still at the incipient stages of development, and there is much work to be done before it may be considered 'production ready.' Fundamental improvements in the accuracy of the algorithm, especially its prediction of spike number changes, are needed before it can be applied to a wide range of networks and bursting models with confidence.

Incorporating information about the state of the slow variable into the discrete map reduction and the coupling algorithm is likely to enhance the method's accuracy significantly, at the price of greater complexity. The progress of the slow variable in the active and quiescent segment of the burst cycle may be thought of as a measure of 'slow phase,' in contrast to the 'fast phase' along the limit cycle of a single spike. Fast-slow dissection and numerical continuation of the fast subsystem with respect to the slow variable should provide the information required to

augment the current discrete map formulation, but the result may be families of maps indexed by the slow or fast phase, substantially complicating the reduction and the coupling algorithm. Using multiple time-scales of phase may allow us to apply topological and geometric reasoning at separate time-scales in order to more accurately convert the phase response of the full system to a set of maps [164].

As the accuracy of the discrete map reduction improves, the spike-time ping-pong method should be tested for other endogenous bursting models and more complicated network architectures. Homogeneous networks of spiking neurons and networks mixing tonically spiking and endogenously bursting neurons are cases for which the method has great potential value, but where it also requires significant testing. The AB/PD-PY-LP subnetwork of the lobster stomatogastric ganglion [111] could serve as a biological example against which the spike-time ping-pong method could be compared.

The present implementation of the discrete map reduction is neither particularly quick nor simple, and would greatly benefit from increased automation and optimization. Although the information needed to construct the maps is obtained simultaneously with direct burst phase response curve calculations, the maps are created *post hoc*, a step which could be eliminated. Automated methods for decomposing multiple time-scale ODE systems into discrete maps have been developed in the context of tonically spiking Hodgkin-Huxley models [45]; integration of those techniques with the spike-time ping-pong algorithm may be useful to explore.

Our discrete map formulation subsumes PRC and spike time response curve methods, but it presently lacks a supporting mathematical theory like those available for the other methods. More analysis is needed to establish rigorous estimates of its predictive behavior and bounds on its accuracy. As our theoretical understanding of the method develops, it will become clearer how applicable its

techniques are for other fast-slow systems.

6.2.4 Software Tools

Excellent computational and numerical tools were essential for the successful undertaking of the projects described in this thesis. The PyDSTool software we co-developed and used for the vast majority of our computations has become a mature, robust platform for simulation and analysis of dynamical systems [44]. It provides high quality numerical integration, continuation, and data analysis routines and domain-specific toolboxes for modeling neuronal components and networks of cells; the utility of integrating many computational tools in one package is difficult to overstate.

It is virtually axiomatic that every software program remains perpetually under development. Beyond the usual desires for speed increases, bug fixes, code refactoring and better documentation, there are many enhancements on our wish list for PyDSTool: Although it includes two very good integrators, a wider menu of methods for particular types of problems, *e.g.* stiff systems, differential-algebraic equations, mechanical systems, and geometric integration, would be welcome. The addition of automatic differentiation routines [96, 168] and Taylor series integrators [168, 129] would make available a number of very useful methods for periodic orbit finding [42, 103] and parameter optimization [36, 219].

PyCont, the continuation module of PyDSTool, builds on the codebase of a now defunct branch of AUTO [65]. Updating it to use the active codebase would enhance its long term support and enable the inclusion of additional continuation methods [93, 94] and expand the array of bifurcations it can track, including homoclinic and sliding system bifurcations [64, 60, 41].

Although PyDSTool already handles hybrid systems well, its implementation

could be improved and expanded to better support simulations of large networks of spiking neurons [13]. The current implementation of map-based routines could be enhanced to facilitate coupled map techniques such as spike-time ping-pong and the Dominant Scale System Reduction Tool [45]. The neural systems toolkit should expand to cover a wider variety of conductance-based models and synapse types, and the network toolbox could be rewritten to conform to the coupled-cell network formalism, which is more general than the current implementation. Additional toolkits for building models of biochemical reaction and genetic regulatory networks, along with parallelization and greater interoperability with packages like SloppyCell [105, 154, 106], would greatly enhance the PyDSTool's usefulness for systems biology problems. Automation of time consuming routine tasks in dynamical systems analysis, such as the computation and verification of phase portraits and bifurcation diagrams would also improve the program substantially [149, 99, 3, 1, 2]. The eventual addition of stochastic and partial differential equation integrators would admit models with noise and spatial structure, maximally broadening the scope of PyDSTool's capabilities to encompass nearly every computational activity in dynamical systems modeling.

Accomplishing all of these tasks will undoubtedly be the work of many hands.

The intersection of neuroscience and dynamical systems is an area rich in compelling scientific problems. The biological, mathematical, and computational challenges associated with modeling central pattern generators and other neuronal networks are myriad. We conclude by expressing the hope that the work in this thesis, while making a valuable contribution to the field on its own, may also serve as a useful basis for future research. *Erit complere hoc opus negotium perpete!*[1]

[1] Chapter VI, page 201, [143].

APPENDIX A

LOCOMOTOR CPG NEURON MODELS

Equations for the rhythmogenic interneurons (RGNs), commissural interneurons (CINs), and motoneurons (MNs) of the rat spinal hindlimb locomotor CPG model, based on model I of [24] for a class of endogenously bursting neurons in the pre-Bötzinger complex of the neonatal rat. Bursting is controlled by the level of persistent sodium current activation. Characteristics of the model in various parameter regimes and network conditions are found in [24, 25], and extensive comparisons of the model with experimental data are presented in [56].

The RGN parameters were modified to correspond to experimental measurements of Hb9 interneuron membrane properties [234]. The CIN and MN equations lack the persistent sodium current and have parameter values that make them passive but excitable (near the threshold for tonic spiking).

A.1 RGN Model Equations

Dynamic variables

$$\dot{V} = -(I_{\mathrm{Na}} + I_{\mathrm{K}} + I_{\mathrm{Na(P)}} + I_{\mathrm{L}} - I_{\mathrm{app}})/C \tag{A.1}$$

$$\dot{n} = (n_\infty(V) - n)/\tau_n(V) \tag{A.2}$$

$$\dot{h} = (h_\infty(V) - h)/\tau_h(V) \tag{A.3}$$

Membrane currents

$$I_{\mathrm{Na}} = (g_{\mathrm{Na}} m_\infty^3(V)(1-n)(V - V_{\mathrm{Na}}) \tag{A.4}$$

$$I_{\mathrm{K}} = g_{\mathrm{K}} n^4 (V - V_{\mathrm{K}}) \tag{A.5}$$

$$I_{\mathrm{Na(P)}} = g_{\mathrm{Na(P)}} m_{\mathrm{Na(P)}_\infty}(V) h (V - V_{\mathrm{Na}}) \tag{A.6}$$

$$I_{\mathrm{L}} = g_{\mathrm{L}}(V - V_{\mathrm{L}}) \tag{A.7}$$

Activation equations

$$m_\infty(V) = (1+\exp((V-\theta_m)/k_m))^{-1} \quad \text{(A.8)}$$

$$m_{\mathrm{Na(P)}_\infty}(V) = (1+\exp((V-\theta_{m_{NaP}})/k_{m_{\mathrm{Na(P)}}}))^{-1} \quad \text{(A.9)}$$

$$h_\infty(V) = (1+\exp((V-\theta_h)/k_h))^{-1} \quad \text{(A.10)}$$

$$\tau_h(V) = \overline{\tau}_h/\cosh[(V-\theta_h)/(2k_h)] \quad \text{(A.11)}$$

$$n_\infty(V) = (1+\exp((V-\theta_n)/k_n))^{-1} \quad \text{(A.12)}$$

$$\tau_n(V) = \overline{\tau}_n/\cosh[(V-\theta_n)/(2k_n)] \quad \text{(A.13)}$$

A.2 CIN and MN Model Equations

Dynamic variables

$$\dot{V} = -(I_{\mathrm{Na}} + I_{\mathrm{K}} + I_{\mathrm{L}} - I_{\mathrm{app}})/C \quad \text{(A.14)}$$

$$\dot{n} = (n_\infty(V) - n)/\tau_n(V) \quad \text{(A.15)}$$

$$\quad \text{(A.16)}$$

Membrane currents

$$I_{\mathrm{Na}} = (g_{\mathrm{Na}} m_\infty^3(V)(1-n)(V-V_{\mathrm{Na}}) \quad \text{(A.17)}$$

$$I_{\mathrm{K}} = g_{\mathrm{K}} n^4 (V - V_{\mathrm{K}}) \quad \text{(A.18)}$$

$$I_{\mathrm{L}} = g_{\mathrm{L}}(V - V_{\mathrm{L}}) \quad \text{(A.19)}$$

Activation equations

$$m_\infty(V) = (1+\exp((V-\theta_m)/k_m))^{-1} \quad \text{(A.20)}$$

$$n_\infty(V) = (1+\exp((V-\theta_n)/k_n))^{-1} \quad \text{(A.21)}$$

$$\tau_n(V) = \overline{\tau}_n/\cosh[(V-\theta_n)/(2k_n)] \quad \text{(A.22)}$$

A.2.1 Parameters

Table A.1: CPG neuron species parameter descriptions

Symbol	Description	Units
C	Membrane capacitance	μF/cm^2
I_{app}	Applied current	μA/cm^2
g_{Na}	Maximum Na^+ conductance	mS/cm^2
V_{Na}	Na^+ reversal potential	mV
θ_m	Na^+ activation half-activation	mV
k_m	Na^+ activation steepness	mV
$g_{\text{Na(P)}}$	Maximum persistent Na^+ conductance	mS/cm^2
$V_{\text{Na(P)}}$	Persistent Na^+ reversal potential	mV
$\theta_{m_{\text{Na(P)}}}$	Persistent Na^+ activation half-activation	mV
$k_{m_{\text{Na(P)}}}$	Persistent Na^+ activation steepness	mV
θ_h	Persistent Na^+ inactivation half-activation	mV
k_h	Persistent Na^+ inactivation steepness	mV
$\overline{\tau}_h$	Persistent Na^+ inactivation time constant	ms
g_{K}	Maximum K^+ conductance	mS/cm^2
V_{K}	K^+ reversal potential	mV
θ_n	K^+ activation half-activation	mV
k_n	K^+ activation steepness	mV
$\overline{\tau}_n$	K^+ activation time constant	ms
g_{L}	Maximum leak conductance	mS/cm^2
V_{L}	Leak reversal potential	mV

Table A.2: CPG neuron species parameter values

Parameter	**CIN/MN**	**RGN (Hb9)**
C	21	10
I_{app}	0	0
g_{Na}	28	28
V_{Na}	50	50
θ_m	-34	-34
k_m	-5	-5
$g_{\text{Na(P)}}$	–	3.3
$V_{\text{Na(P)}}$	–	50
$\theta_{m_{\text{Na(P)}}}$	–	-40
$k_{m_{\text{Na(P)}}}$	–	-6.3
θ_h	–	-47.89
k_h	–	9
$\overline{\tau}_h$	–	7000
g_{K}	11.2	11.2
V_{K}	-85	-85
θ_n	-29	-29
k_n	-4	-3.6
$\overline{\tau}_n$	10	10
g_{L}	2.8	2.8
V_{L}	-53	-60.8

A.2.2 Reference Initial Conditions

Table A.3: Initial conditions for RGN reference burst trajectory

Phase variable	**RGN (Hb9)**
V	-54.35234971337889
n	0.00087326528619
h	0.56373041060320

Table A.4: RGN (Hb9) reference burst characteristics

Characteristic	**Value**
Period	2309.00417887 ms
Duty cycle	0.528941524523
Spike number	28
Mean ISI	44.5923158905 ms
Min ISI	28.3446738803 ms
Max ISI	100.925112895 ms

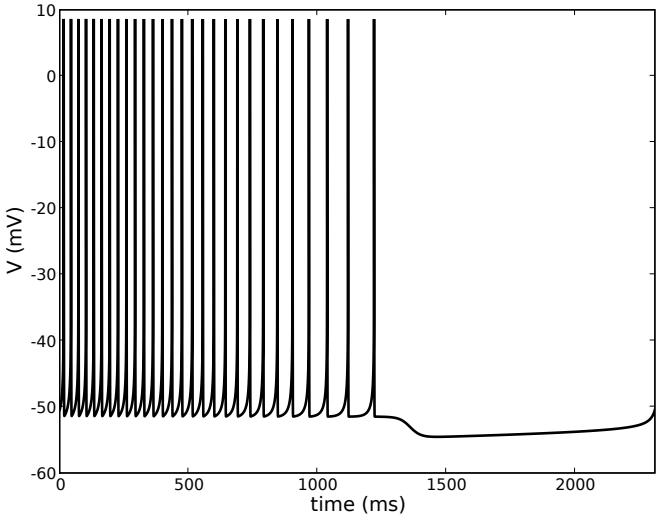

Figure A.1: RGN (Hb9) Reference Trajectory

APPENDIX B

MODELS

B.1 Model Schema

Conductance-based neuronal models typically use activation equations having stereotypical (sigmoidal or exponential) forms [115, 231]. To simplify notation and to facilitate implementation, we define the following 'helper' functions, which are used in the remainder of this appendix:

$$P_1(x, A, B, C) = A \exp\{(B - x)/C\} \tag{B.1}$$

$$P_2(x, A, B, C) = \frac{A}{1 + \exp\{(B - x)/C\}} \tag{B.2}$$

$$P_3(x, A, B, C) = \frac{A(x - B)}{1 + \exp\{(B - x)/C\}} \tag{B.3}$$

$$P_4(x, A, B, C, D, E, F) = \frac{Ax + B}{C + D \exp\{Ex + F\}} \tag{B.4}$$

$$P_5(x, A, B, C, D) = A + B \exp\{Cx + D\} \tag{B.5}$$

$$P_6(x, A, B, C) = \frac{A}{(1 + \exp\{Bx + C\})} \tag{B.6}$$

$$P_7(x, A, B, C, D) = A + \frac{B}{1 + \exp\{(C - x)D\}} \tag{B.7}$$

$$P_8(x, A, B, C) = \frac{A}{1 + \exp\{-(x + B)/C\}} \tag{B.8}$$

$$P_9(x, A, B, C, D) = A + \frac{B}{1 + \exp\{-(x + C)/D\}} \tag{B.9}$$

B.2 Model Characteristics

Table B.1: Burster classification and slow variable correspondence

Model	Burster Type	Slow Variable	Pseudo-spikes
AB	ascending simple	c	1
HR	ascending simple	h	0
PB	descending non-simple	h_{NaP}	0
PD	ascending simple	z	2
R15A	ascending non-simple	z	1

Table B.2: Reference burst characteristics

Model	Period	Duty Cycle	Spike Number
AB	927.416602445	0.48968587877	6
HR	430.775611725	0.412532859788	9
PB	1564.18926458	0.303552584085	7
PD	1165.11554247	0.0882483572185	5
R15A	10791.8214026	0.381091235873	7

Table B.3: Reference burst interspike intervals

Model	Mean ISI	Min ISI	Max ISI
AB	47.2686153345	28.6160555492	96.4633903323
HR	16.2904495182	11.8223231737	25.9911871728
PB	74.0768056611	50.8684078594	120.034647249
PD	15.8346896325	14.7607024674	18.196852294
R15A	473.571638157	264.342097394	1246.43706145

Table B.4: Injected spike characteristics

Model	Half width	Base width	Spike height
AB	2.92649189567	28.60189813	78.6485728339
HR	1.84165586354	11.83795939	3.3998181
PB	1.81495725842	34.0	60.01105726
PD	1.48707358447	15.02820904	121.86771634
R15A	40.1935954413	264.90693623	94.7704082005

B.3 Synapse Models

The synapse equations for the spike injection below are modified from [62]. The conductance pulse model is identical to the synapse model used in [175].

B.3.1 Equations

Conductance pulse synapse model

$$I_{\text{syn}} = g_{\text{syn}}(V - V_{\text{syn}}) \tag{B.10}$$

Spike injection synapse model

$$\begin{aligned} I_{\text{syn}} &= g_{\text{syn}} s (V - V_{\text{syn}}) && \text{(B.11)} \\ \dot{s} &= \alpha_{\text{syn}} T_{\infty}(V_{\text{pre}})(1 - s) - \beta_{\text{syn}} s && \text{(B.12)} \\ T_{\infty}(V_{\text{pre}}) &= (1 + \exp(-(V_{\text{pre}} - V_p)/K_p))^{-1} && \text{(B.13)} \end{aligned}$$

B.3.2 Parameters

Table B.5: Synaptic parameter descriptions and units

Parameter	Description	Units
g_{syn}	Maximum synaptic conductance	mS/cm^2
V_{syn}	Synaptic reversal potential	mV
α_{syn}	Open-closed transition rate	s^{-1}
β_{syn}	Closed-open transition rate	s^{-1}
K_p	Transmitter voltage-response steepness	mV

Table B.6: Synaptic current reversal potentials

Model	Inhibitory V_{syn}	Excitatory V_{syn}
AB	-61.1859566839	8.27414867864
HR	-1.63057945	1.37203985929
PB	-53.0	0.0
PD	-75.12935694	32.5006242822
R15A	-66.0591281805	17.6393078071

B.3.3 Activation

Table B.7: Synaptic activation parameter values

Model	V_p	K_p
AB	-17.9372118355	5.24227210283
HR	0.238975968994	0.22661277806
PB	-20.0	4
PD	-8.11446297144	8.12301745073
R15A	-13.9450076599	6.3168630934

Table B.8: Synaptic activation parameter values, continued

Model	α_{syn}	β_{syn}
AB	3.84399589283	0.384399589283
HR	9.30443182653	0.930443182653
PB	2.16244236116	0.216244236116
PD	7.45221985491	0.745221985491
R15A	0.41612743897	0.041612743897

Table B.9: Model-specific stereotypical synaptic activation levels (input pulse)

Model	**Area**	**Max Activation**
AB	32.7193225163	0.908310680391
HR	14.2501652327	0.908935555972
PB	44.7222156006	0.874474624618
PD	29.0774262247	0.90728306627
R15A	225.463267428	0.908700849544

Table B.10: Model-specific stereotypical synaptic activation level conductance pulse equivalents

Model	**Basewidth height**	**Halfwidth height**
AB	1.14395633351	11.180390612
HR	1.20376872088	7.73769166916
PB	1.31535928237	24.6409194449
PD	1.93485638557	19.5534548716
R15A	0.851103676773	5.60943267086

B.4 Hindmarsh-Rose (HR) Neuron Model

Three dimensional schematic model of a bursting neuron in the visceral ganglion of the pond snail *Lymnaea* from [117]. The parameters below are taken from Figure 6 (b), page 98, of [117].

B.4.1 Equations

$$\dot{V} = n - aV^3 + bV^2 - h + I \tag{B.14}$$

$$\dot{n} = c - dV^2 - n \tag{B.15}$$

$$\dot{h} = r(\sigma(V - V_0) - h) \tag{B.16}$$

B.4.2 Parameters

Table B.11: HR neuron parameter values

Symbol	Description	Value
a	–	1
b	Applied current	3
I	Injected current	2
c	–	1
d	–	5
r	Recovery variable time scale	0.001
σ	–	4
V_0	Resting potential	-1.6

B.4.3 Reference Initial Conditions

Table B.12: Initial conditions for HR reference burst trajectory

Phase variable	Value
V	-1.59334564251545
n	-11.60578248266614
h	2.06060639328996

B.5 Pre-Bötzinger (PB) Neuron Models

Based on model I of [24] for a class of endogenously bursting neurons in the pre-Bötzinger complex of the neonatal rat; bursting is controlled by the level of persistent sodium current activation. Characteristics of the model in various parameter regimes and network conditions are found in [24, 25], and extensive comparisons of the model with experimental data are presented in [56]. The parameter set corresponds to figure 4 (A3), page 386, of [24].

B.5.1 Equations

Dynamic variables

$$\dot{V} = -(I_{\mathrm{Na}} + I_{\mathrm{K}} + I_{\mathrm{Na(P)}} + I_{\mathrm{L}} - I_{\mathrm{app}})/C \tag{B.17}$$

$$\dot{n} = (n_\infty(V) - n)/\tau_n(V) \tag{B.18}$$

$$\dot{h} = (h_\infty(V) - h)/\tau_h(V) \tag{B.19}$$

Membrane currents

$$I_{\mathrm{Na}} = (g_{\mathrm{Na}} m_{\infty}^{3}(V)(1-n)(V-V_{\mathrm{Na}}) \tag{B.20}$$

$$I_{\mathrm{K}} = g_{\mathrm{K}} n^{4}(V-V_{\mathrm{K}}) \tag{B.21}$$

$$I_{\mathrm{Na(P)}} = g_{\mathrm{Na(P)}} m_{\mathrm{Na(P)}_{\infty}}(V) h (V-V_{\mathrm{Na}}) \tag{B.22}$$

$$I_{\mathrm{L}} = g_{\mathrm{L}}(V-V_{\mathrm{L}}) \tag{B.23}$$

Activation equations

$$m_{\infty}(V) = (1+\exp((V-\theta_m)/k_m))^{-1} \tag{B.24}$$

$$m_{\mathrm{Na(P)}_{\infty}}(V) = (1+\exp((V-\theta_{m_{NaP}})/k_{m_{\mathrm{Na(P)}}}))^{-1} \tag{B.25}$$

$$h_{\infty}(V) = (1+\exp((V-\theta_h)/k_h))^{-1} \tag{B.26}$$

$$\tau_h(V) = \overline{\tau}_h / \cosh[(V-\theta_h)/(2k_h)] \tag{B.27}$$

$$n_{\infty}(V) = (1+\exp((V-\theta_n)/k_n))^{-1} \tag{B.28}$$

$$\tau_n(V) = \overline{\tau}_n / \cosh[(V-\theta_n)/(2k_n)] \tag{B.29}$$

B.5.2 Parameters

Table B.13: PB neuron parameter values

Symbol	Description	Units	Value
C	Membrane capacitance	μF/cm^2	21
I_{app}	Applied current	μA/cm^2	0
g_{Na}	Maximum Na^+ conductance	mS/cm^2	28
V_{Na}	Na^+ reversal potential	mV	50
θ_m	Na^+ activation half-activation	mV	-34
k_m	Na^+ activation steepness	mV	-5
$g_{\text{Na(P)}}$	Maximum persistent Na^+ conductance	mS/cm^2	2.8
$V_{\text{Na(P)}}$	Persistent Na^+ reversal potential	mV	50
$\theta_{m_{\text{Na(P)}}}$	Persistent Na^+ activation half-activation	mV	-40
$k_{m_{\text{Na(P)}}}$	Persistent Na^+ activation steepness	mV	-6
θ_h	Persistent Na^+ inactivation half-activation	mV	-48
k_h	Persistent Na^+ inactivation steepness	mV	6
$\overline{\tau}_h$	Persistent Na^+ inactivation time constant	ms	10000
g_{K}	Maximum K^+ conductance	mS/cm^2	11.2
V_{K}	K^+ reversal potential	mV	-85
θ_n	K^+ activation half-activation	mV	-29
k_n	K^+ activation steepness	mV	-4
$\overline{\tau}_n$	K^+ activation time constant	ms	10
g_{L}	Maximum leak conductance	mS/cm^2	2.8
V_{L}	Leak reversal potential	mV	-57.5

B.5.3 Reference Initial Conditions

Table B.14: Initial conditions for PB reference burst trajectory

Phase variable	Value
V	-51.34152805445130
n	0.00373833450475
h	0.46103058900700

B.6 R15 *Aplysia* (R15A) Neuron Model

Originally from a study analyzing Plant's model for the pacemaker R-15 cell of the *Aplysia* abdominal ganglion [187]. Parameter values are taken from Appendix I, pages 673–674, and correspond to figure 4, page 664. Related models are found in [23]

B.6.1 Equations

Dynamic variables

$$\dot{V} = -(I_{\mathrm{Na}} + I_{\mathrm{K}} + I_{\mathrm{K_{Ca}}} + I_{\mathrm{Ca}} + I_{\mathrm{L}} - I_{\mathrm{app}})/C \tag{B.30}$$

$$\dot{n} = \lambda(n_\infty(V) - n)/\tau_n(V) \tag{B.31}$$

$$\dot{h} = \lambda(h_\infty(V) - h)/\tau_h(V) \tag{B.32}$$

$$\dot{x} = (x_\infty(V) - x)/\tau_x \tag{B.33}$$

$$\dot{z} = \rho(K_c x(V_{\mathrm{Ca}} - V) - z) \tag{B.34}$$

Membrane currents

$$I_{\mathrm{Na}} = (g_{Na} m_\infty^3(V) h(V - V_{\mathrm{Na}}) \tag{B.35}$$

$$I_{\mathrm{K}} = g_{\mathrm{K}} n^4 (V - V_{\mathrm{K}}) \tag{B.36}$$

$$I_{\mathrm{K_{Ca}}} = g_{\mathrm{K_{Ca}}}(z/(0.5 + z))(V - V_{\mathrm{K}}) \tag{B.37}$$

$$I_{\mathrm{Ca}} = g_{\mathrm{Ca}} x (V - V_{\mathrm{Ca}}) \tag{B.38}$$

$$I_{\mathrm{L}} = g_{\mathrm{L}}(V - V_{\mathrm{L}}) \tag{B.39}$$

Activation equations

$$
\begin{aligned}
m_\infty(V) &= \alpha_m(V)/(\alpha_m(V)+\beta_m(V)) && \text{(B.40)}\\
\alpha_m(V) &= P_3((C_1V+C_2),0.1,50,10) && \text{(B.41)}\\
\beta_m(V) &= P_1((C_1V+C_2),4,25,18) && \text{(B.42)}\\
h_\infty(V) &= \alpha_h(V)/(\alpha_h(V)+\beta_h(V)) && \text{(B.43)}\\
\tau_h(V) &= (\alpha_h(V)+\beta_h(V))^{-1} && \text{(B.44)}\\
\alpha_h(V) &= P_1((C_1V+C_2),0.07,25,20) && \text{(B.45)}\\
\beta_h(V) &= P_2((C_1V+C_2),1,55,10) && \text{(B.46)}\\
n_\infty(V) &= \alpha_n(V)/(\alpha_n(V)+\beta_n(V)) && \text{(B.47)}\\
\tau_n(V) &= (\alpha_n(V)+\beta_n(V))^{-1} && \text{(B.48)}\\
\alpha_n(V) &= P_3((C_1V+C_2),0.01,55,10) && \text{(B.49)}\\
\beta_n(V) &= P_1((C_1V+C_2),0.125,45,80) && \text{(B.50)}\\
x_\infty(V) &= P_2(V,1,a,b) && \text{(B.51)}
\end{aligned}
$$

B.6.2 Parameters

Table B.15: R15A neuron parameter values

Symbol	Description	Units	Value
C	Membrane capacitance	μF/cm^2	1
I_{app}	Applied current	μA/cm^2	0
C_1	Voltage scaling for m_∞, h_∞, n_∞	–	127/105
C_2	Voltage shift for m_∞, h_∞, n_∞	mV	8265/105
λ	Activation scaling for h_∞, n_∞	ms^{-1}	0.08
g_{Na}	Maximum Na^+ conductance	mS/cm^2	4
V_{Na}	Na^+ reversal potential	mV	30
g_{K}	Maximum K^+ conductance	mS/cm^2	0.3
V_{K}	K^+ reversal potential	mV	-75
g_{KCa}	Maximum Ca^{2+} activated K^+ conductance	mS/cm^2	0.03
g_{Ca}	Maximum Ca^{2+} conductance	mS/cm^2	0.004
V_{Ca}	Ca^{2+} reversal potential	mV	-75
τ_x	I_{Ca} activation time constant	ms	235
a	Voltage scaling for x_∞	–	0.15
b	Voltage shift for x_∞	mV	-50
ρ	Ca^{2+} channel time constant	ms^{-1}	0.0003
K_c	Ca^{2+} channel voltage constant	mV^{-1}	0.0065
g_{L}	Maximum leak conductance	mS/cm^2	0.003
V_{L}	Leak reversal potential	mV	-40

B.6.3 Reference Initial Conditions

Table B.16: Initial conditions for R15A reference burst trajectory

Phase variable	Value
V	-50.2441889999
n	0.0539665845093
h	0.777621762237
x	0.561043636914
z	0.862117514425

B.7 Anterior Burster (AB) Neuron Model

Based on model for anterior burster cell of lobster stomatogastric ganglion [100]. Parameter values are taken from Figure 7 (c), page 355, for six spike regular burster.

B.7.1 Equations

Dynamic variables

$$\dot{V} = -(I_{\mathrm{Na}} + I_{\mathrm{Ca}} + I_{\mathrm{K}} + I_{\mathrm{K_{Ca}}} + I_{\mathrm{A}} + I_{\mathrm{L}} - I_{\mathrm{app}})/C \tag{B.52}$$

$$\dot{c} = \rho(\frac{k_{\mathrm{Ca}} z (V_{\mathrm{Ca}} - V)}{1 + 2c} - c) \tag{B.53}$$

$$\dot{n} = \lambda_n (a_n (1 - n) - b_n n) \tag{B.54}$$

$$\dot{h}_{\mathrm{Na}} = \lambda_h (a_h (1 - h_{\mathrm{Na}}) - b_h h_{\mathrm{Na}}) \tag{B.55}$$

$$\dot{h}_{\mathrm{A}} = (h_{\mathrm{A}i} - h_{\mathrm{A}}) k_{\mathrm{A}} \tag{B.56}$$

$$\dot{z} = (z_v - z)/\tau_z \tag{B.57}$$

Membrane currents

$$I_{\mathrm{Na}} = g_{\mathrm{Na}} m_{\mathrm{Na}}^3 (V) h_{Na} (V - V_{\mathrm{Na}}) \tag{B.58}$$

$$I_{\mathrm{Ca}} = g_{\mathrm{Ca}} \frac{z}{0.5 + c} (V - V_{\mathrm{Ca}}) \tag{B.59}$$

$$I_{\mathrm{K}} = g_{\mathrm{K}} n^4 (V - V_{\mathrm{K}}) \tag{B.60}$$

$$I_{\mathrm{K_{Ca}}} = g_{\mathrm{K_{Ca}}} \frac{c}{0.5 + c} (V - V_{\mathrm{K}}) \tag{B.61}$$

$$I_{\mathrm{A}} = g_{\mathrm{A}} m_{\mathrm{A}}^3 (V) h_{\mathrm{A}} (V - V_{\mathrm{K}}) \tag{B.62}$$

$$I_{\mathrm{L}} = g_{\mathrm{L}} (V - V_{\mathrm{L}}) \tag{B.63}$$

Activation equations

$$
\begin{aligned}
m_{\mathrm{Na}}(V) &= \frac{a_m}{a_m + b_m} && \text{(B.64)}\\
a_m(V) &= P_4(V, \frac{127}{105}, \frac{201}{7}, 10, -10, -\frac{127}{1050}, -\frac{201}{70}) && \text{(B.65)}\\
b_m(V) &= P_5(V, 0, 4, -\frac{127}{1890}, -\frac{188}{63}) && \text{(B.66)}\\
a_h(V) &= P_5(V, 0, \frac{7}{100}, -\frac{127}{2100}, -\frac{94}{35}) && \text{(B.67)}\\
b_h(V) &= P_6(V, 1, -\frac{127}{1050}, -\frac{83}{35}) && \text{(B.68)}\\
a_n(V) &= P_4(V, \frac{127}{105}, \frac{166}{7}, 100, -100, -\frac{127}{1050}, -\frac{83}{35}) && \text{(B.69)}\\
b_n(V) &= P_5(V, 0, \frac{1}{8}, -\frac{127}{8400}, -\frac{59}{140}) && \text{(B.70)}\\
m_{\mathrm{A}} &= P_2(V, 1, -v_a, -s_a) && \text{(B.71)}\\
h_{\mathrm{A}i} &= P_2(V, 1, -v_b, -s_b) && \text{(B.72)}\\
z_v &= P_2(V, 1, -z_b, \frac{100}{15}) && \text{(B.73)}\\
& && \text{(B.74)}
\end{aligned}
$$

B.7.2 Parameters

Table B.17: AB neuron parameter values

Symbol	Description	Units	Value
C	Membrane capacitance	nF	1
I_{app}	Applied current	μA	0
g_{Na}	Maximum Na^+ conductance	μS	15
V_{Na}	Na^+ reversal potential	mV	30
g_{K}	Maximum K^+ conductance	μS	8.0
V_{K}	K^+ reversal potential	mV	-75

Table B.18: AB neuron parameter values, continued

Symbol	Description	Units	Value
$g_{\mathrm{K_{Ca}}}$	Maximum Ca^{2+} activated K^+ conductance	μS	0.03
g_{A}	Maximum A-current conductance	μS	0.03
k_{A}	A-current rate constant	ms^{-1}	1
λ_n	Activation scaling for n	$\mathrm{ms}^{-}1$	0.8
λ_h	Activation scaling for h	ms^{-1}	0.8
g_{Ca}	Maximum Ca^{2+} conductance	μS	0.04
V_{Ca}	Ca^{2+} reversal potential	mV	140
τ_z	I_{Ca} activation time constant	ms	23.5
k_{Ca}	Ca^{2+} channel voltage scaling	mV^{-1}	0.0078
ρ	Ca^{2+} free activity scaling	ms^{-1}	0.003
z_b	I_{Ca} activation voltage shift	mV	-50
v_a	A-current activation voltage shift	mV	-12
s_a	A-current activation voltage scaling	mV	-26
v_b	A-current inactivation voltage shift	mV	-62
s_b	A-current inactivation voltage scaling	mV	6
g_{L}	Maximum leak conductance	μS	0.0854
V_{L}	Leak reversal potential	mV	-40

B.7.3 Reference Initial Conditions

Table B.19: Initial conditions for AB reference burst trajectory

Phase variable	Value
V	-50.2441889999
c	0.0539665845093
n	0.777621762237
h_{Na}	0.561043636914
h_{A}	0.01644904560620938
z	0.862117514425

B.8 Pyloric Dilator (PD) Neuron Model

Based on isolated PD equations of [208]; gap junctional coupling and I_{proc} have been removed. The parameter set is from Table 2, page 593.

B.8.1 Equations

Soma Compartment

Dynamic variables

$$\begin{aligned}
\dot{V}_s &= -(I_{\text{CaT}} + I_{\text{CaS}} + I_{\text{Na(P)}} + I_{\text{K}_s} + I_{\text{K}_{\text{Ca}}} + I_{\text{H}} + I_{\text{A}} + \\
&\quad I_{\text{L}_s} + I_{\text{app}} + g_{\text{axial}}(V_s - V_a))/C_s && \text{(B.75)} \\
\dot{m}_{\text{CaT}} &= (m_{\text{CaT}_\infty}(V_s) - m_{\text{CaT}})/\tau_{m_{\text{CaT}}}(V_s) && \text{(B.76)} \\
\dot{h}_{\text{CaT}} &= (h_{\text{CaT}_\infty}(V_s) - h_{\text{CaT}})/\tau_{h_{\text{CaT}}}(V_s) && \text{(B.77)} \\
\dot{m}_{\text{CaS}} &= (m_{\text{CaS}_\infty}(V_s) - m_{\text{CaS}})/\tau_{m_{\text{CaS}}}(V_s) && \text{(B.78)} \\
\dot{m}_{\text{NaP}} &= (m_{\text{NaP}_\infty}(V_s) - m_{\text{NaP}})/\tau_{m_{\text{NaP}}}(V_s) && \text{(B.79)} \\
\dot{h}_{\text{NaP}} &= (h_{\text{NaP}_\infty}(V_s) - h_{\text{NaP}})/\tau_{h_{\text{NaP}}}(V_s) && \text{(B.80)} \\
\dot{m}_{\text{H}} &= (m_{\text{H}_\infty}(V_s) - m_{\text{H}})/\tau_{m_{\text{H}}}(V_s) && \text{(B.81)} \\
\dot{m}_{\text{K}_s} &= (m_{\text{K}_{s\infty}}(V_s) - m_{\text{K}_s})/\tau_{m_{\text{K}_s}}(V_s) && \text{(B.82)} \\
\dot{m}_{\text{KCa}} &= (m_{\text{KCa}_\infty}(V_s, z) - m_{\text{KCa}})/\tau_{m_{\text{KCa}}}(V_s) && \text{(B.83)} \\
\dot{m}_{\text{A}} &= (m_{\text{A}_\infty}(V_s) - m_{\text{A}})/\tau_{m_{\text{A}}}(V_s) && \text{(B.84)} \\
\dot{h}_{\text{A}} &= (h_{\text{A}_\infty}(V_s) - h_{\text{A}})/\tau_{h_{\text{A}}}(V_s) && \text{(B.85)} \\
\dot{z} &= (z_{\text{Ca}_\infty}(z, m_{\text{CaS}}, m_{\text{CaT}}, h_{\text{CaT}}, V_s) - z)/\tau_{z_{\text{Ca}}} && \text{(B.86)}
\end{aligned}$$

Membrane currents

$$I_{\mathrm{CaT}} = g_{\mathrm{CaT}} m_{\mathrm{CaT}}^3 h_{\mathrm{CaT}} (V_s - 12.2396 \ln(13000/z)) \quad \text{(B.87)}$$

$$I_{\mathrm{CaS}} = g_{\mathrm{CaS}} m_{\mathrm{CaS}}^3 (V_s - 12.2396 \ln(13000/z)) \quad \text{(B.88)}$$

$$I_{\mathrm{Na(P)}} = g_{\mathrm{NaP}} m_{\mathrm{NaP}}^3 h_{\mathrm{NaP}} (V_s - V_{\mathrm{NaP}}) \quad \text{(B.89)}$$

$$I_{\mathrm{K}_s} = g_{\mathrm{K}_a} m_{\mathrm{K}_s}^4 (V_s - V_{\mathrm{K}}) \quad \text{(B.90)}$$

$$I_{\mathrm{K_{Ca}}} = g_{\mathrm{KCa}} m_{\mathrm{KCa}}^4 (V_s - V_{\mathrm{K}}) \quad \text{(B.91)}$$

$$I_{\mathrm{H}} = g_{\mathrm{H}} m_{\mathrm{H}} (V_s - V_{\mathrm{H}}) \quad \text{(B.92)}$$

$$I_{\mathrm{A}} = g_{\mathrm{A}} m_{\mathrm{A}}^4 h_{\mathrm{A}} (V_s - V_{\mathrm{K}}) \quad \text{(B.93)}$$

$$I_{\mathrm{L}} = g_{\mathrm{L}_s} (V_s - V_{\mathrm{L}_s}) \quad \text{(B.94)}$$

$$z_{\mathrm{Ca}_\infty} = 0.5 - (1.128/2.19)(g_{\mathrm{CaS}} m_{\mathrm{CaS}}^3 (V_s - 12.2396 \ln(13000/z)) \quad \text{(B.95)}$$
$$+ g_{\mathrm{CaT}} m_{\mathrm{CaT}}^3 h_{\mathrm{CaT}} (V_s - 12.2396 \ln(13000/z)))$$

Activation equations

$$m_{\mathrm{CaT}_\infty}(V_s) = P_8(V_s, 1, 25, 7.2) \quad \text{(B.96)}$$

$$\tau_{m_{\mathrm{CaT}}}(V_s) = P_9(V_s, 55, -49.5, 58, 17) \quad \text{(B.97)}$$

$$h_{\mathrm{CaT}_\infty}(V_s) = P_8(V_s, 1, 36, -7) \quad \text{(B.98)}$$

$$\tau_{h_{\mathrm{CaT}}}(V_s) = P_9(V_s, 350, -300, 50, 16.9) \quad \text{(B.99)}$$

$$m_{\mathrm{CaS}_\infty}(V_s) = P_8(V_s, 1, 22, 8.5) \quad \text{(B.100)}$$

$$\tau_{m_{\mathrm{CaS}}}(V_s) = P_9(V_s, 16, -13.1, 25.1, 26.4) \quad \text{(B.101)}$$

$$m_{\mathrm{NaP}_\infty}(V_s) = P_8(V_s, 1, 26.8, 8.2) \quad \text{(B.102)}$$

$$\tau_{m_{\mathrm{NaP}}}(V_s) = P_9(V_s, 19.8, -10.7, 26.5, 8.6) \quad \text{(B.103)}$$

$$h_{\mathrm{NaP}_\infty}(V_s) = P_8(V_s, 1, 48.5, -4.8) \quad \text{(B.104)}$$

$$\tau_{h_{\mathrm{NaP}}}(V_s) = P_9(V_s, 666, -379, 33.6, 11.7) \quad \text{(B.105)}$$

$$m_{\mathrm{K}_{s\infty}}(V_s) = P_8(V_s, 1, 14.2, 11.8) \quad \text{(B.106)}$$

$$\tau_{m_{\mathrm{K}_s}}(V_s) = P_9(V_s, 7.2, -6.4, 28.3, 19.2) \quad \text{(B.107)}$$

$$m_{\mathrm{KCa}_\infty}(V_s, z) = \frac{z}{z+30} P_8(V_s, 1, 51, 4) \quad \text{(B.108)}$$

$$\tau_{m_{\mathrm{KCa}}}(V_s) = P_9(V_s, 90.3, -75.09, 46, 22.7) \quad \text{(B.109)}$$

$$m_{\mathrm{H}_\infty}(V_s) = P_8(V_s, 1, 70, -6) \quad \text{(B.110)}$$

$$\tau_{m_{\mathrm{H}}}(V_s) = P_9(V_s, 272, 1499, 42.2, 8.73) \quad \text{(B.111)}$$

$$m_{\mathrm{A}_\infty}(V_s) = P_8(V_s, 1, 27, 8.7) \quad \text{(B.112)}$$

$$\tau_{m_{\mathrm{A}}}(V_s) = P_9(V_s, 11.6, -10.4, 32.9, 15.2) \quad \text{(B.113)}$$

$$h_{\mathrm{A}_\infty}(V_s) = P_8(V_s, 1, 56.9, -4.9) \quad \text{(B.114)}$$

$$\tau_{h_{\mathrm{A}}}(V_s) = P_9(V_s, 38.6, -29.2, 38.9, 26.5) \quad \text{(B.115)}$$

Axon Compartment

Dynamic variables

$$V_a = -(I_{\mathrm{Na}} + I_{\mathrm{K}_a} + I_{\mathrm{L}_a} + g_{\mathrm{axial}}(V_a - V_s))/C_a \quad \text{(B.116)}$$

$$m_{\mathrm{Na}} = (m_{\mathrm{Na}_\infty}(V_a) - m_{\mathrm{Na}})/\tau_{m_{\mathrm{Na}}}(V_a) \quad \text{(B.117)}$$

$$h_{\mathrm{Na}} = (h_{\mathrm{Na}_\infty}(V_a) - h_{\mathrm{Na}})/\tau_{h_{\mathrm{Na}}}(V_a) \quad \text{(B.118)}$$

$$m_{\mathrm{Ka}} = (m_{\mathrm{Ka}_\infty}(V_a) - m_{\mathrm{Ka}})/\tau_{m_{\mathrm{Ka}}}(V_a) \quad \text{(B.119)}$$

Membrane currents

$$I_{\mathrm{Na}} = g_{\mathrm{Na}} m_{\mathrm{Na}}^3 h_{\mathrm{Na}} (V_a - V_{\mathrm{Na}}) \quad \text{(B.120)}$$

$$I_{\mathrm{K}_a} = g_{\mathrm{K}_a} m_{\mathrm{Ka}}^3 m_{\mathrm{Ka}} (V_a - V_{\mathrm{K}}) \quad \text{(B.121)}$$

$$I_{\mathrm{L}_a} = g_{\mathrm{L}_a} (V_a - V_{\mathrm{L}_a}) \quad \text{(B.122)}$$

(B.123)

Activation equations

$$m_{\mathrm{Na}_\infty}(V_a) = P_8(V_a, 1, 24.7, 5.29) \quad \text{(B.124)}$$

$$\tau_{m_{\mathrm{Na}}}(V_a) = P_7(V_a, 1.32, 1.26, 120, -25) \quad \text{(B.125)}$$

$$h_{\mathrm{Na}_\infty}(V_a) = P_8(V_a, 1, 48.9, -5.18) \quad \text{(B.126)}$$

$$\tau_{h_{\mathrm{Na}}}(V_a) = P_8(V_a, 0.67, 62.9, 10) P_9(V_a, 1.5, 1, 34.9, -3.6) \quad \text{(B.127)}$$

$$m_{\mathrm{Ka}_\infty}(V_a) = P_8(V_a, 1, 14.2, 11.8) \quad \text{(B.128)}$$

$$\tau_{m_{\mathrm{Ka}}}(V_a) = P_9(V_a, 7.2, -6.4, 28.3, 19.2) \quad \text{(B.129)}$$

B.8.2 Parameters

Table B.20: PD neuron parameter values, soma compartment

Symbol	Description	Units	Value
g_{axial}	Intercompartmental coupling strength	mS/cm^2	1.05
C_s	Membrane capacitance, soma	μF/cm^2	12
I_{app}	Applied current	μA/cm^2	0
g_{CaT}	Maximum T-type Ca^{2+} conductance	mS/cm^2	35
g_{CaS}	Maximum S-type Ca^{2+} conductance	mS/cm^2	92
g_{NaP}	Maximum persistent $I_{\text{Na(P)}}$ conductance	mS/cm^2	4.38
V_{NaP}	Persistent $I_{\text{Na(P)}}$ reversal potential	mV	50
g_{H}	Maximum h-current conductance	mS/cm^2	0.219
V_{H}	h-current reversal potential	mV	-20
g_{K_a}	Maximum K^+ conductance, soma	mS/cm^2	1576.8
V_{K}	K^+ reversal potential	mV	-80
g_{KCa}	Maximum Ca^{2+} activated K^+ conductance	mS/cm^2	251.85
g_{A}	Maximum A-current conductance	mS/cm^2	39.42
g_{L_s}	Maximum leak conductance, soma	mS/cm^2	0.105
V_{L_s}	Leak reversal potential, soma	mV	-55
$\tau_{z_{\text{Ca}}}$	Ca^{2+} activation time scale	ms	300

Table B.21: PD neuron parameter values, axon compartment

Symbol	Description	Units	Value
C_a	Membrane capacitance, axon	mV	6
g_{Na}	Maximum Na^+ conductance	mS/cm^2	1110
V_{Na}	Na^+ reversal potential	mV	50
g_{K_a}	Maximum K^+ conductance, axon	mS/cm^2	150
g_{L_a}	Maximum leak conductance, axon	mS/cm^2	0.00081
V_{L_a}	Leak reversal potential, axon	mV	-55

B.8.3 Reference Initial Conditions

Table B.22: Initial conditions for PD reference burst trajectory, soma compartment

Phase variable	**Value**
V_s	-68.7796422334141
m_{CaT}	0.028857006864283118
h_{CaT}	0.63497582544442221
m_{CaS}	0.0043336483360708325
m_{NaP}	0.011099305542850013
h_{NaP}	0.49117766528151258
m_{K_s}	0.0093144104981476641
m_{KCa}	0.13458631369992624
m_{H}	0.087437016532535897
m_{A}	0.0077065553081521491
h_{A}	0.83606808655745002
z	21.224176962595457

Table B.23: Initial conditions for PD reference burst trajectory, axon compartment

Phase variable	**Value**
V_a	-69.215152648475367
m_{Na}	0.00022081187469711184
h_{Na}	0.9807430174142493
m_{Ka}	0.0090457259598904338

APPENDIX C

GALLERY

C.1 Gallery Key

Table C.1: PRC line styles and symbols

Linestyle Symbol	Meaning
Solid line	Synapse mediated spike injection
Dotted line	Base-width conductance pulse
Dashed line	Half-width conductance pulse
Vertical dashed black line	Spike maxima position
Vertical green dash-dotted lines	Pseudospike position
Red circle	End of active segment of burst cycle
Green triangle	Start of burst cycle

Table C.2: PRC colors and corresponding perturbation strengths. Color names follow the HTML 4.0 standard.

Line Color	Perturbation strength
Purple	100
Magenta	10
Green	1
Red	10^{-1}
Blue	10^{-2}
Cyan	10^{-3}
Orange	10^{-4}
Brown	10^{-5}
Lime	10^{-6}
Gold	10^{-7}
Plum	10^{-8}
Crimson	10^{-9}
Navy	10^{-10}
Olive	10^{-11}
Indigo	10^{-12}

C.2 Reference Bursts

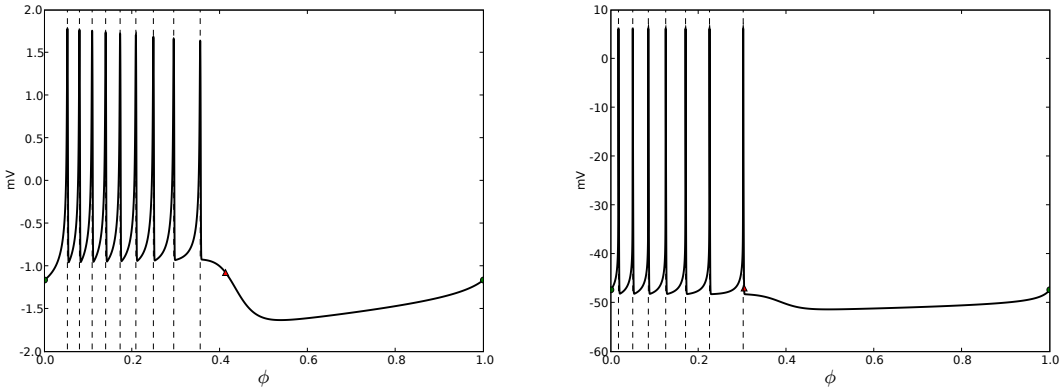

(a) HR model

(b) PB model

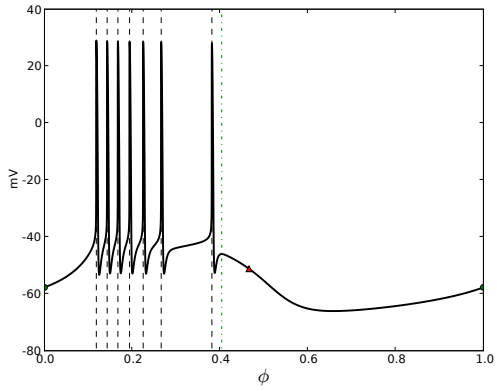

(c) R15A model

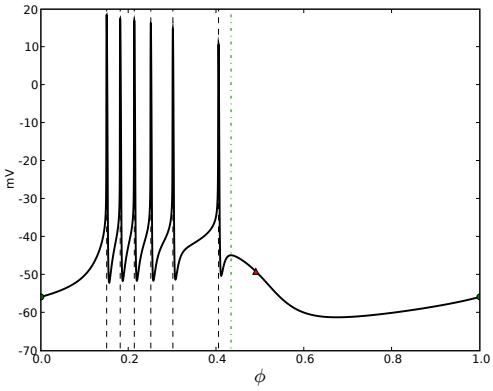

(d) AB model

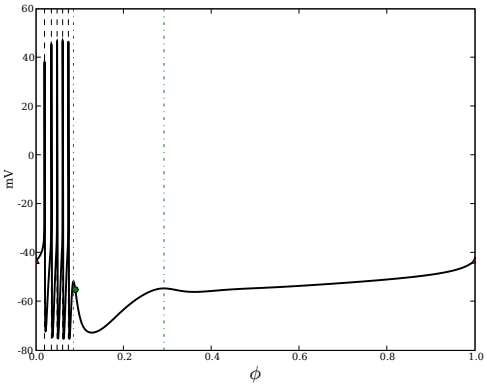

(e) PD model

Figure C.1: Reference trajectories. Dashed black lines: spike phases. Green dash-dotted lines: pseudospike phases. Red circles: end of active segment.

C.3 Hindmarsh-Rose (HR) Neuron Model

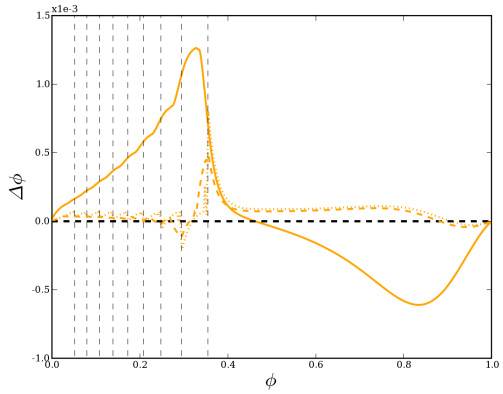

(a) $g_{\text{syn}} = 0.0001$

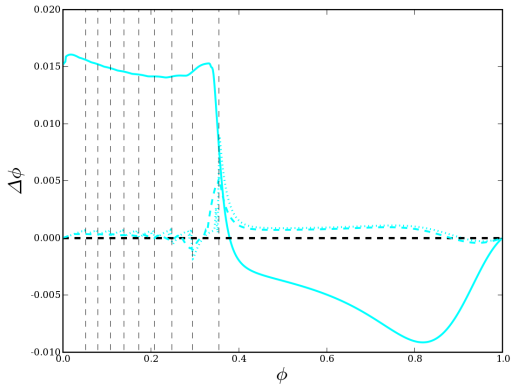

(b) $g_{\text{syn}} = 0.001$

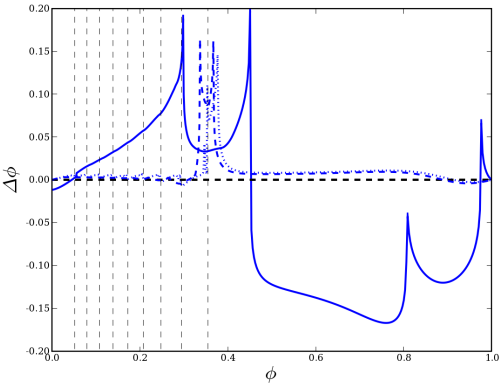

(c) $g_{\text{syn}} = 0.01$

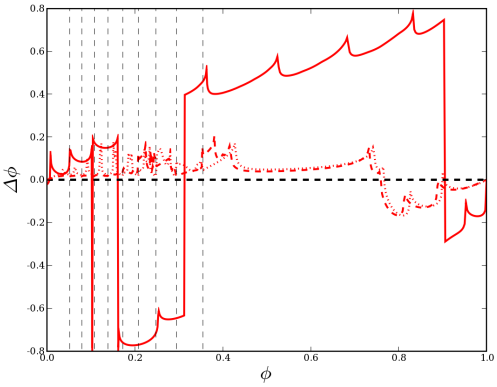

(d) $g_{\text{syn}} = 0.1$

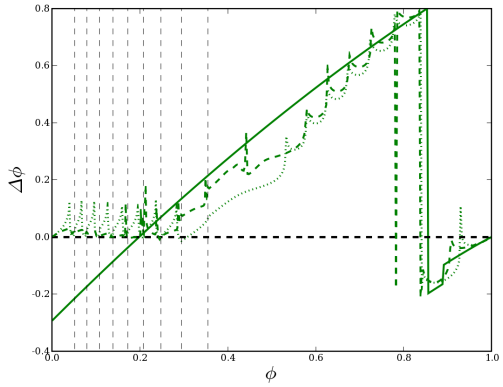

(e) $g_{\text{syn}} = 1$

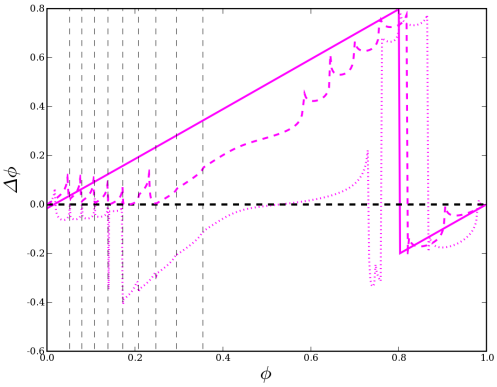

(f) $g_{\text{syn}} = 10$

Figure C.2: HR Excitatory Burst PRCs.

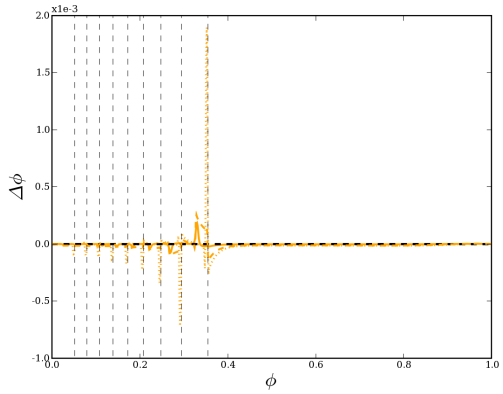

(a) $g_{\text{syn}} = 0.0001$

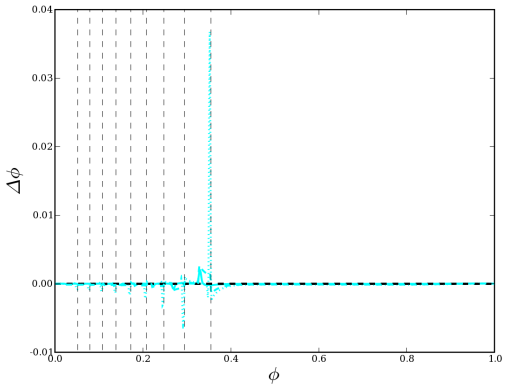

(b) $g_{\text{syn}} = 0.001$

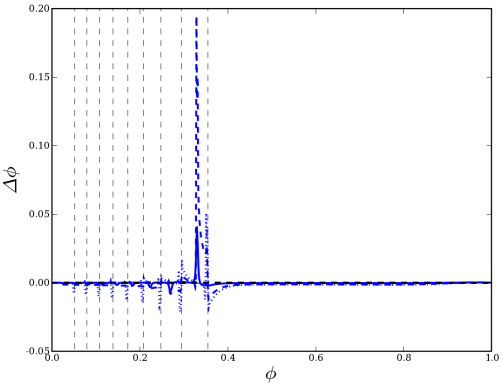

(c) $g_{\text{syn}} = 0.01$

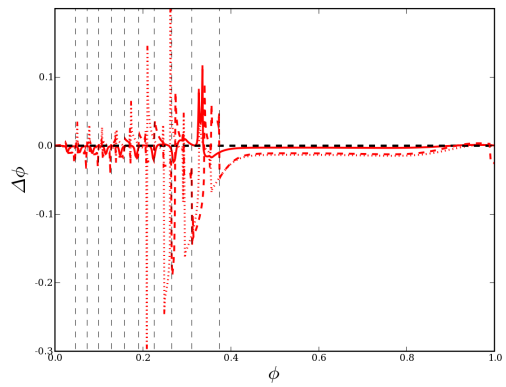

(d) $g_{\text{syn}} = 0.1$

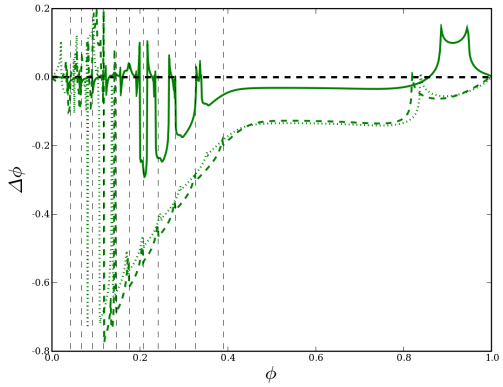

(e) $g_{\text{syn}} = 1$

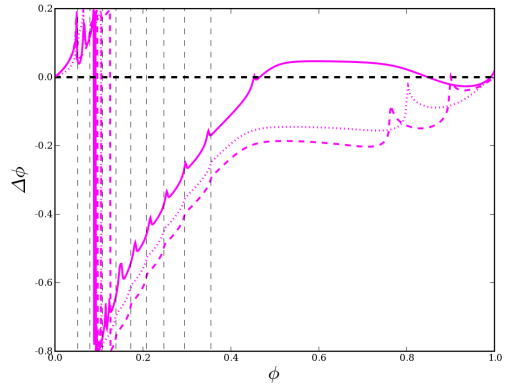

(f) $g_{\text{syn}} = 10$

Figure C.3: HR Inhibitory Burst PRCs.

C.4 Pre-Bötzinger (PB) Neuron Model

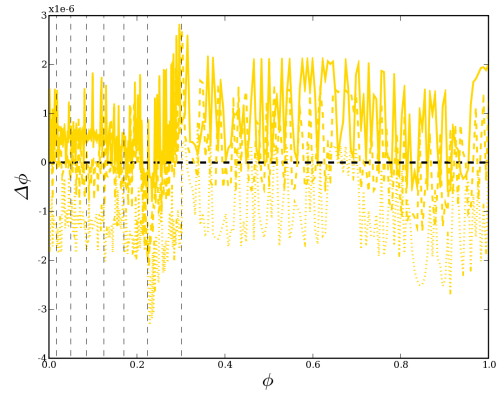

(a) $g_{\text{syn}} = 10^{-7}$

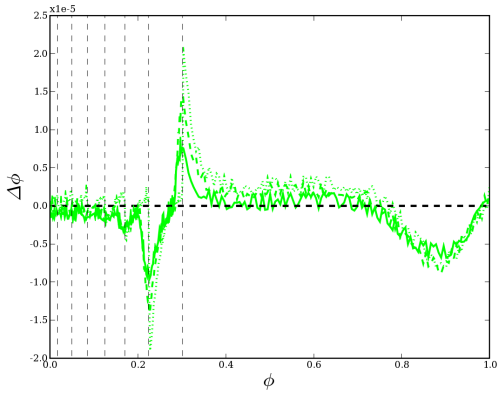

(b) $g_{\text{syn}} = 10^{-6}$

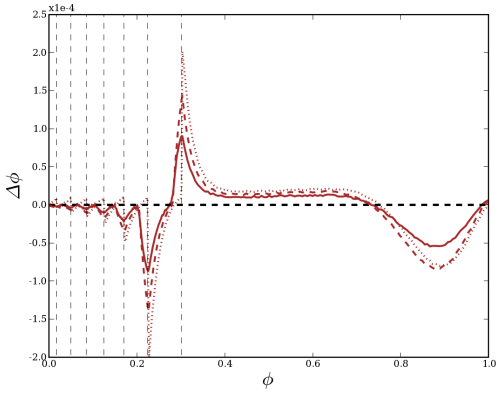

(c) $g_{\text{syn}} = 10^{-5}$

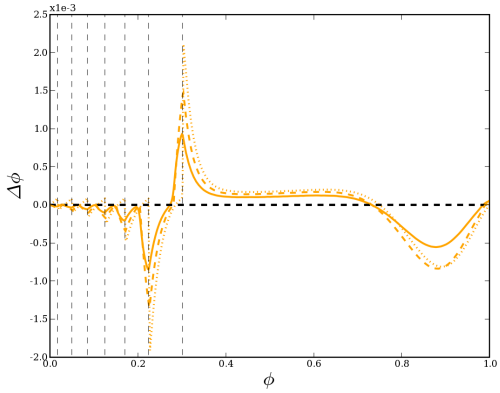

(d) $g_{\text{syn}} = 0.0001$

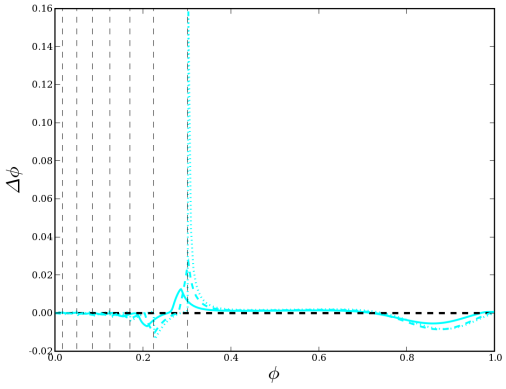

(e) $g_{\text{syn}} = 0.001$

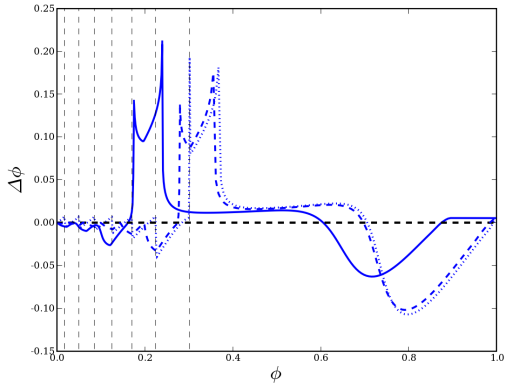

(f) $g_{\text{syn}} = 0.01$

Figure C.4: PB Excitatory Burst PRCs.

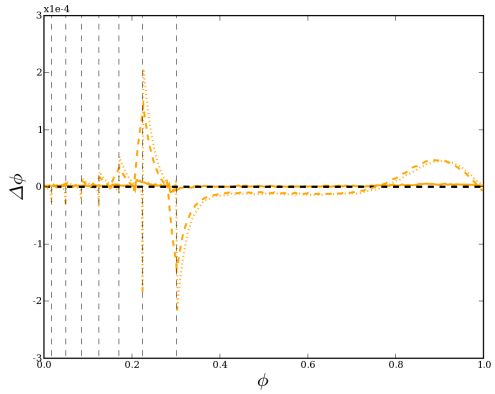

(a) $g_{\text{syn}} = 0.0001$

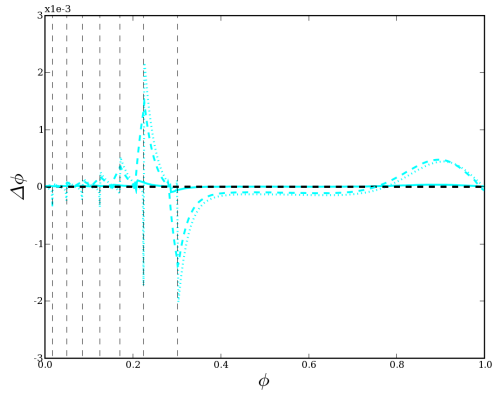

(b) $g_{\text{syn}} = 0.001$

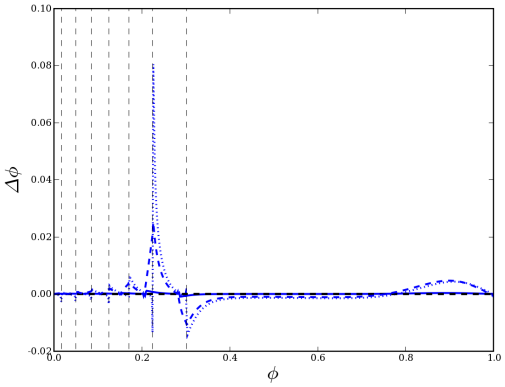

(c) $g_{\text{syn}} = 0.01$

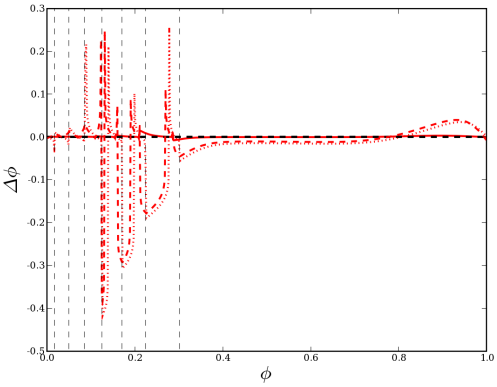

(d) $g_{\text{syn}} = 0.1$

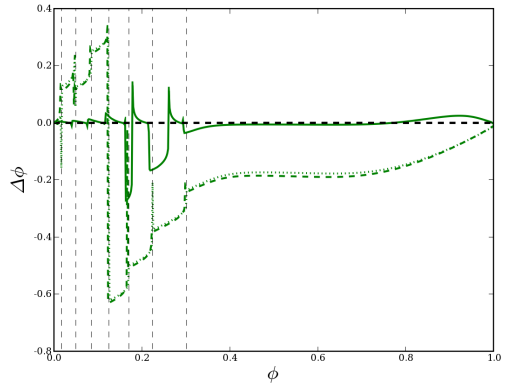

(e) $g_{\text{syn}} = 1$

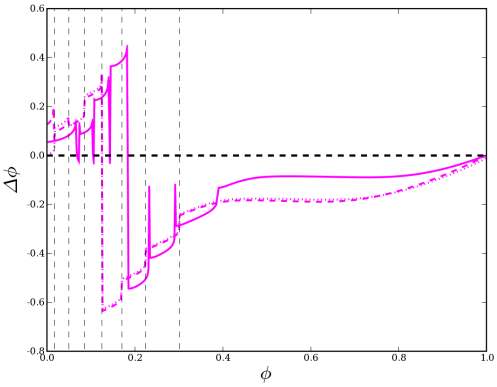

(f) $g_{\text{syn}} = 10$

Figure C.5: PB Inhibitory Burst PRCs. From (a)–(f), g_{syn} ranges from 10^{-4} to 10.

C.5 R15 *Aplysia* (R15A) Neuron Model

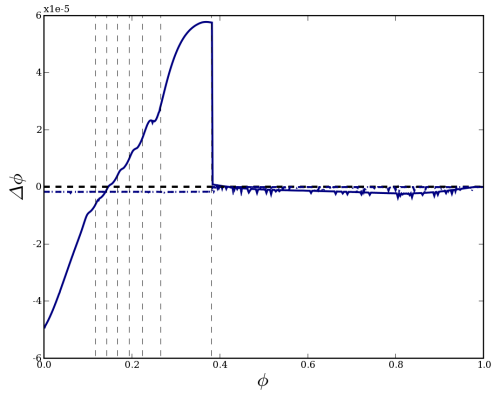

(a) $g_{\text{syn}} = 10^{-10}$

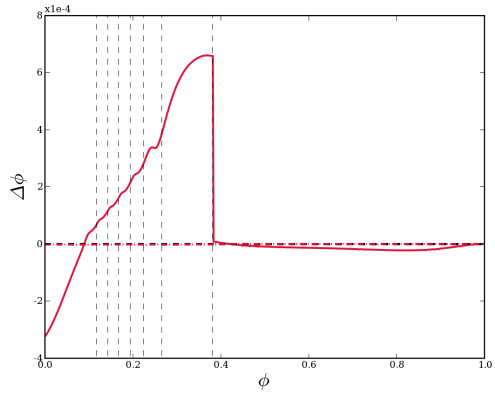

(b) $g_{\text{syn}} = 10^{-9}$

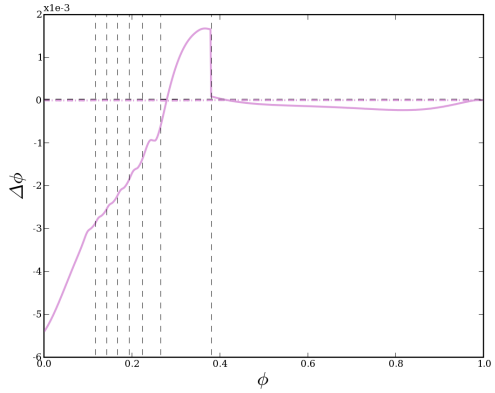

(c) $g_{\text{syn}} = 10^{-8}$

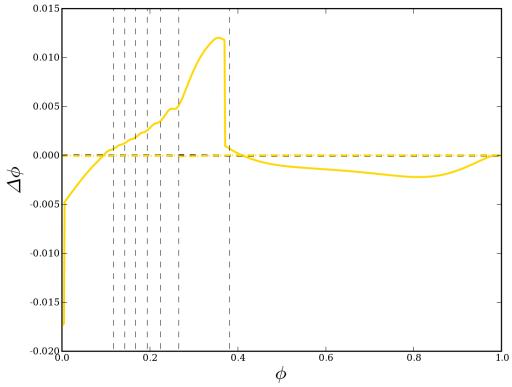

(d) $g_{\text{syn}} = 10^{-7}$

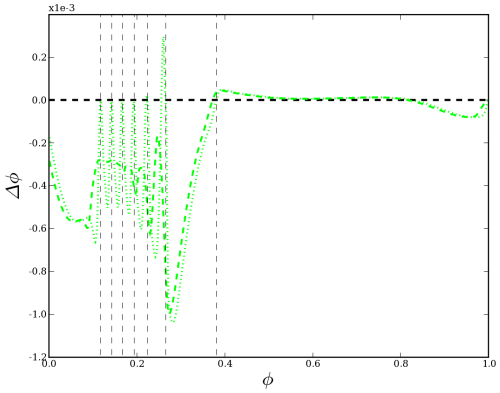

(e) $g_{\text{syn}} = 10^{-6}$

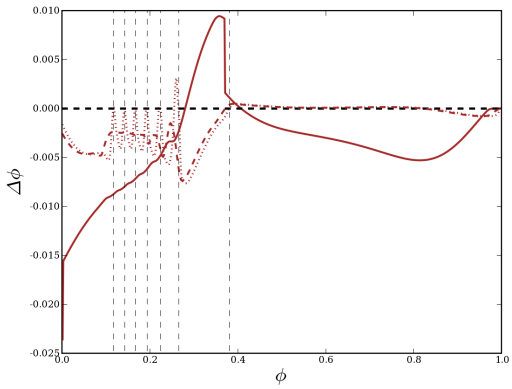

(f) $g_{\text{syn}} = 10^{-5}$

Figure C.6: R15A Excitatory Burst PRCs.

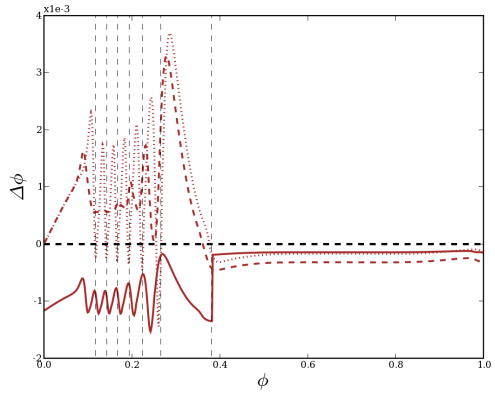

(a) $g_{\text{syn}} = 10^{-5}$

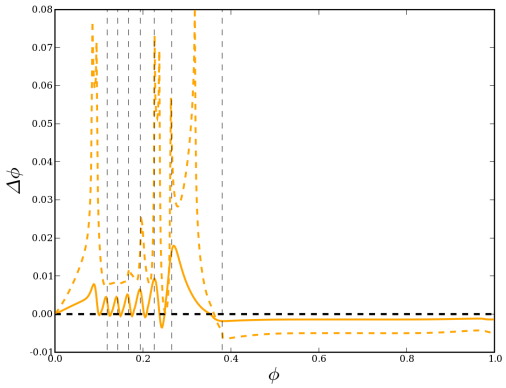

(b) $g_{\text{syn}} = 0.0001$

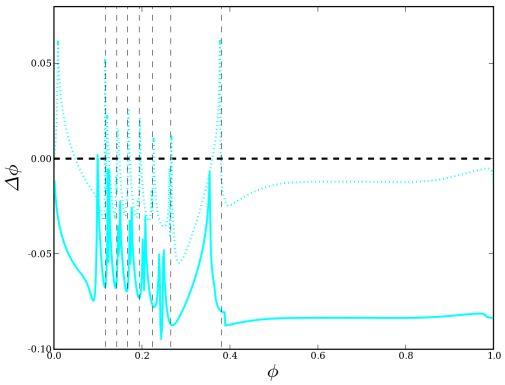

(c) $g_{\text{syn}} = 0.001$

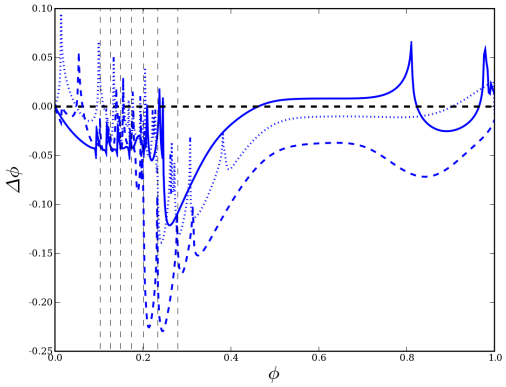

(d) $g_{\text{syn}} = 0.01$

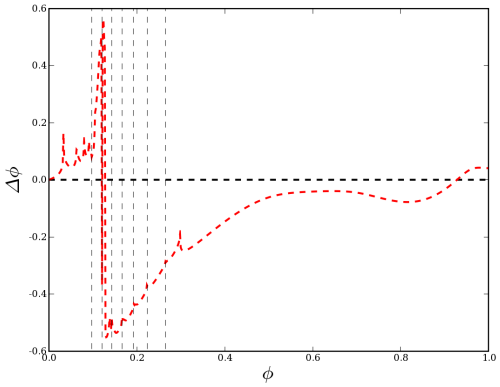

(e) $g_{\text{syn}} = 0.1$

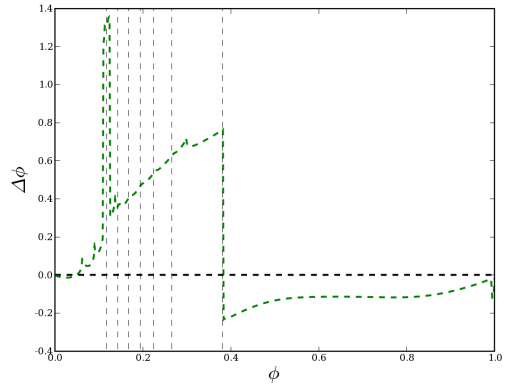

(f) $g_{\text{syn}} = 1$

Figure C.7: R15A Inhibitory Burst PRCs.

C.6 Anterior Burster (AB) Neuron Model

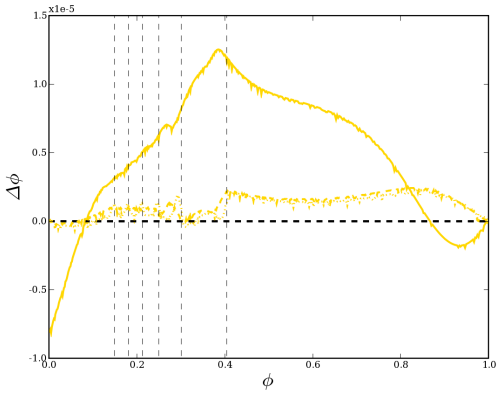

(a) $g_{\text{syn}} = 10^{-7}$

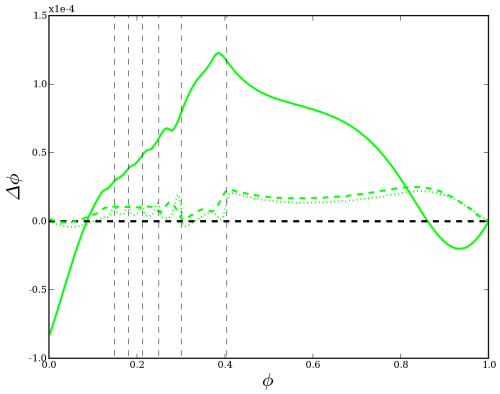

(b) $g_{\text{syn}} = 10^{-6}$

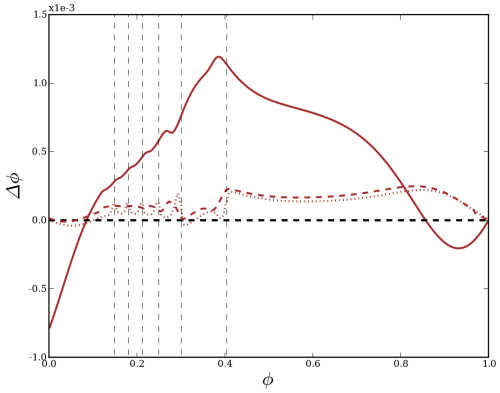

(c) $g_{\text{syn}} = 10^{-5}$

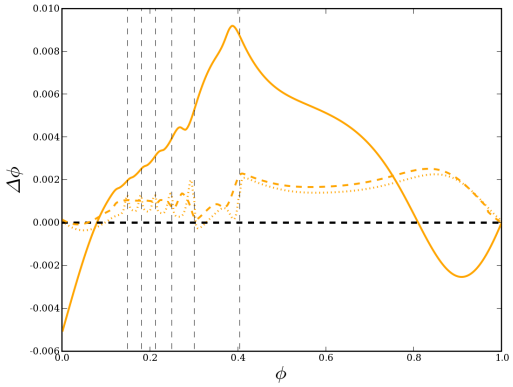

(d) $g_{\text{syn}} = 0.0001$

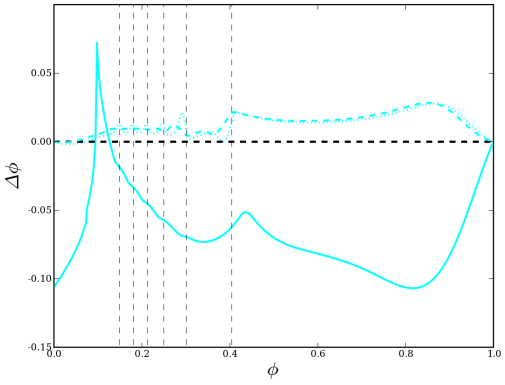

(e) $g_{\text{syn}} = 0.001$

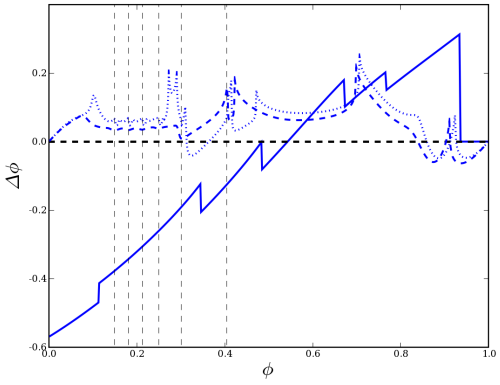

(f) $g_{\text{syn}} = 0.01$

Figure C.8: AB Excitatory Burst PRCs.

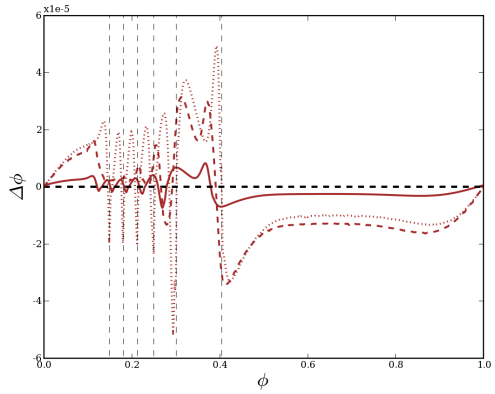

(a) $g_{\text{syn}} = 10^{-5}$

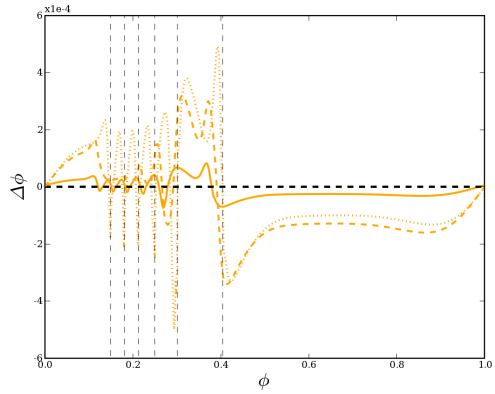

(b) $g_{\text{syn}} = 0.0001$

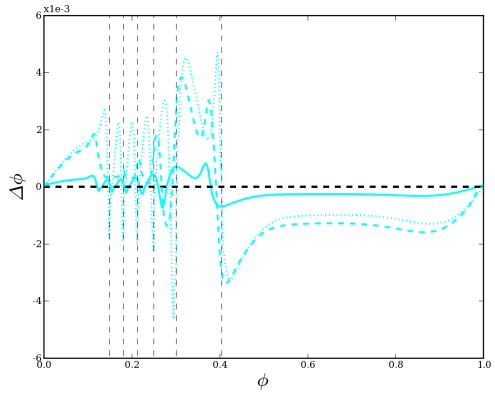

(c) $g_{\text{syn}} = 0.001$

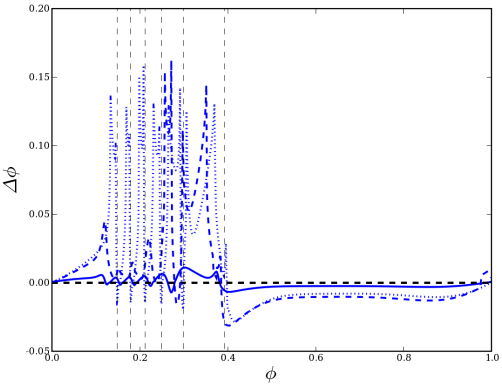

(d) $g_{\text{syn}} = 0.01$

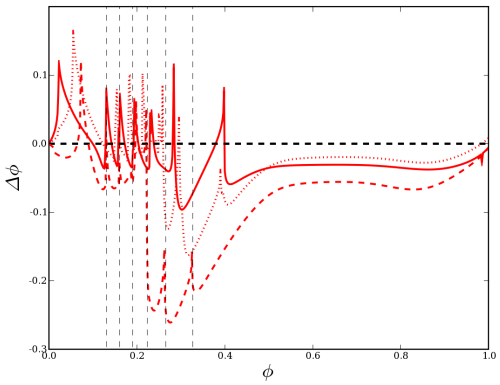

(e) $g_{\text{syn}} = 0.1$

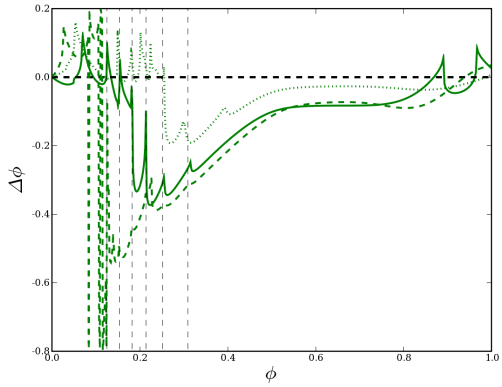

(f) $g_{\text{syn}} = 1$

Figure C.9: AB Inhibitory Burst PRCs.

C.7 Pyloric Dilator (PD) Neuron Model

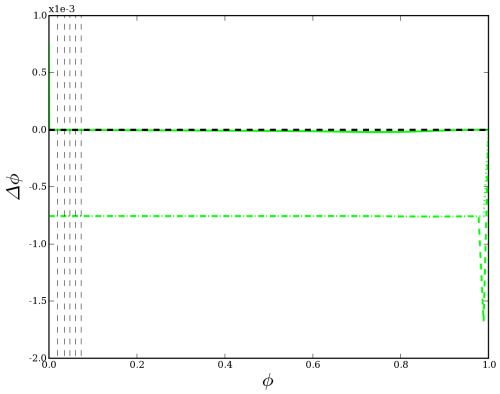

(a) $g_{\text{syn}} = 10^{-6}$

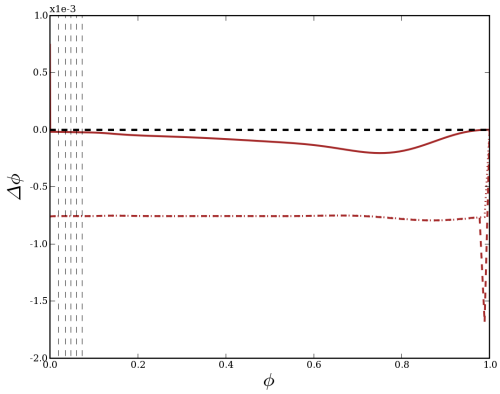

(b) $g_{\text{syn}} = 10^{-5}$

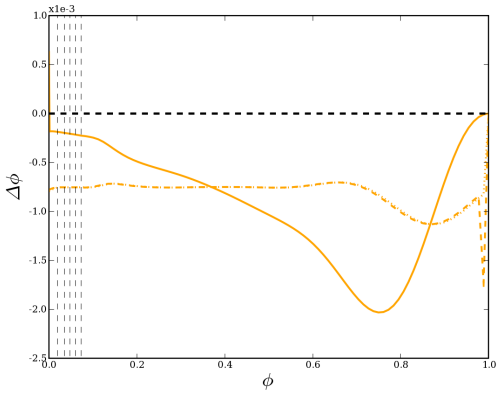

(c) $g_{\text{syn}} = 0.0001$

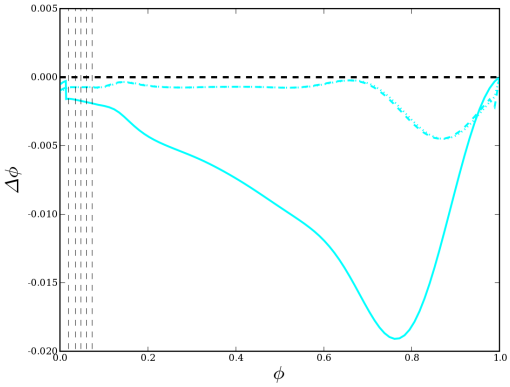

(d) $g_{\text{syn}} = 0.001$

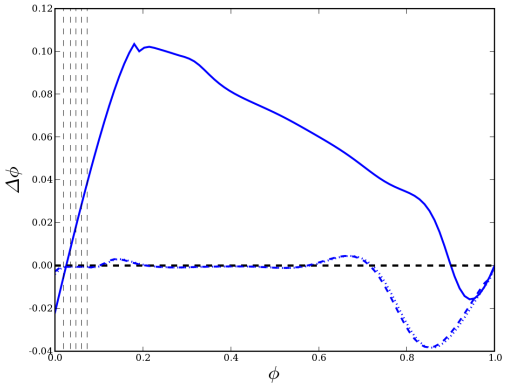

(e) $g_{\text{syn}} = 0.01$

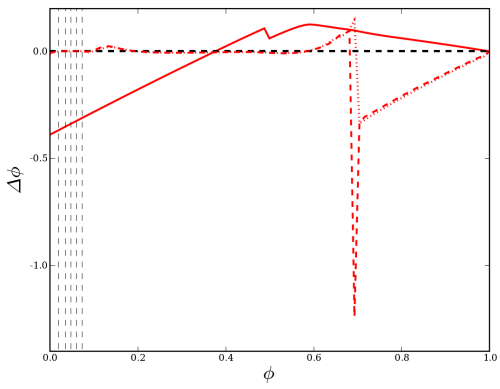

(f) $g_{\text{syn}} = 0.1$

Figure C.10: PD Excitatory Burst PRCs.

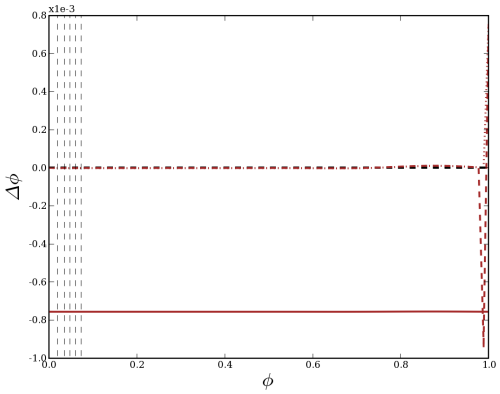

(a) $g_{\text{syn}} = 10^{-5}$

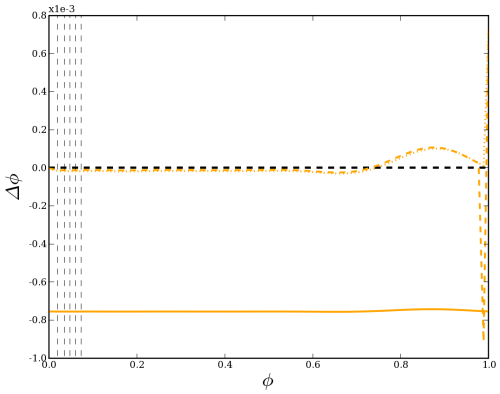

(b) $g_{\text{syn}} = 0.0001$

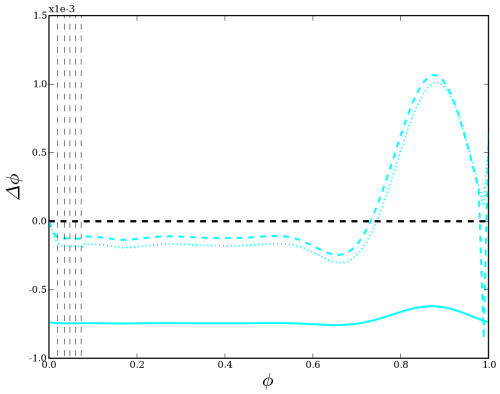

(c) $g_{\text{syn}} = 0.001$

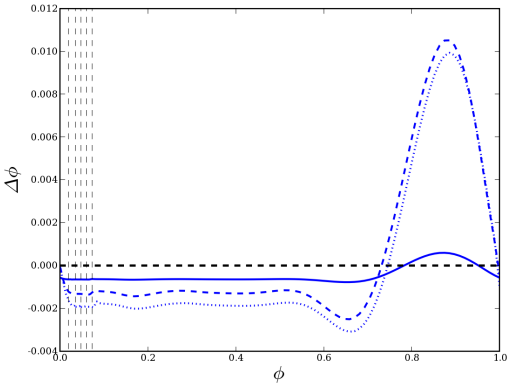

(d) $g_{\text{syn}} = 0.01$

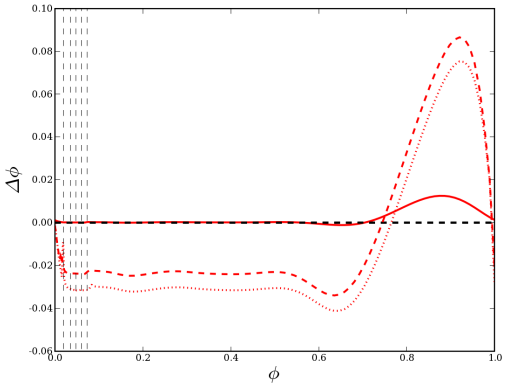

(e) $g_{\text{syn}} = 0.1$

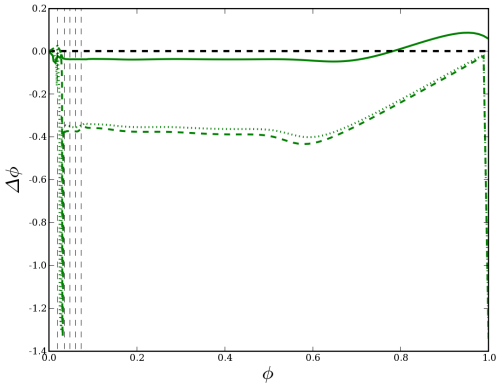

(f) $g_{\text{syn}} = 1$

Figure C.11: PD Inhibitory Burst PRCs.

BIBLIOGRAPHY

[1] Harold Abelson. The Bifurcation Interpreter: A Step Towards the Automatic Analysis of Dynamical Systems. Technical Report 888709, Massachusetts Institute of Technology, 1989.

[2] Harold Abelson, Michael Eisenberg, Matthew Halfant, Jacob Katzenelson, Elisha Sacks, Gerald J. Sussman, Jack Wisdom, and Ken Yip. Intelligence in scientific computing. *Communications of the ACM*, 32(5):546–562, 1989.

[3] Harold Abelson and Gerald J. Sussman. The Dynamicist's Workbench: I — Automatic Preparation of Numerical Experiments. Technical report, Massachusetts Institute of Technology, 1987.

[4] Corey D. Acker, Nancy Kopell, and John A. White. Synchronization of Strongly Coupled Excitatory Neurons: Relating Network Behavior to Biophysics. *Journal of Computational Neuroscience*, 15:71–90, 2003.

[5] M. Beato and A. Nistri. Interaction Between Dishinhibited Bursting and Fictive Locomotor Patterns in the Rat Isolated Spinal Cord. *Journal of Neurophysiology*, 82(5):2029–2038, November 1999.

[6] Richard Bertram, Manish Butte, Tim Kiemel, and Arthur Sherman. Topological and Phenomenological Classification of Bursting Oscillations. *Bulletin of Mathematical Biology*, 57(3):413–439, 1995.

[7] Janet Best, Alla Borisyuk, Jonathan Rubin, David Terman, and Martin Wechselberger. The Dynamic Range of Bursting in a Model Respiratory Pacemaker Network. *SIAM Journal of Applied Dynamical Systems*, 4(4):1107–1139, 2005.

[8] András Birinyi, Kornél Viszokay, Ildikó Wéber, Ole Kiehn, and Miklós Antal. Synaptic Targets of Commissural Interneurons in the Lumbar Spinal Cord of Neonatal Rats. *Journal of Comparative Neurology*, 461:429–440, 2003.

[9] Katherine Bold, Chantal Edwards, John Guckenheimer, Sabyaschi Guharay, Kathleen Hoffman, Judith Hubbard, Ricardo Oliva, and Warren Weckesser. The Forced van der Pol Equation II: Canards in the Reduced System. *SIAM Journal of Applied Dynamical Systems*, 2(4):570–608, 2003.

[10] Amitabha Bose, Yair Manor, and Farzan Nadim. The Activity Phase of Postsynaptic Neurons in a Simplified Rhythmic Network. *Journal of Computational Neuroscience*, 17(2):245–261, 2004.

[11] E. Bracci, M. Beato, and A. Nistri. Afferent Inputs Modulate the Activity of a Rhythmic Burst Generator in the Rat Disinhibited Spinal Cord *In Vitro*. *Journal of Neurophysiology*, 77(6):3157–3167, June 1997.

[12] E. Bracci, M. Beato, and A. Nistri. Extracellular K^+ Induces Locomotor-Like Patterns in the Rat Spinal Cord *In Vitro*: Comparison With NMDA or 5-HT Induced Activity. *Journal of Physiology*, 79(5):2643–2652, 1998.

[13] Romain Brette, Michelle Rudolph, Ted Carnevale, Michael Hines, David Beeman, James M. Bower, Markus Diesmann, Abigail Morrison, Philip H. Goodman, Frederick C. Harris, Jr., Milind Zirpe, Thomas Natschläger, Dejan Pecevski, Bard Ermentrout, Mikael Djurfeldt, Anders Lansner, Olivier Rochel, Thierry Vieville, Eilif Muller, Andrew P. Davison, Sami El Boustani, and Alain Destexhe. Simulation of networks of spiking neurons: A review of tools and strategies. *Journal of Computational Neuroscience*, 23(3):349–398, 2007.

[14] Eric Brown, Jeff Moehlis, and Philip Holmes. On the Phase Reduction and Response Dynamics of Neural Oscillator Populations. *Neural Computation*, 16:673–715, 2004.

[15] Eric Brown, Jeff Moehlis, Philip Holmes, Ed Clayton, Janusz Rajkowski, and Gary Ashton-Jones. The Influence of Spike Rate and Stimulus Duration on Noradrenergic Neurons. *Journal of Computational Neuroscience*, 17:13–29, 2004.

[16] Eric T. Brown. *Neural Oscillators and Integrators in the Dynamics of Decision Tasks*. PhD thesis, Princeton University, June 2004.

[17] T. Graham Brown. The Intrinsic Factors in the Act of Progression in the Mammal. *Proceedings of the Royal Society of London B*, 84(572):308–319, December 1911.

[18] T. Graham Brown. On the nature of the fundamental activity of the nervous centres; together with an analysis of the conditioning of rhythmic activity in progression, and a theory of the evolution of function in the nervous system. *Journal of Physiology*, 48(1):18–46, March 1914.

[19] Nicolas Brunel. Dynamics of Sparsely Connected Networks of Excitatory and Inhibitory Spiking Neurons. *Journal of Computational Neuroscience*, 8:183–208, 2000.

[20] Pietro-Luciano Buono. Models of central pattern generators for quadruped locomotion II. Secondary gaits. *Journal of Mathematical Biology*, 42:327–346, 2001.

[21] Pietro-Luciano Buono and Martin Golubitsky. Models of central pattern generators for quadruped locomotion I. Primary gaits. *Journal of Mathematical Biology*, 42:291–326, 2001.

[22] R. J. Butera, S. M. Johnson, C. A. Del Negro, J. Rinzel, and J. C. Smith. Dynamics of excitatory networks of bursting pacemaking neurons: Modeling and experimental studies of the repiratory central pattern generator. *Neurocomputing*, 32–33:323–330, 2000.

[23] R. J. Butera, Jr., J. W. Clark, Jr., and J. H. Byrne. Dissection and Reduction of a Modeled Bursting Neuron. *Journal of Computational Neuroscience*, 3:199–223, 1996.

[24] Robert J. Butera, John Rinzel, and Jeffrey C. Smith. Models of Respiratory Rhythm Generation in the Pre-Bötzinger Complex. I. Bursting Pacemaker Neurons. *Journal of Neurophysiology*, 81:382–397, 1999.

[25] Robert J. Butera, John Rinzel, and Jeffrey C. Smith. Models of Respiratory Rhythm Generation in the Pre-Bötzinger Complex. II. Populations of Coupled Pacemaker Neurons. *Journal of Neurophysiology*, 81:398–415, 1999.

[26] Simon J. B. Butt, Ronald M. Harris-Warrick, and Ole Kiehn. Firing Properties of Identified Interneuron Populations in the Mammalian Hindlimb Central Pattern Generator. *Journal of Neuroscience*, 22(22):9961–9971, November 2002.

[27] Simon J. B. Butt and Ole Kiehn. Functional Identification of Interneurons Responsible for Left-Right Coordination of Hindlimbs in Mammals. *Neuron*, 38:953–963, June 2003.

[28] Simon J. B. Butt, James M. Lebret, and Ole Kiehn. Organization of left-right coordination in the mammalian locomotor network. *Brain Research Reviews*, 40:107–117, 2002.

[29] Simon J. B. Butt, Line Lundfald, and Ole Kiehn. EphA4 defines a class of excitatory locomotor-related interneurons. *Proceedings of the National Academy of Sciences*, 102(39):14098–14103, September 2005.

[30] Ronald L. Calabrese. Oscillation in motor pattern-generating networks. *Current Opinion in Neurobiology*, 5:816–823, 1995.

[31] Ronald L. Calabrese, Farzan Nadim, and Øystein H. Olsen. Heartbeat Control in the Medicinal Leech: A Model System for Understanding the Origin, Coordination, and Modulation of Rhythmic Motor Patterns. *Journal of Neurobiology*, 27(3):390–402, 1995.

[32] C. C. Canavier, D. A. Baxter, J. W. Clark, and J. H. Byrne. Control of multistability in ring circuits of oscillators. *Biological Cybernetics*, 80:87–102, 1999.

[33] C. C. Canavier, R. J. Butera, R. O. Dror, D. A. Baxter, J. W. Clark, and J. H. Byrne. Phase response characteristics of model neurons determine which patterns are expressed in a ring circuit model of gait generation. *Biological Cybernetics*, 77(6):367–380, December 1997.

[34] Carmen C. Canavier. The application of phase resetting curves to the analysis of pattern generating circuits containing bursting neurons. In Stephen Coombes and Paul C. Bressloff, editors, *Bursting: The Genesis of Rhythm in the Nervous System*, chapter 8, pages 175–200. World Scientific, 2005.

[35] Lorenzo Cangiano and Sten Grillner. Mechanisms of Rhythm Generation in a Spinal Locomotor Network Deprived of Crossed Connections: The Lamprey Hemicord. *Journal of Neuroscience*, 25(4):923–935, 2005.

[36] Richard James Casey. *Periodic Orbits in Neural Models: Sensitivity Analysis and Algorithms for Parameter Estimation*. PhD thesis, Cornell University, 2004.

[37] Enrico Cataldo, Marcello Brunelli, John H. Byrne, Evyatar Ay-Ron, Yidao Cai, and Douglas A. Baxter. Computational Model of Touch Sensory Cells (T Cells) of the Leech: Role of the Afterhyperpolarization (AHP) in Activity-Dependent Conduction Failure. *Journal of Computational Neuroscience*, 18:5–24, 2005.

[38] Jean-René Cazalets, Michel Borde, and François Clarac. Localization and Organization of the Central Pattern Generator for Hindlimb Locomotion in the Newborn Rat. *Journal of Neuroscience*, 15(7):4943–4951, 1995.

[39] Jean-René Cazalets, Michel Borde, and François Clarac. The Synaptic Drive from the Spinal Locomotor Network to Motoneurons in the Newborn Rat. *Journal of Neuroscience*, 16(1):298–306, January 1996.

[40] Y. Chagnac-Amitai and B. W. Connors. Synchronized excitation and inhibition driven by intrinsically bursting neurons in neocortex. *Journal of Neurophysiology*, 62:1149–1162, 1989.

[41] A. R. Champneys, Y. A. Kuznetsov, and B. Sandstede. HomCont: An Auto86 Driver for Homoclinic Bifurcation Analysis. Technical Report 19980013152, NASA, 1995.

[42] Won Gyu Choe and John Guckenheimer. Computing periodic orbits with high accuracy. *Computer methods in applied mechanics and engineering*, 170:331–341, 1999.

[43] John R. Clay. On the Persistent Sodium Current in Squid Giant Axons. *Journal of Neurophysiology*, 89:640–644, 2003.

[44] Robert Clewley, Michael Drew Lamar, William Erik Sherwood, and John Guckenheimer. PyDSTool: An Integrated Simulation, Modeling, and Analysis Package for Dynamical Systems. http://sourceforge.net/projects/pydstool/, 2007.

[45] Robert Clewley, Horacio G. Rotstein, and Nancy Kopell. A Computational Tool for the Reduction of Nonlinear ODE Systems Possessing Multiple Scales. *SIAM Journal of Multiscale Modeling and Simulation*, 4(3):732–759, 2005.

[46] A. H. Cohen, G. B. Ermentrout, T. Kiemel, K. A. Sigvardt, and T. L. Williams. Modelling of intersegmental coordination in the lamprey central pattern generator for locomotion. *TRENDS in Neurosciences*, 15:434–438, 1992.

[47] A. H. Cohen, P. J. Holmes, and R. H. Rand. The Nature of the Coupling Between Segmental Oscillators of the Lamprey Spinal Generator for Locomotion: A Mathematical Model. *Journal of Mathematical Biology*, 13:345–369, 1982.

[48] J. Connor, D. Walter, and R. McKown. Neural repetitive firing: Modifications of the hodgkin-huxley axon suggested by experimental results from crustacean axons. *Biophysical Journal*, 18:81–102, 1977.

[49] K. C. Cowley and B. J. Schmidt. Regional Distribution of the Locomotor Pattern-Generating Network in the Neonatal Rat Spinal Cord. *Journal of Neurophysiology*, 77(1):247–259, January 1997.

[50] Mark O. Cunningham, Miles A. Whittington, Andrea Bibbig, Anita Roopun, Fiona E. N. LeBeau, Angelika Vogt, Hannah Monyer, Eberhard H. Buhl, and Roger D. Traub. A role for fast rhythmic bursting neurons in cortical gamma oscillations *in vitro*. *Proceedings of the National Academy of Sciences*, 101(18):7152–7157, 2004.

[51] Gennady S. Cymbalyuk, Quentin Gaudry, Mark A. Masino, and Ronald L. Calabrese. Bursting in Leech Heart Interneurons: Cell-Autonomous and Network-Based Mechanisms. *Journal of Neuroscience*, 22(24):10580–10592, December 2002.

[52] Gerda De Vries and Arthur Sherman. Channel Sharing in Pancreatic β-Cells Revisited: Enhancement of Emergent Bursting by Noise. *Journal of Theoretical Biology*, 207:513–530, 2000.

[53] Gerda De Vries and Arthur Sherman. From Spikers to Bursters Via Coupling: Help From Heterogeneity. *Bulletin of Mathematical Biology*, 63:371–391, 2001.

[54] Christopher A. Del Negro, Chie-Fang Hsiao, and Scott H. Chandler. Outward Currents Influencing Bursting Dynamics in Guinea Pig Trigeminal Motoneurons. *Journal of Neurophysiology*, 81:1478–1485, 1999.

[55] Christopher A. Del Negro, Chie-Fang Hsiao, Scott H. Chandler, and Alan Garfinkel. Evidence for a Novel Bursting Mechanism in Rodent Trigeminal Neurons. *Biophysical Journal*, 75(1):174–182, 1998.

[56] Christopher A. Del Negro, Sheree M. Johnson, Robert J. Butera, and Jeffrey C. Smith. Models of Respiratory Rhythm Generation in the Pre-Bötzinger Complex. III. Experimental Tests of Model Predictions. *Journal of Neurophysiology*, 86:59–74, July 2001.

[57] Christopher A. Del Negro, Naohiro Koshiya, Jr. Butera, Robert J., and Jeffrey C. Smith. Persistent Sodium Current, Membrane Properties and Bursting Behavior of Pre-Bötzinger Complex Inpiratory Neurons In Vitro. *Journal of Neurophysiology*, 88:2242–2250, 2002.

[58] Christopher A. Del Negro, Consuelo Morgado-Valle, and Jack L. Feldman. Respiratory Rhythm: An Emergent Network Property? *Neuron*, 34:821–830, May 2002.

[59] S. S. Demir, Jr. Butera, R. J., A. A. DeFranceschi, J. W. Clark Jr., and J. H. Byrne. Phase Sensitivity and Entrainment in a Modeled Bursting Neuron. *Biophysical Journal*, 72:579–594, 1997.

[60] Fabio Dercole and Yuri A. Kuznetsov. SlideCont: An Auto97 driver for bifurcation analysis of Filippov systems. *ACM Transactions on Mathematical Software*, 31(1):95–119, 2005.

[61] Alain Destexhe, Zachary F. Mainen, and Terrence J. Sejnowski. Synthesis of Models for Excitable Membranes, Synaptic Transmission and Neuromodulation Using a Common Kinetic Formalism. *Journal of Computational Neuroscience*, 1:195–230, 1994.

[62] Alain Destexhe, Zachary F. Mainen, and Terrence J. Sejnowski. Kinetic Models of Synaptic Transmission. In Christof Koch and Idan Segev, editors, *Methods in Neuronal Modeling: From Ions to Networks*, chapter 1, pages 1–26. The MIT Press, second edition, 1998.

[63] Manuel Díaz-Ríos, Daniel A. Dombeck, Watt W. Webb, and Ronald M. Harris-Warrick. Serotonin Modulates Dendritic Calcium Influx in Commissural Interneurons in the Mouse Spinal Locomotor Network. *Journal of Neurophysiology*, 98:2157–2167, June 2007.

[64] E. J. Doedel, W. Govaerts, and Yu. A. Kuznetsov. Computation of Periodic Solution Bifurcation in ODEs Using Bordered Systems. *SIAM Journal of Numerical Analysis*, 41(2):401–435, 2003.

[65] Eusebius Doedel, Alan Champneys, Thomas Fairgrieve, Yuri Kuznetsov, Bart Oldeman, Randy Paffenroth, Bjorn Sandstede, Xianjun Wang, and Chenghai Zhang. AUTO: Continuation And Bifurcation Software For Ordinary Differential Equations. Available via FTP at http://sourceforge.net/projects/auto2000/, 2007.

[66] Brent Doiron, Carlo Laing, André Longtin, and Leonard Maler. Ghost-bursting: A Novel Neuronal Burst Mechanism. *Journal of Computational Neuroscience*, 12:5–25, 2002.

[67] Mirella Dottori, Lynne Hartley, Mary Galea, George Paxinos, Mark Polizzotto, Trevor Kilpatrick, Perry F. Bartlett, Mark Murphy, Frank Köntgen, and Andrew W. Boyd. EphA4 (Sek1) receptor tyrosine kinase is required for the development of the corticospinal tract. *Proceedings of the National Academy of Sciences*, 95:13248–13253, October 1998.

[68] R. O. Dror, C. C. Canavier, R. J. Butera, J. W. Clark, and J. H. Byrne. A mathematical criterion based on phase response curves for stability in a ring of coupled oscillators. *Biological Cybernetics*, 80:11–23, 1999.

[69] Anne-Lill Eide, Joel Glover, Ole Kjaerulff, and Ole Kiehn. Characterization of Commissural Interneurons in the Lumbar Region of the Neonatal Rat Spinal Cord. *Journal of Comparative Neurology*, 403:332–345, 1999.

[70] Bard Ermentrout. Type I membranes, phase resetting curves, and synchrony. *Neural Computation*, 8:979–1001, 1996.

[71] Bard Ermentrout, Matthew Pascal, and Boris Gutkin. The Effects of Spike Frequency Adaptation and Negative Feedback on the Synchronization of Neural Oscillators. *Neural Computation*, 13:1285–1310, 2001.

[72] Bard Ermentrout and David Saunders. Phase resetting and coupling of noisy neural oscillators. *Journal of Computational Neuroscience*, 20:179–190, 2006.

[73] G. B. Ermentrout and N. Kopell. Oscillator death in systems of coupled neural oscillators. *SIAM Journal of Applied Mathematics*, 50(1):125–146, February 1990.

[74] G. B. Ermentrout and N. Kopell. Multiple pulse interactions and averaging in systems of coupled neural oscillators. *Journal of Mathematical Biology*, 29:195–217, 1991.

[75] Neil Fenichel. Asymptotic Stability with Rate Conditions. *Indiana University Mathematics Journal*, 23:1109–1137, 1975.

[76] Neil Fenichel. Geometric Singular Perturbation Theory for Ordinary Differential Equations. *Journal of Differential Equations*, 31:53–98, 1979.

[77] Richard Fitzhugh. Thresholds and Plateaus in the Hodgkin-Huxley Nerve Equations. *Journal of General Physiology*, 43:867–896, 1960.

[78] Richard Fitzhugh. Impulses and Physiological States in Theoretical Models of Nerve Membrane. *Biophysical Journal*, 1:445–466, 1961.

[79] Roberto F. Galán, G. Bard Ermentrout, and Nathaniel Urban. Efficient estimation of phase-resetting curves in real neurons and its significance for neural-network modeling. *Physical Review Letters*, 94(158101), 2005.

[80] R. M. Ghigliazza and P. Holmes. A Minimal Model of a Central Pattern Generator and Motoneurons for Insect Locomotion. *SIAM Journal of Applied Dynamical Systems*, 3(4):671–700, 2004.

[81] R. M. Ghigliazza and P. Holmes. Minimal Models of Bursting Neurons: How Multiple Currents, Conductances, and Timescales Affect Bifurcation Diagrams. *SIAM Journal of Applied Dynamical Systems*, 3(4):636–670, 2004.

[82] Jean-Marc Goaillard and Eve Marder. Dynamic Clamp Analyses of Cardiac, Endocrine, and Neural Function. *Physiology*, 21:197–207, 2006.

[83] Pranay Goel and Bard Ermentrout. Synchrony, stability, and firing patterns in pulse coupled oscillators. *Physica D*, 163:191–216, 2002.

[84] Johann Wolfgang von Goethe. *Italienische Reise*, 1817.

[85] Jorge Golowasch, Michael Casey, L. F. Abbott, and Eve Marder. Network Stability from Activity-Dependent Regulation of Neuronal Conductances. *Neural Computation*, 11:1079–1096, 1999.

[86] Jorge Golowasch, Mark S. Goldman, L. F. Abbott, and Eve Marder. Failure of Averaging in the Construction of a Conductance-Based Neuron Model. *Journal of Neurophysiology*, 87:1129–1131, 2002.

[87] M. Golubitsky, K. Josic, and E. Shea-Brown. Winding Numbers and Average Frequencies in Phase Oscillator Networks. *Journal of Nonlinear Science*, 16:201–231, 2006.

[88] M. Golubitsky, M. Nicol, and I. Stewart. Some Curious Phenomena in Coupled Cell Networks. *Journal of Nonlinear Science*, 14:207–236, 2004.

[89] Martin Golubitsky, Kresimir Josic, and Tasso J. Kaper. An unfolding theory approach to bursting in fast-slow systems. In Henk W. Broer, Bernd Krauskopf, and Gert Vegter, editors, *Global Analysis of Dynamical Systems: Festschrift dedicated to Floris Takens on the occasion of his 60th birthday*, chapter 10, pages 277–308. Institute of Physics Publishing, 2001.

[90] Martin Golubitsky, Kresimir Josic, and LieJune Shiau. Bursting in Coupled Cell Systems. In Stephen Coombes and Paul C. Bressloff, editors, *Bursting: The Genesis of Rhythm in the Nervous System*, chapter 8, pages 205–225. World Scientific, 2005.

[91] Martin Golubitsky and Ian Stewart. Nonlinear Dynamics of Networks: The Groupoid Formalism. *Bulletin of the American Mathematical Society*, 43(3):305–364, July 2006.

[92] Martin Golubitsky, Ian Stewart, and Andrei Török. Patterns of Synchrony in Coupled Cell Networks with Multiple Arrows. *SIAM Journal of Applied Dynamical Systems*, 4(1):78–100, 2005.

[93] W. Govaerts, J. Guckenheimer, and A. Khibnik. Defining Functions for Multiple Hopf Bifurcations. *SIAM Journal of Numerical Analysis*, 34(3):1269–1288, June 1997.

[94] W. Govaerts, Yu. A. Kuznetsov, and B. Sijnave. Numerical Methods for the Generalized Hopf Bifurcation. *SIAM Journal of Numerical Analysis*, 38(1):329–346, 2000.

[95] W. Govaerts and B. Sautois. Computation of the Phase Response Curve: A Direct Numerical Approach. *Neural Computation*, 18:817–847, April 2006.

[96] Andreas Griewank. A mathematical view of automatic differentiation. *Acta Numerica*, 12:321–398, 2003.

[97] Sten Grillner. The Motor Infrastructure: From Ion Channels to Neuronal Networks. *Nature Reviews Neuroscience*, 4:573–586, July 2003.

[98] J. Guckenheimer. Isochrons and Phaseless Sets. *Journal of Mathematical Biology*, 1(3):259–273, 1975.

[99] John Guckenheimer. Phase portraits of planar vector fields: computer proofs. *Experimental Mathematics*, 4(2):153–165, 1995.

[100] John Guckenheimer, Shay Gueron, and Ronald Harris-Warrick. Mapping the Dynamics of a Bursting Neuron. *Philosophical Transactions of the Royal Society of London: Biological Sciences*, 341(1298):345–359, 1993.

[101] John Guckenheimer, Ronald Harris-Warrick, Jack Peck, and Allan Willms. Bifurcation, Bursting, and Spike Frequency Adaptation. *Journal of Computational Neuroscience*, 4:257–277, 1997.

[102] John Guckenheimer, Kathleen Hoffman, and Warren Weckesser. The Forced van der Pol Equation I: The Slow Flow and Its Bifurcations. *SIAM Journal of Applied Dynamical Systems*, 2(1):1–35, 2003.

[103] John Guckenheimer and Brian Meloon. Computing Periodic Orbits and Their Bifurcations with Automatic Differentiation. *SIAM Journal of Scientific Computing*, 22(3):951–985, 2000.

[104] John Guckenheimer, Joseph H. Tien, and Allan R. Willms. Bifurcations in the Fast Dynamics of Neurons: Implications for Bursting. In Stephen Coombes and Paul C. Bressloff, editors, *Bursting: The Genesis of Rhythm in the Nervous System*, chapter 4, pages 89–122. World Scientific, 2005.

[105] Ryan N. Gutenkunst, Jordan C. Atlas, Fergal P. Casey, Robert S. Kuczenski, Joshua J. Waterfall, Chris R. Myers, and James P. Sethna. SloppyCell. http://sloppycell.sourceforge.net/, 2007.

[106] Ryan Nicholas Gutenkunst. *Sloppiness, Modeling, and Evolution in Biochemical Networks*. PhD thesis, Cornell University, 2008.

[107] Ernst Hairer, Syvert Paul Nørsett, and Gerhard Wanner. *Solving Ordinary Differential Equations I: Nonstiff Problems*. Springer Series in Computational Mathematics. Springer-Verlag, Berlin, 1987.

[108] Ernst Hairer and Gerhard Wanner. *Solving Ordinary Differential Equations II: Stiff and Differential-Algebraic Problems*. Springer Series in Computational Mathematics. Springer-Verlag, Berlin, 1991.

[109] D. Hansel, G. Mato, and C. Meunier. Synchrony in excitatory neural networks. *Neural Computation*, 7:307–337, 1995.

[110] Ronald M. Harris-Warrick and Eve Marder. Modulation of Neural Networks for Behavior. *Annual Review of Neuroscience*, 14:39–57, 1991.

[111] Ronald M. Harris-Warrick, Eve Marder, Allen I. Selverston, and Maurice Moulins, editors. *Dynamic Biological Networks*. The MIT Press, Cambridge, MA, 1992.

[112] Jeanette Hellgren, Sten Grillner, and Anders Lansner. Computer simulation of the segmental neural network generating locomotion in lamprey by using populations of network interneurons. *Biological Cybernetics*, 68(1):1–13, 1992.

[113] A. A. V. Hill, J. Lu, M. A. Masino, Ø. H. Olsen, and R. L. Calabrese. A Model of a Segmental Oscillator in the Leech Heartbeat Neuronal Network. *Journal of Computational Neuroscience*, 10:281–302, 2001.

[114] Andrew A. V. Hill, Mark A. Masino, and Ronald L. Calabrese. Model of Intersegmental Coordination in the Leech Heartbeat Neuronal Network. *Journal of Neurophysiology*, 87:1586–1602, 2002.

[115] Bertil Hille. *Ion Channels of Excitable Membranes*. Sinauer Associates, 3rd edition, 2001.

[116] Christopher A. Hinckley, Robert Hartley, Linying Wu, Andrew Todd, and Lea Ziskand-Conhaim. Locomotor-Like Rhythms in a Genetically Distinct Cluster of Interneurons in the Mammalian Spinal Cord. *Journal of Neurophysiology*, 93:1439–1449, 2005.

[117] J. L. Hindmarsh and R. M. Rose. A Model of Neuronal Bursting Using Three Coupled First Order Differential Equations. *Proceedings of the Royal Society of London B*, 221(1222):87–102, 1984.

[118] S. Hochman, L. M. Jordan, and J. F. MacDonald. N-Methy-D-Aspartate Receptor-Mediated Voltage Oscillations in Neurons Surrounding the Central Canal in Slices of Rat Spinal Cord. *Journal of Neurophysiology*, 1994.

[119] Homer. *Iliad*, *ca.* 700 BCE.

[120] Frank C. Hoppensteadt and Eugene M. Izhikevich. *Weakly Connected Neural Networks*. Springer-Verlag, New York, 1997.

[121] Hull, T. E. and Enright, W. H. and Fellen, B. M. and Sedgwick, A. E. Comparing numerical methods for ordinary differential equations. *SIAM Journal of Numerical Analysis*, 9(4):603–637, December 1972.

[122] H. Hultborn, B. A. Conway, J.-P. Gossard, R. Brownstone, B. Fedirchuk, E. D. Schomburg, M. Enríquez-Denton, and M.-C. Perreault. How Do We Approach the Locomotor Network in the Mammalian Spinal Cord? *Annals of the New York Academy of Sciences*, 860:70–82, 1998.

[123] Arieh Iserles. *A First Course in the Numerical Analysis of Differential Equations*. Cambridge Texts in Applied Mathematics. Cambridge University Press, 1996.

[124] Eugene M. Izhikevich. Neural Excitability, Spiking and Bursting. *International Journal of Bifurcation and Chaos*, 10(6):1171–1266, 2000.

[125] Eugene M. Izhikevich. *Dynamical Systems in Neuroscience: The Geometry of Excitability and Bursting*. The MIT Press, 2007.

[126] Eugene M. Izhikevich, Niraj S. Desai, Elisabeth C. Walcott, and Frank C. Hoppensteadt. Bursts as a unit of neural information: selective communication via resonance. *TRENDS in Neurosciences*, 26(3):161–167, 2003.

[127] Christopher K. R. T. Jones. Geometric Singular Perturbation Theory. In Russell Johnson, editor, *Dynamical Systems: held in Montecatini Terme, Italy, June 13–22, 1994*, volume 1609 of *Lecture Notes in Mathematics*, pages 44–118. Springer-Verlag, 1995.

[128] Stephanie R. Jones, David J. Pinto, Tasso J. Kaper, and Nancy Kopell. Alpha-Frequency Rhythms Desynchronize over Long Cortical Distances: A Modeling Study. *Journal of Computational Neuroscience*, 9:271–291, 2000.

[129] Àngel Jorba and Maorong Zou. A Software Package for the Numerical Integration of ODEs by Means of High-Order Taylor Methods. *Experimental Mathematics*, 14(1):99–117, 2005.

[130] Kresimir Josic, Eric T. Shea-Brown, and Jeff Moehlis. Isochron. *Scholarpedia*, page 2509, 2006.

[131] James Keener and James Sneyd. *Mathematical Physiology*, volume 8 of *Interdisciplinary Applied Mathematics*. Springer-Verlag, 1998.

[132] Joel Keizer, Yue-Xian Li, Stanko Stojilković, and John Rinzel. $InsP_3$-induced Ca^{2+} excitability of the endoplasmic reticulum. *Molecular Biology of the Cell*, 6:945–951, August 1995.

[133] Ole Kiehn and Ole Kjaerulff. Spatiotemporal characteristics of 5-HT and dopamine-induced rhythmic hindlimb activity in the *in vitro* neonatal rat. *Journal of Neurophysiology*, 75(4):1472–1482, 1996.

[134] Ole Kiehn, Ole Kjaerulff, Matthew C. Tresch, and Ronald M. Harris-Warrick. Contributions of intrinsic motor neuron properties to the production of rhythmic motor output in the mammalian spinal cord. *Brain Research Bulletin*, 53(5):649–659, 2000.

[135] Ole Kiehn and Klas Kullander. Central Pattern Generators Deciphered by Molecular Genetics. *Neuron*, 41:317–321, February 2004.

[136] Ole Kiehn, Keith T. Sillar, Ole Kjaerulff, and Jonathan R. McDearmid. Effects of Noradrenaline on Locomotor Rhythm-Generating Networks in the Isolated Neonatal Rat Spinal Cord. *Journal of Neurophysiology*, 82:741–746, August 1999.

[137] Ole Kjaerulff and Ole Kiehn. Distribution of Networks Generating and Coordinating Locomotor Activity in the Neonatal Rat Spinal Cord *In Vitro*: A Lesion Study. *Journal of Neuroscience*, 16(18):5777–5794, September 1996.

[138] Ole Kjaerulff and Ole Kiehn. Crossed Rhythmic Synaptic Input to Motoneurons during Selective Activation of the Contralateral Spinal Locomotor Network. *Journal of Neuroscience*, 17(24):9433–9447, December 1997.

[139] Ole Kjaerulff and Ole Kiehn. 5-HT Modulation of Multiple Inward Rectifiers in Motoneurons in Intact Preparations of the Neonatal Rat Spinal Cord. *Journal of Neurophysiology*, 85:850–593, 2001.

[140] N. Kopell and G. B. Ermentrout. Coupled Oscillators and the Design of Central Pattern Generators. *Mathematical Biosciences*, 90:87–109, 1988.

[141] Rüdiger Krahe and Fabrizio Gabbiani. Burst Firing in Sensory Systems. *Nature Reviews Neuroscience*, 5:13–24, January 2004.

[142] E. Kremer and A. Lev-Tov. Localization of the Spinal Network Associated With Generation of Hindlimb Locomotion in the Neonatal Rat and Organization of Its Transverse Coupling System. *Journal of Neurophysiology*, 77:1155–1170, March 1997.

[143] Ernst Kugel. *Phasengang in Netzwerken explodierender Nervenzellen: Modelierung von zentralen Mustergeneratoren*. PhD thesis, Universität Kornell über Kayugazee, 2008.

[144] Klas Kullander. Genetics moving to neuronal networks. *TRENDS in Neurosciences*, 28(5):239–247, May 2005.

[145] Yuri A. Kuznetsov. *Elements of Applied Bifurcation Theory*, volume 112 of *Applied Mathematical Sciences*. Springer, second edition, 1998.

[146] Carlo R. Laing, Brent Doiron, André Longtin, Liza Noonan, Ray. W. Turner, and Leonard Maler. Type I Burst Excitability. *Journal of Computational Neuroscience*, 14:329–342, 2003.

[147] Anders Lansner, Jeanette Hellgren Kotaleski, and Sten Grillner. Modeling of the Spinal Neuronal Circuitry Underlying Locomotion in a Lower Vertebrate. *Annals of the New York Academy of Sciences*, 860:239–249, 1998.

[148] Timothy J. Lewis and John Rinzel. Dynamics of Spiking Neurons Connected by Both Inhibitory and Electrical Coupling. *Journal of Computational Neuroscience*, 14:283–309, 2003.

[149] Salvador Malo. *Rigorous Computer Verification of Planar Vector Field Structure*. PhD thesis, Cornell University, 1994.

[150] Yair Manor, Farzan Nadim, L. F. Abbott, and Eve Marder. Temporal Dynamics of Graded Synaptic Transmission in the Lobster Stomatogastric Ganglion. *Journal of Neuroscience*, 17(14):5610–5621, July 1997.

[151] Selva K. Maran and Carmen C. Canavier. Using phase resetting to predict 1:1 and 2:2 locking in two neuron networks in which firing order is not always preserved. *Journal of Computational Neuroscience*, 2007.

[152] Eve Marder. From Biophysics to Models of Network Function. *Annual Review of Neuroscience*, 21:25–45, 1998.

[153] Eve Marder and Ronald L. Calabrese. Principles of Rhythmic Motor Pattern Generation. *Physiological Reviews*, 76(3):687–717, July 1996.

[154] Christopher R. Myers, Ryan N. Gutenkunst, and James P. Sethna. Python Unleashed on Systems Biology. *Computing in Science and Engineering*, pages 34–37, May-June 2007.

[155] Farzan Nadim, Victoria Booth, Amitabha Bose, and Yair Manor. Short-term synaptic dynamics promote phase maintenance in multi-phasic rhythms. *Neurocomputing*, 52–54:79–87, 2003.

[156] Farzan Nadim, Yair Manor, Nancy Kopell, and Eve Marder. Synaptic depression creates a switch that controls the frequency of an oscillatory circuit. *Proceedings of the National Academy of Sciences*, 96:8206–8211, 1999.

[157] Farzan Nadim, Øystein H. Olsen, and Ronald L. Calabrese. Modeling the Leech Heartbeat Elemental Oscillator II. Exploring the Parameter Space. *Journal of Computational Neuroscience*, 2:237–257, 1995.

[158] Farzan Nadim, Øystein H. Olsen, Erik De Schutter, and Ronald L. Calabrese. Modeling the Leech Heartbeat Elemental Oscillator I. Interactions of Intrinsic and Synaptic Currents. *Journal of Computational Neuroscience*, 2:215–235, 1995.

[159] Theoden I. Netoff, Corey D. Acker, Jonathan C. Bettencourt, and John A. White. Beyond Two-Cell Networks: Experimental Measurement of Neuronal Responses to Multiple Synaptic Inputs. *Journal of Computational Neuroscience*, 18:287–295, 2005.

[160] Theoden I. Netoff, Matthew I. Banks, Alan D. Dorval, Corey D. Acker, Julie S. Haas, Nancy Kopell, and John A. White. Synchronization in Hybrid Neuronal Networks of the Hippocampal Formation. *Journal of Neurophysiology*, 93:1197–1208, 2005.

[161] T. Nomura, S. Sato, S. Doi, J. P. Segundo, and M. D. Stiber. A modified radial isochron clock with slow and fast dynamics as a model of pacemaker neurons. *Biological Cybernetics*, 72:93–101, 1994.

[162] S. A. Oprisan, A. A. Prinz, and C. C. Canavier. Phase Resetting and Phase Locking in Hybrid Circuits of One Model and One Biological Neuron. *Biophysical Journal*, 87:2283–2298, 2004.

[163] S. A. Oprisan, V. Thirumalai, and C. C. Canavier. Dynamics from a Time Series: Can We Extract the Phase Resetting Curve from a Time Series? *Biophysical Journal*, 84:2919–2928, May 2003.

[164] Sorinel A. Oprisan and Carmen C. Canavier. The Influence of Limit Cycle Topology on the Phase Resetting Curve. *Neural Computation*, 14:1027–1057, 2002.

[165] Sorinel A. Oprisan and Carmen C. Canavier. Stability criterion for a two-neuron reciprocally coupled network based on the phase and burst resetting curves. *Neurocomputing*, 65–66:733–739, 2005.

[166] P. G. Overton and D. Clark. Burst firing in midbrain dopaminergic neurons. *Brain Research Reviews*, 25(3):312–334, December 1997.

[167] Ole Paulsen and Terrence J. Sejnowski. Natural patterns of activity and long-term synaptic plasticity. *Current Opinion in Neurobiology*, 10(2):172–180, April 2000.

[168] Eric Todd Phipps. *Taylor Series Integration of Differential Algebraic Equations: Automatic Differentiation as a Tool for Simulating Rigid Body Mechanical Systems*. PhD thesis, Cornell University, January 2003.

[169] H. M. Pinsker. *Aplysia* bursting neurons as endogenous oscillators. I. Phase-response curves for pulsed inhibitory synaptic input. *Journal of Neurophysiology*, 40:527–543, 1977.

[170] Paul F. Pinsky and John Rinzel. Intrinsic and Network Rhythmogenesis in a Reduced Traub Model for CA3 Neurons. *Journal of Computational Neuroscience*, 1:39–60, 2005.

[171] Carla M. A. Pinto and Martin Golubitsky. Central pattern generators for bipedal locomotion. *Journal of Mathematical Biology*, 53:474–489, 2006.

[172] David J. Pinto, Stephanie R. Jones, Tasso J. Kaper, and Nancy Kopell. Analysis of State-Dependent Transitions in Frequency and Long-Distance Coordination in a Model Oscillatory Cortical Circuit. *Journal of Computational Neuroscience*, 15:283–298, 2003.

[173] Astrid A. Prinz, Cyrus P. Billimoria, and Eve Marder. Alternative to Hand-Tuning Conductance-Based Models: Contstruction and Analysis of Databases of Model Neurons. *Journal of Neurophysiology*, 90:3998–4015, August 2003.

[174] Astrid A. Prinz, Dirk Bucher, and Eve Marder. Similar network activity from disparate circuit parameters. *Nature Neuroscience*, 7(12):1345–1352, December 2004.

[175] Astrid A. Prinz, Vatsala Thirumalai, and Eve Marder. The Functional Consequences of Changes in the Strength and Duration of Synaptic Inputs to Oscillatory Neurons. *Journal of Neuroscience*, 23(3):943–954, February 2003.

[176] A. Prothero and A. Robinson. On the Stability and Accuracy of One-Step Methods for Solving Stiff Systems of Ordinary Differential Equations. *Mathematics of Computation*, 28(125):145–162, January 1974.

[177] Krzystof Ptak, Greer G. Zummo, George F. Alheid, Tatiana Tkatch, D. James Surmeier, and Donald R. McCrimmon. Sodium Currents in Medullary Neurons Isolated from the Pre-Bötzinger Complex Region. *Journal of Neuroscience*, 25(21):5159–5170, May 2005.

[178] Zita Puskár and Miklós Antal. Localization of last-order premotor interneurons in the lumbar spinal cord of rats. *Journal of Comparative Neurology*, 389:377–389, 1997.

[179] Morten Raastad, Manuel Enríquez-Denton, and Ole Kiehn. Synaptic signaling in an active central network only moderately changes passive membrane properties. *Proceedings of the National Academy of Sciences*, 95(17):10251–10256, August 1998.

[180] Morten Raastad, Bruce R. Johnson, and Ole Kiehn. The Number of Postsynaptic Currents Necessary to Produce Locomotor-Related Cyclic Information in Neurons in the Neonatal Rat Spinal Cord. *Neuron*, 17:729–738, October 1996.

[181] Morten Raastad, Bruce R. Johnson, and Ole Kiehn. Analysis of EPSCs and IPSCs Carrying Rhythmic, Locomotor-Related Information in the Isolated Spinal Cord of the Neonatal Rat. *Journal of Neurophysiology*, 78:1851–1859, 1997.

[182] Morten Raastad and Ole Kiehn. Spike Coding During Locomotor Network Activity in Ventrally Located Neurons in the Isolated Spinal Cord From Neonatal Rat. *Journal of Neurophysiology*, 83:2825–2834, 2000.

[183] Mikhail I. Rabinovich, Pablo Varona, Allen I. Selverston, and Henry D. I. Abarbanel. Dynamical principles in neuroscience. *Reviews of Modern Physics*, 78:1213–1265, October-December 2006.

[184] Jan-Marino Ramirez, Andrew K. Tryba, and Fernando Peña. Pacemaker neurons and neuronal networks: an integrative view. *Current Opinion in Neurobiology*, 14:665–674, 2004.

[185] J. Rinzel. A formal classification of bursting mechanisms in excitable systems. In E. Teramoto and M. Yamaguti, editors, *Mathematical Topics in Population Biology, Morphogenesis and Neurosciences*, volume 71 of *Lecture Notes in Biomathematics*, pages 267–281. Springer, Berlin, 1987.

[186] John Rinzel and Bard Ermentrout. Analysis of Neural Excitability and Oscillations. In Christof Koch and Idan Segev, editors, *Methods in Neuronal*

Modeling: From Ions to Networks, chapter 7, pages 251–292. The MIT Press, second edition, 1998.

[187] John Rinzel and Young Seek Lee. Dissection of a model for neuronal parabolic bursting. *Journal of Mathematical Biology*, 25:653–675, 1987.

[188] Peter Roper, Joseph Callaway, and William Armstrong. Burst Initiation and Termination in Phasic Vasopressin Cells of the Rat Supraoptic Nucleus: A Combined Mathematical, Electrical, and Calcium Fluorescence Study. *Journal of Neuroscience*, 24(20):4818–4831, May 2004.

[189] R. M. Rose and J. L. Hindmarsh. A Model of a Thalamic Neuron. *Proceedings of the Royal Society of London B*, 225(1239):161–193, 1985.

[190] R. M. Rose and J. L. Hindmarsh. The assembly of ionic currents in a thalamic neuron I. The three-dimensional model. *Proceedings of the Royal Society of London B*, 237:267–288, 1989.

[191] Peter F. Rowat and Allen I. Selverston. Oscillatory Mechanisms in Pairs of Neurons Connected with Fast Inhibitory Synapses. *Journal of Computational Neuroscience*, 4:103–127, 1997.

[192] I. A. Rybak, J. F. R. Paton, R. F. Rogers, and W. M. St.-John. Generation of the respiratory rhythm: state-dependency and switching. *Neurocomputing*, 44–46:605–614, 2002.

[193] Bart Sautois, Stephen R. Soffe, Wen-Chang Li, and Alan Roberts. Role of type-specific neuron properties in a spinal cord motor network. *Journal of Computational Neuroscience*, 23:59–77, 2007.

[194] Alfons Schnitzler and Joachim Gross. Normal and Pathological Oscillatory Communication in the Brain. *Nature Reviews Neuroscience*, 6:285–296, April 2005.

[195] Murat Sekerli and Robert J. Butera. Oscillations in a Simple Neuromechanical System: Underlying Mechanisms. *Journal of Computational Neuroscience*, 19:181–197, 2005.

[196] L. F. Shampine and C. W. Gear. A User's View of Solving Stiff Ordinary Differential Equations. *SIAM Review*, 21(1):1–17, January 1979.

[197] A.A. Sharp, M. B. O'Neil, L. F. Abbott, and E. Marder. The dynamic clamp: artificial conductances in biological neurons. *TRENDS in Neurosciences*, 16:389–394, 1993.

[198] A.A. Sharp, M. B. O'Neil, L. F. Abbott, and E. Marder. Dynamic clamp: computer-generated conductances in real neurons. *Journal of Neurophysiology*, 69:992–995, 1993.

[199] A.A. Sharp, F. K. Skinner, and E. Marder. Mechanisms of oscillation in dynamic clamp constructed two-cell half-center circuits. *Journal of Neurophysiology*, 1996.

[200] A. Sherman, J. Rinzel, and J. Keizer. Emergence of organized bursting in clusters of pancreatic beta-cells by channel sharing. *Biophysical Journal*, 54(3):411–425, September 1988.

[201] Arthur Sherman. Anti-phase, Asymmetric and Aperiodic Oscillations in Excitable Cells—I. Coupled Bursters. *Bulletin of Mathematical Biology*, 56(5):811–835, 1994.

[202] Arthur S. Sherman, Yue-Xian Li, and Joel E. Keizer. *Computational Cell Biology*, volume 20 of *Interdisciplinary Applied Mathematics*, chapter Whole-Cell Models. Springer-Verlag, 2002.

[203] S. Murray Sherman. Tonic and burst firing: dual modes of thalamocortical relay. *TRENDS in Neurosciences*, 24(2):122–126, February 2001.

[204] C. S. Sherrington. Flexion-reflex of the limb, crossed extension-reflex, and reflex stepping and standing. *Journal of Physiology*, 40(1–2):28–121, April 1910.

[205] C. S. Sherrington. Further observations on the production of reflex stepping by combination of reflex excitation with reflex inhibition. *Journal of Physiology*, 47(3):196–214, November 1913.

[206] Frances K. Skinner, Nancy Kopell, and Eve Marder. Mechanisms for Oscillation and Frequency Control in Reciprocally Inhibitory Model Neural Networks. *Journal of Computational Neuroscience*, 1(69–87), 1994.

[207] P. Smolen, J. Rinzel, and A. Sherman. Why pancreatic islets burst but single beta cells do not. The heterogeneity hypothesis. *Biophysical Journal*, 64(6):1668–1680, June 1993.

[208] Cristina Soto-Treviño, Pascale Rabbah, Eve Marder, and Farzan Nadim. Computational Model of Electrically Coupled, Intrinsically Distinct Pacemaker Neurons. *Journal of Neurophysiology*, 94:590–604, 2005.

[209] Youssef Sqalli-Houssaini, Jean-René Cazalets, and François Clarac. Oscillatory Properties of the Central Pattern Generator for Locomotion in Neonatal Rats. *Journal of Neurophysiology*, 70(2):803–813, August 1993.

[210] Ian Stewart, Martin Golubitsky, and Marcus Pivato. Symmetry Groupoids and Patterns of Synchrony in Coupled Cell Networks. *SIAM Journal of Applied Dynamical Systems*, 2(4):609–646, 2003.

[211] Mathis Frøshaug Stokke, Ulla Vig Nissen, Joel C. Glover, and Ole Kiehn. Projection Patterns of Commissural Interneurons in the Lumbar Spinal Cord of the Neonatal Rat. *Journal of Comparative Neurology*, 447:349–359, 2002.

[212] Attila Szücs and Allen I. Selverston. Consistent Dynamics Suggests Tight Regulation of Biophysical Parameters in a Small Network of Bursting Neurons. *Journal of Neurobiology*, 66:1584–1601, 2006.

[213] Abraha Taddese and Bruce P. Bean. Subthreshold Sodium Current from Rapidly Inactivating Sodium Channels Drives Spontaneous Firing of Tuberomammillary Neurons. *Neuron*, 33:587–600, February 2002.

[214] T. Tateno and H. P. C. Robinson. Phase Resetting Curves and Oscillatory Stability in Interneurons of Rat Somatosensory Cortex. *Biophysical Journal*, 92:683–695, 2007.

[215] Hitoshi Tatsumi and Ryoji Suzuki. Phase Plane Description of Crayfish Swimmeret Oscillator. *Biological Cybernetics*, 47:59–68, 1983.

[216] David Terman. Chaotic Spikes Arising from a Model of Bursting in Excitable Membranes. *SIAM Journal of Applied Mathematics*, 51(5):1418–1450, October 1991.

[217] David Terman. The Transition from Bursting to Continuous Spiking in Excitable Membrane Models. *Journal of Nonlinear Science*, 2:135–182, 1992.

[218] Vatsala Thirumalai, Astrid A. Prinz, Christian D. Johnson, and Eve Marder. Red Pigment Concentrating Hormone Strongly Enhances the Strength of the Feedback to the Pyloric Rhythm Oscillator But Has Little Effect on Pyloric Rhythm Period. *Journal of Neurophysiology*, 95:1762–1770, November 2006.

[219] Joseph Hua Tien. *Optimization for Bursting Neural Models*. PhD thesis, Cornell University, January 2007.

[220] Matthew C. Tresch and Ole Kiehn. Coding of Locomotor Phase in Populations of Neurons in Rostral and Caudal Segments of the Neonatal Rat Lumbar Spinal Cord. *Journal of Neurophysiology*, 82(6):3563–3574, December 1999.

[221] Matthew C. Tresch and Ole Kiehn. Population Reconstruction of the Locomotor Cycle From Interneuron Activity in the Mammalian Spinal Cord. *Journal of Neurophysiology*, 83:1972–1978, 2000.

[222] Matthew C. Tresch and Ole Kiehn. Synchronization of Motor Neurons during Locomotion in the Neonatal Rat: Predictors and Mechanisms. *Journal of Neuroscience*, 22(22):9997–10008, November 2002.

[223] C. van Vreeswijk and H. Sompolinsky. Chaos in Neuronal Networks with Balanced Excitatory and Inhibitory Activity. *Science*, 274(5293):1724–1726, December 1996.

[224] Carl van Vreeswijk, L. F. Abbott, and G. Bard Ermentrout. When Inhibition not Excitation Synchronizes Neural Firing. *Journal of Computational Neuroscience*, 1:313–321, 1994.

[225] Virgil. *Aeneid*, *ca.* 19 BCE.

[226] Kurt Vonnegut, Jr. *Palm Sunday*. Dell Publishing, 1981.

[227] Tom Wadden, Jeanette Hellgren, Anders Lansner, and Sten Grillner. Intersegmental coordination in the lamprey: simulations using a network model without segmental boundaries. *Biological Cybernetics*, 76(1):1–9, 1997.

[228] DeLiang Wang and David Terman. Locally excitatory globally inhibitory oscillator networks. *IEEE Transactions on Neural Networks*, 6(1):283–286, January 1995.

[229] Stephen Wiggins. *Normally Hyperbolic Invariant Manifolds in Dynamical Systems*, volume 105 of *Applied Mathematical Sciences*. Springer-Verlag, 1994.

[230] Stephen R. Williams and Greg J. Stuart. Mechanisms and consequences of action potential burst firing in rat neocortical pyramidal neurons. *Journal of Neurophysiology*, 521.2:467–482, 1999.

[231] Allan R. Willms, Ronald M. Harris-Warrick, and John Guckenheimer. An Improved Parameter Estimation Method for Hodgkin-Huxley Models. *Journal of Computational Neuroscience*, 6:145–168, 1999.

[232] Hugh R. Wilson and Jack D. Cowan. Excitatory and Inhibitory Interactions in Localized Populations of Model Neurons. *Biophysical Journal*, 12:1–24, 1972.

[233] Jennifer M. Wilson, Daniel A. Dombeck, Manuel Díaz-Ríos, Ronald M. Harris-Warrick, and Robert M. Brownstone. Two-Photon Calcium Imaging of Network Activity in XFP-Expressing Neurons in the Mouse. *Journal of Neurophysiology*, 97:3118–3125, 2007.

[234] Jennifer M. Wilson, Robert Hartley, David J. Maxwell, Andrew J. Todd, Ivo Lieberam, Julia A. Kaltschmidt, Yutaka Yoshida, Thomas M. Jessell, and Robert M. Brownstone. Conditional Rhythmicity of Ventral Spinal Interneurons Defined by Expression of the Hb9 Homeodomain Protein. *Journal of Neuroscience*, 25(24):5710–5719, June 2005.

[235] A. T. Winfree. Patterns of Phase Compromise in Biological Cycles. *Journal of Mathematical Biology*, 1:73–95, 1974.

[236] Arthur T. Winfree. *The Geometry of Biological Time*. Springer, second edition, 2001.

[237] J. Wolfart, D. Debay, G. Le Masson, A. Destexhe, and T. Bal. Synaptic background activity controls spike transfer from thalamus to cortex. *Nature Neuroscience*, 8:1760–1767, 2005.

[238] N. Yokoyama, Romero M. I., C. A. Cowan, P. Galvan, F. Helmbacher, P. Charnay, L. F. Parada, and M. Henkemeyer. Forward signaling mediated by ephrin-B3 prevents contralateral corticospinal axons from recrossing the spinal cord midline. *Neuron*, 29(1):85–97, January 2001.

[239] Ying Zhang, Ricardo Oliva, Günter Gisselmann, Hans Hatt, John Guckenheimer, and Ronald M. Harris-Warrick. Overexpression of a Hyperpolarization-Activated Cation Current (I_h) Channel Gene Modifies the Firing Activity of Identified Motor Neruons in a Small Neural Network. *Journal of Neuroscience*, 23(27):9059–9067, October 2003.

[240] M. Zheng, W. O. Friessen, and T. Iwasaki. Systems-level modeling of neuronal circuits for leech swimming. *Journal of Computational Neuroscience*, 22:21–38, 2007.

[241] Guisheng Zhong, Manuel Díaz-Ríos, and Ronald M. Harris-Warrick. Intrinsic and Functional Differences among Commissural Interneurons during Fictive Locomotion and Serotonergic Modulation in the Neonatal Mouse. *Journal of Neuroscience*, 26(24):6509–6517, June 2006.

[242] Guisheng Zhong, Manuel Díaz-Ríos, and Ronald M. Harris-Warrick. Serotonin Modulates the Properties of Ascending Commissural Interneurons in the Neonatal Mouse Spinal Cord. *Journal of Neurophysiology*, 95:1545–1555, 2006.

[243] Guisheng Zhong, Mark A. Masino, and Ronald M. Harris-Warrick. Persistent Sodium Currents Participate in Fictive Locomotion Generation in Neonatal Mouse Spinal Cord. *Journal of Neuroscience*, 27(17):4507–4518, April 2007.